Distribution Agreement

In presenting this thesis or dissertation as a partial fulfillment of the requirements for an advanced degree from Emory University, I hereby grant to Emory University and its agents the non-exclusive license to archive, make accessible, and display my thesis or dissertation in whole or in part in all forms of media, now or hereafter known, including display on the world wide web. I understand that I may select some access restrictions as part of the online submission of this thesis or dissertation. I retain all ownership rights to the copyright of the thesis or dissertation. I also retain the right to use in future works (such as articles or books) all or part of this thesis or dissertation.

Signature:

_____   _____

Chen Qu   Date

Potential Energy Surfaces and the Applications to Reaction Dynamics and Molecular Vibrations

by
Chen Qu
Doctor of Philosophy
Chemistry

_____

Joel M. Bowman, Ph.D
Advisor

_____

Michael C. Heaven, Ph.D
Committee Member

_____

James T. Kindt, Ph.D
Committee Member

Accepted:

_____

Lisa A. Tedesco, Ph.D.
Dean of the James T. Laney School of Graduate Studies

_____

Date

Potential Energy Surfaces and the Applications to Reaction Dynamics and Molecular Vibrations

by

Chen Qu
B.S., University of Science and Technology of China, 2011

Advisor: Joel M. Bowman, Ph.D.

An abstract of
A dissertation submitted to the Faculty of the
James T. Laney School of Graduate Studies of Emory University
in partial fulfillment of the requirements for the degree of
Doctor of Philosophy
in Chemistry
2017

Abstract

Potential Energy Surfaces and the Applications to Reaction Dynamics and Molecular Vibrations

By Chen Qu

The importance of potential energy surface cannot be overemphasized due to the role it plays in theoretical chemistry. With the potential, the kinetics and dynamics of chemical reactions can be modeled, and molecular eigenenergies and eigenstates can be calculated, which could be used to explain molecular spectroscopy.

In this work, the analytical representations of potential energy surfaces for molecules and clusters such as H_7^+, CH_3OH, and formic acid dimer were constructed by fitting to tens of thousands of scattered *ab initio* energies. These potential energy surfaces were employed in subsequent studies of dynamics or spectroscopy. The potential energy surfaces for hydrogen and methane clathrate hydrates were obtained by many-body expansion strategy, and the binding energies of $(H_2)_n(H_2O)_{20}$ and $(H_2)_n(H_2O)_{24}$ and barrier height of H_2 diffusion in clathrates has been investigated using the many-body potential. The invariance of potential when permuting the like atoms is incorporated in the analytical expressions, following the method developed by Braams, Bowman, and co-workers.

Molecular vibrational properties of H_7^+, formic acid dimer and CH_4 confined in clathrate cages have been investigated. Diffusion Monte Carlo calculations were applied to characterize the vibrational ground state properties, while the vibrational eigenenergies and eigenstates were calculated using the vibrational self-consistent and virtual-state configuration interaction method. The treatment of the large amplitude motion and the reduction of dimensionality are highlighted in these calculations.

The analytical potential energies were also used in studies of the dynamics of chemical reactions. Molecular dynamics calculations was performed to simulate the unimolecular decomposition of methanol to estimate the branching ratio of different product channels. Similar simulations have been carried out to model the dissociation of vinyl chloride that produces cold vinylidene, however, using direct "on-the-fly" potential. In addition to these applications, the use of adiabatic switching method to prepare initial condition in quasi-classical trajectories has been investigated.

Potential Energy Surfaces and the Applications to Reaction Dynamics and Molecular Vibrations

by

Chen Qu
B.S., University of Science and Technology of China, 2011

Advisor: Joel M. Bowman, Ph.D.

A dissertation submitted to the Faculty of the
James T. Laney School of Graduate Studies of Emory University
in partial fulfillment of the requirements for the degree of
Doctor of Philosophy
in Chemistry
2017

Acknowledgements

Of the many people who helped and supported me a lot during the past six years, I would like to first deliver my thanks to my advisor, Dr. Joel M. Bowman, without whom this dissertation would not be possible, for his patient guidance and continuous support. He not only helped me with his knowledge in research projects, but also showed me what good science is and how to pursue it.

I would like to thank Dr. James T. Kindt and Dr. Michael C. Heaven for their time and helpful suggestions. I would also like to thank Dr. Stuart Carter for his patient guidance on the code "Multimode".

I must also thank all the current and past members of the Bowman group: Dr. Yimin Wang, Dr. Bina Fu, Dr. Yongchang Han, Dr. Zahra Homayoon, Dr. Riccardo Conte, Dr. John S. Mancini, Dr. Hanchao Liu, Dr. Xiaohong Wang, Qi Yu, Qingfeng Wang, especially Dr Hanchao Liu and Dr. Xiaohong Wang for all the valuable discussions, and Dr. Yimin Wang for her help and effort to solve problems on the computation facilities. I'm also grateful to Ann Dasher and Susan Browne for their coordination work.

Last but not least, I would like to deliver my appreciation to my parents, for their unconditional love and support.

Table of Contents

List of Tables

List of Figures

Citations to Previously Published Work

Chapter 5 contains research from three publications:

1. Qu, C.; Conte, R.; Houston, P. L.; Bowman, J. M. "Plug and Play" Full-Dimensional ab Initio Potential Energy and Dipole Moment Surfaces and Anharmonic Vibrational Analysis for CH_4-H_2O. *Phys. Chem. Chem. Phys.* **2015**, *17*, 8172

2. Conte, R.; Qu, C.; Bowman, J. M. Permutationally Invariant Fitting of Many-Body, Non-covalent Interactions with Application to Three-Body Methane-Water-Water. *J. Chem. Theory Comput.* **2015**, *11*, 1631–1638

3. Homayoon, Z.; Conte, R.; Qu, C.; Bowman, J. M. Full-Dimensional, High-Level ab Initial Potential Energy Surfaces for $H_2(H_2O)$ and $H_2(H_2O)_2$ with Application to Hydrogen Clathrate Hydrates. *J. Chem. Phys.* **2015**, *143*, 084302

Chapter 7 contains research from three publications:

1. Barragán, P.; Pérez de Tudela, R.; Qu, C.; Prosmiti, R.; Bowman, J. M. Full-Dimensional Quantum Calculations of the Dissociation Energy, Zero-Point, and 10 K Properties of H_7^+/D_7^+ Clusters Using an ab Initio Potential Energy Surface. *J. Chem. Phys.* **2013**, *139*, 024308

2. Qu, C.; Prosmiti, R.; Bowman, J. M. MULTIMODE Calculations of the Infrared Spectra of H_7^+ and D_7^+ Using ab Initio Potential Energy and Dipole Moment Surfaces. *Theor. Chem. Acc.* **2013**, *132*, 1413

3. Qu, C.; Bowman, J. M. Diffusion Monte Carlo Calculations of Zero-Point Structures of Partially Deuterated Isotopologues of H_7^+. *J. Phys. Chem. B* **2014**, *118*, 8221–8226

Large portion of Chapter 8 appear in one publication:

1. Qu, C.; Bowman, J. M. An ab Initio Potential Energy Surface for the Formic Acid Dimer: Zero-Point Energy, Selected Anharmonic Fundamental Energies, and Ground-State Tunneling Splitting Calculated in Relaxed 1–4-Mode Subspaces. *Phys. Chem. Chem. Phys.* **2016**, *18*, 24835–24840

Chapter 9 has been published as:

1. Qu, C.; Bowman, J. M. Ab Initio, Embedded Local-Monomer Calculations of Methane Vibrational Energies in Clathrate Hydrates. *J. Phys. Chem. C* **2016**, *120*, 3167–3175

Part of Chapter 10 has been published as:

1. Qu, C.; Bowman, J. M. Full-Dimensional, ab Initio Potential Energy Surface for $CH_3OH \rightarrow CH_3 + OH$. *Mol. Phys.* **2013**, *111*, 1964–1971

Chapter 11 consists of the study from one publication:

1. Fernando, R.; Qu, C.; Bowman, J. M.; Field, R. W.; Suits, A. G. Does Infrared Multiphoton Dissociation of Vinyl Chloride Yield Cold Vinylidene? *J. Phys. Chem. Lett.* **2015**, *6*, 2457–2462

Chapter 12 has been published as:

1. Qu, C.; Bowman, J. M. Revisiting Adiabatic Switching for Initial Conditions in Quasi-Classical Trajectory Calculations: Application to CH_4. *J. Phys. Chem. A* **2016**, *120*, 4988–4993

Chapter 1

Introduction

In chemistry, systems we are interested in all consist of electrons and nuclei. The motions of electrons and nuclei are governed by the Schrödinger equation, except in extreme cases. In principle, if we are able to solve the Schrödinger equation exactly, we solve the mysteries in any chemical processes. Unfortunately, however, even with the rapidly growing power in computers, solving the Schrödinger equation exactly for systems only consist of a couple of atoms is still almost impossible. Therefore, various approximations have to be made to simplify the equation.

The most important approximation made is the Born-Oppenheimer approximation, which is based on the fact that the mass of an electron is much smaller than that of a nucleus. Because of the great difference in mass, the fast electrons can almost instantaneously adapt to the slow displacement of the nuclei. Therefore, instead of solving the Schrödinger equation simultaneously for all the electrons and nuclei, we can apply a two-step approach. The first step is to solve the Schrödinger equation for the electrons at a set of instantaneous nuclear configurations. This allows us to construct the potential energy curve of a diatomic molecule, and in general, a potential energy surface (PES)

for any polyatomic species. The second step is to solve the Schrödinger equation of the nuclei, using the PES obtained in the first step. In most cases, the Born-Oppenheimer approximation is exceptionally good, and the research presented in this dissertation is based on this approximation.

Even with the separation of the electronic and nuclear Schrödinger equation, solving either one of them is still very challenging. To solve the electronic part, a popular approach starts from the Hartree-Fock approximation, in which any one electron is assumed to move in an "average" potential due to all the other electrons. More accurate methods such as Møllet-Plesset perturbation (MP_n), coupled-cluster, and configuration interaction are all based on the Hartree-Fock theory. Another popular method worth mentioning is the density functional theory, in which functionals of electron density is used instead of the traditional wavefunction. These methods for the electronic structure problem are available in most of the quantum chemistry packages.

Next we consider the Schrödinger equation of the nuclei. When the Born-Oppenheimer approximation still holds, in principle, the dynamics of any molecule can be revealed if the time-dependent nuclear Schrödinger equation is solved, and the molecular eigenstates and eigenenergies can be obtained if the time-independent Schrödinger equation is solved. The computational cost of solving these problems increases exponentially with increasing degrees of freedom, and this is the "curse of dimensionality". (Note that the electronic problem in fact also suffers from this "curse".) Many efforts have been made to tackle the dimensionality problem: in dynamics simulations, the nuclei are often treated as classical particles that are governed by Newton's equation of motion, when the nuclear quantum effect is not significant, and thus greatly reduces the computational cost; in calculations of the molecular eigenstates, reduced-dimensional models have been proposed.

The research presented in this work basically follows the procedure described above.

I first perform electronic structure calculations to construct the PES, and then study the dynamics and molecular vibrations using the PES. This dissertation is structured into four parts. The first part describes the theories and computational methods I applied in all my simulations. In Chapter 2, the Born-Oppenheimer approximation is explained in details, and the method to construct the analytical representation of the PES is presented. The algorithms and methods used in vibrational calculations and dynamics simulations are described in Chapter 3 and 4, respectively. The second part emphasizes on the construction of analytical PESs for complex systems. In Chapter 5, I describe the strategy and the procedures to construct PESs for clathrate hydrates and Chapter 6 focuses on the application of the clathrate PES to determine energetics such as the binding energy of H_2 molecules with water cages, and the barrier of H_2 diffusion in clathrates. In the third part I present my work on molecular vibrations, with particular emphasis on "floppy" molecules and reduced-dimensional models. Chapter 7 focuses on the molecular ion H_7^+. In this study, the vibrational ground state properties and proton exchange were investigated, and the infrared spectra of H_7^+ and D_7^+ were calculated. Chapter 8 involves the calculations of the ground state tunneling splitting and the anharmonic fundamental frequencies of formic acid dimer, using reduced-dimensionality approaches. In Chapter 9, I present the calculations of frequency shifts when a methane molecule is confined in different clathrate cages. The last part covers my study on dynamics of gas-phase molecules. Chapter 10 and 11 describe the unimolecular dissociation of methanol and vinyl chloride respectively. While in Chapter 12, I investigated the application of adiabatic switching method for preparing the initial conditions in quasiclassical trajectory calculations.

Part I

Theories and Methods

Chapter 2

Potential Energy Surface

2.1 Born-Oppenheimer Approximation

In atomic units, the nonrelativistic Hamiltonian for a molecule is:

$$\hat{H} = -\frac{1}{2}\sum_i \nabla_i^2 - \sum_A \frac{1}{2M_A}\nabla_A^2 - \sum_{i,A}\frac{Z_A}{r_{iA}} + \sum_{A<B}\frac{Z_A Z_B}{r_{AB}} + \sum_{i<j}\frac{1}{r_{ij}}, \qquad (2.1)$$

where A, B refer to the nuclei and i, j refer to the electrons; M_A and Z_A are the mass and charge of nucleus A. In a more compact notation, the Hamiltonian can be written as

$$\hat{H} = \hat{T}_N(\boldsymbol{R}) + \hat{T}_e(\boldsymbol{r}) + \hat{V}_{eN}(\boldsymbol{r}, \boldsymbol{R}) + \hat{V}_{ee}(\boldsymbol{r}) + \hat{V}_{NN}(\boldsymbol{R}), \qquad (2.2)$$

where $\boldsymbol{R}$ denotes the set of nuclear coordinates and $\boldsymbol{r}$ is the set of electronic coordinates; $\hat{T}$ and $\hat{V}$ are the kinetic energy and potential operators, respectively.

First we neglect the kinetic energy operator of the nuclei, $\hat{T}_N(\boldsymbol{r})$, because it is more than three orders of magnitude smaller than $\hat{T}_e(\boldsymbol{r})$. Then according to Born-Oppenheimer approximation, the electrons can almost instantaneously respond to the nuclei motion,

and we make the term $\hat{V}_{eN}(\boldsymbol{r}, \boldsymbol{R})$ parametrically depend on $\boldsymbol{R}$. That is, we can fix the $\boldsymbol{R}$ at a certain value $\boldsymbol{R_0}$, and solve for the electronic wavefunction $\Psi(\boldsymbol{r}; \boldsymbol{R_0})$:

$$\hat{H}_{el}\Psi(\boldsymbol{r}; \boldsymbol{R_0}) = E_{el}\Psi(\boldsymbol{r}; \boldsymbol{R_0}), \tag{2.3}$$

where

$$\hat{H}_{el} = \hat{T}_e(\boldsymbol{r}) + \hat{V}_{eN}(\boldsymbol{r}; \boldsymbol{R_0}) + \hat{V}_{ee}(\boldsymbol{r}) + \hat{V}_{NN}(\boldsymbol{R_0}). \tag{2.4}$$

When we repeat this for a set of $\boldsymbol{R_0}$, we obtain the potential energy surface (PES) of the molecule.

Suppose we have already solved Eq. 2.3 and obtained a set of eigenfunctions $\Psi_n(\boldsymbol{r}; \boldsymbol{R})$ and eigenvalues $E_n(\boldsymbol{R})$, i.e.

$$\hat{H}_{el}\Psi_n(\boldsymbol{r}; \boldsymbol{R}) = E_n(\boldsymbol{R})\Psi_n(\boldsymbol{r}; \boldsymbol{R}). \tag{2.5}$$

The exact solution of the original Hamiltonian in Eq. 2.2 can always be written in an infinite expansion

$$\Phi(\boldsymbol{r}, \boldsymbol{R}) = \sum_k \Psi_k(\boldsymbol{r}; \boldsymbol{R})\chi_k(\boldsymbol{R}). \tag{2.6}$$

Insert this expansion into the original Schrödinger equation, multiply by $\Psi_n(\boldsymbol{r}; \boldsymbol{R})^*$, and integrate over the electronic coordinates $\boldsymbol{r}$, we obtain

$$\left[\hat{T}_N(\boldsymbol{R}) + E_n(\boldsymbol{R})\right]\chi_n(\boldsymbol{R}) - \sum_k \sum_A \left[\frac{1}{M_A}d_{nk}^A(\boldsymbol{R}) \cdot \nabla_A - \frac{1}{2M_A}D_{nk}^A(\boldsymbol{R})\right]\chi_k(\boldsymbol{R}) = \mathcal{E}\chi_n(\boldsymbol{R}), \tag{2.7}$$

where $d_{nk}^A(\boldsymbol{R}) = \langle\Psi_n(\boldsymbol{r}; \boldsymbol{R})|\nabla_A|\Psi_k(\boldsymbol{r}; \boldsymbol{R})\rangle$ and $D_{nk}^A(\boldsymbol{R}) = \langle\Psi_n(\boldsymbol{r}; \boldsymbol{R})|\nabla_A^2|\Psi_k(\boldsymbol{r}; \boldsymbol{R})\rangle$ are called nonadiabatic couplings. In most cases, the couplings are very small and can be

safely neglected, and we obtain the following equation for the nuclear wavefunction:

$$\left[\hat{T}_N(\boldsymbol{R}) + E_n(\boldsymbol{R})\right]\chi_{nv}(\boldsymbol{R}) = \mathcal{E}_{nv}\chi_{nv}(\boldsymbol{R}). \tag{2.8}$$

The $E_n(\boldsymbol{R})$ is the PES and it is a hyper-dimensional function of the nuclear configuration for polyatomic molecules. With the PES, Eq. 2.8 could then be solved.

2.2 Permutationally Invariant Potential Energy Surface

In principle, we can always solve the electronic Schrödinger Eq. 2.3 "on the fly" at the desired nuclear configurations when necessary, for example, in *ab initio* molecular dynamics simulations, but these calculations are extremely intensive and would not be feasible even if a low-level *ab initio* method were to be applied. A more practical approach is to obtain the functional representation of the PES. This is still a challenging problems because the exact analytical function form of the PES is unknown. The PES can be constructed using interpolation, i.e., the analytical potential agrees with *ab initio* energy exactly on any point in the database.[1–6] For systems with moderate size, this becomes more challenging, because the dimensionality of the problem increase so that simple functions are not able to provide accurate representation. The best strategy we can apply is that we select a well-behaved mathematical function $f(\boldsymbol{R};\boldsymbol{C})$ with a set of adjustable parameters $\boldsymbol{C}$ to represent the PES. The optimal parameters $\boldsymbol{C}$ can be determined via least-square process. A set of electronic energies on different configurations $\{\boldsymbol{R}_i, V_i\}$ $(i = 1, \cdots, N)$ is first calculated, and then the parameters are those that minimize the residual $\sum_i (f(\boldsymbol{R}_i;\boldsymbol{C}) - V_i)^2$. There is extensive literature about obtaining

the functional representation of the PES (e.g., see Ref. 7 and references therein).

Several function forms of $f(\boldsymbol{R}; \boldsymbol{C})$ are available, e.g., neural network,[8–16] and a polynomial form which is adopted in this work.[17–20] The variables in the polynomial are "Morse variables" y_{ij}, which is obtained from the internuclear distances r_{ij} via $y_{ij} = \exp(r_{ij}/a)$, where a is in principle also an adjustable parameter but usually fixed at 2.0 Bohr. The use of Morse variables instead of simply internuclear distances guarantees that the potential does not diverge when the molecule dissociates. Therefore, the mathematical function is

$$f(\boldsymbol{R}_i; \boldsymbol{C}) = \sum_{m=0}^{M} C_{\boldsymbol{b}} \left[\prod_{i<j}^{N} y_{ij}^{b_{ij}} \right] \quad \left(m = \sum b_{ij} \right), \tag{2.9}$$

where M is the maximum polynomial order, $\boldsymbol{b}$ stands for the ordered collection of the exponents b_{ij}, $C_{\boldsymbol{b}}$ are the linear coefficients need to be determined, and N is the number of atoms.

The use of Morse variables transformed from the internuclear distances ensures that the potential is invariant with respect to translations and rotations of the molecule. Yet another symmetry has to be satisfied, that is, the potential has to be invariant with respect to permutations of like atoms. A straightforward way to achieve this permutational invariance is to replicate the electronic energies to all the equivalent configurations and fit the polynomial to this expanded dataset. However, a more elegant approach is to use a mathematical function with the invariance built in. Two techniques developed in our group will be discussed here. In addition to these two techniques, progresses have been made recently to incorporate the permutational invariance into neural-network potentials.[21,22]
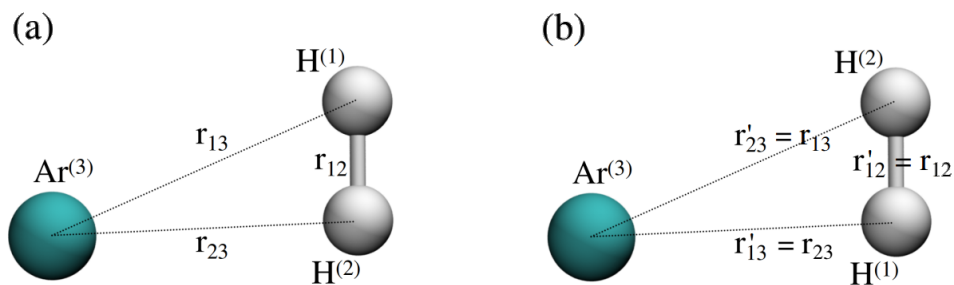
Figure 2.1: Permutation of the two identical H atoms in $Ar-H_2$.

2.2.1 Monomial symmetrization

The general polynomial form is shown in Eq. 2.9, which is not permutationally invariant, but this is the starting point of monomial symmetrization. Here I just use a simple triatomic system as an example to illustrate the concept of this method, and then this method could be generalized to arbitrary molecules.

To begin with, consider the system $Ar-H_2$. For this triatomic system, the expression of the potential is simply:

$$V(\boldsymbol{y}) = \sum_{a+b+c=0}^{M} C_{abc} y_{12}^a y_{13}^b y_{23}^c.$$ (2.10)

This expression in general is not permutationally invariant, and to show this, we just look at the sum of two particular terms $C_{123} y_{12} y_{13}^2 y_{23}^3 + C_{132} y_{12} y_{13}^3 y_{23}^2$, without loss of generality. Figure 2.1 shows the labels of each atom and all the internuclear distances (and thus the Morse variables) before and after the permutation. The permutation maps y_{13} to y_{23} and y_{23} to y_{13}. Therefore the value of the sum after the permutation becomes $C_{123} y'_{12} y'^2_{13} y'^3_{23} + C_{132} y'_{12} y'^3_{13} y'^2_{23} = C_{123} y_{12} y_{23}^2 y_{13}^3 + C_{132} y_{12} y_{23}^3 y_{13}^2$. Comparing this with the original value of the sum before permutation $(C_{123} y_{12} y_{13}^2 y_{23}^3 + C_{132} y_{12} y_{13}^3 y_{23}^2)$, it's clear that they are not equal unless the coefficients C_{123} and C_{132} have the same value. Replicating

and enlarging the dataset can enforce these two coefficients to be equal; however, we can also use one single coefficient for the two terms and the permutational invariance is built into the polynomial:

$$V(\boldsymbol{y}) = \sum_{a+b+c=0}^{M} C_{abc} \left[y_{12}^a y_{13}^b y_{23}^c + y_{12}^a y_{13}^c y_{23}^b \right].$$ (2.11)

For a general polyatomic molecule, we can find the mappings of all the possible permutations, and use one coefficient to all the permutationally equivalent monomials. A general expression of the symmetrized monomials is

$$V(\boldsymbol{y}) = \sum_{m=0}^{M} C_{\boldsymbol{b}} \mathcal{S} \left[\prod_{i<j}^{N} y_{ij}^{b_{ij}} \right] \quad \left(m = \sum b_{ij} \right),$$ (2.12)

where $\mathcal{S}$ is the operator that symmetrizes the monomials. When the number of possible permutations gets larger, finding the equivalent monomials becomes more difficult. Therefore this approach was implemented and programmed by Xie and Bowman[18] in 2010.

2.2.2   Invariant polynomials

A more efficient way to find the invariant polynomials is based on the invariant polynomial theory. The rigorous mathematical derivation and proof of the theory is provided in Ref. 23. The details are beyond the scope of this work, and are skipped here. According to the theory, the potential can be expressed as

$$V(\boldsymbol{y}) = \sum_{d=0}^{M} C_{ab} h_a \left(\boldsymbol{p}(\boldsymbol{y}) \right) q_b(\boldsymbol{y}),$$ (2.13)

where $\boldsymbol{p}(\boldsymbol{y})$ is the vector formed by the primary invariant polynomials and h_a is a polynomial of the primary invariants; $q_b(\boldsymbol{y})$ are secondary invariant polynomials, and d is the polynomial order whose maximum is set to M. For a molecule consists of N atoms, there are $N(N-1)/2$ primary invariant polynomials. The software MAGMA[24] is used to find these primary and secondary invariant polynomials, and they have been implemented in a fitting library by Braams and Bowman.[17]

The polynomials generated by the two methods mentioned are numerically equivalent, but the mathematical expressions are different. Compared to the monomial symmetrization method, invariant polynomials are generally more efficient to evaluate because of the factorization, but at the cost of less accessibility of the fitting basis functions. For example, in some cases we would like to only include selected terms from the complete polynomial basis, and this can be easily achieved if the polynomial is formed by symmetrized monomials, but this could be very difficult if the polynomial is factorized as the products of primary and secondary invariant polynomials. This will be discussed in details in the next section. In addition, obtaining the analytically first derivatives from the unfactorized, monomial symmetrized function is trivial, but the factorization in the invariant polynomial approach makes the derivation of the analytical first derivatives very difficult.

2.2.3   Purified fitting basis

The single, global expression Eq. 2.12 or 2.13 is not rigorously separable in fragment coordinates. Here H_2 + CO is used as an example to illustrate this. For simplicity, y_1 and y_2 are used to represent the Morse variable of the C–O and H–H bond lengths, and consider the maximum polynomial order of 2. When the distance of the two fragments

is sufficiently large, all the Morse variables of the intermolecular distances become zero and vanish, and only the intramolecular Morse variables survive. The potential then can be expressed as:

$$V(y_1, y_2) = 1 + y_1 + y_2 + y_1 y_2 + y_1^2 + y_2^2. \tag{2.14}$$

Consider the energy difference between the fragments with arbitrary configurations and the fragments at equilibrium, $V(y_1, y_2) - V(y_{1,e}, y_{2,e})$, where e means equilibrium. Since the fragments are separated at large distance, this energy difference should be the same as the sum of the difference for each individual fragment, i.e., $V(y_1, y_2) - V(y_{1,e}, y_{2,e}) = V(y_1, y_{2,e}) - V(y_{1,e}, y_{2,e}) + V(y_{1,e}, y_2) - V(y_{1,e}, y_{2,e})$. By inserting Eq. 2.14 in, we can see that this requires $y_1 y_2 = y_1 y_{2,e} + y_{1,e} y_2 - y_{1,e} y_{2,e}$, but this is not guaranteed for arbitrary y_1 and y_2. In real applications, if we include sufficient fragment configurations in the dataset, this artificial dependency is very small. However, a more elegant way is to remove non-separable terms in the polynomial basis. Of course we still need to make sure that the permutational invariance is not spoiled. If the monomial symmetrization expression is used, each polynomial is invariant under permutations so it could be safely removed; however, in primary and secondary invariant polynomial approach, since all the terms are well factorized into products and the expression is much more compact than the monomial symmetrization, removing such terms is not trivial. Truhlar and co-workers implemented this fitting basis purification in their application of the monomial symmetrization for N_4, following the suggestion by Xie and Bowman.[25] This approach was also employed used in a recent potential describing the Ar-HOCO interaction.[26]

2.3 Many-body Expansion

For complex systems with large degrees of freedom, the single expression for the potential becomes so complicated and is almost inapplicable. However, for molecular clusters consist of weakly interacting small molecules, a strategy called many-body expansion could be applied to construct the PES. This method has been adopted recently to build the PESs for water, HCl, and mixed HCl-water clusters.[27–31]

In a molecular cluster, we define the "monomer" as a single molecule, and "dimer" as the subsystem that consists of two monomers, and so on. The total energy of the cluster can be decomposed into the sum of one-body, intrinsic two-body, three-body energies, etc:

$$V = \sum_i V_i^{(1)} + \sum_{i<j} V_{i,j}^{(2)} + \sum_{i<j<k} V_{i,j,k}^{(3)} + \cdots , \qquad (2.15)$$

where

$$\begin{aligned}
V_i^{(1)} &= V_i, \\
V_{i,j}^{(2)} &= V_{i,j} - V_i^{(1)} - V_j^{(1)}, \qquad\qquad (2.16)\\
V_{i,j,k}^{(3)} &= V_{i,j,k} - V_{i,j}^{(2)} - V_{i,k}^{(2)} - V_{j,k}^{(2)} - V_i^{(1)} - V_j^{(1)} - V_k^{(1)}
\end{aligned}$$

are the one-body, intrinsic two-body and three-body energies, and V_i, $V_{i,j}$, $V_{i,j,k}$ are the energies of the monomer, dimer, and trimer, respectively. For the system consists of p monomers, this expansion is rigorous if the summation is up to the intrinsic p-body terms. However, for weakly interacting monomers, this series decays fast, and convergence can be achieved with only the first a few terms. For example, the one, two, and three-body contribute to more than 98% of the total energy in water clusters, so the four-body and higher-order terms in this expansion usually can be neglected. The monomer, dimer, and trimer are relatively small systems and single polynomial expressions for these potentials

are feasible. In this way, the potential of a cluster with arbitrary number of monomers can be obtained.

2.4   Dipole Moment Surface

In addition to the PES, the same approach can be used to fit the dipole moment surface (DMS). The dipole moment is a three-dimensional vector, and the expression

$$\vec{\mu}(\boldsymbol{R}) = \sum_i q_i(\boldsymbol{R})\vec{x}_i \tag{2.17}$$

is used to represent the dipole, where $\boldsymbol{R}$ denotes the configuration, w_i is the effective charge on the i-th nucleus, and $\vec{x}_i$ is the position vector of the i-th nucleus. The effective charge is a scalar quantity, which can be expressed in the polynomials that are similar to those used for PESs.

The dipole moment should be invariant under permutations of identical atoms, and to guarantee this invariance, the charges transform like a covariant: if we exchange identical nuclei i and j (the configuration transforms from $\boldsymbol{R}$ to $\boldsymbol{R}'$), the effective charges on these two nuclei have to satisfy

$$(q_j(\boldsymbol{R}'), q_i(\boldsymbol{R}')) = (q_i(\boldsymbol{R}), q_j(\boldsymbol{R})), \tag{2.18}$$

and the charges on unique atoms are still invariant. Therefore, the same permutationally invariant polynomials for potentials can be used to represent the effective charge on unique atoms. On the other hand, the polynomials for identical atoms are different; it turns out that the permutationally invariant polynomials of a reduced symmetry could be used here. Consider an A_mB_nC molecule, the effective charge on atom C is represented

in polynomial that are invariant with respect to all the $m!n!$ permutations; the charges on A atoms are expressed using the invariant polynomials for the $A_{m-1}B_nCD$ molecule, and the charges on B atoms use polynomials for $A_mB_{n-1}CD$. The coefficients are obtained, similar to the potential fitting, via the least-squares procedure.

In addition to the covariant charges under permutations, the sum of the effective charges has to be the net charge of the molecule. Ideally this property should be built in the fitting basis, but in reality, we simply impose this as an additional constraint in the least-squares problem. Therefore, this condition is not strictly satisfied. This causes a drawback of the dipole fitting approach when we consider the dipole moment under translations. Let Z be the total charge of the molecule, and we apply a uniform displacement $\vec{r}$ to all the atoms. It must be $\vec{\mu}(\boldsymbol{R} + \vec{r}) = \vec{\mu}(\boldsymbol{R}) + Z\vec{r}$, but in the fitted dipole, the total charge is not exactly satisfied, and thus this property of the dipole under translations is not strictly satisfied as well.

2.5   Procedures

Depending on the purpose of the PES, the procedures may vary slightly, and here I describe the general procedures to construct a PES. The details of each individual PES will be discussed in the following chapters and can also be found in the corresponding references.

The first step is sampling the configuration space. A straightforward way is the direct-product grid. However, this could only apply for very small molecules. If 10 points were to be selected, the total number of configurations would be 10^{3N-6} for nonlinear polyatomic molecules, where N is the number of atoms. Even for $N = 4$, the number of configurations becomes too large. Another way of sampling the configuration space is *ab initio* molecular

dynamics (AIMD), using low-level electronic structure method such as DFT and MP2 with small basis sets. The AIMD simulations are carried out at each stationary point (global or local minima, and saddle points), at several total energies, to make sure that a large range in the configuration space could be sampled. The initial dataset is extracted from the AIMD trajectories.

Once the geometries are collected, high-level *ab initio* calculations are performed on these configurations. First, test calculations are carried out for the accuracy and time of a certain method/basis combination. Usually CCSD(T)-F12 method[32,33] with Dunning basis set (aug-)cc-pVXZ (X=D, T, . . .)[34] provides good accuracy and efficiency. When bond-breaking is involved, the single-reference coupled-cluster method fails, and multireference method is used. After all the *ab initio* energies are obtained, a linear least-squares fit is performed to determine the coefficients of the initial PES.

The next step is to improve the initial fit. First the stationary points can be located on the fitted potential and the geometries and harmonic frequencies are compared with *ab initio* results. If the agreement is not satisfactory, additional geometries are sampled by adding random displacements to those stationary configurations. The energies of the additional geometries are calculated and added to the dataset. Furthermore, molecular dynamics and diffusion Monte Carlo simulations are used to detect regions with unphysically low energy (lower than the global minimum), and additional configurations are added. This iteration goes on until we are satisfied with the PES.

Chapter 3

Molecular Vibrations

In this chapter I'll present the methods to study the molecular vibrations. The first approach involves a series of hierarchical methods to solve the nuclear Schrödinger equation rigorously. It starts with the harmonic approximation, which assumes that the potential is harmonic. The anharmonicity and mode-coupling are neglected here. Then the results could be systematically improved when vibrational self-consistent field (VSCF) and virtual-state configuration interaction (VCI) methods are used. These methods have been implemented in the code MULTIMODE. In addition to VSCF+VCI approach, diffusion Monte Carlo (DMC) is another strategy to solve the vibrational ground state properties and it is also described here.

3.1   Normal Mode Analysis

We start with the classical Hamiltonian of a molecule

$$H = \sum_{i=1}^{3N} \frac{1}{2} m_i \dot{x_i}^2 + V(x_1, x_2, \cdots, x_{3N}), \tag{3.1}$$

where $\dot{x}_i$ and x_i are velocities and positions, and m_i are masses. The subscript i runs from 1 to $3N$, where N is the number of atoms. Here $i = 1, 2, 3$ refers to the x, y, and z coordinates of the first atom, $i = 4, 5, 6$ refers to the x, y, and z of the second atom, etc. V is the potential and it is a function of the positions of all the atoms.

As an approximation, we can expand the potential about the minimum $\{x_i^{(0)}\}$ in a Taylor series up to second-order terms:

$$V = V(\{x_i^{(0)}\}) + \sum_i V_i'(\{x_i^{(0)}\})(x_i - x_i^{(0)}) + \frac{1}{2}\sum_i\sum_j V_{ij}''(\{x_i^{(0)}\})(x_i - x_i^{(0)})(x_j - x_j^{(0)}), \quad (3.2)$$

where $V(\{x_i^{(0)}\})$ is the potential at the minimum, which could be an arbitrary value and it is set to zero here for simplicity. $V_i'(\{x_i^{(0)}\})$ are the first derivatives of the potential with respect to the coordinates. These first derivatives are zero because the potential is expanded about the minimum. The only terms that survive are the second derivatives:

$$V_{ij}''(\{x_i^{(0)}\}) = \left.\frac{\partial^2 V}{\partial x_i \partial x_j}\right|_{\{x_i^{(0)}\}}. \quad (3.3)$$

This Hamiltonian is non-separable due to the coupling in second-order terms. However, for a potential truncated at the second-order level, a coordinate system Q exists such that in this new coordinate, the Hamiltonian is separable: $H = \sum_{i=1}^{3N}[T_i + V_i(Q_i)]$. This coordinate is the normal mode and it can be found using normal mode analysis.

First we define the mass-scaled Cartesian displacements q_i as $q_i \equiv \sqrt{m_i}(x_i - x_i^{(0)})$. Thus, the classical Hamiltonian becomes

$$H = \frac{1}{2}\sum_{i=1}^{3N}\dot{q}_i^2 + \frac{1}{2}\sum_i\sum_j q_i F_{ij} q_j, \quad (3.4)$$

where F_{ij} are mass-scaled force constants:

$$F_{ij} \equiv \frac{\partial^2 V}{\partial q_i \partial q_j}\bigg|_{\{0\}}. \tag{3.5}$$

In matrix notation, $\boldsymbol{q} = [q_1 \; q_2 \; \cdots \; q_{3N}]^\top$, and the Hamiltonian is written as

$$H = \frac{1}{2}\dot{\boldsymbol{q}}^\top \dot{\boldsymbol{q}} + \frac{1}{2}\boldsymbol{q}^\top \boldsymbol{F} \boldsymbol{q}. \tag{3.6}$$

$\boldsymbol{F}$ is the mass-scaled Hessian, which is a symmetric matrix. We know that for a symmetric matrix, an orthogonal matrix $\boldsymbol{L}$ exists that can diagonalize $\boldsymbol{F}$: $\boldsymbol{L}^\top \boldsymbol{F} \boldsymbol{L} = \boldsymbol{\Lambda}$, where $\boldsymbol{\Lambda} = \mathrm{diag}(\lambda_1, \cdots, \lambda_{3N})$. Let $\boldsymbol{q} = \boldsymbol{L}\boldsymbol{Q}$, and thus

$$H = \frac{1}{2}\dot{\boldsymbol{Q}}^\top \dot{\boldsymbol{Q}} + \frac{1}{2}\boldsymbol{Q}^\top \boldsymbol{\Lambda} \boldsymbol{Q} \tag{3.7}$$

$$= \sum_{i=1}^{3N} \left[\frac{1}{2}\dot{Q}_i^{\,2} + \frac{1}{2}\lambda_i Q_i^2 \right] \tag{3.8}$$

$$= \sum_{i=1}^{3N} \left[\frac{1}{2}\dot{Q}_i^{\,2} + \frac{1}{2}\omega_i^2 Q_i^2 \right], \tag{3.9}$$

where $\omega_i = \sqrt{\lambda_i}$.

Therefore, we've found the new coordinate $\boldsymbol{Q}$ in which the Hamiltonian can be written as the sum of individual Hamiltonians for each normal mode Q_i. The system now looks like $3N$ uncoupled harmonic oscillators, with the harmonic frequencies $\omega_i = \sqrt{\lambda_i}$. Among the $3N$ normal modes, there are six zero-frequency ones, corresponding to three translations and three rotations of the molecule.

Under the harmonic approximation, the quantum Hamiltonian is simply

$$\hat{H} = \sum_{i=1}^{3N-6} \left[-\frac{1}{2}\frac{\partial^2}{\partial Q_i^2} + \frac{1}{2}\omega_i^2 Q_i^2 \right]. \tag{3.10}$$

The eigenfunctions are just the direct products of $3N-6$ harmonic-oscillator wavefunctions, and the eigenvalues are the sums of harmonic-oscillator eigenenergies:

$$\psi_{n_1\cdots n_{3N-6}} = \prod_{i=1}^{3N-6} \chi_{n_i}(Q_i); \tag{3.11}$$

$$E_{n_1\cdots n_{3N-6}} = \sum_{i=1}^{3N-6} \hbar\omega_i(n_i + \frac{1}{2}), \tag{3.12}$$

where $\chi_{n_i}(Q_i)$ and n_i are the harmonic-oscillator eigenfunction and the quantum number of the i-th normal mode.

However, in this harmonic approximation, higher-order terms in the potential expansion are neglected. In many applications, those non-harmonic terms are also very important and should be considered. The non-harmonic terms can be treated as a perturbation, and this leads to the vibrational second-order perturbation (VPT2) theory.[35,36]. In this work, I employ a more rigorous method, VSCF+VCI, which is very similar to Hartree-Fock and post-Hartree methods in electronic structure theory.[37]

3.2 Vibrational Self-Consistent Field and Configuration Interaction

Here we write the molecular Hamiltonian in normal mode coordinates:

$$\hat{H} = \sum_{i=1}^{3N-6} \hat{T}_i + V(\boldsymbol{Q}), \tag{3.13}$$

where $\boldsymbol{Q} = [Q_1 \ \cdots \ Q_{3N-6}]$ and $\hat{T}_i$ is the kinetic-energy operator of the i-th normal mode. The potential here is the full potential.

We use the variational method to solve this problem, and the trial wavefunction is a direct product of one-mode wavefunctions:

$$\psi(\boldsymbol{Q}) = \prod_{i=1}^{3N-6} \phi_i(Q_i). \tag{3.14}$$

The goal is to find a set of optimal one-mode functions $\{\phi_i(Q_i)\}$ $(i = 1, \cdots, 3N-6)$ that minimizes the energy functional

$$E[\{\phi_i\}] = \langle \psi | \hat{H} | \psi \rangle \tag{3.15}$$

under the restriction $\langle \phi_i | \phi_i \rangle = 1$, i.e., ϕ_i are normalized. This problem could be solved using Lagrange multiplier method, and we construct the Lagrangian

$$\mathcal{L}[\{\phi_i\}, \varepsilon_1, \cdots, \varepsilon_{3N-6}] = \langle \psi | \hat{H} | \psi \rangle - \sum_{i=1}^{3N-6} \varepsilon_i \left(\langle \phi_i | \phi_i \rangle - 1 \right). \tag{3.16}$$

By setting

$$\frac{\delta \mathcal{L}}{\delta \phi_i} = \frac{\delta \mathcal{L}}{\delta \varepsilon_i} = 0, \tag{3.17}$$

a set of $3N - 6$ coupled equations $(i = 1, 2, \cdots, 3N - 6)$

$$\left[\hat{T}_i + \left\langle \prod_{k \neq i}^{3N-6} \phi_k(Q_k) \middle| V(\boldsymbol{Q}) \middle| \prod_{k \neq i}^{3N-6} \phi_k(Q_k) \right\rangle \right] \phi_i(Q_i) = \varepsilon_i \phi_i(Q_i) \qquad (3.18)$$

are obtained. These coupled equations are solved iteratively until self-consistency is reached. This VSCF method is similar to the Hartree-Fock in electronic structure theory. It is a one-mode method, and the coupling between one mode and the others is taken into account in an "averaged" manner.

Like the electronic structure problem, the result of the VSCF calculation can be improved with a further configuration interaction calculation. For each mode, we solve the VSCF equations to obtain a set of eigenfunctions $\phi_i^{(v_i)}(Q_i)$ with different quantum number v_i. Therefore, a series of total wavefunctions can be constructed:

$$\psi_{\boldsymbol{v}}^{\text{VSCF}}(\boldsymbol{Q}) = \prod_{i=1}^{3N-6} \phi_i^{(v_i)}(Q_i). \quad (v_i = 0, 1, 2, \cdots; \text{ and } i = 1, \cdots, 3N - 6) \qquad (3.19)$$

One of them is the VSCF ground state, and the others are virtual states. In the virtual-state configuration interaction (VCI) calculation, we expand the total wavefunction using the VSCF ground and virtual states:

$$\Psi(\boldsymbol{Q}) = \sum_{\boldsymbol{v}} C_{\boldsymbol{v}} \psi_{\boldsymbol{v}}^{\text{VSCF}}(\boldsymbol{Q}), \qquad (3.20)$$

and the coefficients $C_{\boldsymbol{v}}$ are obtained by diagonalizing the Hamiltonian matrix.

3.3 The Code "MULTIMODE"

The VSCF and VCI methods are implemented in the code "MULTIMODE".[38,39] For real applications, there are also practical issues. In VSCF, integrals

$$\left\langle \prod_k \phi_k(Q_k) \middle| V(\boldsymbol{Q}) \middle| \prod_k \phi_k(Q_k) \right\rangle \tag{3.21}$$

have to be evaluated, and this multi-dimensional integration could be very expensive computationally, when the number of modes is large. In addition, in the VCI calculation, the Hamiltonian matrix could be very large without any restriction in the expansion in Eq. 3.20. The strategies in MULTIMODE to settle these issues will be presented below.

3.3.1 Hamiltonian

In the derivation of VSCF and VCI, the rotation-vibration coupling is neglected in the Hamiltonian. However, in MULTIMODE, the rigorous Watson Hamiltonian is used.[40] For any non-linear molecule, the Watson Hamiltonian is

$$\begin{aligned}
\hat{H} =& \frac{1}{2} \sum_{\alpha,\beta} \left(\hat{J}_\alpha - \hat{\pi}_\alpha \right) \mu_{\alpha\beta} \left(\hat{J}_\beta - \hat{\pi}_\beta \right) - \frac{1}{2} \sum_{k=1}^{3N-6} \frac{\partial^2}{\partial Q_k^2} \\
& - \frac{1}{8} \sum_\alpha \mu_{\alpha\alpha} + V(Q_1, \cdots, Q_{3N-6}),
\end{aligned} \tag{3.22}$$

where $\alpha, \beta = x, y, z$; $\hat{J}_\alpha$ and $\hat{\pi}_\alpha$ are the total and vibrational angular momenta, respectively; $\mu_{\alpha\beta}$ is the inverse of the effective moment of inertia tensor. The vibrational angular momenta are given by

$$\hat{\pi}_\alpha = -i \sum_{k,l} \zeta_{k,l}^\alpha Q_k \frac{\partial}{\partial Q_l}, \tag{3.23}$$

where $\zeta_{k,l}^{\alpha}$ are Coriolis coupling constants, and these vibrational angular momentum terms usually cannot be neglected. In most cases, we solve the $J = 0$ Schrödinger equations.

This Hamiltonian works for semi-rigid molecules; however, for molecules with one large-amplitude motion, the reaction path version of MULTIMODE should be used, which is based on the reaction path Hamiltonian.[41] This has been applied to molecules with internal rotation, such as CH_3OH and H_2O_2.[42,43] This reaction path MULTIMODE is not used in this work, so it will not be described here. The theory and details are given in Ref. 41 and 44.

3.3.2   Potential representation

In MULTIMODE, the potential is written as a hierarchical n-mode representation (nMR):

$$V(Q_1, Q_2, \cdots, Q_m) = \sum_i V_i^{(1)}(Q_i) + \sum_{i<j} V_{ij}^{(2)}(Q_i, Q_j) + \sum_{i<j<k} V_{ijk}^{(3)}(Q_i, Q_j, Q_k) + \\ \sum_{i<j<k<l} V_{ijkl}^{(4)}(Q_i, Q_j, Q_k, Q_l) + \cdots, \tag{3.24}$$

where

$$V_i^{(1)} = V(Q_i, Q_{l\neq i} = 0), \tag{3.25}$$

$$V_{ij}^{(2)} = V(Q_i, Q_j, Q_{l\neq i,j} = 0) - V_i^{(1)}(Q_i) - V_j^{(1)}(Q_j), \tag{3.26}$$

$$V_{ijk}^{(3)} = V(Q_i, Q_j, Q_k, Q_{l\neq i,j,k} = 0) - V_{ij}^{(2)} - V_{ik}^{(2)} - V_{jk}^{(2)} - V_i^{(1)} - V_j^{(1)} - V_k^{(1)}. \tag{3.27}$$

In MULTIMODE, this expansion is truncated, and the maximum number of modes allowed is six. Therefore, numerical quadratures with maximum dimensionality of six are needed, instead of $3N - 6$, and this could greatly reduce the computational cost. In

addition, efficient Gauss-Hermite quadrature is used in MULTIMODE for numerical integration.

3.3.3   VCI excitation space and matrix pruning

Without any constraint, the full-CI matrix size would be the direct product of the number of basis for each mode, and it could be enormous when the molecule is large. Similar to the truncated CI in electronic structure theory (for example, CISD only includes terms with single and double excitation), constraints are imposed in MULTIMODE. We use an "m-mode basis" to restrict the excitation space to a maximum of m modes excited simultaneously. For each mode, we specify a maximum value of the quanta of excitation (called MAXBAS in MULTIMODE), and in addition, the sum of quanta is limited by a user-specified value (called MAXSUM in MULTIMODE). With all these restrictions, the size of the CI matrix is greatly reduced.

However, sometimes the matrix size is still too large for a direct diagonalization, so we utilize other strategies to diagonalize the matrix. First, symmetry of the molecule could be exploited so that the final CI matrix is block diagonal and we only need to diagonalize each block instead of the full matrix. In addition, we only need the lowest a few hundred or thousand eigenstates so that more efficient iterative method can be used for diagonalization. In MULTIMODE, the iterative block-Davidson method is implemented. Furthermore, rows and columns of the CI matrix can be eliminated, based on a perturbation test. This was initially implemented in MULTIMODE by Handy and Carter,[45] and have been optimized recently in a vibrational calculation of CH_3NO_2.[46]

3.3.4   Infrared intensity

The intensities of vibrational transitions in MULTIMODE are calculated using the "dump-restart" procedure.[47] In the "dump" step, the VCI wavefunctions are written to a file on the disk, and in the "restart" step, the transition elements are calculated according to

$$R_{\alpha i f} = \int \Psi_i(\boldsymbol{Q})\mu_\alpha(\boldsymbol{Q})\Psi_f(\boldsymbol{Q})d\boldsymbol{Q}, \tag{3.28}$$

where $\boldsymbol{Q}$ is the set of normal coordinates and $\mu_\alpha(\boldsymbol{Q})$ is the α component $(\alpha = x, y, z)$ of the dipole moment. Ψ_i and Ψ_f are the initial and final state of the transition.

The infrared intensity of the $i \rightarrow f$ transition is evaluated using the expression

$$I_{if} = \frac{8\pi^3 N_A}{3hc(4\pi\epsilon_0)}\nu \sum_\alpha |R_{\alpha if}|^2 (N_i - N_f), \tag{3.29}$$

where N_A is the Avogadro's number, ν is the wavenumber of the transition, and N_i is the number of the molecules in state i. If we only consider the transition originated from the vibrational ground state, $N_i - N_f$ is 1.

3.4   Local Monomer Model

The vibrational calculations for large clusters or condensed phase matters can be very intensive. Various approximations have been made to reduce the dimensionality of the calculations. When the cluster consists of weakly bounded molecules and the intramolecular vibrations are of interest, the local-monomer model[48] is a very good approximation. The local-monomer model has been applied in the calculation of the anharmonic vibrations and infrared spectra of water clusters,[49] ice and liquid water,[50,51] HCl clusters,[52]

and mixed HCl-water clusters,[30,53] as well as vibrational relaxation of HOD in hexagonal ice.[54]

In the local-monomer model, one monomer is treated at a time, but it is assumed to be interacting with all the other monomers, which are held fixed. The theory of local-monomer also starts from the harmonic level. A local-monomer normal-mode analysis is performed for each monomer. Thus, for each monomer, a $3N_m$-dimensional mass-weighted Hessian matrix is calculated, where N_m is the number of atoms in the monomer. Diagonalization of this local-monomer Hessian leads to $3N_m$-6 intramolecular modes and 6 nonzero-frequency frustrated rotations and translations. After the local-monomer normal modes are obtained, we solve the Schrödinger equation of the embedded monomer m, given by

$$\left[\hat{T}_m + V_m(\boldsymbol{Q}_m)\right]\psi_m(\boldsymbol{Q}_m) = E\psi_m(\boldsymbol{Q_m}), \tag{3.30}$$

where $\boldsymbol{Q}_m$ is the set of intramolecular local normal modes. $\hat{T}_m$ is the kinetic energy operator with vibrational angular momentum included, and $V_m(\boldsymbol{Q}_m)$ is the full potential of the monomer, perturbed by other monomers, which depends dynamically on the local modes of the monomer, with all the other monomers frozen.

3.5   Diffusion Monte Carlo

The DMC method can be used to solve the nuclear Schrödinger equation for the vibrational ground state energy and wavefunction.[55–59] Here the basic theory and a practical algorithm of DMC are described.

3.5.1   Theory

Consider a one-dimensional time-dependent Schrödinger equation

$$i\hbar \frac{\partial \psi}{\partial t} = \hat{H}\psi = -\frac{\hbar^2}{2m}\frac{\partial^2 \psi}{\partial x^2} + V(x)\psi, \qquad (3.31)$$

and the solution can be expressed as

$$\psi(x,t) = \sum_n c_n \phi_n \exp\left[\frac{-iE_n t}{\hbar}\right], \qquad (3.32)$$

where ϕ_n and E_n are the eigenstates and eigenvalues of the Hamiltonian $\hat{H}$. If we perform an shift in energy by E_R and replace the time t with the imaginary time $\tau = it$, the Schrödinger equation becomes

$$\frac{\partial \psi}{\partial \tau} = -\frac{\hbar}{2m}\frac{\partial^2 \psi}{\partial x^2} + \frac{V(x) - E_R}{\hbar}\psi, \qquad (3.33)$$

and the solution becomes

$$\psi(x,\tau) = \sum_n c_n \phi_n \exp\left[\frac{(E_n - E_R)\tau}{\hbar}\right]. \qquad (3.34)$$

If $E_R > E_0$, $\psi(x,\tau)$ diverges when τ approaches ∞; if $E_R < E_0$, $\psi(x,\tau)$ decays to zero; only if $E_R = E_0$, $\psi(x,\tau)$ converges to ϕ_0. That means, if we choose the E_R to be the ground state energy E_0 and propagate the system to large imaginary time values, $\psi(x,\tau)$ converges to the ground state of the Hamiltonian $\hat{H}$. Of course E_0 is unknown in advance, and its value could be determined by diffusion Monte Carlo method.

The DMC method is based on the similarity between Eq. 3.33 and the diffusion

equation with a first-order rate term

$$\frac{\partial C}{\partial t} = D\frac{\partial^2 C}{\partial x^2} - kC. \tag{3.35}$$

The "diffusion coefficient" of the imaginary-time Schrödinger equation is $D = \sqrt{\hbar/2m}$. The second derivative part can be modeled with a random walker process with large number of walkers, and the first-order term can be viewed as a source or sink of the walkers.

At sufficiently short times, the solution of Eq. 3.35 can be approximated as

$$C(x,t) \approx U(x,t)C(x,0)\exp\left(-kt\right), \tag{3.36}$$

where

$$U(x,t) = \frac{1}{\sqrt{4\pi Dt}}\exp\left[-\frac{(x-x_0)^2}{4Dt}\right] \tag{3.37}$$

is the solution to the diffusion problem without the first-order term, using δ-function as the initial condition. Therefore, in the simulations, each time increment consists of two steps: in the first step the walkers are assigned a random displacement based on the distribution specified by Eq. 3.37, and in the second step, the walkers are removed or replicated based on the probability density $\exp(-kt)$ from Eq. 3.36. A practical algorithm is given next.

3.5.2 Algorithm

Initially all the walkers are at the reference geometry, so that the initial condition can be viewed as a δ-function. At each step, a random displacement Δx is assigned to each

walker. This displacement is selected from a Gaussian distribution

$$P(\Delta x) = \frac{1}{\sqrt{4\pi D \Delta \tau}} \exp\left[-\frac{(\Delta x)^2}{4D\Delta\tau}\right], \tag{3.38}$$

with $D = \sqrt{\hbar/2m}$ and $\Delta\tau$ is the step size in the simulation. After the displacement, the potential of each walker is calculated and the corresponding weight function

$$W = \exp\left[-(V(x) - E_R)\Delta\tau\right] \tag{3.39}$$

is computed. For each walker, if $W < 1$, it will be removed with probability $1 - W$; if $W > 1$, $\text{int}(W)$ new walkers with the same configuration will first be added, and then an additional one may be added with probability $W - \text{int}(W)$, where $\text{int}(W)$ is the largest integer that does not exceed W. When these are done for all the walkers, the reference energy is calculated as

$$E_R(\tau) = \langle V(\tau) \rangle - \alpha \frac{N(\tau) - N(0)}{N(0)}, \tag{3.40}$$

where $\langle V(\tau) \rangle$ is the average potential over all walkers, and $N(\tau)$ is the number of live walkers at imaginary time τ. Here α is a feed-back parameter that controls the fluctuations of the number of the walkers and the reference energy. After equilibration, the average of the reference energy over the imaginary time gives an estimate of the zero-point energy, and the distribution of the walkers, when properly normalized, represents the ground-state wavefunction.

Chapter 4

Dynamics Simulations

In principle, even with Born-Oppenheimer approximation, we have to solve the time-dependent nuclear Schrödinger equation for the motion of nuclei. However, this is also very challenging, and rigorous quantum calculations were seldom used for systems with more than four atoms.

In many cases where the nuclear quantum effects can be neglected, the motions of the nuclei can be described sufficiently well by classical mechanics. The motions of the nuclei follow the Hamilton's equations (also equivalent to Newton's and Lagrange's equations):

$$\frac{dq_i}{dt} = \frac{\partial H}{\partial p_i}, \ \frac{dp_i}{dt} = -\frac{\partial H}{\partial q_i}, \tag{4.1}$$

where q_i and p_i are the position and momentum, respectively. H is the classical Hamiltonian, which is the sum of the kinetic and potential energy. In molecular dynamics (MD) simulations, the classical equations of motion in Eq. 4.1 are integrated numerically if the potential is known. Note that our potential energy surfaces (PESs) allow very efficient integration, compared to "on-the-fly" *ab initio* molecular dynamics. The MD simulation

is the method used in this work to model chemical reaction dynamics.

4.1   Initial Conditions

The MD simulation is deterministic, i.e., the motion of each nucleus is completely determined by the initial momentum and position (when the numerical error is neglected). Therefore, a good sampling of the initial conditions is crucial in MD simulations. Next I describe the methods used in my research that sample the initial condition.[60]

Microcanonical sampling samples the phase space with a constrained total energy E. One of the implementation is simple and straightforward. The molecular configuration is fixed, and the velocity of each atom is selected from a uniform distribution in $(-0.5, 0.5)$. Then the velocities are scaled so that the total kinetic energy equals to the constraint. However, this simple implementation fails to describe the zero-point motion of the molecule, and the total energy E could even be lower than the zero-point energy (ZPE) of the molecule. The ZPE of a polyatomic molecule could be a large amount of energy (tens of kcal/mol), so the lack of it could lead to poor estimate of reaction barriers. In addition, the simple microcanonical sampling is not able to model mode-specific reactions where one or more normal modes are excited. Therefore, the normal mode sampling is introduced.

Normal mode sampling is also a microcanonical sampling, with the total energy E equals to the energy of a particular vibrational states. It is done in normal mode coordinates: the normal mode coordinates $\boldsymbol{Q}$ and momenta $\boldsymbol{P}$ are obtained, and then are transformed back to Cartesian coordinates $\boldsymbol{q}$ and $\boldsymbol{p}$. So first normal mode analysis is performed to determine the frequencies $\boldsymbol{\omega}$ and normal mode vectors $\boldsymbol{L}$. Random values

for Q_i and P_i are chosen by assigning a random phase to each mode:

$$Q_i = \frac{\sqrt{2E_i}}{\omega_i}\cos(2\pi r_i); \tag{4.2}$$

$$P_i = -\sqrt{2E_i}\sin(2\pi r_i), \tag{4.3}$$

where r_i is a random number from a uniformed distribution in $(0,1)$, and E_i is the energy one would like to put in the i-th mode. Typically E_i is the harmonic zero-point energy (ZPE) of that mode, and in mode-specific dynamics, it could be the energy of a certain excited state. Then the $\boldsymbol{Q}$ and $\boldsymbol{P}$ are transformed to Cartesian coordinates and momenta using

$$\boldsymbol{q} = \boldsymbol{q}_0 + \boldsymbol{M}^{-1/2}\boldsymbol{L}\boldsymbol{Q} \tag{4.4}$$

$$\boldsymbol{p} = \boldsymbol{M}^{1/2}\boldsymbol{L}\boldsymbol{Q}, \tag{4.5}$$

where $\boldsymbol{q}_0$ is the coordinates of the equilibrium configuration, and $\boldsymbol{M}$ is a diagonal matrix whose elements are masses of the nuclei.

A spurious angular momentum $\boldsymbol{j}_s$ could be generated from the procedures above, and this spurious angular momentum can be calculated by

$$\boldsymbol{j}_s = \sum_i \boldsymbol{r}_i \times m_i \dot{\boldsymbol{r}}_i, \tag{4.6}$$

where $\boldsymbol{r}_i$ is the position of the i-th nucleus. Assume that the desired angular momentum is $\boldsymbol{j}_0$ so $\boldsymbol{j} = \boldsymbol{j}_0 - \boldsymbol{j}_s$ is the amount that should be added to the system. Therefore the velocity $(\boldsymbol{I}^{-1}\boldsymbol{j}) \times \boldsymbol{r}_i$ is added to each atom, where $\boldsymbol{I}$ is the moment of inertia tensor.

Finally the internal energy E after the two steps mentioned above usually slight

deviates from the desired total internal energy E_0. So the Cartesian coordinates and momenta are scaled according to

$$q'_i = q_{i,0} + (q_i - q_{i,0})\sqrt{E_0/E} \tag{4.7}$$

$$p'_i = p_i\sqrt{E_0/E}. \tag{4.8}$$

The possible spurious translation is removed and loops back to the angular momentum procedure until the actual internal energy agrees with the desired internal energy.

4.2 Final Conditions

In dynamics simulations, properties of the products such as the translational energy release, the rotational and vibrational energy distribution are of interest. These can be calculated from the coordinates and velocities of the nuclei at the termination of a classical trajectory. The procedures of final condition analysis are described here.[61]

4.2.1 Translations and Rotations

A reaction may have several products and here we just focus on one fragment that is of interest. Upper case letters are used for the center-of-mass positions and velocities of the product, and lower case letters for each individual atom. The center-of-mass velocity of the fragment can be calculated by

$$\boldsymbol{V} = \frac{\sum_i m_i \boldsymbol{v}_i}{M}, \tag{4.9}$$

where the sum is over all the atoms in the fragment and M is the total mass of this fragment. Therefore the translational energy of this fragment is simply $E_{\text{trans}} = \frac{1}{2}M\,|\boldsymbol{V}|^2$. Then this translational motion is removed from the fragment $\boldsymbol{v}_i' = \boldsymbol{v}_i - \boldsymbol{V}$, and the internal energy of the fragment is

$$E_{\text{int}} = T + V = \sum_i \frac{1}{2}m_i\,|\boldsymbol{v}_i'|^2 + V, \tag{4.10}$$

where V is the potential energy relative to the equilibrium structure.

This internal energy consists of vibrational energy and rotational energy. The rotational angular momentum can be calculated by $\boldsymbol{j} = \sum_i m_i \boldsymbol{r}_i' \times \boldsymbol{v}_i'$, where $\boldsymbol{r}_i'$ and $\boldsymbol{v}_i'$ are the position and velocity of atom i in center-of-mass frame. Then the rotational energy is given by

$$E_{\text{rot}} = \frac{1}{2}\boldsymbol{j}^\top \boldsymbol{I}^{-1}\boldsymbol{j}, \tag{4.11}$$

where $\boldsymbol{I}$ is the moment of inertial tensor of the fragment. For diatomic molecules, the rotational quantum number J can be determined using $|\boldsymbol{j}| = \sqrt{J(J+1)}\hbar$ and rounded to the nearest integer.

4.2.2   Vibration and Zero-point Energy Constraint

The vibrational energy is determined by

$$E_{\text{vib}} = E_{\text{int}} - E_{\text{rot}}. \tag{4.12}$$

For diatomic molecules, the vibrational quantum number n can be determined by

$$\left(n + \frac{1}{2}\right)\hbar\omega = E_{\text{vib}}, \tag{4.13}$$

where ω is the harmonic frequency.

One common problem of the classical simulation is ZPE violation. The vibrational energy of the product could be lower than the ZPE, which is not allowed in quantum mechanics. If these trajectories were included in the analysis, the rotational and translational energy would be overestimated. A straightforward ZPE constraint could be applied to avoid this. If the total vibrational energy of the products is smaller than the sum of ZPEs of each individual product, the trajectory is discarded and will not be considered in the final condition analysis, or if the vibrational energy of any fragment is smaller than its ZPE, the trajectory is discarded. The former is the soft ZPE constraint and the latter is hard ZPE constraint.

Part II

Many-body Potentials for Clathrate Hydrates

Chapter 5

Many-body Potentials for Clathrate Hydrates

5.1 Overview

Clathrate hydrates are crystalline inclusion compounds in which small gas molecules such as CH_4, H_2, CO_2 are trapped in hydrogen-bonded water cages.[62,63] The clathrates are of widespread interest owing to their role in energy storage. The methane hydrate is a potential source of hydrocarbon fuel in the future. On the other hand, the formation of methane hydrate may be responsible for the flow reduction in gas pipeline. Another example is the hydrogen clathrate, which is potentially an environmentally friendly and efficient material for hydrogen storage.[64,65]

Three typical crystal structures of clathrate hydrates have been observed: a cubic structure I (sI), a cubic structure II (sII) and a hexagonal structure H (sH). In a unit cell of sI, 46 water molecules form two pentagonal dodecahedral (5^{12}) and six tetrakaidecahedral ($5^{12}6^2$) cages. A sII unit cell consists of 136 water molecules that form sixteen 5^{12} and

eight hexakaidecahedral ($5^{12}6^4$) cages. A unit cell of sH is made of 34 water molecules and they form three 5^{12}, two irregular dodecahedral ($4^35^66^3$) and one icosahedral ($5^{12}6^8$) cages. Simple methane or CO_2 hydrate crystallize in sI, while the H_2 clathrate is sII. The cooperation of two guest molecules (one large and one small) could lead to sH clathrate hydrates, for example, the H_2-tetrahydrofuran clathrate.

Due to the important role these clathrate hydrates play in energy-related area, their properties such as structure, stability and storage capacity,[66–95] Raman and infrared spectroscopy,[96–111] nucleation, formation and dissociation dynamics,[70,112–126] and diffusion of the guest molecule[127–138] have been investigated extensively using both experiment and computational modeling. They are also good models to study the dynamics of confined molecules. When small gas molecules such as CH_4 and H_2 are trapped in the cages, they have coupled anharmonic translational oscillations (rattling) and almost free rotation, and the dynamics is highly quantum mechanical. Experimentally, inelastic neutron scattering has been applied to probe the translation-rotation motions of confined H_2 and CH_4.[139–147] The rotation-translation eigenstates of confined molecules have been computed by means of full-dimensional quantum calculation.[148–157]

In theoretical modeling of the clathrate hydrate, the potential energy surface (PES) plays an important role. In general three types of potentials were used in these studies. The first type is empirical model potential/force field that is parametrized to agree with experimental measurements on certain properties. Such potentials are efficient to evaluate so they can be applied to large-scale simulations. However, they are not reliable for properties that are not used in the parametrization. Another type is the "on-the-fly" potential: the potential is calculated when needed in the simulation directly. This type avoids the potential parametrization so that it's more generic for different properties, but the computational cost is so high that high-level *ab initio* theories are prohibited.

Finally, there are *ab initio*-based potentials by fitting to tens of thousands of *ab initio* energies. Similar to "on-the-fly" potentials, these *ab initio* potentials are generic. In addition, they have several advantages over the "on-the-fly" one: they are much faster to evaluate (though still slower than the empirical potentials/force fields), and higher level *ab initio* method can be used. The challenge here comes from the high dimensionality. The number of geometries is huge in order to sample a sufficiently large portion of the molecular configuration space, and each *ab initio* calculation is very expansive when the dimensionality is high. In addition, the function that represents the potential becomes complicated.

Fortunately, the clathrate hydrates consist of weakly bounded molecules, so the many-body expansion introduced in Chapter 2 is applicable to build the PESs. In the many-body expansion, the total potential is decomposed into the sum of lower-dimensional intrinsic potentials. These lower-dimensional potentials are described in this chapter, together with tests of fidelity for each of them. Finally the potentials of the clathrates and preliminary applications of the potentials are presented.

5.2   Fitting of Non-covalent Interactions

In many-body expansion, the intrinsic p-body potential vanishes when a single monomer is separated from the other $p-1$ monomers. However, as mentioned in Chapter 2, the single expression of the permutationally invariant polynomial is not rigorously separable in fragment coordinates. When fitting intrinsic p-body potential, the energy is not zero when the two molecules are separated. Therefore, in addition to the full fitting bases, the purified ones are also used here.

The original expression of monomial symmetrization (given in Chapter 2) is

$$V(\boldsymbol{y}) = \sum_{m=0}^{M} C_{\boldsymbol{b}} \mathcal{S} \left[\prod_{i<j}^{N} y_{ij}^{b_{ij}} \right] \quad \left(m = \sum b_{ij} \right), \tag{5.1}$$

and these polynomial bases are referred to as full (F) bases. Then certain terms in the full bases are removed, leading to what we call the purified (P) bases. A practical way for purification is described as follows. First, a set of cluster configurations is generated where each monomer (one at a time) is set far away from the others. For each configuration, inter-monomer Morse variables involving atoms of the isolated monomer are set equal to zero, while the remaining Morse variables are given different, non-zero values. All the polynomials in the F basis are then evaluated and those returning a value different from zero are discarded. The final outcome is a smaller polynomial basis able to ensure the correct zero-interaction limit. This procedure can be undertaken independently from the permutational symmetry employed.

The purification technique, which reduces the size of the fitting basis, can be further advanced by restricting the P basis to polynomials dependent exclusively on inter-monomer variables. In practice, only intra-monomer Morse variables are set to zero and then all the polynomials in the P basis are evaluated. Only polynomials returning a value different from zero are maintained. The final outcome of the technique is a very compact fitting basis, that we term a pruned purified (PP) basis.

Since the purified and pruned purified bases reduce the number of polynomials, they are expected to be fast to evaluate, and this substantially speeds up potential calls. This is an additional advantage because in large clusters there are a large number of intrinsic potentials to evaluate (e.g., 190 terms of 3-body $CH_4-H_2O-H_2O$ potential in $CH_4(H_2O)_{20}$). Each individual potential has to be efficient; otherwise the total poten-

tial becomes too expensive. Of course the correct asymptotic energy and the speed are achieved by sacrificing the fitting accuracy slightly because the number of adjustable parameters is reduced.

In this chapter, the intrinsic potentials are represented by the notation "B-xyz/M". "B" stands for "basis", and it could be F, P, and PP; "xyz" indicates the permutational symmetry of the molecule; M is the maximum polynomial order.

5.3 CH_4–H_2O Potential

The methane-water interaction has been examined with various *ab initio* methods, and several analytical forms of the PES for rigid monomers have been presented. The earliest studies (for example see Ref. 158–161) either fail to correctly identify the minimum structure or do not explore the full configuration space, due to low-level *ab initio* methods. Szczęśniak et al.[162] and Rovira et al.[163] successfully identified two minima in the PES, but the electronic binding energy of the global minimum was underestimated. Two six-dimensional PESs with rigid monomers have been reported.[164,165] In the work of Akin-Ojo and Szalewicz[165] the electronic binding energy was given as 361 cm^{-1} by extrapolating CCSD(T)/aug-cc-pVQZ and aug-cc-pV5Z results to the complete basis set (CBS) limit. More recently, Copeland and Tschumper[166] characterized the energetics of the dimer PES with high-level CCSD(T)-F12b/VTZ-F12 calculations, and reported the binding energy of 339 cm^{-1} with counterpoise (CP) correction and 353 cm^{-1} without the correction for the global minimum, and a binding energy of 224 or 231 cm^{-1} for the higher energy minimum with or without CP correction. However, none of the analytical PESs mentioned[159,160,162,164,165] is full-dimensional and so cannot be used to investigate observables that depend on the monomer vibrational motion. So I construct such a PES

here. In addition, an intrinsic dipole moment surface is constructed.

5.3.1   Ab initio calculation and potential fitting

The database of 36930 configurations and energies was obtained as follows. Seven C-O distances were picked in the range from 3.0 to 10.0 Å, and at each distance, 3200 monomer geometries were chosen with different orientations. 4932 additional configurations of the dimer were generated using *ab initio* molecular dynamics at the DFT (B3LYP) level of theory. An initial fit then was performed based on the 27332 points described above. The remaining 9598 points were calculated to provide better coverage of the initial PES, based primarily on running DMC calculations of the dimer zero-point energy and also to improve the harmonic frequencies at the two minima.

The CCSD(T)-F12b method[32,33] with haTZ (aug-cc-pVTZ for C and O, and cc-pVTZ for H) basis set was employed to calculate the energies, using MOLPRO 2010.[167] For each dimer configuration, the energies of the dimer and the isolated monomers at that configuration were calculated, and the intrinsic two-body energy was obtained according to

$$V_{\mathrm{CH_4-H_2O}}^{(2)} = V_{\mathrm{CH_4-H_2O}} - V_{\mathrm{CH_4}} - V_{\mathrm{H_2O}},\qquad(5.2)$$

without CP correction. Overall the computational cost of calculating the 36930 energies in the database can be converted to roughly 16 days of CPU time on a 16-core computer.

The dipole moments of the 36930 dimer configurations were calculated at MP2 level of theory with haTZ basis set. The dipole moments of the isolated monomers were also calculated at the same level of theory in order to obtain the intrinsic two-body dipole given by:

$$\vec{\mu}_{2b} = \vec{\mu}_{\mathrm{dimer}} - \vec{\mu}_{\mathrm{CH_4}} - \vec{\mu}_{\mathrm{H_2O}}.\qquad(5.3)$$

Two fitting bases were applied for the intrinsic CH_4-H_2O potential: the F and PP bases. The permutation group "4211" was used, which means the hydrogen atoms belonging to different monomers do not permute. This is reasonable because the intermolecular hydrogen exchange is not feasible for the interactions of interest. The maximum polynomial order is five. The intrinsic dipole moment surface (DMS) was also fitted in F basis with maximum polynomial order of five, using the standard procedures described in Chapter 2.

The number of coefficients, root-mean-square (rms) fitting error, and the time to evaluate the potential are listed in Table 5.1. F-4211/5, as expected, is the most accurate. PP-4211/5 removes all the terms containing intramolecular distances, so the number of coefficients is decreased by an order of magnitude. The effect is that potential calls are much faster, and only 8% of the time for F-4211/5 is necessary. PP-4211/5 is globally less accurate with a higher but still acceptable rms fitting error.

Table 5.1: Number of coefficients, rms fitting error for different energy regions (cm^{-1}), and computational times (arbitrary units) for the two fitted two-body potentials. The computational time for F-4211/5 is arbitrarily set equal to 100 to facilitate the comparison

	F-4211/5	PP-4211/5
N. coeff.	10,220	841
rms (E<0)	3.4	39.8
rms (0<E<1,500)	3.5	95.0
rms (E>1,500)	3.5	162.6
rms (total)	3.5	64.1
t	100.0	8.0

Figure 5.1 shows the energy distribution of the database and the cumulative rms error of the F-4211/5 PES. Many points were sampled in the attractive region to ensure
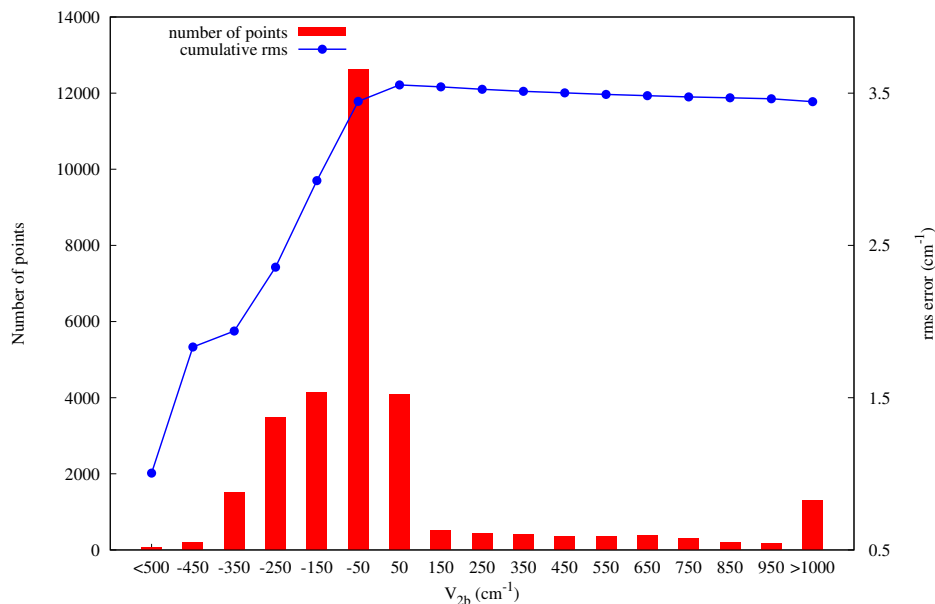
Figure 5.1:   Energy distribution of the points and cumulative rms error of F-4211/5.

a good description near the potential minima. In addition, more than 10000 energies are in the range from -50 to 50 cm^{-1}. Most of the corresponding geometries have a large C-O distance, so the interaction is very weak. This set of points forces F-4211/5 towards the correct zero value of the intrinsic two-body energy at large monomer separation.

5.3.2   Test of the potential

The full PES and DMS are the sum of the intrinsic two-body terms, described above, and the methane and water monomer PESs and DMSs. The methane monomer PES and DMS are taken from previous global *ab initio* ones using the invariant polynomial approach by Warmbier et al.[168]. This PES dissociates to fragments CH_3+H and so is suitable for use in studies of energy transfer involving highly excited methane. The water monomer PES is due to Partridge-Schwenke,[169] which is spectroscopically accurate, while

for convenience the monomer dipole of H_2O is extracted from the WHBB water dipole moment.[28] The full CH_4-H_2O potentials using the two fits for the intrinsic potential are denoted, using obvious notation, PES-F and PES-PP. Other monomer PESs and DMSs are available, such as the methane monomer potential by Yurchenko et al[170] and the H_2O monomer dipole by Lodi et al.[171].
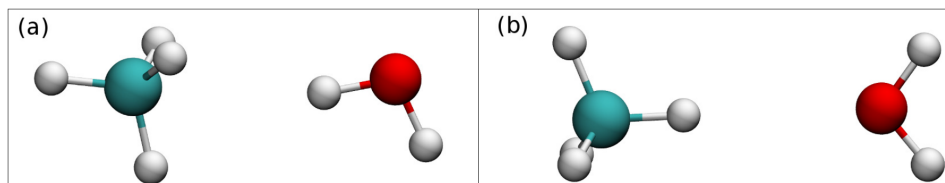
Figure 5.2:   Structures of the two stationary points on the PES: (a) global minimum; (b) secondary minimum

Two minima are located on the PESs. Both PES-F and PES-PP reproduce the correct geometries indicated in Figure 5.2. In the lower energy one the water monomer is a hydrogen bond donor, while it becomes an acceptor in the higher-energy minimum. The energies of the minima on the PESs as well as the *ab initio* results with and without CP correction are listed in Table 5.2. The CP correction for the global and secondary minima is about 20 cm $^{-1}$, which is not large. The binding energy of the global minimum without CP correction agree very well with the CCSD(T)/CBS result,[165] presumably by cancellation of errors due to basis set superposition and basis incompleteness. Because of the fortuitously close agreement with the benchmark, the intrinsic two-body potentials were fitted using electronic energies without the CP correction. Our binding energy for the secondary minimum is slightly larger than the value reported by Copeland and Tschumper[166].

Table 5.2: Interaction energies (cm^{-1}) of the global and secondary minima

	Global minimum	Secondary mimimum
ab initio with CP	330	223
ab initio without CP	356	243
PES-PI	357	243
PES-CSM	366	243
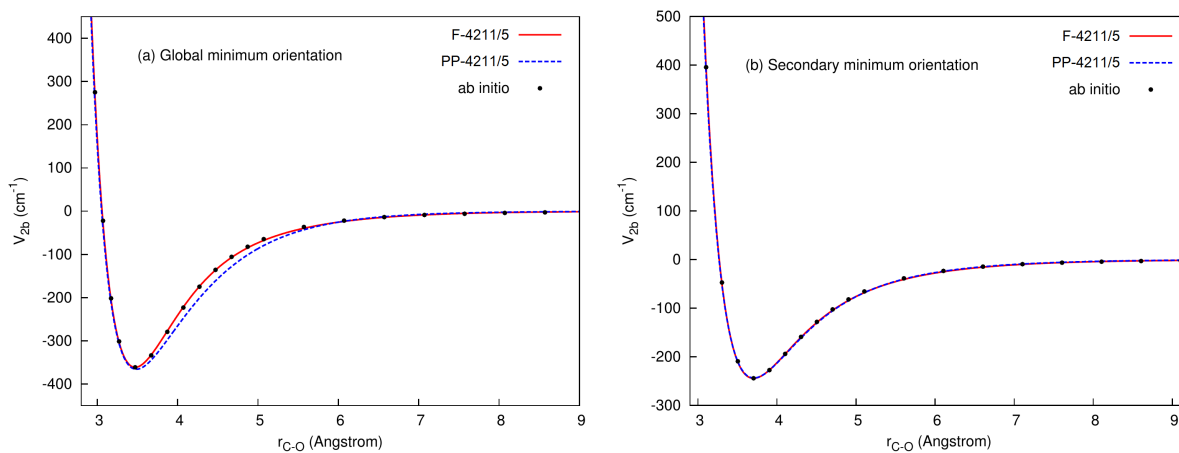
Figure 5.3:   Two unrelaxed one-dimensional cuts from F-4211/5, PP-4211/5 and *ab initio* calculations: intrinsic two-body energy as a function of C-O distance at (a) the global minimum orientation, and at (b) the secondary minimum orientation.

Figure 5.3 shows two unrelaxed one-dimensional cuts as a function of the C-O distance and calculated with F-4211/5 and PP-4211/5, as well as *ab initio* energies along these cuts, at global minimum and secondary minimum orientations. F-4211/5 agrees very well with *ab initio* points, as anticipated by the small rms fitting error. Generally, PP-4211/5 is also excellent, except between 3.5 and 5.0 Å at the global minimum orientation. The energies of both fitted two-body potentials go to zero when the distance becomes large, but due to different reasons. PP-4211/5 is by construction zero at large C-O distances, while F-4211/5 is zero because I sampled a large number of data in that region.

To go a step further from the electronic binding energy to the measurable dissociation energy, I rigorously calculated the zero-point energy (ZPE) of the bound dimer and isolated fragments using DMC. The simple unbiased algorithm described in Chapter 3 is adopted. Ten simulations were performed for the bound dimer and the fragments; in each simulation, 20000 walkers were propagated for 25000 steps, with a step size of 5.0 au. The walkers were first equilibrated for 5000 steps and the energies of the remaining 20000 steps were collected to compute the reference energy. The ZPE of the dimer is 14510 ± 5 cm^{-1}, when using the PES-F, and the sum of the ZPEs of the isolated fragments is 14663 ± 4 cm^{-1} relative to the global minimum. Thus, I determine the dissociation energy D_0 of the dimer is 153 ± 11 cm^{-1}. The statistical error in the ZPE of the dimer (5 cm^{-1}) and sum of ZPEs of the isolated fragments (4 cm^{-1}) leads to a statistical error of 6.4 cm^{-1} for D_0. a conservative estimate of the uncertainty is given as the sum of the statistical error (6.4 cm^{-1}) and the systematic error of our D_e compared to the CCSD(T)/CBS value (4 cm^{-1}). DMC simulations were also performed on PES-PP, and the ZPE of the bound dimer is 14514 ± 6 cm^{-1}, which agrees very well with the ZPE value from PES-F, and remarkably predicts a D_0 value (149 cm^{-1}) within the uncertainty range of PES-F.

The vibrational ground-state wavefunction was also obtained from DMC calculation.
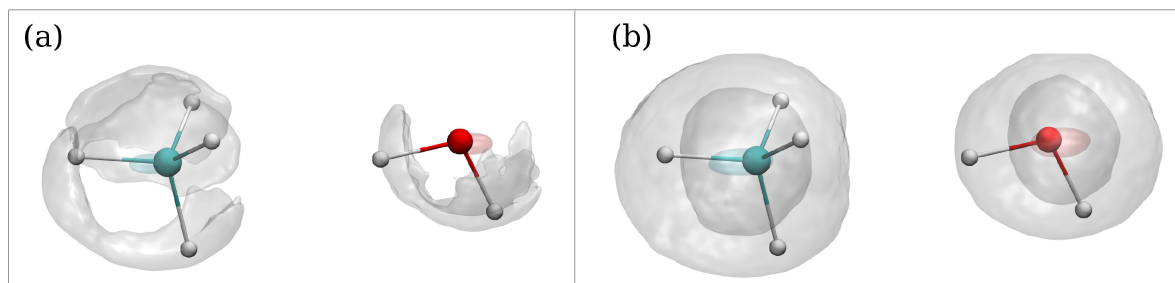
Figure 5.4: Vibrational ground state wavefunction of CH_4-H_2O dimer. The isovalue is 50% of the maximum wavefunction amplitude in (a), and 25% in (b).

It is represented by an isosurface. Each walker was optimally aligned into a reference frame. The space was divided into volume elements and a statistical analysis was performed for each volume element to obtain the wave function amplitude in that volume. The vibrational ground state wavefunction obtained from a DMC simulation that employs the PES-F potential is shown in Figure 5.4. As expected, the motions of heavy atoms (C and O) are more localized than the H atom. When the isovalue is 50% of the maximum, the hydrogen wave function is still somewhat localized, while at 25% of the maximum amplitude, the wave function is spherical. This indicates that the monomers are undergoing large-amplitude internal rotation in the bound dimer, which agrees with experimental findings.[172,173] The experimental microwave and far infrared spectra obtained in these experiments are in fact reproduced reasonably well by simulations employing an internal-rotation model. In the two experiments, the authors reported a average distance of 3.70 Å bewteen CH_4 and H_2O centers of mass, based on their analysis using a model Hamiltonian. This distance lies between our global minimum (3.44 Å) and the secondary minimum (3.77 Å). This also agrees with our DMC result that the ground vibrational state of the CH_4-H_2O dimer samples the two minima. Our estimate of this distance using DMC walkers is 3.78 Å.

Table 5.3: Harmonic frequencies (cm^{-1}) of the global minimum from indicated sources. (I) indicates the intermolecular modes; (M) and (W) the intramolecular modes of methane and water, respectively

mode	*ab initio* [a]	PES-F	PES-PP	LMon [b]	Frag. [c]
1 (I)	49	26	47		
2 (I)	74	75	41		
3 (I)	80	86	87		
4 (I)	87	92	75		
5 (I)	111	113	113		
6 (I)	170	172	215		
7 (M)	1347	1342	1349	1342	1346
8 (M)	1349	1344	1355	1344	1346
9 (M)	1351	1353	1347	1353	1346
10 (M)	1573	1556	1559	1556	1555
11 (M)	1576	1561	1556	1563	1555
12 (W)	1651	1653	1650	1651	1649
13 (M)	3029	3027	3031	3027	3032
14 (M)	3148	3148	3156	3148	3156
15 (M)	3151	3149	3157	3149	3156
16 (M)	3159	3154	3160	3154	3156
17 (W)	3832	3829	3831	3829	3833
18 (W)	3940	3939	3941	3939	3944

[a] CCSD(T)-F12b/haTZ.
[b] Performed on PES-F.
[c] Frequencies from the monomer PESs in Ref. 168 and 169.

The harmonic frequencies of the complex at the global minimum from CCSD(T)-F12b/haTZ calculations, PES-F and PES-PP are listed in Table 5.3. In addition, intramolecular harmonic frequencies from the local-monomer (LMon) calculations using PES-F and the frequencies of the isolated monomers are given. First, as seen, the results using PES-F and PES-PP are in good agreement with each other and also with the direct *ab initio* results. Note, that even with a "perfect" fit of the intrinsic two-body interaction, perfect agreement with the CCSD(T)-F12b/haTZ frequencies is not expected because the monomer potentials used in the PESs are calculated at a different level of theory. The frequencies from the LMon and full normal mode analysis using PES-PI are virtually identical, indicating, as expected, that LMon is a very good approximation for this weakly bound dimer. Finally, if we compare the frequencies of the intramolecular modes in the dimer with those of the isolated monomers, as a consequence of symmetry breaking, the degeneracy of the frequencies of methane split in the dimer and the magnitude of the splitting is certainly large enough to be detected experimentally. I also did the same analysis for the higher energy minimum and find that the intramolecular frequencies differ from those of the global minimum by less than 5 cm^{-1}. This is not surprising given the weak binding of the monomers and the highly delocalized nature of the ground vibrational state wave function.

To obtain the anharmonic eigenstates for high-frequency intramolecular vibrations of the CH_4-H_2O dimer, vibrational self-consistent field and virtual-state configuration interaction calculations (VSCF/VCI) with total angular momentum $J = 0$ were performed using the code MULTIMODE. Two approaches were taken. In the first, a standard normal-mode analysis is performed at the global minimum structure and selected the twelve intramolecular modes in subsequent VSCF/VCI calculations. Specifically, a

twelve-dimensional Schrödinger equation

$$\hat{H}(\boldsymbol{Q})\Psi(\boldsymbol{Q}) = E\Psi(\boldsymbol{Q}) \tag{5.4}$$

was solved, where $\hat{H}$ is the Watson Hamiltonian,[40] and $\boldsymbol{Q} = [Q_1, Q_2, \cdots, Q_{12}]$ denotes the twelve intramolecular modes. The remaining intermolecular modes were fixed at zero. In the second approach, I employed the local-monomer model described in Chapter 3 for the two monomers. The potential term in the Hamiltonian was represented in a hierarchical n-mode representation truncated at 4-mode representation (4MR). The truncation at 4-mode representation is adequate to produce well-converged results, as demonstrated for methane.[174] I employed seven harmonic oscillator wavefunctions for each mode as basis to expand the VSCF states. The VSCF ground and virtual states were then used to expand the CI states in the VCI calculation. In the VCI calculation, simultaneous excitation of up to four modes were done (4-mode basis); the maximum excitation of a single mode (MAXBAS) was 7, 6, 5 and 4 respectively in 1-, 2-, 3- and 4-mode basis, and the sum of quanta of excitation (MAXSUM) was 7. In addition, the C_s symmetry of the dimer is exploited, which allowed to separate the Hamiltonian matrix into two symmetry blocks of sizes 15374 and 11122.

The anharmonic intramolecular fundamental energies at the global minimum with the indicated approaches are listed in Table 5.4, and the corresponding IR spectra are presented in Figure 5.5. Both the spectra in Figure 5.5 panel (a) and (b) are from PES-F. The LMon frequencies and spectrum agree well with the calculation using the twelve intramolecular modes, with difference of no more than 10 cm^{-1}. The good agreement is expected, since the interaction between water and methane is weak and the normal modes of the dimer are localized in the monomer. In addition, the same LMon calculations were
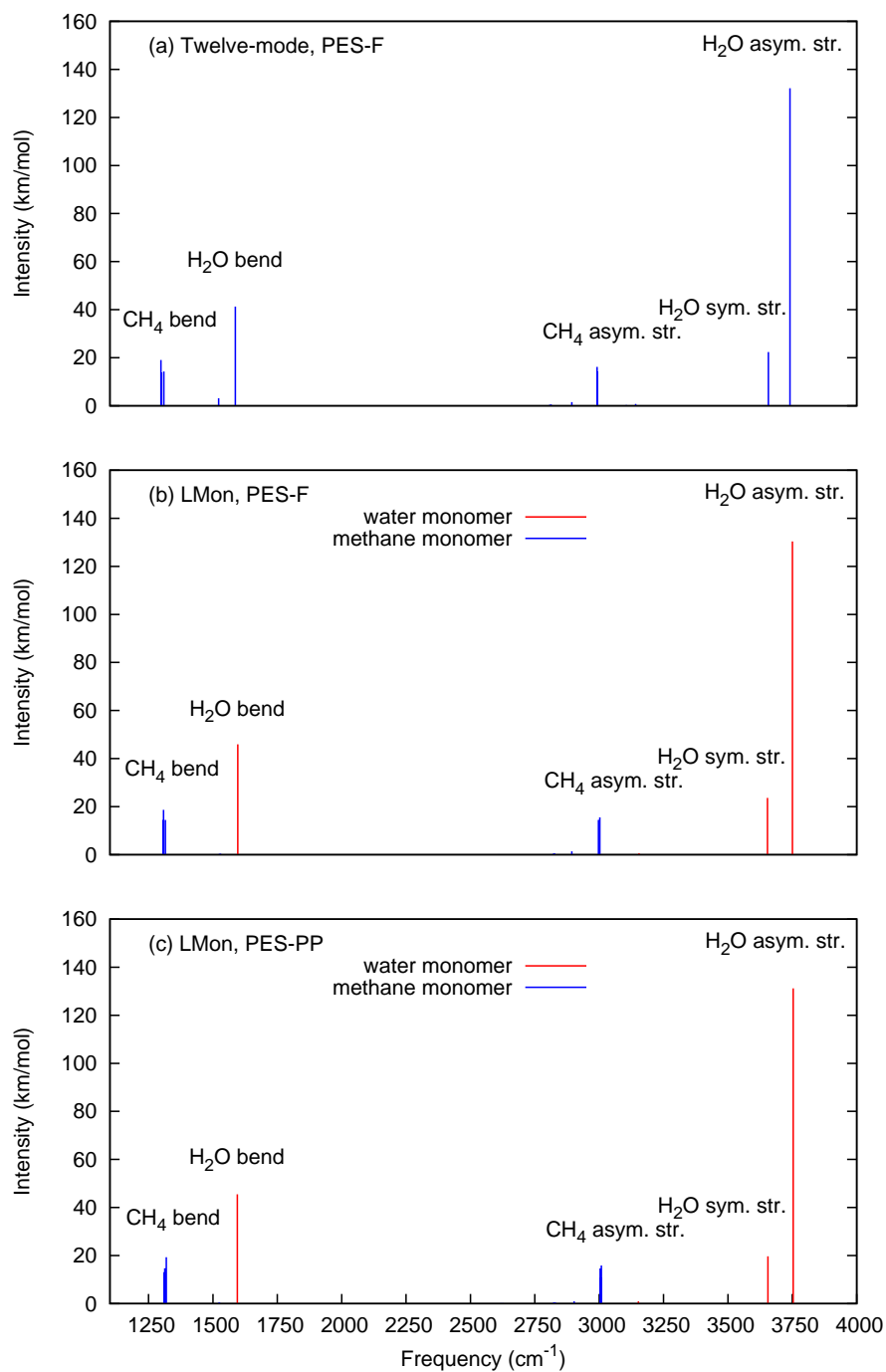
Figure 5.5: IR spectra of global minimum (a) in the twelve-mode calculation using PES-F; (b) in LMon calculation using PES-F; (c) in LMon calculation using PES-PP.

Table 5.4:   Anharmonic intramolecular fundamental energies (cm^{-1}) of the global minimum, using the indicated method and PES. (M) and (W) indicates the intramolecular modes of methane and water

mode	12-mode/PES-F	LMon/PES-F	LMon/PES-PP
7 (M)	1300	1306	1313
8 (M)	1298	1308	1319
9 (M)	1309	1315	1311
10 (M)	1521	1525	1527
11 (M)	1521	1529	1533
12 (W)	1587	1596	1595
13 (M)	2894	2894	2903
14 (M)	2993	2997	3004
15 (M)	2994	3000	3007
16 (M)	2992	3003	3008
17 (W)	3657	3653	3655
18 (W)	3741	3750	3753

performed using PES-PP and the spectrum, shown in Figure 5.5-(c), are in very good agreement with those from the benchmark PES-F. Finally, there are significant shifts in the energies shown in these panels compared to the harmonic ones. The results in this figure are the ones predicted to guide experiments. We stress that these spectra are not intended to be of "line-list" quality. Clearly, such quality would require a more accurate DMS and exact ro-vibrational calculations of the transition moment.

In combustion chemistry, energy transfer and dissociation of methane is of interest.[175,176] In future work, we intend to investigate collisions of methane with water using the two PESs reported here. To test the suitability of these PESs for scattering calculations, we investigated the impact-parameter (b) dependence of the average trajectory time and average energy transfer, and determined the maximum impact parameter (b_{max}) in preliminary simulations of methane-water collisions. In these simulations the collisional energy was set to 1 kcal/mol. The initial internal energies were set to 10000 cm^{-1} and

5000 cm^{-1} for methane and water respectively. Starting internal energies were distributed by means of a microcanonical sampling. For every PES available, small batches of 100 collisional trajectories were evolved for each chosen value of the impact parameter. As already pointed out in a previous work,[177] the average trajectory time is expected to peak before the b_{max} value is reached. After that, the average trajectory time drops steeply while approaching and finally exceeding b_{max}. On the other hand, the b-dependent average energy transfer ($\langle \Delta E \rangle (b)$) is expected to approach zero at b_{max} and larger impact parameter values, since interaction and energy transfer become negligible. We identified b_{max} as the smallest impact parameter for which the two previous conditions are met, considering the condition $\langle \Delta E \rangle (b) \approx 0$ satisfied when $|\Delta E| (b) < 0.2$ cm^{-1}. Figure 5.6 shows that b_{max} values for PES-F (12.5 au) and PES-PP (13.0 au) are in very good agreement. Furthermore, all the two average trajectory times peak at about 2.7 ps for impact parameter $b = 9$ au. As expected, collisional energy transfer simulations are less sensitive to the potential adopted than energetics and spectroscopy calculations.

5.3.3 Summary

For $CH_4 - H_2O$, I have constructed two fitted two-body potentials. The most elaborated fit is very accurate with rms error of 3.5 cm^{-1}. It can reproduce the *ab initio* attractive well depth and harmonic frequencies of the dimer very well. DMC calculations indicate a weak binding of the dimer, with dissociation energy of 153±11 cm^{-1}, while the two monomers undergo near free internal rotation. The anharmonic vibrational frequencies and the intensity of the transitions were predicted by VSCF/VCI calculations. The preliminary simulations of methane-water collisional energy transfer also show that dynamics simulations can be readily performed using our PESs. By comparing the well depth, the
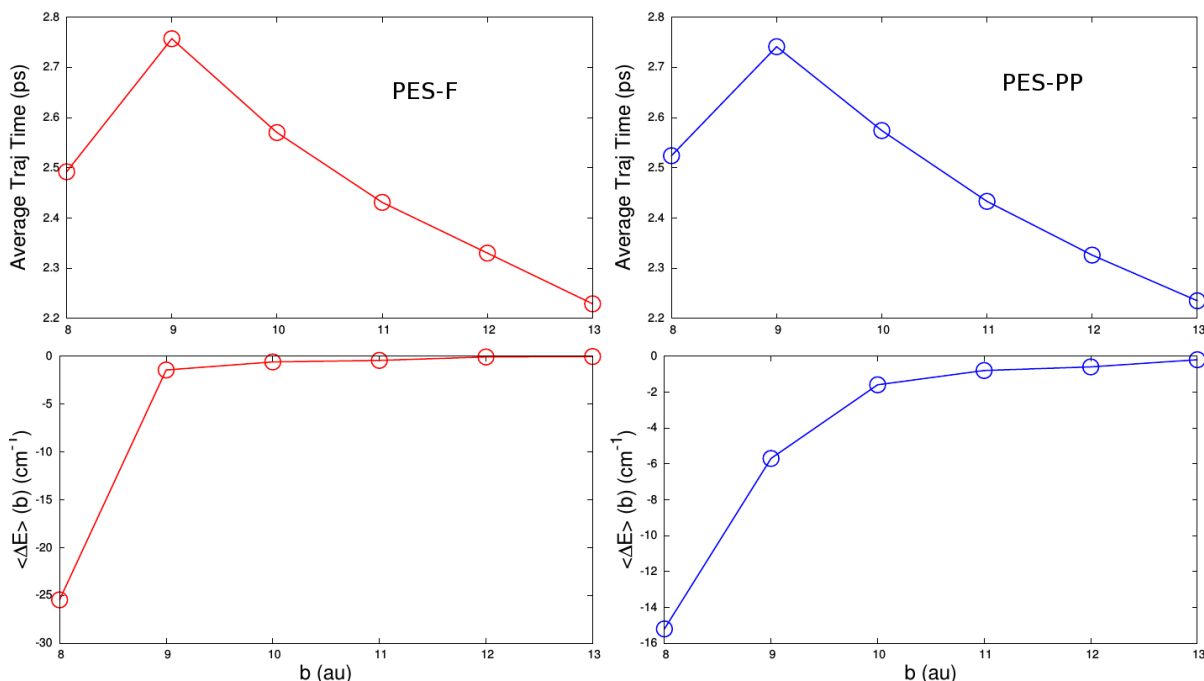
Figure 5.6:   Evaluation of maximum impact parameter in CH_4-H_2O scattering simulations using PES-F and PES-PP potentials.

harmonic and anharmonic frequencies, as well as maximum impact parameter with our best PES, we conclude that the CH_4-H_2O two-body PES using pruned-purified basis is also quite accurate. The purified fitting bases are able to speed up calculations by a factor of about ten.

5.4 $CH_4(H_2O)_2$ Potential

To construct the potential for methane hydrate, in addition to the CH_4-H_2O intrinsic two-body, the potential for $CH_4-H_2O-H_2O$ (MWW) three-body was also constructed.

5.4.1   Ab initio calculation and fitting

The intrinsic three-body energy was calculated from *ab initio* data as

$$V_{\text{MWW}}^{(3)} = V_{\text{MWW}} - V_{\text{MW}_1} - V_{\text{MW}_2} - V_{\text{WW}} + V_{\text{M}} + V_{\text{W}_1} + V_{\text{W}_2}, \qquad (5.5)$$

where the methane is labeled as M and two water monomers are labeled as W_1 and W_2 when only one of the two is involved. Eq. 5.5 is a rearrangement of the three-body term in Eq. 2.16. All electronic energies were obtained using MP2-F12/haTZ theory computed with MOLPRO 2010.[167] In total, 22592 $CH_4-H_2O-H_2O$ configurations were obtained as follows. A first set of 3226 points was obtained as follows: 2000 points were chosen to cover various O-C-O angles and C-O distances; 380 points were selected from molecular dynamics simulations of $CH_4-H_2O-H_2O$ employing preliminary PES fits; 846 points were sampled from $CH_4(H_2O)_{20}$ and $CH_4(H_2O)_{24}$ geometries (methane trapped in cages) for future application of this intrinsic potential to methane clathrates. The monomers were kept almost rigid in these 3226 points. Finally, the remaining 19366 points were randomly sampled around the 3226 points to cover the distortion of monomers.

Figure 5.7 reports the distribution of energies in the database. Most of them are in the range -100 cm^{-1} to 100 cm^{-1}. This small range in energies is mainly a consequence of the weak three-body interaction, but a reasonable fraction of energies is sampled at short monomer distances.

The full and purified fitting bases were adopted to fit the intrinsic potentials, and different permutational group were used in this work because inter-monomer atom exchange does not occur. However, when two or more monomers are of the same kind, we require an additional permutational invariance with respect to this monomer interchange. This particular symmetry is of course included in full permutational groups, but

it must be added to low-order groups. In the case where this is done, our notation is to label the group with an additional * symbol. Operationally, since a modification of the existing software to include the star symmetry into low-order symmetry groups is not straightforward, we incorporate it by duplicating the database of energies upon collective permutation of atoms of like monomers. For the intrinsic three-body $CH_4-H_2O-H_2O$ potential the database needs only to be doubled.
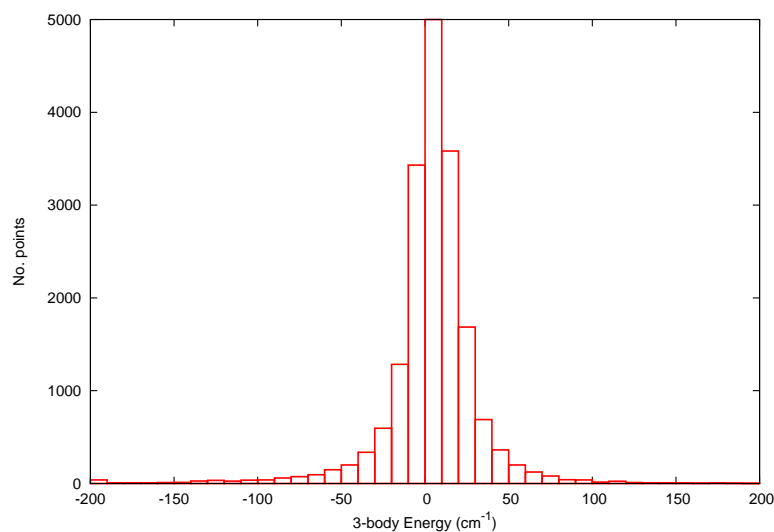
Figure 5.7:   Distribution of the 22592 MP2-F12/haTZ energies in the database. Bin width is 10 cm^{-1}. The most populated bin is truncated to better appreciate the population in the high-energy bins. Bins labeled as 200 and -200 contain also all populations from energies above and below those values.

This database of intrinsic three-body energies was fitted by nine PESs. These are given along with a variety of performance metrics in Table 5.5. As seen, and as expected, the number of coefficients increases with the maximum polynomial order M for the given basis type. Furthermore, and also as expected, there are fewer coefficients for PESs of higher permutational order. The purified potentials have a substantially lower number of

Table 5.5: Number of coefficients, fitting rms error in cm^{-1}, computational times, and intrinsic three-body energy in cm^{-1} of the trimer for different analytical $CH_4-H_2O-H_2O$ potentials. Time is arbitrarily set equal to 100 for PP-422111*/4. The *ab initio* value has been calculated with MP2-F12/haTZ.

Potential	No. Coeff.	rms	time (arb. units)	$V_{MWW}^{(3)}$
F-821/4	716	15.9	1944.6	-62.7
F-821/3	153	23.0	83.1	-11.3
F-4421/4	4698	5.1	927.8	-134.8
F-4421/3	654	13.8	49.5	-102.8
P-422111*/4	15551	2.2	301.0	-131.7
PP-422111*/4	5809	4.6	100.0	-133.5
F-422111*/3	2553	7.9	33.4	-137.1
P-422111*/3	1245	8.8	27.8	-130.9
PP-422111*/3	729	10.5	13.6	-135.1
ab initio				-130.7

polynomials than the corresponding full ones. The impact of this reduction increases with the maximum polynomial order within a group. The rms errors are small, partially due to the fact that three-body interactions are themselves small. However, the variation of the fitting error is significant. Within a given permutational group, the fit precision increases with the number of polynomials, as expected. A more complicated dependence concerns computational time. We have averaged over batches of ten repetitions the time needed by the different potentials in evaluating 50000 potential calls. For comparison purposes, we have set equal to 100.0 the time required by PP-422111*/4. We note that within the same permutational group the computational effort grows with the number of polynomials to evaluate, of course. However, this is no longer true when comparing between different groups. For instance, PP-422111*/4 with 5809 terms is more than 9 times faster than F-4421/4 with 4698 terms. The reason is that monomial symmetrization requires evaluation of a much larger number of monomials for groups of higher permutational order. In other

words, the fewer polynomials in the F basis with high symmetry are more expensive to evaluate because they contain more monomials. For example, F-4421/4 with 4698 terms requires calculation of about 121 K monomials against the 16 K required by PP-422111*/4 with 5809 terms.

5.4.2   Test of the potential

Fitting errors do not necessarily translate into accuracy of the potentials in energy calculations. To investigate this, I have employed the potentials to evaluate the intrinsic three-body contribution to the energy of the $CH_4-H_2O-H_2O$ trimer. The trimer equilibrium configuration has been optimized at CCSD(T)-F12a/haDZ level of theory to best evaluate the *ab initio* binding energy. The last row of Table 5.5 reports the *ab initio* intrinsic three-body energy calculated with MP2-F12/haTZ, the same level of theory employed for the database, thus allowing for a direct comparison to the results of our potentials. The last column of Table 5.5 presents the intrinsic three-body contribution of the potentials to the $CH_4-H_2O-H_2O$ trimer energy. F-821/3, F-821/4, and F-4421/3 are far off the *ab initio* value and will not be further considered. As for the remaining six potentials, those with maximum polynomial order $M = 4$ provide excellent approximations, while F-422111*/3 is less accurate but still acceptable. Remarkably, the two very fast purified potentials with $M = 3$ (P-422111*/3 and PP-422111*/3) yield much better energies than the corresponding F potential even if based on a lower number of polynomials. We will employ all six potentials in the final and more complex energy calculations before drawing our conclusions about the accuracy of the fitted potentials.

By summing up the pre-existing potentials (including water monomer,[169] intrinsic two-body $(H_2O)_2$,[178,179] and the methane intramolecular potentials[168]) and the intrinsic

two-body CH_4-H_2O and the present three-body $CH_4-H_2O-H_2O$ potentials, we obtain the PES for the $CH_4-H_2O-H_2O$ trimer. By employing the same optimized geometry for the $CH_4-H_2O-H_2O$ trimer as before, high-level CCSD(T)-F12b/haTZ *ab initio* calculations were performed to evaluate each term of one-, two- and three-body interactions. For comparison, the same calculations were performed with the analytical PES using P-422111*/3, the potential that better approximates the intrinsic three-body *ab initio* value for the trimer geometry. The zero of energy was set for the three isolated monomers in their equilibrium configurations. The energy of each term in the many-body representation is listed in Table 5.6. As seen, the two-body energy from F-4211/5 potential is almost exact if compared to the *ab initio* value, and the estimate of PP-4211/5 two-body potential is also very accurate. Our most reliable estimate of D_e for the trimer is 2371.3 cm^{-1}. It is obtained by using F-4211/5 for the intrinsic two-body CH_4-H_2O interactions. Our value agrees well with the *ab initio* result of 2403.3 cm^{-1}. The difference is mainly due to the intrinsic two-body H_2O-H_2O term, the error of which is partially compensated by the overestimation of the three-body contribution. The main reason for these discrepancies lies in the different levels of electronic theory adopted. In fact, the two-body H_2O-H_2O PES is fitted to CCSD(T)/aVTZ energies, P-422111*/3 to MP2-F12/haTZ energies, while *ab initio* calculations in this test were performed with CCSD(T)-F12b/haTZ. The three-body interaction is shown to have a non-negligible impact, accounting for about 5% of the dissociation energy.

To further point out the accuracy of our three-body potentials, we present in Figure 5.8 three 1-d cuts for the three potentials with lowest fitting error. Starting from the optimized equilibrium geometry of the trimer, the cuts describe the change in three-body interaction energy against variation of the distance between the methane carbon atom and the oxygen atom of one of the two water monomers. In the cuts reported, all monomer

Table 5.6:   Energy of each term in the many-body representation of the $CH_4-H_2O-H_2O$ trimer. Energies are in cm^{-1}. *Ab initio* calculations employ CCSD(T)-F12b/haTZ.

	ab initio	PES
CH_4 1-body	16.4	12.3
$H_2O(1)$ 1-body	16.8	18.4
$H_2O(2)$ 1-body	5.1	5.8
$CH_4-H_2O(1)$ 2-body	-232.9	-233.9 [a], -252.6 [b]
$CH_4-H_2O(2)$ 2-body	-330.0	-330.5 [a], -331.7 [b]
H_2O-H_2O 2-body	-1756.3	-1712.5
$CH_4(H_2O)_2$ 3-body	-122.4	-130.9 [c]
$CH_4(H_2O)_2$ D_e	-2403.3	-2371.3 [a,c]

[a] F-4211/5 for CH_4-H_2O;
[b] PP-4211/5 for CH_4-H_2O;
[c] P-422111*/3 for $CH_4-H_2O-H_2O$.

internal geometries are frozen along the cut and the C-O distance is modified in one case moving the methane (upper panel) and in the other case shifting the water monomer (lower panel). The second water monomer is held at its initial position. The three potentials show excellent accuracy down to C-O distances of about 3 Å, a short distance where two-body repulsive interactions start to be increasingly predominant. The upper panel clearly points out that purified potentials rigorously ensure the zero-interaction asymptotic limit.

5.4.3   Summary

I have constructed several fits to represent the $CH_4-H_2O-H_2O$ three-body interaction, with different symmetry group, polynomial order, and fitting bases. These three-body potentials have been employed for calculations involving the methane-water-water trimer. Results are excellent from the point of view of both accuracy and reduction of computa-
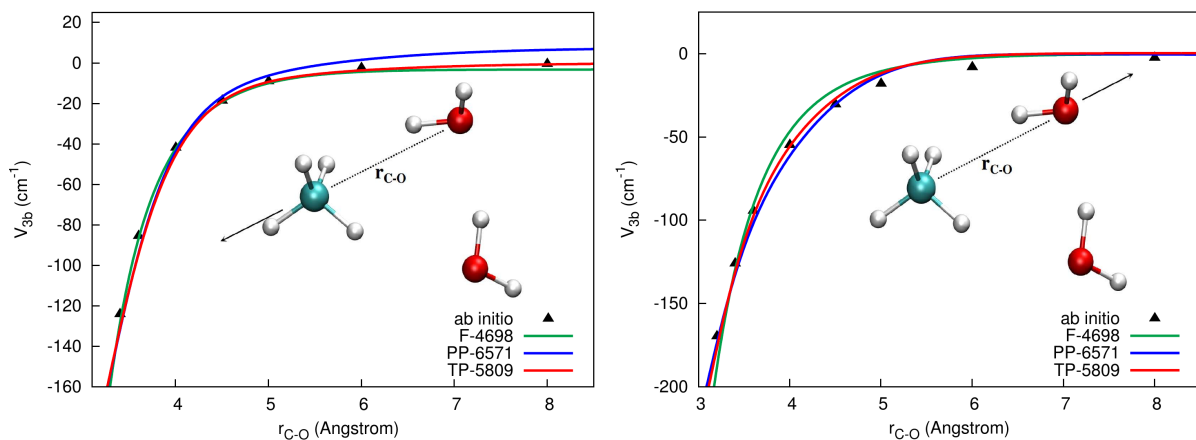
Figure 5.8: 1-D cuts for the intrinsic $CH_4-H_2O-H_2O$ three-body potential ($V_{MWW}^{(3)}$).

tional overheads. For instance, with the maximum polynomial order of 4, the P-422111*/4 potential is about three times faster than the one with full fitting bases (F-4421/4), and another speed up of three times is achieved by using the pruned-purified fitting bases. As for accuracy, the three-body contribution to the binding energy of the trimer is reproduced with errors of just a handful of wavenumbers.

5.5 H_2-H_2O Potential

The interaction between H_2 and H_2O has also drawn considerable attention experimentally and theoretically.[180–185] In the H_2-H_2O dimer, the water molecule exhibits an interesting dual identity as either either proton donor or acceptor.

An early PES of the H_2-H_2O dimer has been reported by Hodges et al.[186] in 2004. This was a rigid-body, five-dimensional PES obtained with scaled perturbation theory. In 2005, Faure et al.[187] presented a full-dimensional interaction potential, calibrated using highly accurate CCSD(T) with explicitly correlated R12 method. The authors first calculated the H_2-H_2O interaction by performing rigid-rotor five-dimensional calculations

for a large number of geometries at "medium accuracy" CCSD(T) level. The resulting surface was further calibrated by means of high-precision explicitly correlated CCSD(T)-R12 calculations on a subset of the rigid-rotor intermolecular geometries. Finally, the five-dimensional rigid-rotor PES was extended to all nine dimensions. Later they reported a vibrationally averaged potential for the dimer.[188] This PES was then used to investigate rovibrational states of the H_2-H_2O dimer, showing good agreement with experimental observations.[184] The extension beyond the rigid rotor was made using a quadratic Taylor series expansion about the rigid rotor reference configuration. It has not, to the best of our knowledge, been used for vibrational applications beyond zero-point averaging of the full potential.

In this section, flexible, *ab initio* potential energy surfaces for the intrinsic two-body energies of H_2-H_2O is presented.

5.5.1 Ab initio calculation and potential fitting

For calculations of the intrinsic two-body H_2-H_2O energies, the CCSD(T)-F12 method was employed, and tests of various basis sets were performed to evaluate their accuracy and efficiency, in order to come up with a reasonable choice for the database of energies. For this purpose the *ab initio* dissociation energy (D_e) of the H_2-H_2O dimer was calculated at the CCSD(T)-F12a level of theory using aVTZ, aVQZ, aV5Z and haQZ (aVQZ for O and VQZ for H) basis sets for the global and secondary minima. The results are given in Table 5.7, along with the result from previous CCSD(T)-R12 calculations using theoretical equilibrium geometries.[187] Compared to the aV5Z results, haQZ energies are off by only a few (though maybe fortuitously) wavenumbers. Furthermore, it's considerably faster than the aVQZ basis. Therefore, the haQZ basis seems to be a reasonable

choice for both computational cost and accuracy, and the estimated computational cost of the calculations for the database of roughly three days of CPU time on a sixteen-processor computer, was deemed quite feasible.

Table 5.7: Comparison of D_e (in cm^{-1}) for H_2-H_2O dimer at CCSD(T)-F12a level of theory using different basis sets, and from a previous study.

Minimum Geometry	aVTZ	aVQZ	aV5Z	haQZ	Ref. 187
Global	241.4	227.8	223.2	224.0	221.2
Secondary	220.8	203.0	197.7	194.7	-

Thus, for the intrinsic two-body potential we generated a database of 44623 *ab initio* energies at CCSD(T)-F12a level of theory with haQZ basis set. A first set of H_2-H_2O configurations was obtained by means of direct-dynamics simulations performed using normal-mode sampling of initial conditions at several internal excitation energies up to the dissociation limit and employing B3LYP/6-31G(d,p) level of theory. Then, starting from many of the distorted monomer configurations thus generated, additional dimer geometries were randomly sampled by varying inter-monomer H-O or H-H distances in the range between 2.0 and 9.0 Angstroms. At these configurations, the intrinsic two-body interaction was obtained according to

$$V^{(2)}_{H_2-H_2O} = V_{H_2-H_2O} - V_{H_2} - V_{H_2O}. \tag{5.6}$$

Thus, three electronic energies are needed per configuration. From the database of these energies, a preliminary two-body fit was performed to assess the appropriateness of the sampled configurations. Harmonic frequencies of the global minimum and some one-

dimensional cuts obtained with this preliminary PES were compared to the corresponding values from *ab initio* calculations. Thereby, about 3000 points were added to the preliminary dataset to provide a better coverage of the surface. We did not employ counterpoise correction because basis superposition errors are expected to be small for the basis set used. All the *ab initio* calculations were carried out using MOLPRO 2010.[167]

For the H_2-H_2O two-body potential, the permutational group we have adopted is 221, meaning that the two hydrogens of H_2 can be interchanged without modification of the potential energy. The same applies to the two hydrogens of the H_2O monomer, while the single oxygen atom does not have a permutational counterpart. The full (F) and purified (P) fitting bases are used to fit this two-body potential.

We have obtained several fits for the intrinsic H_2-H_2O interactions, adopting the techniques described in the previous section. The potentials have been first assessed on the basis of their rms fitting error and relative computational costs. Table 5.8 summarizes these for each potential, identified by the label introduced in the previous section. The computational times are evaluated by averaging batches of 10 series of 50000 potential calls, and compared by setting arbitrarily to 100 the cost of F-221/6.

Table 5.8: Number of coefficients, fitting rms error, and relative computational times, for different fitted H_2-H_2O intrinsic potentials. Time is arbitrarily set equal to 100 for F-221/6.

H_2-H_2O	No. Coeff.	rms (cm^{-1})	time (arb. units)
F-221/6	2304	3.8	100
P-221/6	2174	5.0	53
PP-221/6	260	114.8	7
P-221/7	5216	4.2	153

Table 5.8 shows that for the two-body interaction, F-221/6 is characterized by a very small fitting error. The purified potential (P-221/6) still has low rms error and speeds up calculations by a factor of two. The pruned purified potential (PP-221/6) depends on a much smaller number of coefficients and it is extremely fast but, on the other hand, its fitting error is much higher. This can be explained by recalling that PP potentials depend exclusively on inter-monomer variables. In the two-body system presented here, there are only six inter-monomer distances, which is fewer than the dimensionality of the H_2-H_2O surface (nine). Finally, we notice that an increment of the maximum polynomial order (P-221/7) decreases only slightly the fitting error but increases about three times computational overheads. For these reasons, F-221/6 and P-221/6 are employed in our further calculations.

5.5.2   Test of the potential

Figure 5.9 shows the distribution of the intrinsic two-body energy and the corresponding fitting error of F-221/6. The interaction between H_2 and water is fairly small, with most of the sampled energies between -250 and 150 cm^{-1}. A large number of points were sampled at large monomer separation so that the F-potential does numerically reproduce the correct asymptotic energy (which is zero). These energies contribute to the high peak at $V_{2b} = 0$ in panel (a) on the left. The panel (b) shows the distribution of the fitting error, which, in general, is lower than 15 cm^{-1}, with rms of 3.8 cm^{-1}. The rms error in repulsive short range, van der Waals minimum and long range regions are listed in Table 5.9. Overall the error is small and varies little in different regions, but in the long range it is relatively large compared to the (small) energies in this region. This is because our fits employ exponentially decaying functions, which do not have the correct long

range decay. However, the database and the fit do yield energies that are in the few wavenumber range. For applications that require very precise potential evaluations in the long range, investigators can easily switch at large distances to a potential that has the correct analytical H_2-H_2O interaction.
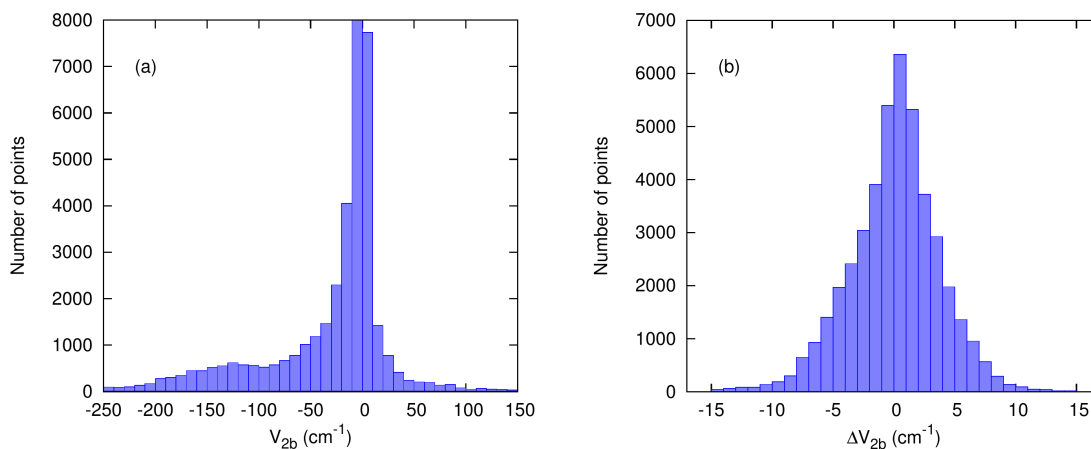
Figure 5.9: Distribution of (a) energy and (b) fitting error (full fitting basis) of intrinsic two-body energies.

Table 5.9: Root-mean-square error (in cm^{-1}) of the F-221/6 potential in the repulsive, van der Waals minimum and long range regions. The average absolute potential in each region is also listed.

Center-of-mass distance	< 2.7 Å	2.7 Å– 5.0 Å	> 5.0 Å
Average $|V_{2b}|$	11032.4	81.3	5.7
rms error	5.8	4.2	3.2

Two one-dimensional cuts at two different orientations of the H_2-H_2O dimer from *ab initio* calculations and the PES are given in Figure 5.10, which shows very good

agreement between the F-221/6 and P-221/6 fits, and both agree with the *ab initio* energies excellently.
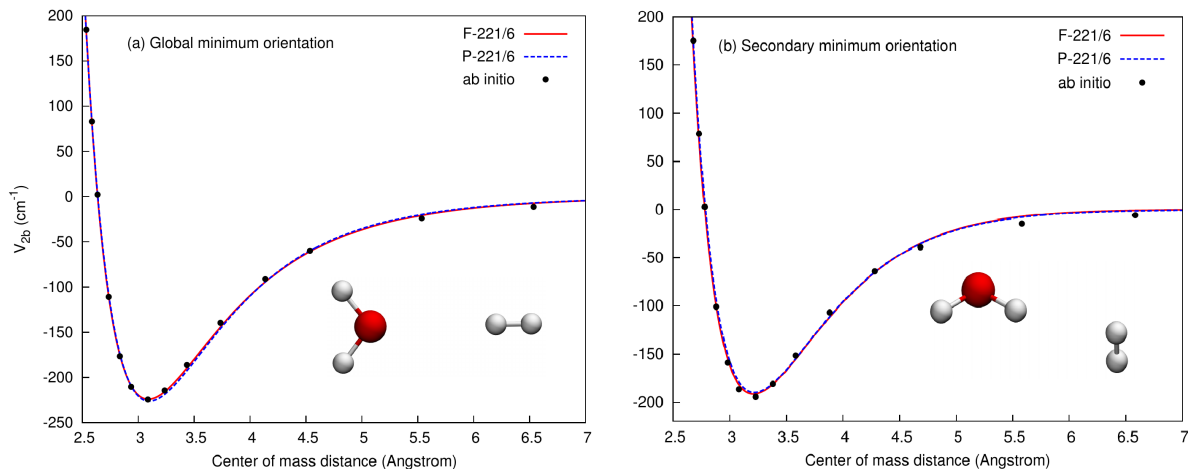
Figure 5.10:   Two one-dimensional cuts from the two-body PESs and *ab initio* calculations, at two different orientations.

The global full PES of the H_2-H_2O dimer is the sum of the intrinsic two-body potential (here either F-221/6 or P-221/6) and pre-existing hydrogen[189] and water monomer potentials.[169] This global H_2-H_2O PES was employed for geometry optimization, calculation of the dissociation energy, normal mode analysis and DMC calculations of the zero-point energy and wavefunction of the dimer.

The two minima were located on the full PESs, and their configurations are depicted in panels (a) and (b) of Figure 5.11. The global minimum has a planar structure, while in the higher-energy minimum, the H_2 is perpendicular to the H_2O plane. The dissociation energies of these two minima are given in Table 5.10. Dissociation energies obtained from the analytical PESs agree well with the *ab initio* values.

The harmonic frequencies of the two minima are reported in Table 5.11. The *ab*
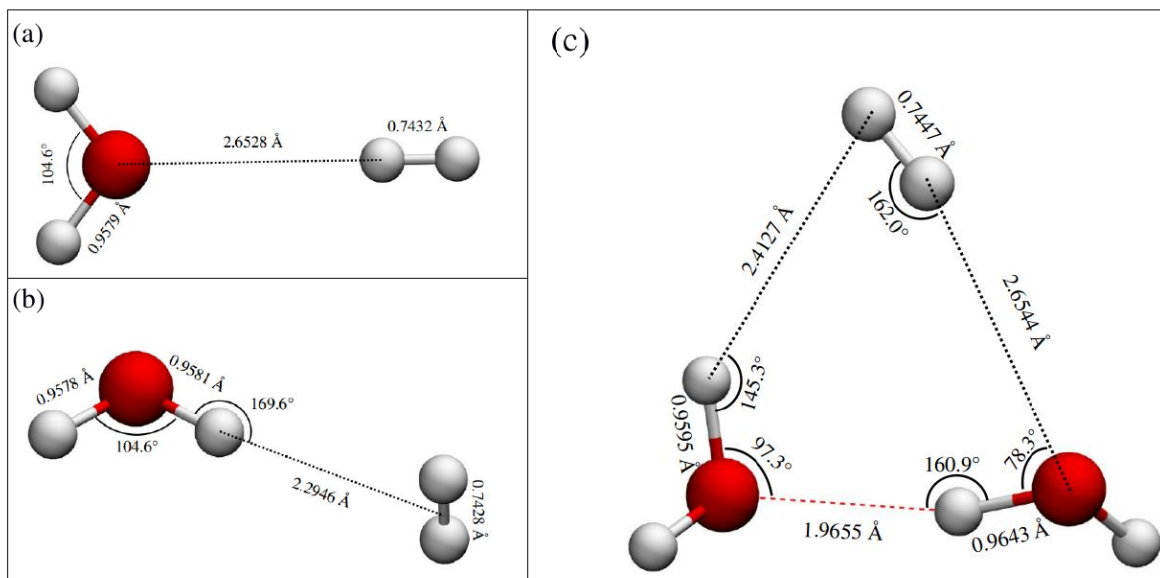
Figure 5.11: The structures of (a) global minimum of H_2-H_2O dimer, (b) secondary minimum of H_2-H_2O and (c) global minimum of $H_2(H_2O)_2$ trimer.

Table 5.10: D_e (in cm^{-1}) for the H_2-H_2O dimer from *ab initio* CCSD(T)-F12a/haQZ calculations and two different PESs.

Structure	*ab initio*	F-221/6	P-221/6
Global minimum	224.0	223.7	225.8
Secondary minimum	194.7	191.4	189.8

initio frequencies for the first two modes are not shown because it's computationally too demanding to get well-converged frequencies for those low-frequency librations. Results for the two PESs agree well with each other. The agreement with the *ab initio* frequencies is also very good. Note also the small differences between the sets of frequencies for the intramolecular modes of each minimum. This is already an indication that these minima are actually quite "floppy". This is investigated in detail next.

Table 5.11: Harmonic frequencies of the two H_2-H_2O minima from *ab initio* and PES calculations.

Global minimum			Secondary minimum		
ab initio	F-221/6	P-221/6	*ab initio*	F-221/6	P-221/6
-	33.1	36.9	-	39.3	39.4
-	34.9	38.3	-	82.7	85.4
135.9	132.8	132.8	117.3	100.7	101.1
257.5	259.0	262.3	142.2	135.8	133.9
287.0	281.4	281.2	356.9	337.3	330.8
1648.8	1649.4	1650.0	1650.7	1651.0	1651.1
3834.7	3831.0	3831.6	3831.7	3832.4	3834.9
3945.0	3943.0	3943.5	3940.8	3943.2	3943.0
4382.7	4380.6	4379.7	4388.6	4387.6	4387.9

The ZPEs of the dimer and the fragments have been calculated using DMC simulations. For each system studied, ten simulation were carried out, and in each simulation, 20000 walkers were propagated for 55000 steps. The walkers were equilibrated in the first 5000, and the energies in the remaining steps were collected to calculate the ZPE. The ZPE of the bound dimer is 7003.8 ± 1.2 cm^{-1} when employing F-221/6. If P-221/6 is used, then the ZPE is 7005.3 ± 0.7 cm^{-1}, which agrees very well with the F-221/6 result. The sum of ZPEs of the two fragments were calculated with two different approaches.

The first approach still consists of DMC simulations but uses only the monomer PESs. The result is 6814.3 ± 1.0 cm^{-1}. In the second approach, the H_2 ZPE was calculated with a one-dimensional discrete variable representation (DVR), while the ZPE of water was calculated using the software MULTIMODE.[38,39] The sum of the two ZPEs of the fragments is in this case 6816.2 cm^{-1}, in agreement with the value obtained with DMC calculations. Finally, we evaluated the measurable dissociation energy (D_0) of the H_2-H_2O dimer, and our best estimate is 34.5 ± 1.6 cm^{-1}, using the DMC ZPEs for both the bound dimer (7003.8 ± 1.2 cm^{-1} from the F-221/6 fit) and the fragments (6814.3 ± 1.0 cm^{-1}), and the CCSD(T)-F12a/haQZ electronic dissociation energy (224.0 cm^{-1}).
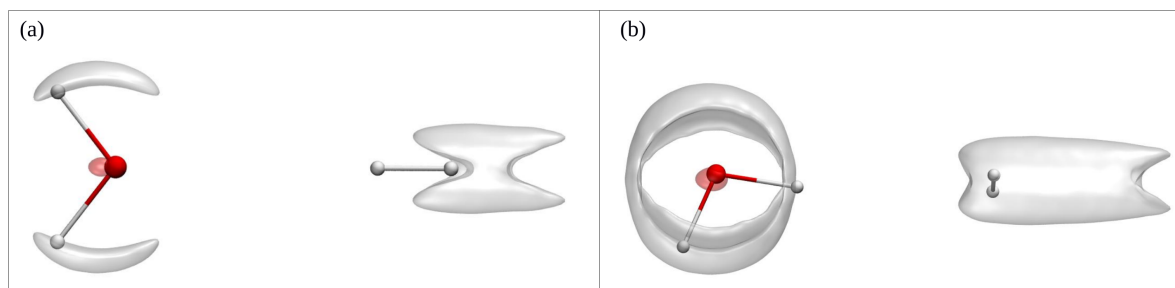
Figure 5.12:   Iso-surfaces of the vibrational ground state wavefunction for the H_2-H_2O dimer from the DMC simulations with two different iso-values. The global and secondary structures are also indicated as reference structures in panels (a) and (b), respectively.

The vibrational ground state wavefunction of the dimer can also be obtained from the DMC simulation. About 2000000 geometries of the walkers were collected from the simulations and these geometries were optimally aligned into the principal axis frame. The wavefunction amplitude was obtained by dividing the space into volume elements and performing histogram binning in the atomic coordinates, as was done for CH_4-H_2O. The vibrational ground state wavefunction of the H_2-H_2O dimer is shown as cloud-like iso-

surfaces in Figure 5.12, with two different iso-values. In panel (a), the iso-value is 70.7%
of the maximal amplitude, while, in panel (b), the iso-value is 45% of the maximum. As
a reference, the geometries of the global and secondary minima of the H_2-H_2O dimer are
also shown. As one can see from the figure, the wavefunction has larger amplitude near
the global minimum, but also has significant amplitude near the secondary minimum.
We conclude that, overall, the vibrational ground state wavefunction is broad and spans
both minima, indicating that the dimer is characterized by large amplitude motion (i.e.
nearly free monomer rotation).

5.5.3   Summary

We have presented four different intrinsic two-body potentials for H_2-H_2O. The most
accurate fit has rms error of 3.8 cm^{-1}, and it is obtained upon least-squares fit based on
full fitting bases. For this two-body potential, the pruned-purified bases (PP) contains
fewer variables than the degrees of freedom; therefore, the PP potential has a significant
error. These intrinsic two-body potentials using full and purified fitting bases have been
employed to build the potential of H_2-H_2O dimer. The PES can reproduce the electronic
dissociation energy and the harmonic frequencies of the dimer precisely. Our best esti-
mation of the dissociation energy D_0 of the dimer is 34.5 $\pm$ 1.6 cm^{-1}, based on DMC
calculations of the zero-point energies of the dimer and isolated monomers. Further ex-
amination of the vibrational ground state wavefuntion obtained in the DMC simulations
indicates that the hydrogen and water monomers undergo nearly free internal rotation.

5.6 $H_2-H_2O-H_2O$ Potential

Xu et al.[148] performed quantum translation-rotation calculations for the H_2 trapped inside clathrate cages, based on two different types of H_2-H_2O pair potentials, such as a simple point charge model (SPC/E)[75], and the *ab initio* one by Hodges et al.[186]. However, calculations using the five-dimensional *ab initio* PES overestimate the angular anisotropy of the H_2-H_2O cage interaction, yielding too large H_2 rotational splittings, and underestimate the translational frequencies; on the contrary, the same calculations using SPC/E potential, which actually incorporates approximately some effect of nonadditive, many-body induced polarizations, yield better agreement with experiment. This implies that three-body $H_2(H_2O)_2$ interactions cannot be neglected. So we have also constructed PESs for the three-body interactions.

5.6.1   Ab initio calculation and PES fitting

For the intrinsic three-body potential, we employed the CCSD(T)-F12a level of theory and haTZ (aVTZ for O and VTZ for H) basis set. The database consists of 36603 *ab initio* energies. A first set of 29757 points was generated following the same procedure adopted for the H_2-H_2O two-body database, as described above. The remaining 6846 points were selected from clathrate structures. The intrinsic $H_2(H_2O)_2$ three-body energies was obtained according to

$$V^{(3)}_{H_2(H_2O)_2} = V_{H_2(H_2O)_2} - V^{(2)}_{(H_2O)_2} - \sum_{i=1}^{2} V^{(2)}_{H_2-H_2O(i)} - \sum_{i=1}^{2} V_{H_2O(i)} - V_{H_2}. \qquad (5.7)$$

The *ab initio* calculations were carried out using MOLPRO 2010.[167]

Similar to the $CH_4-H_2O-H_2O$ and H_2-H_2O intrinsic potentials, different fitting

Table 5.12: Number of coefficients, fitting root mean square error, and relative computational times, for different fitted H_2-H_2O intrinsic potentials. Time is arbitrarily set equal to 100 for F-221/6.

$H_2(H_2O)_2$	No. Coeff.	rmse (cm^{-1})	time (arb. units)
F-422/5	5801	2.9	2378
P-422/5	2850	9.4	1128
PP-22211*/5	9649	6.5	390
P-22211*/4	4455	12.7	186

bases and symmetry groups were adopted to fit this $H_2(H_2O)_2$ intrinsic three-body potential. Table 5.12 summarizes the number of coefficients, rmse, and computational cost for each potential, identified by the label introduced in the previous section. The computational times are evaluated by averaging batches of 10 series of 50000 potential calls, and the cost of the F-221/6 fit of the H_2-H_2O two-body is set to 100. We first notice that the potential obtained by means of the invariant polynomial technique (F-422/5) is very accurate but also very slow, and the purified potential for the same permutational group (P-422/5) cut costs just in half. Better results are obtained by lowering the order of the permutational group. The potentials for group 22211* are faster to evaluate even if they depend on a larger number of coefficients (and consequently polynomials). The reason is that the single polynomials are much cheaper to calculate than in the case of symmetry 422. The precision of PP-22211*/5 and P-22211*/4 is also very good. In the case of the three-body interaction, the pruned-purified potential depends on 21 intermonomer variables, a number larger than the dimensionality of the $H_2(H_2O)_2$ surface (18), and the fitting rmse remains small. Due to their combined fitting accuracy and speed, PP-22211*/5 and P-22211*/4 will be employed in the trimer calculations together with F-422/5. Finally, we note, that computational times for the three-body fits are much

larger than for the two-body fits, as expected.

5.6.2   Test of the potential

Similar to the two-body case, Figure 5.13 shows the distribution of energy and fitting error for the F-422/5 intrinsic three-body potential. The intrinsic three-body energy is weaker than the two-body one, and consequently the distribution of the energy is narrower. We also needed a large number of points at large monomer separation to guarantee zero asymptotic value in the case of the full fitting basis. Rmse (2.9 cm^{-1}) and fitting error distribution are comparable to those of the intrinsic two-body.
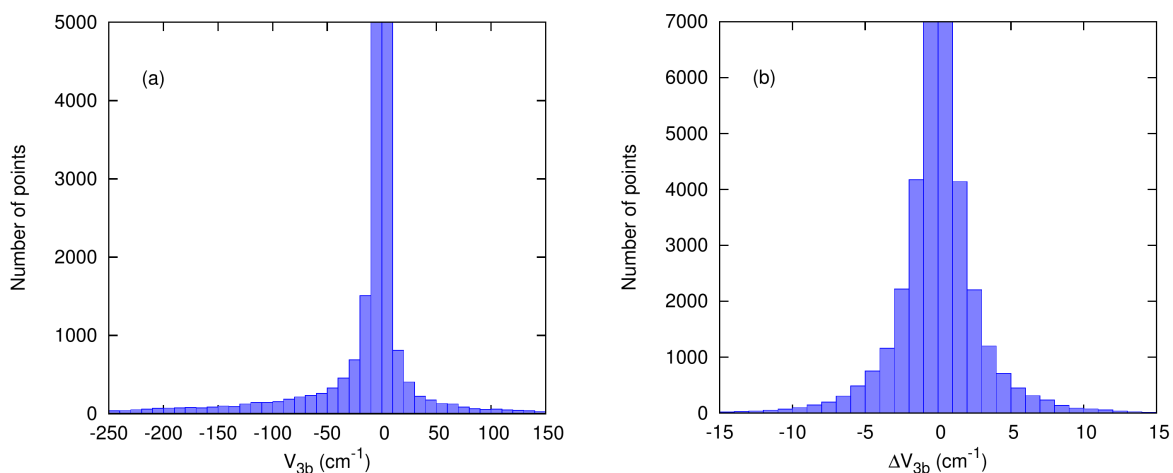
Figure 5.13: Distribution of (a) energy and (b) fitting error (F-422/5 potential) of intrinsic $H_2(H_2O)_2$ three-body energies.

Two one-dimensional cuts that are not included in the fitting database are shown in Figure 5.14. Three fits of the three-body energy have been tested here. In one of the cuts, the fitted intrinsic potentials agree almost perfectly with the *ab initio* energies, while, in the other cut, the agreement is not perfect for F-422/5. It approaches zero slightly too

fast when the O-O distance increases. However, overall, the fitted three-body potentials are precise representations of the *ab initio* energies.
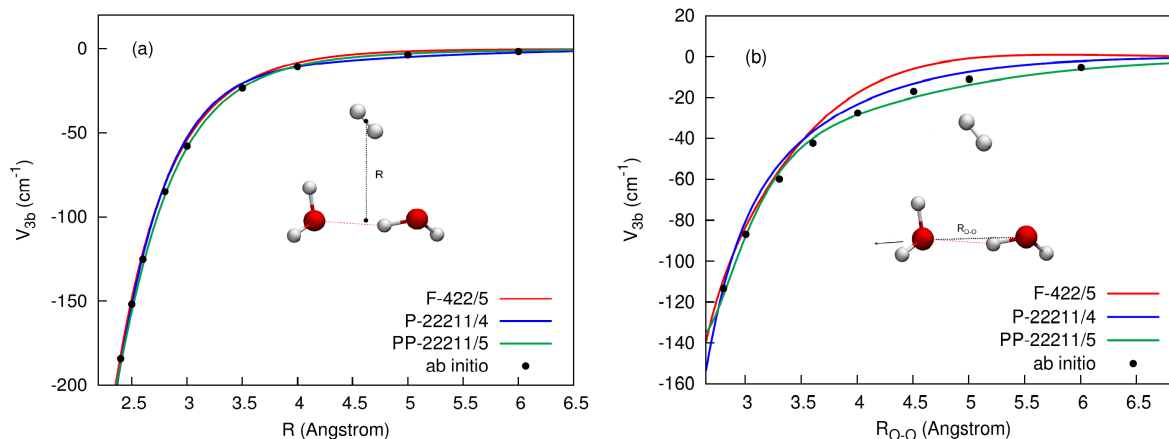
Figure 5.14:   Two one-dimensional cuts of the three-body interaction for the $H_2(H_2O)_2$ trimer from *ab initio* calculations and the indicated intrinsic three-body PESs.

The full, global PES of the $H_2(H_2O)_2$ trimer is the sum of five potentials: water monomer, H_2 monomer, water two-body from our group, and the present H_2-H_2O intrinsic two-body (F-221/6) and $H_2(H_2O)_2$ intrinsic three-body. For the latter, three potentials were tested and compared, i.e. F-422/5, P-22211*/4 and PP-22211*/5. The structure of the trimer minimum with some geometric parameters is depicted in panel (c) of Figure 5.11. The H_2 and the hydrogen bonded OH form a nearly planar ring, with one free OH above and one below the ring. The electronic dissociation energy of the trimer, D_e, was determined by setting the zero of energy for the three isolated monomers in correspondence of their equilibrium geometry. The contribution of all the one-body, two-body and three-body terms as well as the final D_e are listed in Table 5.13. Note, the minima all differ slightly for each column in the table and so the contributions from all one-body

and two-body terms differ slightly among the PESs, even though the same one-body and two-body potentials are used in all PESs. The three analytical PESs all have somewhat smaller values of D_e compared to the *ab initio* value. The difference is mainly due to the $(H_2O)_2$ two-body energy. The reason is that different *ab initio* methods were employed in the calculations. The potential we use for the water two-body in our analytical PESs has a near-exact D_e, and thus more accurate than the one obtained with the present *ab initio* calculations, which use CCSD(T)-F12a/haTZ level of theory without counterpoise correction. Thus, we believe that accurate D_e is within a few wavenumbers of 2140 cm^{-1}.

Table 5.13: Energy of each term in the many-body decomposition of the $H_2(H_2O)_2$ trimer.

	ab initio	F-422/5	PP-22211*/5	P-22211*/4
H_2 one-body	1.7	1.4	1.5	1.4
H_2O one-body	15.6	13.7	14.0	13.7
H_2-H_2O two-body	-356.6	-354.4	-358.2	-351.3
$(H_2O)_2$ two-body	-1745.0	-1703.3	-1690.9	-1703.4
$H_2(H_2O)_2$ three-body	-103.0	-95.9	-113.3	-100.5
D_e	2187.3	2138.5	2146.9	2140.1

Table 5.14 gives the harmonic frequencies for the $H_2(H_2O)_2$ trimer. All the three PESs reproduce the frequencies accurately. However, if we just include the two-body interaction and neglect the $H_2(H_2O)_2$ interaction, the frequency of the H_2 stretch (the last row in the table) is overestimated. Overall the effects of the three-body interaction on the frequencies is small but not negligible. This is another confirmation that the $H_2(H_2O)_2$ intrinsic three-body contribution is notable and should not be neglected in both energetics calculations and harmonic-frequency analysis.

Table 5.14: Harmonic frequencies of intramolecular modes of the $H_2(H_2O)_2$ trimer from *ab initio* calculations and two different analytical potentials. Frequencies obtained neglecting the intrinsic three-body potential are listed in the last column.

ab initio	F-422/5	PP-22211*/5	P-22211*/4	Without three-body
1648	1650	1651	1651	1650
1666	1666	1665	1664	1664
3740	3746	3748	3746	3754
3821	3823	3823	3822	3825
3914	3916	3916	3915	3916
3928	3931	3931	3932	3933
4355	4358	4356	4360	4372

5.6.3 Summary

The intrinsic three-body potentials presented in this section have been tested by employing them in the PES of the $H_2-H_2O-H_2O$ trimer. The potentials using the purified and pruned-purified bases are much faster than that uses the full bases, and at the same time retain relatively high accuracy. For the trimer, the PES also reproduces dissociation energy and harmonic frequencies quite accurately.

5.7 Many-body "Plug and Play" Potential for Clathrate Hydrate

By summing up the pre-existing WHBB water potential,[28] which includes the water intramolecular potential,[169] intrinsic two-body $(H_2O)_2$[178,179] and three-body $(H_2O)_3$ potentials,[27] the monomer potentials (methane[168,170] or hydrogen[189]), and the intrinsic two-body and three-body potentials described in this chapter, we are able to approximate precisely the PES for a gas molecule (CH_4 or H_2 here, but this approach can be extended

to other molecules) surrounded by an arbitrary number of water monomers. The approximation is at the three-body level of the many-body representation. Besides accuracy, computational costs of potential calls made with the fitted three-body potentials need to be estimated when building such a complex PES. The many-body potentials of the $X(H_2O)_n$ (X=H_2, CH_4) has the "plug-and-play" feature. This feature allows us to use different fits for different purposes. For example, we could use spectroscopically accurate monomer potentials and the most accurate fits for the intrinsic two-body and three-body energies for spectroscopic studies, and use the most efficient fits when the computational cost is high but the requirement for the accuracy is relatively low.

A final and more challenging application of our intrinsic potentials is the calculation of the dissociation energy of a methane or hydrogen molecule in a dodecahedral water cage. The empty $(H_2O)_{20}$ dodecahedral cage has been optimized by employing the WHBB water potential, and the corresponding energy were calculated. Geometry of CH_4 or H_2 in the $(H_2O)_{20}$ cage has been optimized by means of the analytical PES for $X(H_2O)_n$ (n=20). The energies of the two $X(H_2O)_{20}$ systems were calculated. D_e was obtained as the difference between the calculated energies of $X(H_2O)_{20}$ and the corresponding empty water cage. (The potential of the monomer at equilibrium is set to zero) To assess the impact of the intrinsic two-body and three-body interaction on D_e, 20 terms of $X-H_2O$ two-body interactions and the 190 $X(H_2O)_2$ terms in the cluster were also evaluated. For comparison, *ab initio* calculations of the two-body or three-body interactions were also performed.

The results for $CH_4(H_2O)_{20}$ are presented in Table 5.15. For this system, three different conformers of the cage with different proton arrangements were considered. *Ab initio* calculations demonstrate that the three conformers have similar three-body $CH_4-H_2O-H_2O$ interactions, with conformer 2 and 3 slightly higher in energy. This

feature is best reproduced by P-422111*/4 and PP-422111*/4. Looking at the single con-former energies, P-422111*/4 and PP-422111*/4 give the best estimate for conformer 2 and conformer 3, while conformer 1 is best approximated by F-4421/4. The best poten-tials provide energies that are within 0.1-0.15 kcal/mol (or less) of the *ab initio* value. This is a small error (about 40-50 cm^{-1}) if one considers that there is a total of 190 terms that sum up to yield the three-body energy. A combination of previous results for the trimer and results for cluster systems shows that potentials with maximum polynomial order M=4 are in general more accurate than those with M=3. However, the latter are much faster and have good accuracy, so in some applications they could be the preferred choice. Cluster calculations point out once more that three-body contributions to the total energy are not negligible.

As a comparison, we note that recently, Deible et al.[190] performed *ab initio* and quantum Monte Carlo calculations to determine the D_e of $CH_4(H_2O)_{20}$. The struc-ture they employed is labeled as conformer 3 in this work, and the authors reported a D_e of 5.3 kcal/mol. However, they froze the geometry of $(H_2O)_{20}$ when methane is enclathrated, thus underestimating D_e. They have also calculated the 20 terms in the two-body CH_4-H_2O interaction and the 190 terms of the three-body $CH_4-H_2O-H_2O$ interaction for their geometry, employing the high-level CCSD(T)-F12b method with VTZ-F12 basis set and counterpoise correction. The sum of two-body energies and the sum of three-body energies are -5.85 kcal/mol and 1.01 kcal/mol. The difference with our estimates is mainly due to the different geometries (which impact to the two-body energy for about 0.2 kcal/mol), level of electronic theory and counterpoise correction employed.

For the hydrogen-water system, we just calculated the dissociation energy of the con-former 1, because the dissociation energy is not sensitive to the proton arrangement, based on the results of the $CH_4(H_2O)_{20}$. The "F" potentials for both H_2-H_2O and $H_2(H_2O)_2$ are

used in this application. The D_e, two-body and three-body contributions are presented in Table 5.16. For the two-body, the difference between *ab initio* and the PES values is only 0.26 kcal/mol, and this can be due to the different levels of electronic structure theory employed. The *ab initio* calculations were based on CCSD(T)-F12a/haTZ, while the PES employs CCSD(T)-F12a/haQZ. The many three-body interactions are small and of opposite signs in this cluster, so contribute only 0.14 kcal/mol to the dissociation energy. Finally the PES predicts that the D_e of $H_2(H_2O)_{20}$ is 2.67 kcal/mol, which is about 1 kcal/mol larger than the value predicted by MP2/6-31G(d) calculation.[81]

Table 5.15: Binding energies and three-body energies for three conformers of $CH_4(H_2O)_{20}$. *Ab initio* calculations are at the MP2-F12/haTZ level. Energies are in kcal/mol.

	Conformer 1 [a]	Conformer 2 [b]	Conformer 3 [c]
2-body	-6.77	-6.81	-6.79
F-4421/4 3-body	0.72	0.54	0.54
P-422111*/4 3-body	0.59	0.63	0.66
PP-422111*/4 3-body	0.61	0.63	0.65
F-422111*/3 3-body	0.66	0.53	0.53
P-422111*/3 3-body	0.67	0.59	0.57
PP-422111*/3 3-body	0.63	0.60	0.56
ab initio	0.75	0.77	0.77
D_e (PP-422111*/4)	6.16	6.18	6.14

[a] Structure extracted from crystal structure in Appendix of Ref. 67
[b] Structure from WHBB[28]
[c] Structure from the supplementary material of Ref. 190

Table 5.16: The dissociation energy (in kcal/mol) of $H_2(H_2O)_{20}$ and the contributions of the H_2-H_2O two-body and $H_2(H_2O)_2$ three-body interactions.

	ab initio	PES	MP2/6-31G(d) [a]
D_e	-	2.67	1.68
H_2-H_2O 2-body	-2.29	-2.55	-
$H_2(H_2O)_2$ 3-body	-0.22	-0.14	-

[a] Ref. 81

5.8   Summary and Conclusions

We have constructed the intrinsic two-body and three-body potentials of different accuracies and complexities for the CH_4-H_2O, $CH_4-H_2O-H_2O$, H_2-H_2O, and $H_2-H_2O-H_2O$ interactions. These potentials are least-squares fits to high-level *ab initio* data, based on permutationally invariant polynomials. The full permutationally invariant fitting bases can be purified so the potential becomes exactly zero when one or more monomers are separated with the others. The full and purified fitting bases have been employed in building these potentials of non-covalent interactions.

We have employed the intrinsic PESs in the many-body PESs of the $CH_4(H_2O)_n$ and $H_2(H_2O)_n$ systems. The binding energy of a methane or a hydrogen molecule with the 5^{12} clathrate cage has been calculated, and the two-body and three-body contributions agree quite well with the *ab initio* calculation. More importantly, the purified and pruned-purified PESs run much faster than our conventional permutationally invariant fits.

These results point out that the the fitting procedure with purified bases is promising for studies of more complex systems or even condensed phase clusters, where a larger number of two-body and three-body interactions necessitate to be considered. In these cases, a substantial reduction of computational cost allows to follow the real dynamics

of the system for much longer times.

Chapter 6

Storage Capacity and H_2 Diffusion in Clathrate Hydrates

6.1 Overview

The hydrogen clathrate is a potential material for hydrogen storage and transport.[64,65,71] Therefore, the storage capacity of clathrate has been investigated extensively by both experiment and theory. Hydrogen and water crystallize in the form of structure II clathrate (sII), whose unit cell consists of 136 water molecules that form 8 large $5^{12}6^4$ and 16 small 5^{12} cages.[62] The H_2 molecules occupy both small and large cages in this case. This pure H_2 clathrate is produced at extreme pressure ($\sim$200 MPa), which makes it impractical for hydrogen storage.[69] Florusse et al.[72] showed that the synthesis pressure can be greatly reduced if large molecules such as tetrahydrofuran (THF) is introduced to fill the large cage. However, compared to the pure H_2 clathrate, the storage capacity of the binary clathrate is much smaller, because most of the large cages are occupied by large molecules, and H_2 molecules only occupy small cages. The number of hydrogen molecules

that can be trapped inside the small 5^{12} cages is still under debate. Mao et al.[69] suggested that the small cavities are occupied with two H$_2$ molecules, and this is supported by a theoretical work with a statistical mechanical model in conjunction with first-principles quantum chemistry calculations[70], and an *ab initio* study using isolated cages as model systems.[81,82] Studies of the binary clathrate also showed that the small cages are doubly occupied.[72,74,84] On the other hand, some experiments[76,79,112], molecular dynamics (MD)[75] and Monte Carlo simulations[77] supported single occupancy of the small cages. Recently, Koh et al.[89] suggested that only $\sim 1\%$ expansion of the cage dimensions is sufficient to provide stable room for double occupancy in the small cavity.

Another related question is the barrier for the H$_2$ diffusion (intercage hopping) in clathrate hydrate, because fast diffusion of H$_2$ is necessary in order for the hydrate to be a practical storage medium. Experimentally, Okuchi et al.[127] directly measured the H$_2$ diffusion using nuclear magnetic resonance (NMR) spectroscopy, and they estimated that the activation energy of the diffusion is about 3 kJ/mol. However, in a decomposition experiment of the H$_2-$THF binary clathrate, an activation energy of 52–64 kJ/mol was extracted from the Arrhenius plot of the diffusion coefficient,[131] and this is one order of magnitude larger than the NMR measurement. Theoretically, Alavi and Ripmeester[128] performed DFT (B3LYP) and MP2 calculations of the potential energy barrier of a H$_2$ moving through the cage's faces, and the barriers are 21–25 kJ/mol for the hexagonal faces and 105–120 kJ/mol for the pentagonal faces. In this study the cage was kept rigid. Frankcombe and Kroes[129] carried out MD simulations, from which an activation energy of 32 kJ/mol was obtained. Static calculations in this work suggested the barrier of the H$_2$ through the hexagonal faces is 23.8–27.6 kJ/mol, which agrees reasonably well with the MD result. In a DFT study of the barrier using the lattice model that allowed relaxation, the barrier is about 20 kJ/mol,[80] which is close to the result using rigid cage.

Another classical equilibrium MD simulation shows that the H$_2$ in the small cage cannot migrate if the small cage is singly occupied, but when the small cage is doubly occupied, the intercage hopping can be observed by temporary openings of pentagonal small-cage faces.[132] Recently the free-energy barrier of the H$_2$ migration were calculated using MD simulations with umbrella sampling, based on DFT theory[135] or empirical potential[136]. Both studies show that the barrier for the hexagonal faces decreases when increasing occupancy of the $5^{12}6^4$ cage. However, in one study, the barrier is 5–10 kJ/mol,[135] while in the other one , the barrier is 14–31 kJ/mol.[136] High-level CCSD(T) benchmark of the potential-energy barrier has been reported,[137] though the authors only employed the H$_2$ passing through a water ring hexamer as the model system, due to the computational cost.

Therefore, discrepancies about the cage occupancy and the diffusion barrier in hydrogen clathrate still exist. In this work I apply the potential energy surface (PES) of the hydrogen clathrate presented in Chapter 5 to investigate the storage capacity and the H$_2$ diffusion. Instead of the unit cell with period boundary condition, the isolated cages are used as the model system, in order to reduce the computational effort. Though the pure H$_2$ clathrate crystallizes in sII, which consists of two types of cages (5^{12} and $5^{12}6^4$), the binary clathrates could have other crystal structures. Therefore, I did not use the two sII cages; instead, as a start, I investigated the two most common cages in clathrate hydrate, i.e., 5^{12} and $5^{12}6^2$. The energetics of multiple H$_2$ trapped inside a single cage are calculated with the PES, and the relative stability of each occupancy is obtained. Reaction paths of H$_2$ escaping through different windows were obtained with rigid cages, and the barrier heights of different windows were estimated.

6.2 Potential Energy Surface

The potential energy of $(H_2)_m(H_2O)_n$ is decomposed into the potential of H$_2$ molecules, the potential of water, and the interaction between H$_2$ molecules and water. Each of the three components is further decomposed using many-body expansion, presented in Chapter 2. The potential of H$_2$ molecules consists of H$_2$ monomer and pairwise H$_2$−H$_2$ interaction. The H$_2$ monomer potential is due to Schwenke[189], and the H$_2$−H$_2$ interaction is a six-dimensional (6D) potential[191] that combines a 4D H$_2$−H$_2$ interaction (with rigid monomers)[192] and a 6D one constructed using slightly lower-level *ab initio* theory.[193] The interaction potentials between H$_2$ and water have been presented in Chapter 5, and here the F-221/5 and P-22211/4 were used for the H$_2$−H$_2$O two-body and H$_2$(H$_2$O)$_2$ three-body, respectively. Three water potentials were considered in this work: WHBB,[28] MB-pol,[194–196] and TTM3-F.[197] The WHBB and MB-pol are *ab initio*-based water models and they are more accurate than the empirical TTM3-F, at the cost of much more expensive computations. Recently we re-fitted the (H$_2$O)$_3$ intrinsic three-body potential using the purified fitting basis by Conte,[26,198] and in this work, this new three-body is used in the WHBB water potential and therefore, the new version of WHBB in this work is referred to as "WHBB/P".

6.3 Storage Capacity

The 5^{12} and $5^{12}6^4$ cages are taken from Xantheas,[199] and the geometries of the two cages were optimized using three different water potentials. The geometries of nH$_2$@5^{12} (n=1, 2, $\cdots$, 5) and nH$_2$@$5^{12}6^2$ (n=1, 2, $\cdots$, 7) were optimized using the clathrate PES. Here two versions of the H$_2$-water interaction were used: one with only the H$_2$−H$_2$O two-body

interaction and the other with the $H_2(H_2O)_2$ three-body included. The energy differences between the $(H_2)_n$@cage and the empty cage were calculated by

$$\Delta E = E_{nH_2@cage} - E_{empty\ cage}. \qquad (6.1)$$

Because the energy of an isolated H_2 molecule at equilibrium is zero in the PES, this energy difference is the binding energy of nH_2+cage. Negative values of ΔE mean that the system is stabilized with the H_2 molecule(s) trapped inside the cage; on the other hand, positive ΔE indicates the molecular cluster is not stable.

Table 6.1: ΔE's (in kcal/mol) for systems listed below, calculated with WHBB or MB-pol water potential, and two-body H_2-water interaction, and with MP2/aVDZ calculation

System	WHBB/P	MB-pol	MP2
H_2@5^{12}	-2.508	-2.563	-3.425
$2\,H_2$@5^{12}	-3.408	-3.255	-3.721
$3\,H_2$@5^{12}	-3.018	-2.467	-3.004
$4\,H_2$@5^{12}	-0.096	0.800	0.085
$5\,H_2$@5^{12}	6.364	7.829	7.133
H_2@$5^{12}6^2$	-2.185	-2.201	-2.953
$2\,H_2$@$5^{12}6^2$	-4.241	-4.207	-5.364
$3\,H_2$@$5^{12}6^2$	-6.084	-5.986	-7.001
$4\,H_2$@$5^{12}6^2$	-6.261	-5.917	-7.034
$5\,H_2$@$5^{12}6^2$	-4.950	-4.266	-5.720
$6\,H_2$@$5^{12}6^2$	-4.606	-3.729	-5.541
$7\,H_2$@$5^{12}6^2$	-0.745	0.595	-1.008

The ΔE's calculated with different combinations of the PESs are summarized in Table 6.1 and 6.2, and the MP2/aVDZ calculation by Xantheas[199] is also shown. The three columns from Table 6.1 are plotted in Figure 6.1. From the figures and tables, one can

Table 6.2: ΔE's (in kcal/mol) for systems listed below, calculated with three water potentials and H$_2$-water interaction up to three-body.

System	WHBB/P	MB-pol	TTM3-F
H$_2$@5^{12}	-2.095	-2.036	-2.043
2 H$_2$@5^{12}	-3.071	-3.167	-2.756
3 H$_2$@5^{12}	-3.175	-3.438	-2.610
4 H$_2$@5^{12}	-0.278	-0.571	0.738
5 H$_2$@5^{12}	5.531	7.859	7.850
H$_2$@5^{12}6^2	-2.032	-1.935	-1.961
2 H$_2$@5^{12}6^2	-3.976	-3.829	-3.785
3 H$_2$@5^{12}6^2	-5.964	-5.665	-5.266
4 H$_2$@5^{12}6^2	-5.188	-5.260	-4.496
5 H$_2$@5^{12}6^2	-4.567	-4.756	-3.702
6 H$_2$@5^{12}6^2	-3.612	-3.801	-2.481
7 H$_2$@5^{12}6^2	0.203	1.233	1.233
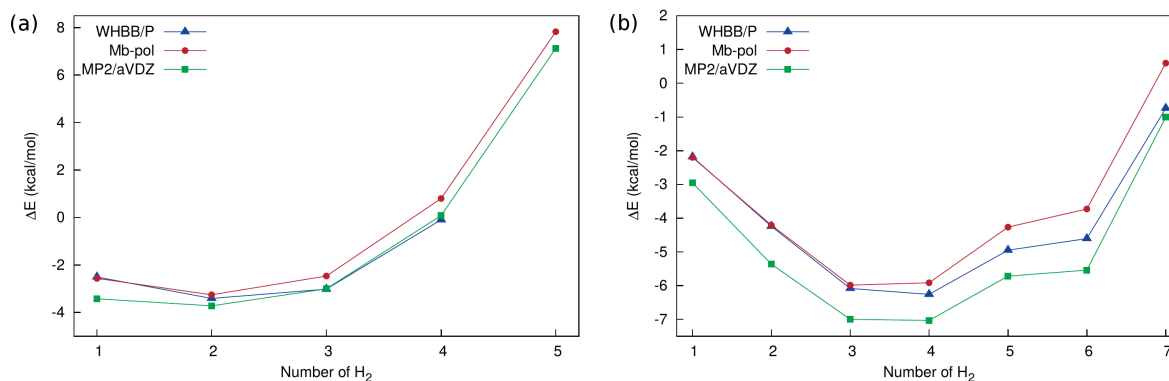
Figure 6.1: ΔE against the number of H$_2$ molecules in 5^{12} cage and (b) 5^{12}6^2 cage, calculated with indicated potential or *ab initio* method.

find that the results from different water models and different H$_2$-water interaction potentials agree with each other semi-quantitatively, and the agreement with MP2/aVDZ calculation is also good. The contribution of the three-body H$_2$(H$_2$O)$_2$ interaction is quite small and it is in general less than 1 kcal/mol. Thus in a lot of cases, the three-body H$_2$(H$_2$O)$_2$ can be safely neglected. The ΔE values are also not sensitive to the water models used in the calculation. The agreement between WHBB and MB-pol is expected, as both of them are *ab initio*-based potentials for water with comparable accuracy; however, the TTM3-F is a empirical potential and yet the results show very similar trend as the WHBB and MB-pol.

When only the electronic energies are considered, these calculations predict that n=2 or 3 (the difference is quite small) is the most stable species for 5^{12} cage and n=3 or 4 is the most stable for 5^{12}6^4 cage. However, the zero-point motion of the H$_2$ molecule(s) should also be taken into account when comparing the stability of these enclathrated species. Diffusion Monte Carlo (DMC) calculations were performed to calculate the zero-point energy (ZPE) of the enclathrated hydrogen molecules. The cages were frozen in the diffusion Monte Carlo simulations, and the confined H$_2$ molecules were treated in full dimensionality. The simple unbiased algorithm described in Chapter 3 was applied here. Specifically, for each cluster, 50000 walkers were propagated for 35000 steps with a step size 5.0 au. The walkers were first equilibrated for 5000 steps, and then the energies of walkers were collected to calculate the ZPE of the H$_2$ molecules. Based on the ZPEs, I obtained the binding energy D$_0$ of the clusters:

$$D_0 = \Delta E + \Delta \text{ZPE,} \tag{6.2}$$

where $\Delta \text{ZPE} = \text{ZPE}_\text{confined} - \text{ZPE}_\text{isolated}$ is the difference in ZPE of the confined and iso-
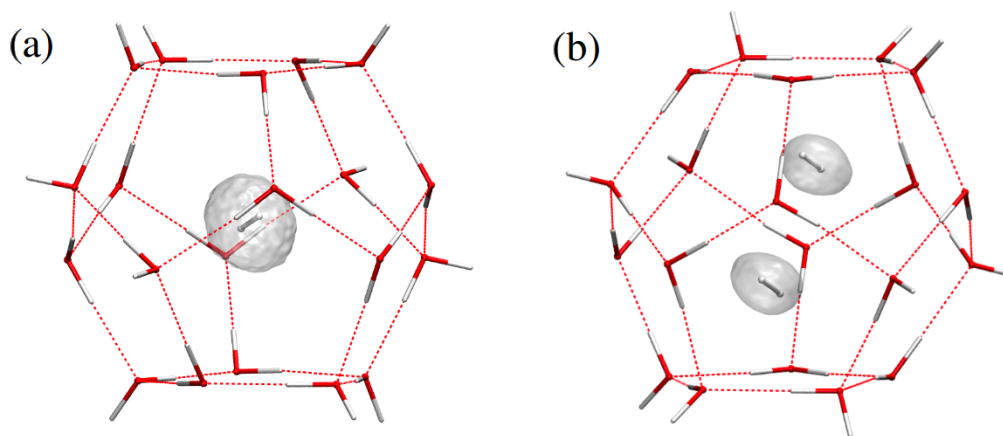
Figure 6.2:   The nuclear wavefunction of one and two H$_2$ molecules trapped inside the 5^{12} cage.

lated H$_2$ molecule(s). I use the ΔE values calculated with WHBB water potential and the H$_2$-water interaction up to three-body, i.e., the column "WHBB/P" in Table 6.2. Similar to the ΔE, more negative value means the system is more stable. The D$_0$ values are listed in Table 6.3, as well as the MP2/aVDZ calculation with harmonic ZPE correction.

Table 6.3:   D$_0$ values (in kcal/mol) enclathrated H$_2$ molecule(s) based on DMC calculations, as well as the MP2 calculation with harmonic ZPE correction.

System	ΔE	ΔZPE	D$_0$	MP2
H$_2$@5^{12}	-2.095	0.457	-1.683	-2.770
2 H$_2$@5^{12}	-3.071	2.247	-0.824	-0.892
3 H$_2$@5^{12}	-3.175	5.112	1.937	2.545
H$_2$@$5^{12}6^2$	-2.032	0.540	-1.492	-2.441
2 H$_2$@$5^{12}6^2$	-3.976	1.591	-2.385	-2.816
3 H$_2$@$5^{12}6^2$	-5.964	3.481	-2.483	-2.585
4 H$_2$@$5^{12}6^2$	-5.188	5.395	0.207	-0.714

Figure 6.2 shows the wavefunction of one and two H$_2$ molecule(s) trapped inside the

5^{12} cage. One can see that the wavefunction is delocalized and H_2 can almost rotate freely inside the cage. However, the wavefunction of two H_2 is not as delocalized as the one H_2 case, and the two H_2 tends to avoid each other. According to Table 6.3, the ZPE of two H_2 in the cage is more than twice the ZPE of a single enclathrated H_2 due to this repulsion between the H_2 molecules. Though $2\,H_2@5^{12}$ has lower electronic energy, the ZPE of the two enclathrated H_2 is much higher and therefore it is actually less stable than $H_2@5^{12}$. Based on the D_0 values, we conclude that among $nH_2@5^{12}$ species, n=1 is the most stable. For $nH_2@5^{12}6^2$, n=2 or 3 is the most stable, depending on the ΔE values used. Note that D_0 of n=2 is still negative, which means the two H_2 molecules can be stabilized when they are trapped in the cage, compared with completely isolated case. The energy of n=2 is higher than n=1, so at thermal equilibrium, one H_2 molecule would like to find its way out. However, if the barrier for this H_2 diffusion is high enough, $2\,H_2@5^{12}$ is metastable and the two H_2 molecules would still be trapped inside the cage. Therefore, the barrier of H_2 diffusion will be discussed in the following section.

6.4 H_2 Diffusion

First consider one H_2 molecule trapped in a single cage. Reaction paths of H_2 diffusion through different windows of the 5^{12} and $5^{12}6^2$ cages are obtained as follows. First, the cage is frozen and the H_2 molecule is moved from inside to outside of the cage, through the center of the pentagonal or hexagonal window, and thus rigid cuts were obtained. At each point along the rigid cut, the orientation of the H_2 (determined by the polar and azimuthal angles) was optimized and the energy of the optimal orientation was computed. Figure 6.3 shows the reaction path of a H_2 molecule through the pentagonal window in 5^{12}, and pentagonal or hexagonal window in $5^{12}6^2$. There are 12 pentagonal windows
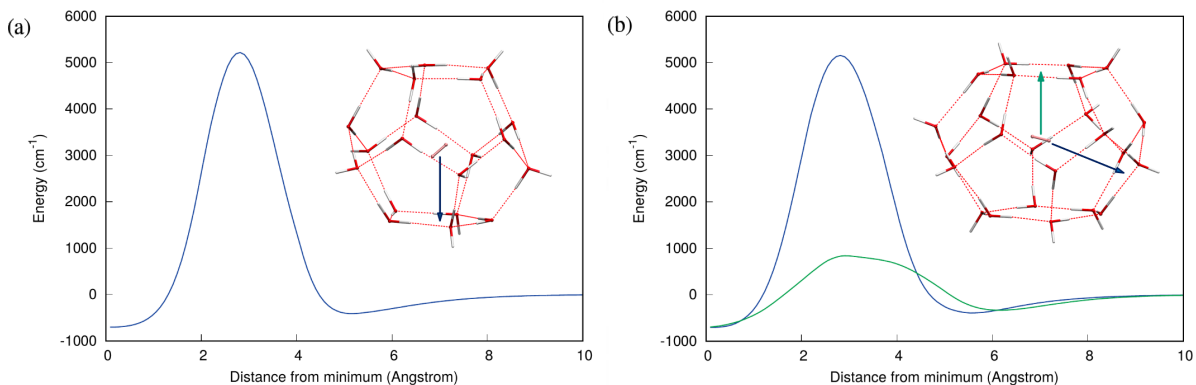
Figure 6.3:   Reaction paths of a H$_2$ molecule (a) through the pentagonal window in 5^{12}; (b) through pentagonal and hexagonal windows in $5^{12}6^2$.

in a single cage, and 2 hexagonal windows in $5^{12}6^2$ cage, and in the figure only one of such paths is shown. Even for the same type of window, due to slight difference in ring diameters and the proton arrangement, the barrier height are different. The barrier height of the pentagonal window ranges from about 5000 to 7000 cm^{-1}, and the average is 5909 cm^{-1} (70.7 kJ/mol) relative to the minimum (the H$_2$ trapped in the cage), with standard deviation of 605 cm^{-1} (7.2 kJ/mol). While the average barrier height of the pentagonal window is only 1624 cm^{-1} (19.4 kJ/mol), which is significantly lower than that of the pentagonal window, with standard deviation of 81 cm^{-1} (1.0 kJ/mol). Compared to the earlier rigid cage calculation[128] that predicts a barrier height of 105–120 kJ/mol through pentagonal faces, this work predicts a significantly smaller barrier height; while the barrier for the hexagonal window is just slightly lower than the earlier rigid cage calculation.

Next consider the barrier for H$_2$ passing through the shared pentagonal window between two 5^{12} cages. Using this model, the relation between the barrier height and the occupancy of the initial or adjacent cage could be investigated. The notation "(n_1, n_2)" is used to represent the occupancy of two cages: cage 1 is occupied by n_1 H$_2$ molecules and cage 2 is occupied by n_2 H$_2$ molecules. I started from $(1, 0) \rightarrow (0, 1)$, and Figure 6.4
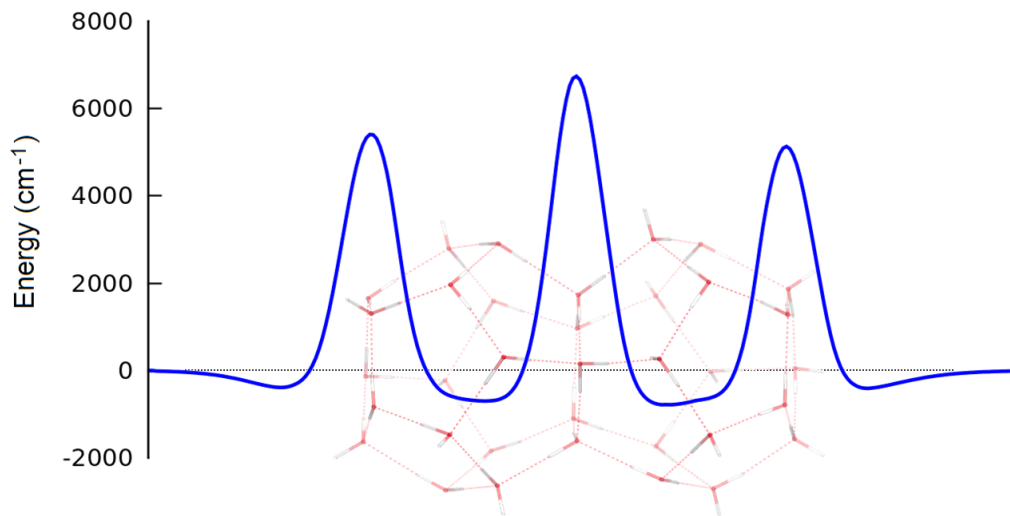
Figure 6.4: Energy profile of a H_2 molecule hopping between two adjacent 5^{12} cages.

shows the energy profile of a H_2 molecule moving along the dashed axis. This energy profile was obtained in the similar way described above: the cage was frozen and the orientation of the H_2 molecule was optimized at each point along the path. For this particular local structure of the pentagonal window, the barrier of H_2 hopping is 7434 cm^{-1} (88.9 kJ/mol) relative to the minimum. This is the barrier height for $(1,0) \rightarrow (0,1)$. Then I studied $(2,0) \rightarrow (1,1) \rightarrow (0,2)$. For this system, the full energy profile was not calculated; instead only the energies of five geometries (the three minima and the two transition state) were calculated. The barrier for $(2,0) \rightarrow (1,1)$ is about 7056 cm^{-1} (84.4 kJ/mol) while the barrier for $(1,1) \rightarrow (0,2)$ is about 7506 cm^{-1} (89.8 kJ/mol). These results indicate that higher occupancy in the initial cage leads to a lower barrier (88.9 kJ/mol for $(1,0) \rightarrow (0,1)$ v.s. 84.4 kJ/mol for $(2,0) \rightarrow (1,1)$), while the occupancy of the destination has little effect on the barrier height (88.9 kJ/mol for $(1,0) \rightarrow (0,1)$ v.s. 89.8 kJ/mol for $(1,1) \rightarrow (0,2)$).

The calculations above all used the rigid cage, so the effect of cage relaxation is not
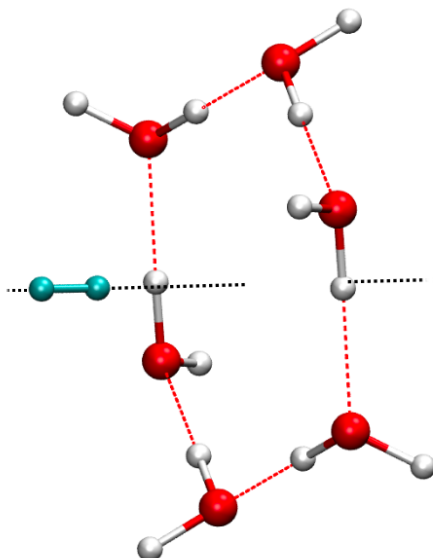
Figure 6.5: Geometry of one H$_2$ molecule passing through (H$_2$O)$_6$ ring.

considered. When the cage is flexible, the window could expand a little to allow the H$_2$ molecule to go through, which could lower the barrier height compared to rigid cage model. However, such calculations using even the isolated cage model is very computationally demanding. Therefore, in order to investigate the importance of relaxation, I performed calculations for one H$_2$ molecule pass through a flexible (H$_2$O)$_5$ or (H$_2$O)$_6$ ring. The cages in crystals should be more rigid than the (H$_2$O)$_5$ and (H$_2$O)$_6$ rings, so the decrease of the barrier height in the rings sets the upper limit for the barrier decrease in clathrate hydrate. In these calculations, the H$_2$ is rigid and passes through the ring at the perpendicular orientation, as is shown in Figure 6.5. At each H$_2$-ring distance, I scanned ten different ring diameters, and at each ring diameter, the O atoms were frozen and the positions of H atoms in water were optimized. The minimum energy and the optimal ring diameter at each H$_2$-ring distance were recorded. Without any ring relaxation, the barrier for H$_2$ diffusion through the (H$_2$O)$_5$ and (H$_2$O)$_6$ rings are 74.6 and 15.6 kJ/mol,

respectively. And this is actually very close to the barrier in the isolated cages. When the ring diameters are allowed to change, the barriers further decrease to 36.9 and 10.6 kJ/mol, respectively.

6.5   Summary and Conclusion

The many-body potential energy surface for hydrogen clathrate presented in Chapter 5 was employed to investigate the occupancy of the cages, and barrier for H$_2$ diffusion in the hydrate. When only the electronic binding energies are considered, the most stable systems are $2\,$H$_2$@5^{12}, and $3/4$H$_2$@$5^{12}6^2$ for the small and large cage, respectively. However, when the ZPE of the confined H$_2$ molecules is taken into account, the most stable ones are $1\,$H$_2$@5^{12} and $2/3$H$_2$@$5^{12}6^2$. The barrier of H$_2$ diffusion through pentagonal faces is estimated to be about 36–75 kJ/mol, while for the hexagonal faces, the barrier is between 10 and 20 kJ/mol, where the lower bound is obtained from the relaxed $(\text{H}_2\text{O})_5$ or $(\text{H}_2\text{O})_6$ ring. This barrier is small for the hexagonal faces, but quite large for pentagonal ones. This work suggests that at thermal equilibrium, each small 5^{12} cage should be singly occupied. However, doubly occupied small cages are also possible, due to the relatively high barrier of the pentagonal windows.

Part III

Molecular Vibrations

Chapter 7

Ground State Properties and Vibrational Spectra of H_7^+

7.1 Overview

The protonated hydrogen clusters H_{2n+1}^+ (n>1) have been extensively studied, due to the important role they play in interstellar chemistry.[200–202] The first member of this series, H_3^+, has been detected in the interstellar medium.[203,204] The larger clusters can be described as a central H_3^+ solvated by H_2 molecules.[205–209] Characterization of the potential energy surfaces (PESs) of these clusters[210–215] illustrates that the potential is very flat in the region around the minimum, with several low-lying saddle points. This indicates that these ions are fluxional ("floppy"). Investigation of the vibrational ground states of these floppy molecules, which could provide insights for understanding the spectroscopy and dynamics, is of great importance.

As the first member of the protonated hydrogen cluster family and a fluxional ion, H_5^+ has attracted many theoretical studies. H_5^+ has several low-lying stationary points on

the PES: the saddle point for proton exchange lies at only 52 cm^{-1} above the minimum, and the saddle point for the torsion of the outer H_2 is roughly 100 cm^{-1} above the minimum. Its vibrational ground state properties and large-amplitude motion have been investigated.[216–220] Based on these theoretical works, the H_5^+ could be best described as two H_2 molecules sharing a proton, instead of H_3^+ solvated by one H_2 molecule, and the shared-proton mode plays an important role in the infrared spectrum of H_5^+. Theoretical calculations of the spectrum have been performed, using the knowledge obtained from the investigation of the PES and large-amplitude motion.[220–229] These theoretical spectra agree reasonably well with the experimental measurements.[222,223,230,231]

However, for the second member, H_7^+, little work has been done. Experimentally, Okumura et al.[230],[231] recorded the infrared predissociation spectrum, and recently Young et al.[232] revisited the photodissociation spectrum of H_7^+. The experimental spectrum of H_7^+ is simpler than that of H_5^+. A weak and broad feature at about 2200 cm^{-1} and a peak at 3982 cm^{-1} were reported. The authors performed DFT(B3LYP)/6-311+G** and MP2/6-311+G** calculations with double harmonic approximation, and they assigned the feature at about 2200 cm^{-1} to the asymmetric stretch of the central H_3^+, and the 3982 cm^{-1} peak to the stretch of outer H_2.[232] Theoretically, Barbatti and Nascimento[233] performed vibrational self-consistent field calculation, followed by second-order vibrational Møller-Plesset perturbation for H_5^+, H_7^+, and H_9^+. In this calculation, the *ab initio* theory was relatively low-level and only two-mode coupling was employed. Recently, a DFT-based PES[214] and a full-dimensional, permutationally invariant PES[215] became available. In addition to the PES reported by Barragán et al.[215], I also constructed a spectroscopic one that only describes the global minimum and a few low-lying stationary points, and a DMS in order to calculate the infrared intensities. Details of the new PES and DMS will be presented later in the chapter.

Inspired by the recent infrared photodissociation experiment and the development of the full-dimensional PESs, we investigated the vibrational ground state properties and the infrared spectrum of H_7^+. We performed diffusion Monte Carlo (DMC) simulations to characterize the vibrational ground state. From the DMC simulation, the dissociation energy of H_7^+ was obtained. The stability of the partially deuterated species and the (possible) H-exchange in this cluster was also investigated in the DMC. Finally with the preliminary information obtained from the DMC simulations, I carried out VSCF and VCI calculations to obtain the infrared spectra of H_7^+ and D_7^+, using the code "MULTIMODE".

7.2 Potential Energy and Dipole Moment Surface

Two PESs have been used in the simulations: one is constructed at MP2/cc-pVQZ level of theory and describes the dissociation of H_7^+ to H_5^+ and H_2 (denoted as PES I in this chapter);[215] the other is computed at CCSD(T)-F12b/cc-pVQZ-F12[32,33,234] level of theory and this is a local PES that does not describe the dissociation (denoted as PES II). Both PESs employ the fitting procedures described in Chapter 2, and PES-I was applied in the calculation of the dissociation energy D_0 of H_7^+. However, this PES underestimates the electronic dissociation energy, D_e of H_7^+ by 65 cm^{-1}, compared to the CCSD(T) benchmark at complete-basis-set (CBS) limit. Moreover, the MP2 harmonic frequencies of the H_3^+ and H_2 stretches differ from the CCSD(T) results by 50 to 100 cm^{-1}, and this is not accurate for spectroscopic calculations. Therefore, We employed higher-level CCSD(T)-F12b/cc-pVQZ-F12 method and obtained the improved PES II in the bound region of H_7^+.

7.2.1 Ab initio calculations for PES II

Different levels of *ab initio* calculations were performed and the corresponding electronic dissociation energies were computed. Table 7.1 shows the results. One can see that compared to the CCSD(T)-CBS value, MP2/cc-pVQZ underestimates the D_e by about 65 cm^{-1} and CCSD(T)/cc-pVQZ underestimates it by 46 cm^{-1}. With the explicitly correlated CCSD(T)-F12 method, the difference in the D_e compared to the CBS limit becomes 27 cm^{-1}, and finally with cc-pVQZ-F12 basis set, the difference further decreases to about 20 cm^{-1}. On the other hand, a single-point calculation of the electronic energy with CCSD(T)-F12b/cc-pVQZ-F12 already costs about two minutes on a 16-processor computer, so it's not feasible to apply higher-level theories or larger basis sets, and this combination of method and basis was employed.

Table 7.1: Total energies (in a.u.) of the optimal structure of the H_7^+ and H_5^+ + H_2, together with the D_e values (in cm^{-1}) at the indicated level of theory and basis sets.

Method/Basis set	$E_{H_7^+}$	$E_{H_5^+} + E_{H_2}$	D_e
MP2/cc-pVQZ	-3.690091	-3.682229	1726
CCSD(T)/cc-pVQZ	-3.712379	-3.705714	1745
CCSD(T)-F12b/cc-pVQZ	-3.713718	-3.705681	1764
CCSD(T)-F12b/cc-pVQZ-F12	-3.714058	-3.705989	1771
CCSD(T)/CBS [a]	-3.71453	-3.70637	1791

[a] From Ref. 215.

A subset of 42525 configurations were selected from the database of PES I, and additional 195 geometries were added to the dataset in regions where the energies from the PES are unphysically low or differ substantially from the *ab initio* results. The *ab initio* calculations on these 42720 configurations were performed using MOLPRO 2010.1,[167]

and the expectation values of the dipole moments were also computed, at the MP2 level.

7.2.2   Potential energy and dipole moment surfaces fitting

The fitting methods for the PES and DMS have been described in Chapter 2, and here the invariant primary and secondary polynomials were applied as the fitting basis. The full symmetry of H_7^+ was used so that all the H atoms are allowed to permute. The maximum polynomial order is seven, leading to 739 terms for the analytical expression of PES, and 3528 for the DMS, respectively.

7.2.3   Properties of the potential energy and dipole moment surfaces
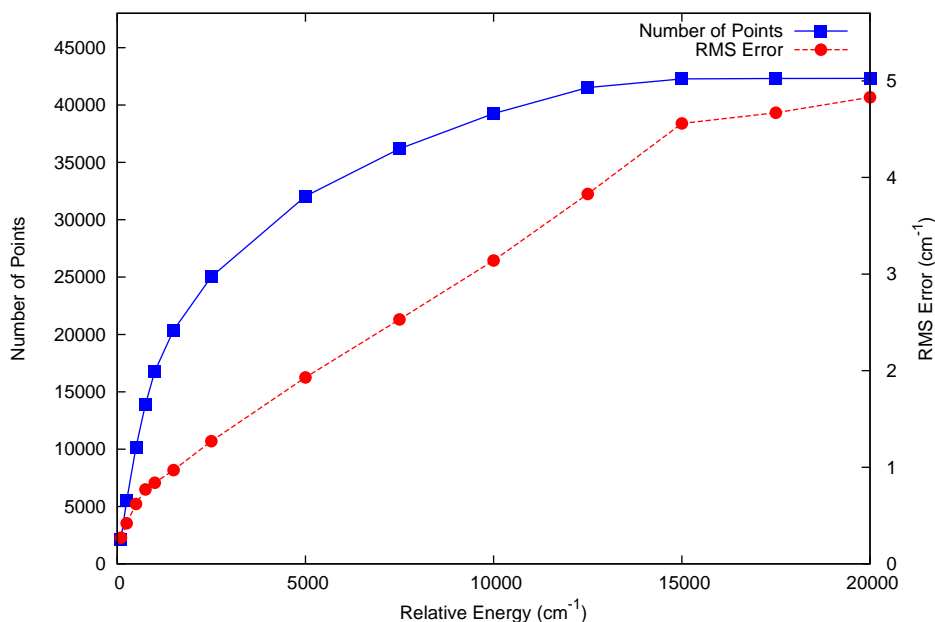
Figure 7.1:   Number of points and root-mean-square error below each energy.

The overall root-mean-square (rms) error of the PES II is 17.2 cm^{-1}, which is an order of magnitude smaller than that in PES I. Figure 7.1 shows the number of points and rms error below each energy in the PES. As is shown in the figure, most of the configurations in the data set are below 15000 cm^{-1}, and the rms error for this region is only 5 cm^{-1}. Thus, this fit provides an accurate representation of H_7^+ potential surface in the bound region, up to energies of about 15000 cm^{-1} above the global minimum.
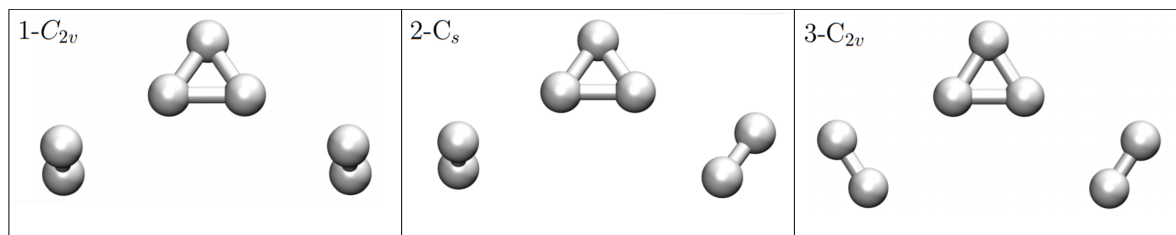
Figure 7.2:   Geometries of the three lowest stationary points of H_7^+.

Table 7.2:   The energy of the minimum structure (in a.u.) and the relative energies of two stationary points (in cm^{-1}) from CCSD(T)-F12b/cc-pVQZ-F12 calculations, the PES I and II.

Config.	CCSD(T)-F12b	PES II	PES I [a]
1-C_{2v}	-3.714058	-3.714058	-3.690083
2-C_s	47.3	46.9	45.2
3-C_{2v}	113.5	113.9	122.8

[a] From Ref. 215

Figure 7.2 shows the geometries of the lowest three stationary points, and these three configurations are labeled as 1-C_{2v}, 2-C_s, and 3-C_{2v}, respectively. In Table 7.2 I list the

energies of them on PES I and II, as well as the CCSD(T)-F12b *ab initio* energies. One can see that the differences between energies from the PES II and *ab initio* values are less than 1 cm^{-1}. The PES I does not agree well with the CCSD(T)-F12b energies, because it is based on MP2 calculations.
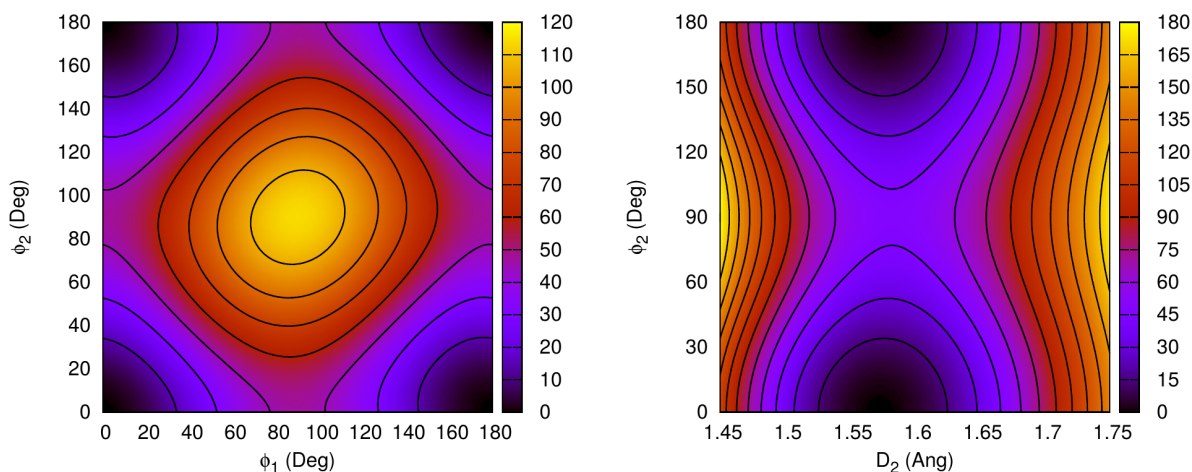
Figure 7.3:   Contour plots of the PES. In the left panel, H_7^+ is initially at 1-C_{2v}, and ϕ_1 and ϕ_2 are torsional angles of two H_2; in the right panel, H_7^+ is also initially at the minimum, and ϕ_2 is the torsional angle of H_2 and D_2 is the H_3^+-H_2 distance.

Figure 7.3 shows the contour plots of PES II. In the panel on the left, we show the contour lines of the potential with the H_3^+ core fixed, while the two H_2 units are both rotating in the ϕ_1 and ϕ_2 coordinates, where ϕ_1 and ϕ_2 are the torsional angles of the two H_2 units. The torsional angle is zero for the minimum configuration and is 90 degree for the saddle point. One can see the behavior of the PES around the four symmetric 1-C_{2v} minima, the four equivalent 2-C_s saddle points connecting them, and the 3-C_{2v} stationary point. In the panel on the right, the H_7^+ is originally at the 1-C_{2v} configuration and the contour plot is presented as a function of the D_2, which is the H_3^+-H_2 distance and ϕ_2

coordinates. The region around the two symmetric 1-C_{2v} minima and their 2-C_s barrier are shown up to energies of 180 cm^{-1}.

Normal-mode analysis was carried out for the minimum, and the harmonic frequencies predicted by the PES as well as *ab initio* calculation are listed in Table 7.3. The difference between the PES II and the *ab initio* data is less than 5 cm^{-1}.

Table 7.3:   Comparison of harmonic frequencies (in cm^{-1}) calculated from the *ab initio* program at CCSD(T)-F12b/cc-pVQZ-F12 level of theory and the PES.

Mode	Description	CCSD(T)-F12b	PES
1	torsion of H_2	98	96
2	torsion of H_2	124	122
3		168	167
4		562	565
6		572	571
7		695	694
8		732	733
9		797	798
10		907	908
11	bending of H_3^+	2294	2293
12	asymmetric stretch of H_3^+	2525	2527
13	asymmetric stretch of H_3^+	3288	3286
14	out-of-phase stretch of two H_2	4237	4235
15	in-phase stretch of two H_2	4237	4237
ZPE		10821	10818

The rms fitting error of the dipole moment is 0.0006 au. The x-, y- and z-components of the dipole moments along specified normal modes (see the descriptions of the normal modes in Table 7.3) at the minimum are plotted in Figure 7.4. As one can see, the dipole along the asymmetric stretch of H_3^+ (mode 12) and out-of-phase stretch of two H_2 (mode 14) has significant change. So these two modes should have large contribution
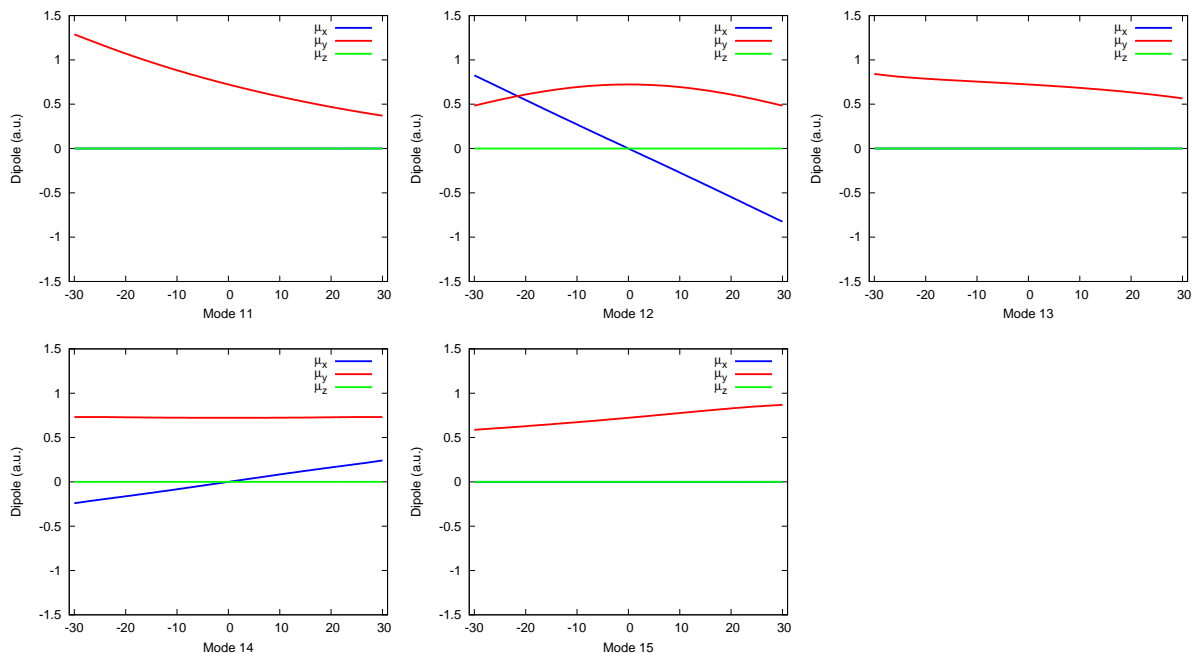
Figure 7.4:   One-dimensional cuts of the dipole moment surface along the specified normal modes at the minimum configuration.

in the infrared spectrum of H_7^+ (see Section 4).

7.3   Diffusion Monte Carlo Calculations

7.3.1   Computational details

In order to determine the dissociation energy D_0 of H_7^+ (or D_7^+), DMC calculations were performed for H_7^+ (D_7^+) and $H_2+H_5^+$ ($D_2+D_5^+$), using PES I. The simple unbiased algorithm described in Chapter 4 was applied here, with the step size $\Delta\tau = 5.0$ au and $\alpha = 0.2$. The convergence of the DMC calculations with respect to the step size was also tested with step sizes fof 2.5 and 7.5 au, and the difference is only about 3 cm^{-1}. For simulations of H_7^+ (D_7^+), all the walkers were initiated at the equilibrium configura-

tion, and for $H_2+H_5^+$ ($D_2+D_5^+$), the fragments were separated by 15 Åwith each at its equilibrium configuration. For each system, five independent simulations were performed and in each simulation, 20000 walkers were propagated for 10000 steps. The walkers were equilibrated in the first 2000 steps, and the reference energies in the remaining 8000 steps were collected and averaged to compute the final ZPE. The standard deviation from the five simulations was used to estimate the statistical error of the DMC simulations.

Both PES I and PES II were applied in the DMC calculations of the partially deuterated H_7^+. Simulations were carried out for all the possible partially deuterated isotopologues and isotopomers, and the walkers were initiated at the equilibrium configuration of H_7^+, with hydrogen atom(s) at different positions replaced by deuterium. For simulations on PES I, three simulations were performed for each species, and in each simulation, 20000 walkers were propagated for 10000 steps, with first 2000 step for equilibration. For simulations on PES II, only one simulation was carried out for each counterpart, but the 20000 walkers were propagated for 65000 steps with first 5000 steps for equilibration.

The vibrational ground-state wavefunction is visualized as an isosurface, and it is obtained as follows. The equilibrated walkers from the DMC simulations are recorded and optimally aligned into the Eckart frame. The space was divided into volume elements and a statistical analysis was performed for each volume element to obtain the wavefunction amplitude there.

7.3.2   Results and discussions

Figure 7.5 shows the imaginary time evolution of an illustrative DMC simulation, initiated from the separated H_5^+ and H_2 fragments, and after about 4500 steps ends in H_7^+ complex. (This simulation was not used in computing the D_0; it is presented here just

because the D_0 can be shown conveniently in this imaginary time evolution.) The ZPE

of H_7^+, averaged from five DMC simulations, is 10490 cm^{-1}, with a standard deviation

of 10 cm^{-1}, while for the H_5^+ and H_2 fragments, the total ZPE is 11242 cm^{-1} with a

standard deviation of 5 cm^{-1}. These results provide a dissociation energy of 752 $\pm$ 15

cm^{-1} for the H_7^+ cluster. The ZPEs are 7530 $\pm$ 8 and 8510 $\pm$ 6 cm^{-1} for D_7^+ and D_2 +

D_5^+ fragments, respectively. Therefore, the D_0 value of D_7^+ is 980 $\pm$ 14 cm^{-1}. However,

PES I underestimates the D_e by 65 cm^{-1}, and when the DMC values of D_0 are corrected

by this amount, our best estimations of D_0 are 817 $\pm$ 15 and 1045 $\pm$ 14 cm^{-1} for H_7^+

and D_7^+ respectively.
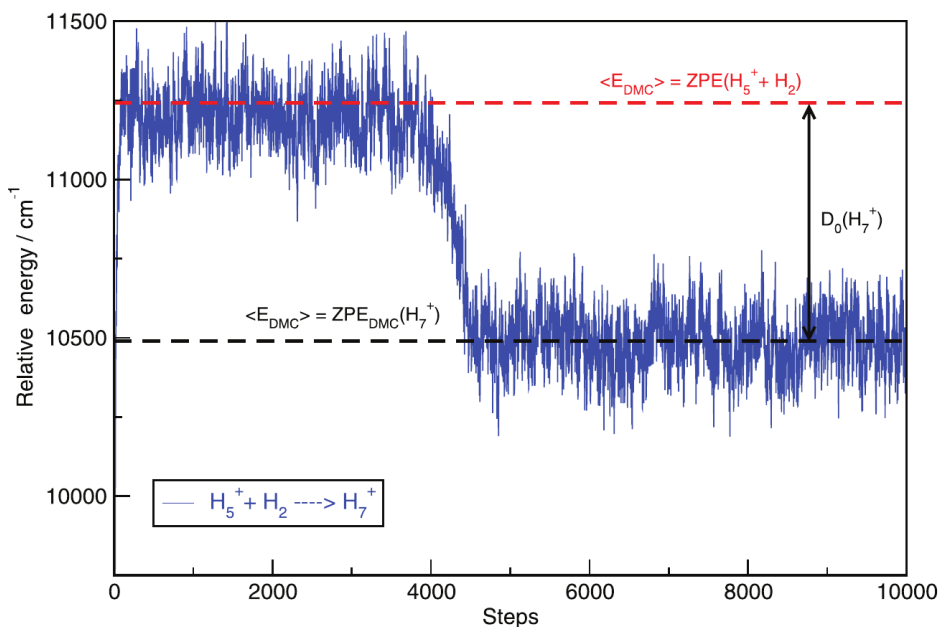
Figure 7.5: DMC simulation starting from the H_5^+ + H_2 fragments and ends at H_7^+. The calculated ZPEs and D_0 values are also indicated.

The ground state wavefunction of H_7^+ is shown in Figure 7.6. According to this plot,

the H_3^+ core is relatively localized; on the other hand, the amplitude for the torsional motion of the two H_2 units is significant, indicating that the H_2 units are highly delocalized and behave like nearly free rotors.
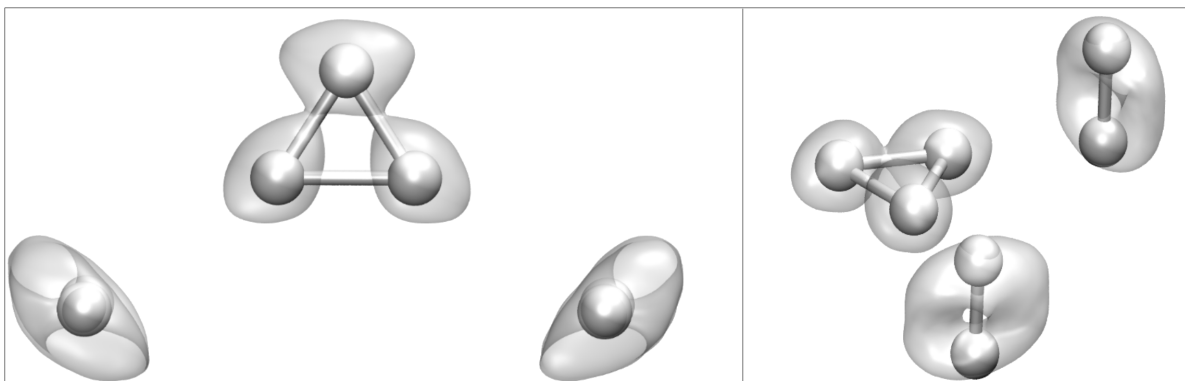
Figure 7.6: Isosurface of the vibrational ground state wavefunction of H_7^+ from DMC simulations.

The ZPEs of all the possible isotopomers of partially deuterated H_7^+ calculated by DMC simulations are summarized in Table 7.4. Here the notation $[H_2-HHH-H_2]^+$ is used to represent the H_7^+. The first and last "H" in "HHH" represent the two atoms in the central H_3^+ that are bonded to the diatom H_2 units, and the "H" in the middle is the un-bonded atom.

For some isotopomers, I was not able to obtain accurate ZPEs because they isomerized (Here isomerization occurs in imaginary-time, so this is not real-time dynamics.) to more stable counterparts very quickly. Though the ZPE values from the two potential energy surfaces differ, relative stability of each isotopomer obtained from two PESs agrees with each other. Based on the ZPEs calculated by DMC, the following rules can be summarized for the position that deuterium prefers. (1) Deuterium prefers to stay in the central H_3^+

Table 7.4: Zero-point energies (cm^{-1}) of indicated species calculated by DMC.

Isotopomer	DMC (PES II)	DMC (PES I)	Harmonic (PES II)
$[H_2-HDH-H_2]^+$	9847.4 ± 2.6	10021.3 ± 3.6	10315.8
$[H_2-DHH-H_2]^+$	9866.8 ± 1.1 [a]	10051.2 ± 7.2	10330.7
$[HD-HHH-H_2]^+$	N/A [b]	10137.6 ± 7.7 [a]	10444.8
$[H_2-DDH-H_2]^+$	9373.8 ± 1.3	9549.8 ± 6.4	9800.4
$[H_2-DHD-H_2]^+$	9413.3 ± 1.1 [a]	9578.6 ± 7.7 [a]	9824.7
$[HD-HDH-H_2]^+$	9502.5 ± 0.5	9674.7 ± 4.1	9941.8
$[HD-DHH-H_2]^+$	9524.4 ± 2.0 [a]	9693.6 ± 3.5	9956.1
$[HD-HHD-H_2]^+$	9525.9 ± 2.1 [a]	9698.0 ± 5.3	9957.2
$[D_2-HHH-H_2]^+$	N/A [b]	N/A [b]	10019.3
$[HD-HHH-HD]^+$	N/A [b]	9798.5 ± 4.0 [a]	10072.3
$[H_2-DDD-H_2]^+$	8889.6 ± 2.2	9052.8 ± 4.7	9267.6
$[HD-DDH-H_2]^+$	9030.4 ± 3.6	9201.8 ± 3.8	9424.1
$[HD-HDD-H_2]^+$	9030.0 ± 2.6	9196.4 ± 6.1	9425.1
$[HD-DHD-H_2]^+$	9064.7 ± 1.8 [a]	9225.1 ± 6.2 [a]	9448.8
$[D_2-HDH-H_2]^+$	9106.0 ± 5.9 [a]	9274.8 ± 6.5	9514.6
$[D_2-DHH-H_2]^+$	N/A [b]	9289.8 ± 6.5 [a]	9528.6
$[D_2-HHD-H_2]^+$	N/A [b]	9292.2 ± 7.4 [a]	9530.4
$[HD-HDH-HD]^+$	9158.3 ± 3.1	9328.1 ± 2.7	9567.3
$[HD-HHD-HD]^+$	9182.0 ± 5.5 [a]	9346.6 ± 2.9 [a]	9582.1
$[D_2-HHH-HD]^+$	N/A [b]	N/A [b]	9646.3
$[HD-DDD-H_2]^+$	8544.1 ± 2.1	8701.7 ± 4.9	8890.3
$[D_2-DDH-H_2]^+$	8636.8 ± 0.8 [a]	8791.8 ± 9.3	8995.2
$[D_2-HDD-H_2]^+$	8629.6 ± 2.4	8784.9 ± 3.5	8996.9
$[HD-DDH-HD]^+$	8686.9 ± 1.3	8845.3 ± 3.7	9048.4
$[D_2-DHD-H_2]^+$	8665.4 ± 1.1 [a]	8822.1 ± 6.6	9020.2
$[HD-DHD-HD]^+$	8719.4 ± 1.5 [a]	8876.3 ± 2.9 [a]	9072.5
$[D_2-HDH-HD]^+$	N/A [b]	8918.0 ± 5.7 [a]	9139.7
$[D_2-DHH-HD]^+$	N/A [b]	8946.3 ± 5.5 [a]	9154.1
$[D_2-HHD-HD]^+$	N/A [b]	8942.2 ± 6.4	9154.8
$[D_2-HHH-D_2]^+$	N/A [b]	8992.6 ± 5.7 [a]	9220.0
$[D_2-DDD-H_2]^+$	8143.2 ± 2.1	8286.8 ± 5.4	8460.4
$[HD-DDD-HD]^+$	8198.0 ± 1.8	8348.8 ± 3.3	8512.4
$[D_2-DDH-HD]^+$	8288.8 ± 1.1 [a]	8445.0 ± 5.0	8619.0
$[D_2-HDD-HD]^+$	8283.9 ± 2.4	8435.7 ± 4.2	8619.7
$[D_2-DHD-HD]^+$	8320.3 ± 2.2 [a]	8469.3 ± 4.2	8643.5
$[D_2-HDH-D_2]^+$	N/A [b]	8517.0 ± 6.0	8711.7
$[D_2-DHH-D_2]^+$	8389.9 ± 3.8 [a]	8534.1 ± 6.4 [a]	8726.5
$[D_2-DDD-HD]^+$	7797.2 ± 1.4	7935.7 ± 3.7	8082.1
$[D_2-DDH-D_2]^+$	7889.8 ± 1.5 [a]	8035.6 ± 5.4	8190.0
$[D_2-DHD-D_2]^+$	7922.0 ± 1.6 [a]	8063.9 ± 6.1	8214.1

[a] Isomerization occurred in the calculations for these species, but the date collected were adequate so that the ZPE can be obtained.

[b] Isomerization occurred quickly (in imaginary-time) so that the ZPE value cannot be obtained.

positions rather than the outer H_2 position. Furthermore, in H_3^+, deuterium prefers the un-bonded position. (2) If two deuteriums are in the outer H_2, forming D_2 is more stable than two HD's.

In addition, if we compare the order of the ZPEs of different isotopomers calculated by DMC with that calculated by harmonic approximation, we can find that the harmonic approximation gives the correct order, and it is adequate to describe the relative stability of the isotopomers qualitatively. However, as seen, the harmonic ZPEs are much higher than the correct DMC ones, due to the anharmonicity of H_7^+.

When analyzing the DMC results, we found some isotopomers can rearrange to a more stable configuration on the imaginary-time-scale of the propagations done. All these isomerizations could be classified into two types: the first type is that the unstable isotopomer rearranges to the one with more deuterium atoms in the H_3^+ core; the other type is that the number of deuterium atoms in the central H_3^+ doesn't change, but the deuterium moves from the bonded to the unbounded location in the complex. For example, $[HD-HHH-H_2]^+ \rightarrow [H_2-HDH-H_2]^+$ belongs to the first type, while $[H_2-DHH-H_2]^+$ $\rightarrow [H_2-HDH-H_2]^+$ belongs to the second type. In Figure 7.7 we show the imaginary time evolution of the reference energy for two DMC simulations. The upper panel shows the isomerization $[H_2-DHH-H_2]^+ \rightarrow [H_2-HDH-H_2]^+$; however, since the ZPEs of the two isotopomers differ only 20 cm^{-1}, one cannot see a significant change in the reference energy. In the lower panel, the initial configuration was $[D_2-HHH-HD]^+$, and it first became $[D_2-DHH-H_2]^+$, and then became $[H_2-DDD-H_2]^+$.

The second type of isomerization is accomplished through a reaction path that connects two equivalent minima and the saddle point $4-C_{2v}$, which has also been reported in PES I[215] (see Figure 7.9 for the structure). The reaction path is shown in Figure 7.8, with the computational details to determine the path given below. However, this type
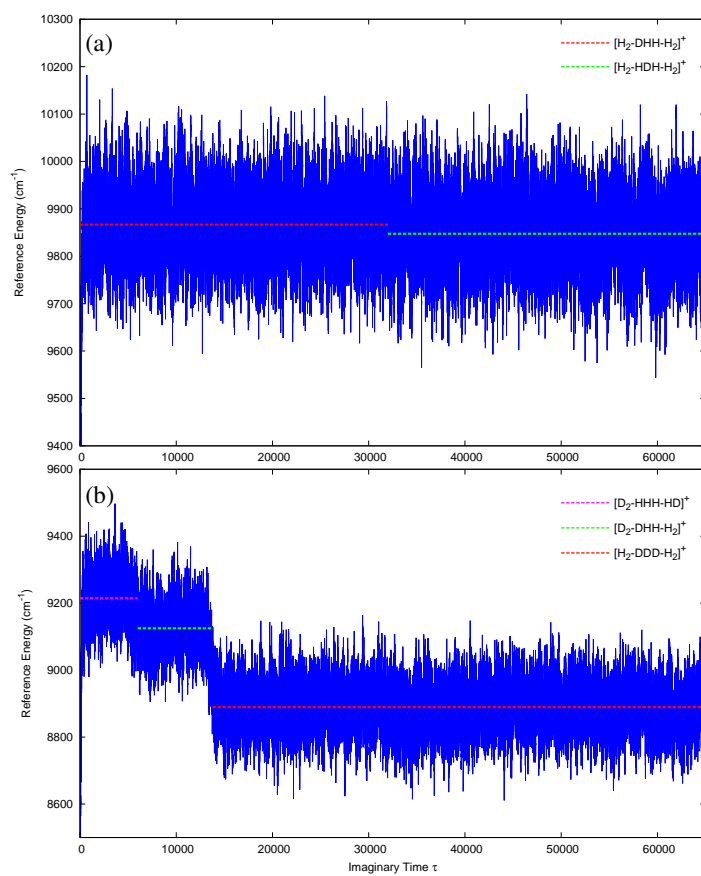
Figure 7.7:   Imaginary time evolution of the reference energy for two DMC simulations: (a) $[H_2-DHH-H_2]^+ \to [H_2-HDH-H_2]^+$; (b) $[D_2-HHH-HD]^+ \to [D_2-DHH-H_2]^+ \to [H_2-DDD-H_2]^+$.
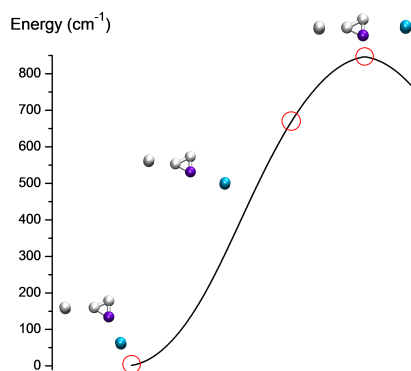
Figure 7.8: Reaction path obtained from "quenched" molecular dynamics simulation that starts from 4-C_{2v}. The geometries shown along the path correspond to the red circles on the path.

of isomerization can also be accomplished by simply the torsion of the central H_3^+, for which motion the saddle point was not reported in the PES I. Furthermore, none of the ten stationary points reported in the PES I could be the transition state of the exchange in the first type of isomerization. This motivated us to try to locate the two saddle points for the torsional motion of the central H_3^+ and for the H-exchange.

The analytical PES allows me to perform a thorough search for stationary points. Specifically, I used the geometries of the walkers in the DMC calculations as the initial guesses, and then apply Newton's method to optimize the structure on the analytical PES. If the geometry of the walker is close to a stationary point, Newton's method converged to that stationary structure quickly; on the other hand, if the walker is far from a stationary point, Newton's method cannot converge and I simply discarded that walker. Most of the walkers were discarded, but since there were thousands of random walkers, I was able to locate several stationary points on the PES. I found two saddle points that may relate to the isomerization, and their structures were further optimized

and then normal mode analysis was carried out using MOLPRO. Figure 7.9 shows the structures of the global minimum and the 4-C_{2v}, 11-C_{2v}, as well as 12-C_{2v} saddle points. As one can see, 11-C_{2v} can be viewed as one H_2 molecule bonded to the H_5^+ at its D_{2h} configuration; thus this exchange is very similar to that in H_5^+. The exchange saddle point is 661.4 cm^{-1} above the minimum, and the barrier height for the H_3^+ rotation is about 1450 cm^{-1}. Both of 11-C_{2v} and 12-C_{2v} have one imaginary frequency, corresponding to the proton exchange mode and the torsional motion of the central H_3^+, respectively. These two saddle points are now also included in PES II, and the energies of them as well as the 4-C_{2v} are listed in Table 7.5.
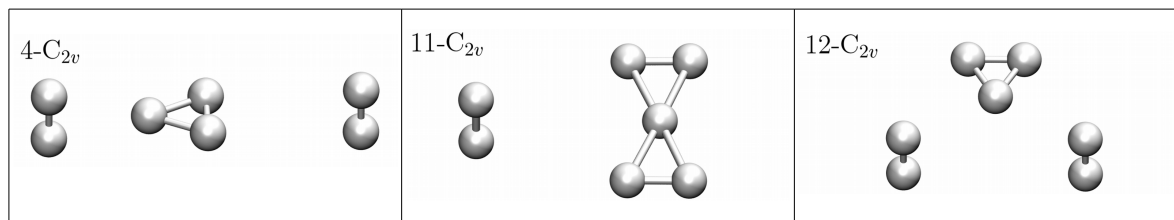
Figure 7.9: Geometries of three stationary points of H_7^+ that are related to the H-exchange.

Table 7.5: The energies relative to the minimum (in cm-1) of 4-C_{2v}, 11-C_{2v}, and 12-C_{2v} computed at the indicated levels of theory as well as the value from PES I and II.

Config.	PES I [a]	PES II	CCSD(T)-F12b
4-C_{2v}	828.3	847.3	839.4
11-C_{2v}	707.1	659.4	661.4
12-C_{2v}	1198.2	1457.6	1457.6

[a] From Ref. 215

For the two new saddle points as well as the 4-C_{2v}, "quenched" molecular dynamics calculations were carried out on PES II: the molecule was initially at the saddle point and was given small initial internal energy. After each step I reduced the velocity of each atom to 95% so that they would basically follow the potential gradient, and the trajectory is a good approximation to the reaction path. The reaction paths from 11-C_{2v} and 12-C_{2v} to the minimum are shown in Figure 7.10.
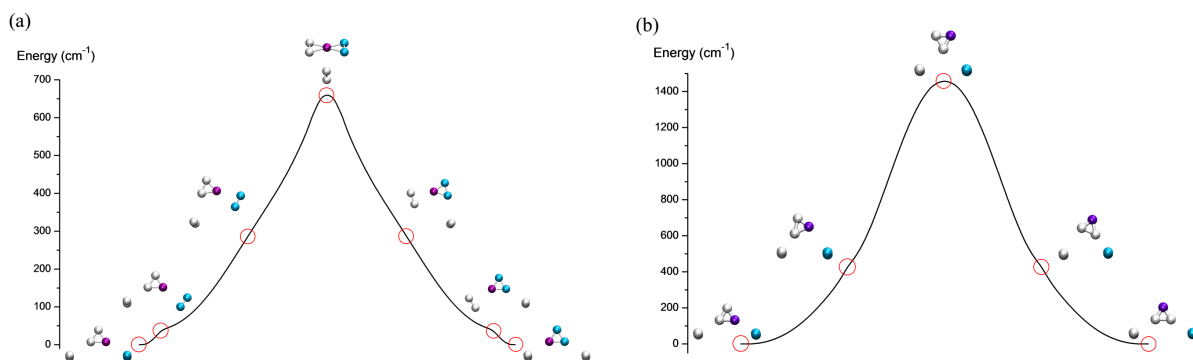
Figure 7.10:   Reaction paths to the minimum that start from: (a) 11-C_{2v} and (b) 12-C_{2v}. As mentioned in the text, the paths are obtained from molecular dynamics simulations, and the geometries shown along the path correspond to the red circles on the path.

Therefore, for partially deuterated isotopologs, isomerization between the isotopomers is possible at vibrational ground state. Now the question arises whether the two types of isomerization could also occur at the vibrational ground state of H_7^+. To answer this question, I analyzed the 98714 walkers collected from five DMC trajectories of H_7^+ using the PES II. Among these walkers, I found about 2000 of them has hydrogen atom at the interior that moved to the exterior, and confirmed that the H-exchange occurred. These results indicate that H_7^+ is indeed fluxional in the ground vibrational state. However, based on the rarity of the events (only about 2% walkers show H-exchange) leading to

these isomerizations, we cautiously assert that H_7^+ is not as fluxional as CH_5^+, which isomerizes readily, owing to much smaller barriers separating the isomers.

7.4   IR Spectrum of H_7^+

7.4.1   Computational detail

The code "MULTIMODE" was used for vibrational calculations. As mentioned in Chapter 3, this code uses the Watson Hamiltonian[40] in mass-scaled normal coordinates. However, the Watson Hamiltonian has difficulty in describing the large amplitude motions such as torsion. For molecules with low torsional barriers, the reaction-path version (MM-RPH) is employed to include one large-amplitude coordinates by the "reaction-path Hamiltonian"[41,44]. For H_7^+, the two H_2 units act almost like free rotors, based on the DMC calculations. However, here I did not perform MM-RPH calculations; instead, I employed the single-reference version (MM-SR) limited to the five highest-frequency modes. The reason for choosing MM-SR is that I only focus on the experimental part of the spectrum, which is probed the high frequency H_3^+ and H_2 internal modes. Therefore, it's reasonable to restrict the calculations to the five high frequency modes and these calculations can be conveniently done with MM-SR. However, in recognition of the nearly free-rotor motion of the two H_2 groups, I carried out MM-SR calculations at three configurations on the torsion path, i.e., 1-C_{2v}, 2-C_s, and 3-C_{2v}, as described below.

In brief, we solve the five-mode Schrödinger equation

$$\hat{H}\psi(\vec{Q}) = E\psi(\vec{Q}), \tag{7.1}$$

where $\vec{Q} = [Q_1\ Q_2\ Q_3\ Q_4\ Q_5]$ denotes the five high-frequency modes, and the $\hat{H}$ is the

Watson Hamiltonian, given by Eq. 3.22 in Chapter 3. The $V(\vec{Q})$ here is the full potential with respect to the five modes while the other modes are fixed at zero. In this work, the 4MR and 5MR potential are used. Note that in this five-mode calculation, 5MR potential is a complete expansion.

I solved the time-independent nuclear Schrödinger equation for zero total angular momentum using the VSCF+VCI approach. In order to test the convergence, two different sizes of basis functions were employed in the calculation. In the calculation with smaller basis, 11 harmonic oscillator basis functions were used for each mode in the VSCF step. Simultaneous excitation of up to four modes in the VCI step was allowed. The MAXBAS's for each mode in 1-, 2-, 3-, and 4-mode basis were all 10, and the MAXSUM was 10. (See Chapter 3 for the definition of MAXBAS and MAXSUM) In the calculation with larger basis, the number of harmonic oscillator basis functions became 13. Simultaneous excitation of up to five modes were allowed, with MAXBAS and MAXSUM equaled to 12.

The infrared intensities were calculated with the two step "dump-restart" method described in Chapter 3. To finally get the spectra, the stick line shapes were replaced by Gaussian line shapes to achieve a similar line width as the experiment.

7.4.2   Results and discussions

In total I performed four VSCF+VCI calculations (4MR/5MR + small/large basis). The frequencies of the five fundamentals and a combination band obtained in these calculations are listed in Table 7.6. As one can see, the difference between these calculations are mostly less than 1 cm^{-1}. Therefore, calculation employing 4MR potential and 11 basis functions is enough to achieve converged results for this problem, and thus it is used for

the calculations of the spectra.

Table 7.6: Anharmonic frequencies (cm^{-1}) of the intramolecular modes of H_7^+ with 4MR and 5MR of the potential and different number of basis functions.

Config.	Mode	4MR		5MR	
		11 basis	13 basis	11 basis	13 basis
1-C_{2v}					
	ν_{11}	1909.7	1909.1	1909.7	1909.1
	ν_{12}	2172.9	2172.7	2172.9	2172.7
	ν_{13}	2907.0	2906.5	2907.0	2906.5
	$\nu_{11} + \nu_{12}, \nu_{14}$	3941.1	3939.5	3941.3	3939.6
	ν_{15}	3983.9	3983.8	3983.9	3983.8
	$\nu_{14}, \nu_{11} + \nu_{12}$	4004.2	4003.5	4004.0	4003.2
2-C_s					
	ν_{11}	1928.1	1927.6	1928.1	1927.6
	ν_{12}	2174.3	2174.1	2174.3	2174.1
	ν_{13}	2908.9	2908.4	2908.9	2908.4
	$\nu_{11} + \nu_{12}, \nu_{14}, \nu_{15}$	3952.8	3951.7	3952.8	3951.6
	$\nu_{15}, \nu_{14}, \nu_{11} + \nu_{12}$	3983.9	3983.8	3983.9	3983.8
	$\nu_{15}, \nu_{11} + \nu_{12}, \nu_{14}$	4012.0	4011.0	4012.1	4011.1
3-C_{2v}					
	ν_{11}	1928.2	1927.7	1928.2	1927.7
	ν_{12}	2185.1	2184.8	2185.0	2184.8
	ν_{13}	2912.8	2912.3	2912.8	2912.3
	$\nu_{14}, \nu_{11} + \nu_{12}$	3960.7	3959.6	3960.9	3959.8
	ν_{15}	3989.2	3989.1	3989.2	3989.1
	$\nu_{14}, \nu_{11} + \nu_{12}$	4018.6	4017.5	4018.4	4017.2

From the VSCF+VCI calculation I find that for the 1-C_{2v} and 3-C_{2v} reference configurations two states show strong mixing: (1) the out-of-phase stretch of the two H_2; (2) the combination mode of the H_3^+ bending and H_3^+ asymmetric stretch. While for 2-C_s, three states, namely two stretches of the two H_2 and combination mode of H_3^+ bending and asymmetric stretch, have strong coupling.
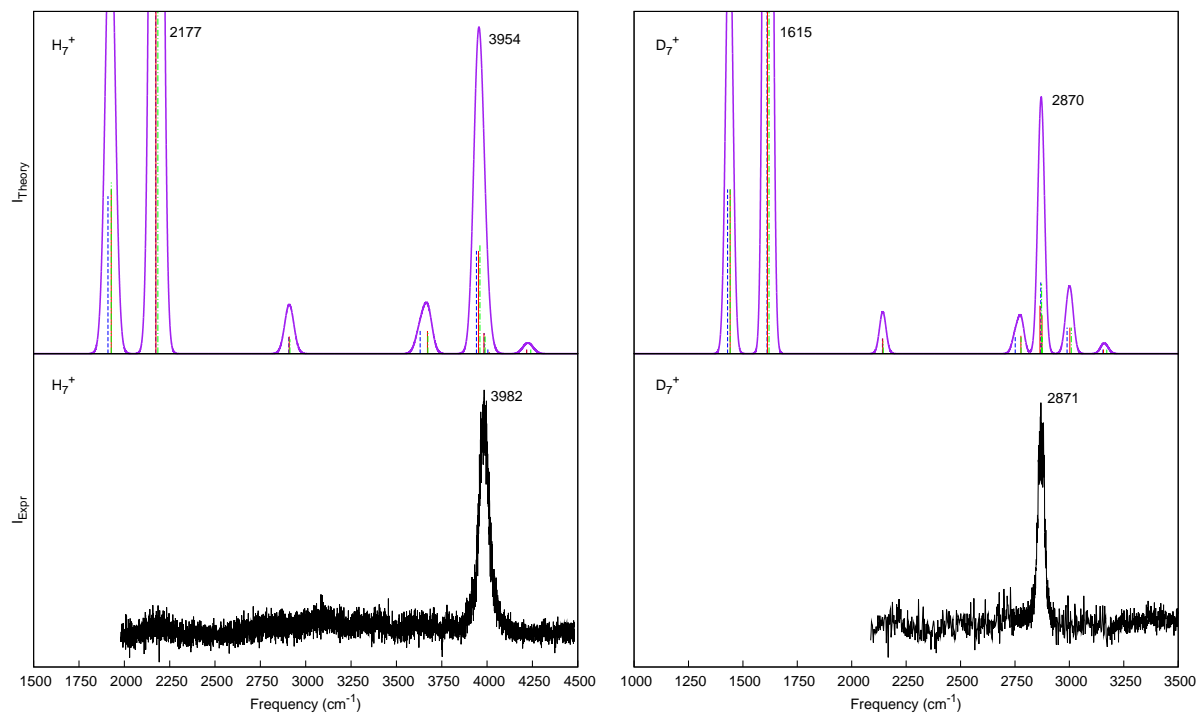
Figure 7.11: Comparison of the calculated and experimental spectra for H_7^+ and D_7^+, respectively. We combined the spectra of 1-C_{2v} (blue sticks), 2-C_s (red sticks) and 3-C_{2v} (green sticks) in one figure, and replace the stick line shape with Gaussian line shape to obtain the calculated spectra (purple lines).

Since the DMC simulations suggest that the two H_2 almost rotate freely at vibrational ground state, I combined the three spectra of the three reference configuration, to obtain an overall spectrum for H_7^+, which is shown in Figure 7.11. In the range from 2000 to 4500 cm^{-1}, the calculated spectrum has two relatively intense peaks at 2177 and 3954 cm^{-1}, respectively, which are in good agreement with the experimental ones at about 2200 and 3982 cm^{-1}. As is explained in Ref. 232, the relative intensity between the two bands can be attributed to the lower laser power at low frequency and the lower photodissociation yield with lower energy photons. Therefore, the differences of the intensities between our computations and the experiment is understandable. Comparing with the scaled DFT spectrum[232] of H_7^+, which overestimates the peak at 3982 cm^{-1} by about 100 cm^{-1}, the spectrum from the VCI calculations is in better agreement with the experiment. In addition, I can assign the peak at 3982 cm^{-1} to the mixed state mentioned above, instead of the pure stretch of the H_2. The spectrum for D_7^+ is also shown in Figure 7.11. As is shown, it doesn't exhibit significant differences compared to that of H_7^+, except that the positions of the peaks are shifted by a factor of roughly $\sqrt{2}$.

7.5   Conclusions and Remarks

I constructed a new PES of H_7^+ based on high-level CCSD(T)-F12b/VQZ-F12 energies. Unlike the PES presented by Barragán et al.[215] which could describe the $H_7^+ \rightarrow H_5^+ + H_2$ channel, this new PES is only in the bound region of H_7^+, but it's more precise. The rms fitting error is only 5 cm^{-1} for energies up to 15000 cm^{-1}. This PES, together with the one due to Barragán et al.[215], were used in the DMC simulations that characterize the vibrational ground states of H_7^+. In addition, a DMS is also reported here, which is a fit to MP2 dipole expectation values, with an rms fitting error of 0.0006 au. The new

CCSD(T)-F12 PES and the DMS were employed in the calculation of the IR spectra of H_7^+ and D_7^+.

I performed DMC simulations to investigate the dissociation energies and vibrational ground states of H_7^+ and D_7^+ clusters, using two *ab initio*, full-dimensional PESs. The dissociation energy is 817 ± 15 cm^{-1} for $H_7^+ \to H_5^+ + H_2$, while it is 1045 ± 15 cm^{-1} for D_7^+. The DMC simulations also show that the H_3^+ core in H_7^+ is relatively localized, while the two H_2 behave like quasi-free rotors. Several H-exchange pathways have been located: one involves the exchange of H between the central H_3^+ and the outer H_2, and the other could be the migration of the outer H_2 or the torsion of the central H_3^+. For relatively unstable isotopomers, the H-exchange is quite common in the DMC simulations, so that the molecules can isomerize to more stable isotopomers. However, for H_7^+ and D_7^+, the exchange is very rare. The ZPEs obtained from DMC calculations for partially deuterated H_7^+ species also reveal the stability of different isotopomers. The most stable isotopomer first maximizes the number of deuterium in the H_3^+ and then maximize the deuterium in one H_2. Furthermore, the un-bonded position in the central H_3^+ is preferred over the two equivalent bonded positions.

According to the DMC simulations, the H-exchange is very rare so that it should have little effects on the IR spectra of H_7^+ and D_7^+. However, the two H_2 units still undergo nearly free rotations, which may have an effect on the IR spectroscopy. Therefore, I performed VSCF+VCI calculations using three structures as the reference, and combined the results from these three reference geometries to obtain the IR spectrum. In addition, since the experiment focused on the high-frequency intramolecular vibrations, so I only considered these modes in the calculation. The spectra of H_7^+ and D_7^+ obtained from these calculations agree reasonably well with the experiment.

Chapter 8

Tunneling Splitting and Fundamentals of Formic Acid Dimer

8.1 Overview

The cyclic formic acid dimer, $(HCOOH)_2$, (FAD) has attracted considerable attention as it is a prototype for doubly hydrogen-bonded complexes, as well as deep double-proton tunneling, owing to the large barrier (roughly 2900 cm^{-1}) separating two equivalent minima. The frequency of the hydrogen bonded O–H stretch is strongly perturbed by the strong hydrogen bonds and so the vibrational spectrum of FAD in the O–H stretching region also presents a challenge to experiment and theory.

The tunneling splitting of FAD and its deuterated counterparts have been measured experimentally using high-resolution IR spectroscopy.[235–240] From two independent measurements,[236,240] the splitting of $(HCOOH)_2$ is 0.016 cm^{-1}. This splitting is small, implying a high barrier for the double-proton transfer. (By contrast, the ground-state tunneling splitting in malonaldehyde is roughly 22 cm^{-1} and the barrier height for this single-proton

transfer is roughly half that of FAD.) For $(DCOOH)_2$, the ground state tunneling splitting could be either 0.0029 or 0.0125 cm^{-1} and it could not be determined unambiguously.[235] The tunneling splitting of $(DCOOD)_2$ could not be resolved in experiment, but an upper limit of 0.002 cm^{-1} was reported.[237]

The IR and Raman spectra to probe the molecular vibrations of FAD have also been measured. Early experiments were performed at room temperature,[241–244] so the spectra were complicated by hot-band absorptions, making the assignment very difficult. Later the spectra were taken in supersonic jet[245–248] and in rare gas matrix.[249,250] The O–H stretch bands in the experimental spectra spreads over a big range, and has a rich substructure.

Theoretically, calculating the ground-state tunneling splitting of FAD is a challenge, certainly to within say 10% of experiment, because the splitting is small. It is clearly very sensitive to the barrier height and shape, and coupling of modes. Also, it is clear that the high dimensionality (24 modes) makes a rigorous, full-dimensional quantum calculation highly challenging, if not prohibitive. Previous theoretical calculations for the tunneling splitting of $(HCOOH)_2$ have necessarily made compromises with both the electronic structure method (all used DFT theory) and the number of degrees of freedom considered. The results from these do find a splitting less than 1 cm^{-1}; however, virtually all the more recent calculations obtain a splitting that is smaller than experiment by a factor of 2 to 10,[251–260] with the exception of an approximate instanton calculation,[255] which is in very good agreement with experiment. These authors also calculated the tunneling splitting for $(DCOOH)_2$, and suggested that the splitting is 0.0125 cm^{-1}. However, another instanton calculation using B3LYP/6-311++G($3df, 3pd$) with CCSD(T) correction leads to a much smaller splitting of 0.0038 cm^{-1} for $(DCOOH)_2$, in favor of the alternative assignment for the ground state tunneling splitting.[256] Recent seven-dimensional quantum

calculations by Luckhaus[261] with B3LYP/6-31+G* and a barrier of 2924 cm^{-1} obtained a splitting of 0.008 cm^{-1} for $(HCOOH)_2$, about half of the experimental value. Jain and Sibert[262] carried out a three-mode calculation using a model B3LYP-based potential, with a barrier of 2909 cm^{-1} for $(HCOOH)_2$, and obtained a splitting of 0.0017 cm^{-1}, about a factor of ten smaller than the experiment.

In addition to tunneling splitting, there have also been *ab initio* molecular dynamics studies on tunneling dynamics, and support a concerted mechanism for double-proton transfer,[263–267] though stepwise[268] and quantum entanglement mechanisms[269] have also been proposed. Recently, from direct-dynamics, path-integral metadynamics calculations, it was concluded that the double-proton transfer in FAD is concerted but not correlated.[270]

The O–H stretching region of IR spectrum has also been examined by several theoretical studies. Florio et al.[271] modeled the spectrum of FAD using cubic anharmonic coupling, and suggests that the coupling between the O–H stretch with C–O–H bend has a profound effect. Matanović and Došlić[272] investigated the C–H and O–H stretch region of the spectrum using both vibrational second-order perturbation theory (VPT2) and non-perturbative treatment in reduced dimensionality. They stated that the red-shift of the O–H frequency is mainly due to the coupling with the symmetric O–H stretch, while the broadening of the spectrum is due to the coupling to low-frequency modes and Fermi resonance. Barnes and Sibert[273] employed a reaction surface Hamiltonian to model the symmetric O–H stretching Raman spectrum, and they concluded that extensive state mixing is found, which leads to broad spectral features. Recently, Pitsevich et al.[274] attempted to assign the bands by using a hybrid method that combines VPT2 calculation and a two-dimensional PES for the O–H stretches. Except the C–H and O–H stretches, VPT2 calculations agree reasonably well with experimental frequencies.[272,274]

An *ab initio*, full-dimensional PES for FAD has not been reported, to the best of our knowledge, and I present one here, using techniques described in Chapter 2. FAD is a high-dimensional system, i.e., 45 Morse variables, and yet I was able to develop a PES that accurately describes the two equivalent minima and saddle-point region separating them with only 13475 configurations and electronic energies. This would amount to 1.24 points per Morse variable, if a direct-product grid were to be used. Obviously, permutational symmetry is a great help here. The full symmetry group was used which is of order $4!4!2! = 1152$.

8.2   Potential Energy Surface

The CCSD(T)-F12a method[32,33] was employed to obtain electronic energies. However, given the large number of electrons, the modest-sized haXZ basis sets (X=D and T; haXZ means VXZ for H atoms, and aVXZ for C and O atoms) were investigated and tested for the barrier height. Geometries of the minimum and saddle point were optimized with the haDZ basis, and then single point calculations were done with haDZ and haTZ bases at these geometries to determine the barrier height. Table 8.1 compares the corresponding barrier heights, along with results from previous calculations, of which the one from Ivanov et al.[270] is considered the most rigorous. Clearly, the result using the haDZ basis set is not accurate enough for the present application; however, the barrier height using the haTZ basis is only 50 cm^{-1} below the CCSD(T)/aV5Z//MP2/aV5Z result. Given that a single CCSD(T)-F12a/haTZ calculation takes about 40 minutes on the computing system, using MOLPRO 2010[167], calculations with a larger basis are not feasible, considering that more than 10000 energies are needed for the PES fit.

The configurations for the dataset were selected as follows. First, direct-dynamics

Table 8.1: Barrier height (cm^{-1}) for double proton transfer in formic acid dimer from different methods. The method before and after the "//" is the level used for the single point calculation and geometry optimization, respectively

Method	Ref.	Barrier height
CCSD(T)-F12a/haDZ// CCSD(T)-F12a/haDZ	This work	2781
CCSD(T)-F12a/haTZ// CCSD(T)-F12a/haDZ	This work	2853
CCSD(T)/aV5Z// MP2/aV5Z	270	2903
B3LYP/6-31+G*	261	2933

trajectories were run using the efficient MP2/VDZ method from minimum and saddle point configurations with kinetic energies in the range 500–10000 cm^{-1}. From these trajectories, 8325 "scattered" configurations were selected for an initial fit, using CCSD(T)-F12a/haTZ energies obtained at these configurations. Additional configurations were obtained as follows: 2200 geometries were selected from normal-mode sampling around the two stationary points to give accurate harmonic frequencies; 1400 geometries were randomly sampled along the minimum energy path connecting the minima and the saddle point; and finally 1550 geometries were added, based on information from diffusion Monte Carlo (DMC) calculations, i.e., energies from the PES that are un-physically low or otherwise differ substantially from *ab initio* results. The final dataset consists of 13475 geometries and corresponding energies.

As noted above, the PES is a least-squares fit to the dataset, using fitting basis functions that are permutationally invariant polynomials in Morse variables $y_{ij} = \exp(-r_{ij}/a)$, where r_{ij} are inter-nuclear distances and $a = 2.0$ Bohr. A weight is assigned to each point in the dataset, given by $0.004/(0.02 + \Delta V)(0.2 + \Delta V)$, where ΔV is the energy relative to the minimum in Hartree. The maximum order of the polynomials is

four, resulting in 1784 linear coefficients. Typically maximum orders of five or six is used for PESs; however, for the FAD, the number of coefficients grows rapidly with the order and maximum order of five contains more than 10000 coefficients. Because the dataset only consists of 13475 points (and due to the high cost of the *ab initio* calculations, it's not feasible to calculate much more points for the fifth-order fit), this would cause over-fitting. Nevertheless, the overall weighted root-mean-square (rms) fitting error is 11 cm^{-1}, and the absolute error for 6908 energies that are less than 4400 cm^{-1} is about 13.8 cm^{-1}.

The configurations of the minimum and the saddle point from the PES are shown in Figure 8.1. The key geometrical parameters of these configurations are given in Table 8.2. The barrier height from the PES is 2848 cm^{-1}, which agrees well with the direct CCSD(T)-F12a/haTZ calculation.
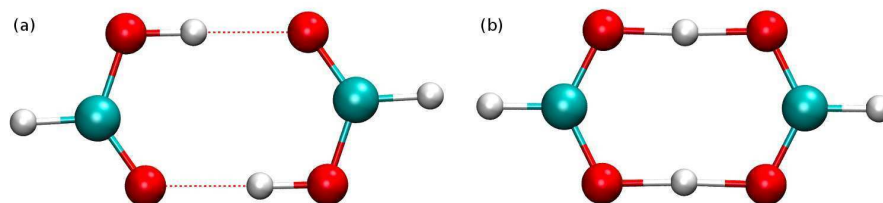
Figure 8.1:   Configurations of the two stationary points of formic acid dimer: (a) the minimum and (b) the saddle point.

Next, consider the harmonic frequencies of the minimum and the saddle points. These are given in Table 8.3, together with the CCSD(T)-F12a/haDZ frequencies. Pictures and descriptions of these normal modes are given in Figure 8.2 and 8.3. The PES is based on higher-level *ab initio* calculations than CCSD(T)-F12a/haDZ, but the agreement is quite good. The PES frequencies for the minimum are also in very good agreement with

Table 8.2:   Key geometrical parameters of minimum and the saddle point of the formic acid dimer from the PES and CCSD(T)-F12a/haDZ geometries. Bond lengths are in Angstroms and angles in degrees.

Minimum				Saddle point		
Parameter	PES	*ab initio*		Parameter	PES	*ab initio*
r(O–H)	0.993	0.994		r(O–H)	1.205	1.204
r(C–H)	1.093	1.095		r(C–H)	1.092	1.095
r(C–O)	1.312	1.312		r(C–O)	1.260	1.260
r(O$\cdots$O)	2.678	2.673		r(O$\cdots$O)	2.409	2.407
r(C=O)	1.218	1.218				
∠O=C–O	126.2	126.1		∠O–C–O	126.6	126.6
∠O=C–H	122.1	122.0		∠O–C–H	116.7	116.7
∠C–O–H	109.7	109.7		∠C–O–H	115.4	115.4
∠O–H$\cdots$O	179.0	178.7		∠O–H–O	177.4	177.4

CCSD(T)/aVQZ frequencies reported recently.[275]

DMC[55–57,59] calculations were done for the zero-point state of the FAD using the PES. The unbiased "birth-death" process is used in our simulation, and the details of this algorithm are given in Ref. 58 and in Chapter 3. To compute the ZPE of the formic acid dimer, ten simulations were performed, and in each simulation, 30000 walkers were initiated at the saddle point and were propagated for 40000 steps with step size, $\Delta\tau$, of 5.0 au. The first 10000 steps were used for equilibration, and the remaining 30000 steps to compute the ZPE. These simulations give a ZPE of 15337 ± 7 cm^{-1}. (As noted above, these calculations were also done using initial PESs to locate additional needed configurations.) These calculations typically require of the order of 10^9 potential evaluations, so a PES is a necessity in order to do them.

Table 8.3: Harmonic wavenumbers (in cm^{-1} of the formic acid dimer at minimum and saddle point geometries, from the PES and *ab initio* CCSD(T)-F12a/haDZ calculations.

	Minimum			Saddle point	
Mode	PES	*ab initio*		PES	*ab initio*
1	70	92		1355i	1356i
2	167	183		80	79
3	170	222		219	222
4	209	230		226	222
5	254	290		317	298
6	275	293		514	518
7	693	691		592	586
8	716	716		744	748
9	956	972		814	796
10	970	989		1065	1071
11	1084	1093		1079	1076
12	1100	1094		1241	1236
13	1255	1260		1341	1312
14	1258	1263		1395	1361
15	1406	1396		1397	1399
16	1408	1422		1400	1405
17	1448	1466		1404	1407
18	1481	1492		1408	1409
19	1715	1721		1604	1585
20	1780	1785		1691	1692
21	3095	3101		1743	1747
22	3097	3107		1749	1759
23	3232	3204		3101	3106
24	3326	3303		3106	3107

1 (A_u): 70 cm^{-1} dimer twist	2 (A_g): 167 cm^{-1} in-plane rock	3 (A_u): 170 cm^{-1} out-of-plane wag	4 (A_g): 209 cm^{-1} dimer stretch
5 (B_g): 254 cm^{-1} out-of-plane wag	6 (B_u): 275 cm^{-1} in-plane rock	7 (A_g): 693 cm^{-1} O–C=O bend	8 (B_u): 716 cm^{-1} O–C=O bend
9 (B_g): 956 cm^{-1} O–H out-of-plane	10 (A_u): 970 cm^{-1} O–H out-of-plane	11 (B_g): 1084 cm^{-1} C–H out-of-plane	12 (A_u): 1100 cm^{-1} C–H out-of-plane
13 (A_g): 1255 cm^{-1} C–O stretch	14 (B_u): 1258 cm^{-1} C–O stretch	15 (B_u): 1406 cm^{-1} O–C–H bend	16 (A_g): 1408 cm^{-1} O–C–H bend
17 (B_u): 1448 cm^{-1} O–C–H bend	18 (A_g): 1481 cm^{-1} O–C–H bend	19 (A_g): 1715 cm^{-1} C=O stretch	20 (B_u): 1780 cm^{-1} C=O stretch
21 (A_g): 3095 cm^{-1} C–H stretch	22 (B_u): 3097 cm^{-1} C–H stretch	23 (A_g): 3232 cm^{-1} O–H stretch	24 (B_u): 3326 cm^{-1} O–H stretch
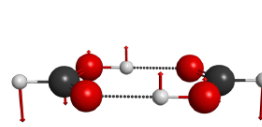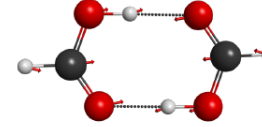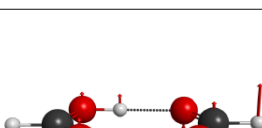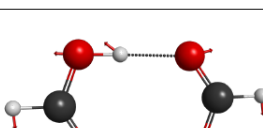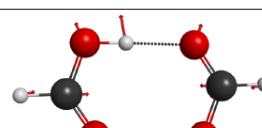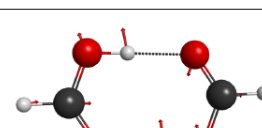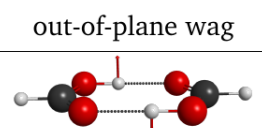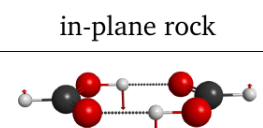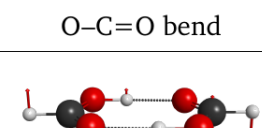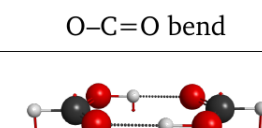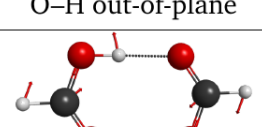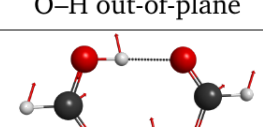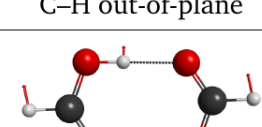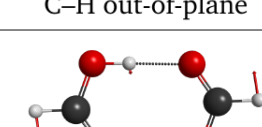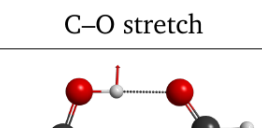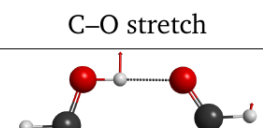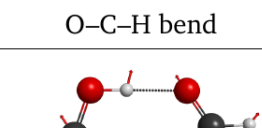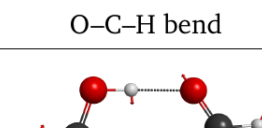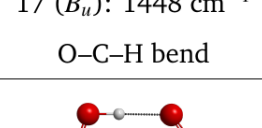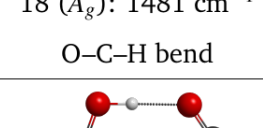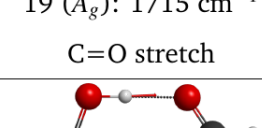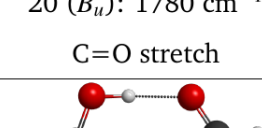
Figure 8.2:   Normal modes of the minimum of formic acid dimer.

1: 1355i cm^{-1}	2: 80 cm^{-1}	3: 219 cm^{-1}	4: 226 cm^{-1}
proton transfer	dimer twist	in-plane rock	out-of-plane wag
5: 317 cm^{-1}	6: 514 cm^{-1}	7: 592 cm^{-1}	8: 774 cm^{-1}
out-of-plane wag	dimer stretch	in-plane rock	O–C=O bend
9: 814 cm^{-1}	10: 1065 cm^{-1}	11: 1079 cm^{-1}	12: 1241 cm^{-1}
O–C=O bend	C–H out-of-plane	C–H out-of-plane	O–H stretch
13: 1341 cm^{-1}	14: 1395 cm^{-1}	15: 1397 cm^{-1}	16: 1400 cm^{-1}
O–H out-of-plane	O–C–H bend	O–C–H bend	O–H out-of-plane
17: 1404 cm^{-1}	18: 1408 cm^{-1}	19: 1604 cm^{-1}	20: 1691 cm^{-1}
O–C–O symm. stretch	O–C–O symm. stretch	O–H–O bend	O–H–O bend
21: 1743 cm^{-1}	22: 1749 cm^{-1}	23: 3101 cm^{-1}	24: 3106 cm^{-1}
O–C–O asym. stretch	O–C–O asym. stretch	C–H stretch	C–H stretch
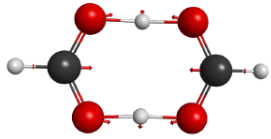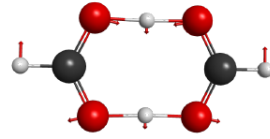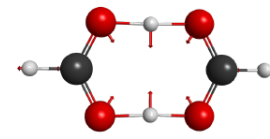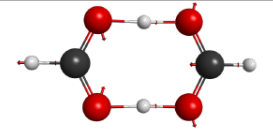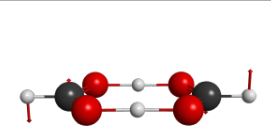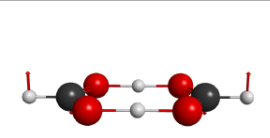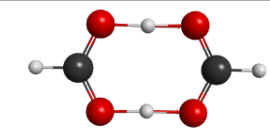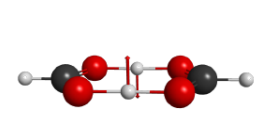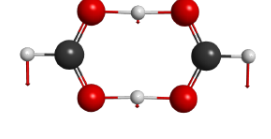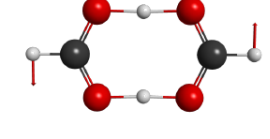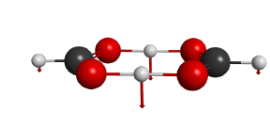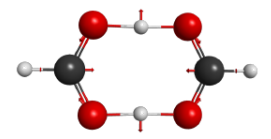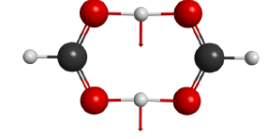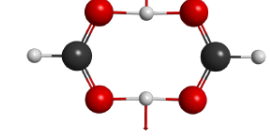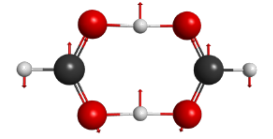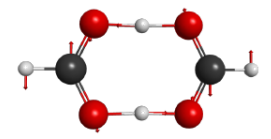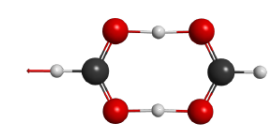
Figure 8.3: Normal modes of the saddle point of formic acid dimer.

8.3 Computational Details and Results

8.3.1 Tunneling splittings

I carried out reduced-dimensionality quantum calculations for the tunneling splitting, as described in Ref. 276. In brief, the m-mode Hamiltonian, neglecting the vibrational angular momentum terms, is given by

$$\hat{H} = -\frac{1}{2} \sum_{i=1}^{m} \frac{\partial^2}{\partial Q_i^2} + V(Q_1, Q_2, \cdots, Q_m), \tag{8.1}$$

where $V(Q_1, Q_2, \cdots, Q_m)$ is the potential relaxed with respect to the remaining degrees of freedom, at fixed values of $Q_1, \cdots, Q_m$. In the one-dimensional case, Q_1 is the imaginary-frequency mode Q_{im}, and this one-dimensional approach has been successfully applied in computing the tunneling splitting of malonaldehyde.[277,278] In my calculation, the potential was not rigorously relaxed; instead, in $V(Q_1, Q_2, \cdots, Q_m)$, the $Q_{m+1}, \cdots, Q_{3N-6}$ were simply determined by their values at Q_1 in the one-dimensional Q_{im} path. In this approach, the barrier height is the correct one, and the calculation is much more efficient, especially when m is large. This is also justified by the fact that many modes either do not change or change very little along the rectilinear Q_{im}-reaction path.

I applied this approach with m up to 4 to calculate the ground state tunneling splitting of FAD. As noted Q_1 is the imaginary-frequency mode, and the selection of $Q_2, \cdots, Q_m$ is described as follows. I first obtained the value of the saddle point normal coordinates at the minimum. The mode with the largest displacement is Q_2, the mode with second largest displacement is Q_3, etc. In the case of FAD, Q_2 is the dimer stretch (mode 6) of the saddle point; Q_3 is dimer in-plane rock (mode 3); Q_4 is O–C=O bend (mode 8). Figure 8.4 shows the contour plot of the potential with respect to (Q_1, Q_2) and (Q_1, Q_3). One can
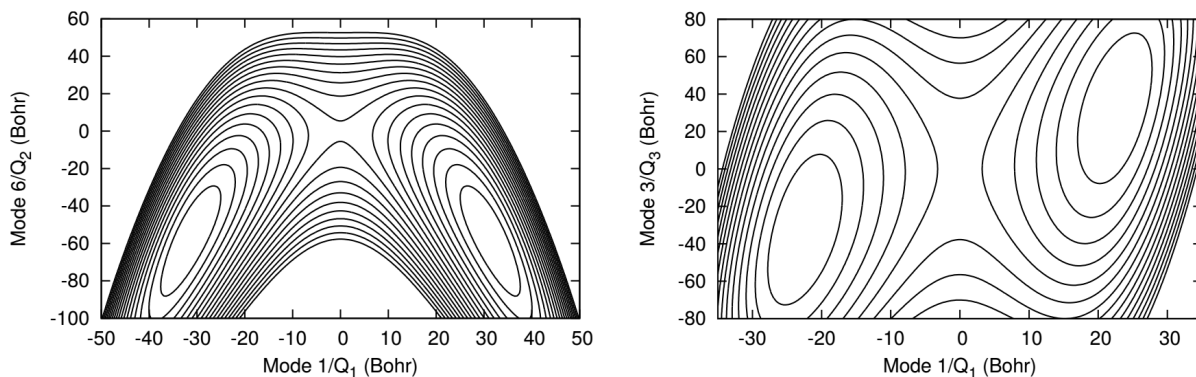
Figure 8.4: Contour plots of the FAD potential energy surface.

see strong coupling among these modes, so they should be included in the calculation of the tunneling splitting. This selection of the modes to couple with Q_{im} is consistent with the choice made by Jain and Sibert.[262] In their three-mode calculation they also chose the in-plane dimer rocking and dimer stretching modes. This approach is also very similar to the one by Luckhaus[261], except that I use relaxed potential while his is not relaxed. Therefore, my choice of $V(Q_1, Q_2, \cdots, Q_m)$ always has the correct barrier height, but in the calculation by Luckhaus,[261] the barrier height was slightly lower, though it's only 9 cm^{-1} lower than the full-dimensional barrier.

For $m = 1$, the one-dimensional Schrödinger equation was solved using a standard discrete variable representation (DVR) approach. For $m = 2, 3, 4$, the multi-dimensional Schrödinger equations were solved using a direct-product of particle-in-a-box functions. The ranges of the boxes are: $-120.0 \leq Q_1 \leq 120.0$, $-250.0 \leq Q_2 \leq 20.0$, $-150.0 \leq Q_3 \leq 150.0$, and $-70.0 \leq Q_4 \leq 200.0$. These are large enough to cover the region of the saddle point and both minima. Particle-in-a-box functions were used owing to the large displacement of the four normal modes (all zero at the saddle point of course) at each minimum. The matrix elements of the potential were obtained using numerical

quadrature with equally spaced quadrature grids. In the three-dimensional calculation, 75 grid points were used for each mode, and 60 grid points per mode were used in the four-mode calculations. Finally, symmetry was exploited to separate the Hamiltonian matrix into two blocks. The symmetries of Q_1, Q_2, Q_3, Q_4 are odd, even, odd, even, respectively. The Hamiltonian matrix was diagonalized and the splitting is just the energy difference between the lowest two energy levels. In the two-mode calculations, I used 25, 30 and 35 basis functions for each mode to test the convergence, and 30 is sufficient to get a converged result. In the three-mode calculations, I used 30 basis functions per mode. In addition, as the calculation is very expensive in four modes, I experimented with fewer basis functions than 30 in the three-mode calculation, and found that 30 functions for Q_1 and 12 functions for other two modes leads to splitting that differed by 0.003 cm^{-1} from the largest three-mode calculation. Therefore, in the four-mode calculations, I used 30 basis functions for Q_1, and 12 functions for the other three modes. No restrictions on the direct-product bases were used and so the order of the corresponding Hamiltonian matrices is just the product of the basis for each mode. However, symmetry was used so each block is 13500 by 13500 in the three-mode calculation, and 25920 by 25920 in the four-mode calculation.

The same procedures were used to calculate the ground-state tunneling splitting of (DCOOH)$_2$ and (DCOOD)$_2$. The results for the three complexes are given in Table 8.4. For (HCOOH)$_2$, the one-mode calculation gives a tunneling splitting of 0.44 cm^{-1}, which is close to the value of 0.55 cm^{-1} reported by Jain and Sibert using the same method.[262] As seen in the table, as the coupling increases the splitting goes down, with the three and four-mode results nearly the same and giving a splitting that is roughly twice the experimental one. The number of basis in the four-mode calculations is not very large and the convergence of the splitting cannot be tested thoroughly. Additional coupling

Table 8.4:   Ground-state tunneling splitting (cm^{-1}) from m-mode quantum calculations for the indicated FAD complex.

	$(HCOOH)_2$	$(DCOOH)_2$	$(DCOOD)_2$
1-Mode	0.44	0.41	0.015
2-Mode	0.16	0.15	~ 0.003
3-Mode	0.032	0.028	~ 0.0003
4-Mode	0.037		
Exp.	0.016 [a]	0.0029 or 0.0125 [b]	< 0.002 [c]

[a] Ref. 236 and 240
[b] Ref. 235
[c] Ref. 237

with more modes would be small, because $Q_5, \cdots, Q_{24}$ vary little, if at all, from saddle point to the minimum. However, given that the difference with experiment is only roughly 0.016 cm^{-1}, additional coupling cannot be ruled out. Of course, some inaccuracy of the potential, in particular the barrier height, could be responsible for the residual difference. For $(DCOOH)_2$, the splitting is only slightly smaller than that of $(HCOOH)_2$ in accord with the small experimentally determined reduction to 0.0125 cm^{-1} for the ground state tunneling splitting of $(DCOOH)_2$. The calculated splitting for $(DCOOD)_2$ is roughly 0.0003 cm^{-1}, which is well within the experimental bound of less than 0.002 cm^{-1}.

The splitting of the excited states of HCOOH and comparison with the recent calculation by Jain and Sibert are presented in Table 8.5.

8.3.2   Anharmonic frequencies

To theoretically calculate the fundamental frequencies of FAD, I applied vibrational self-consistent-field and virtual-state configuration interaction (VSCF+VCI) method,[37] using the code "MULTIMODE".[38,39] The calculation used the minimum geometry as reference,

Table 8.5: Tunneling splittings (cm^{-1}) for a few excited states of FAD. (v_2, v_3) are the quantum numbers for Q_2 and Q_3.

(v_2, v_3)	This work			Ref. 262	
	E_{sym}	E_{asym}	ΔE	E_{sym}/E_{asym}	ΔE
$(0,0)$	0.000	0.031	0.031	0.000	0.0017
$(1,0)$	193.687	193.998	0.311	179.9	0.019
$(0,1)$	275.790	275.801	0.011	223.2	0.0080
$(2,0)$	386.109	387.596	1.486	359.6	0.080
$(1,1)$	469.118	469.115	-0.003	403.2	0.090
$(0,2)$	551.789	551.774	-0.015	446.8	0.023

since the barrier separating the two minima is quit high and the tunneling splitting cannot be resolved in most of the spectra. Full-dimensional calculations for the fundamental frequencies are not feasible, either, due to the large number of vibrational modes (24). Therefore, we performed the calculation in reduced dimensionality, and the same strategy was also applied in the calculation for the IR spectrum of H_7^+ and D_7^+. In brief, we solved the reduced-dimensional m-mode (with $m < 3N-6$) Schrödinger equation $\hat{H}(\boldsymbol{Q})\psi(\boldsymbol{Q}) = E\psi(\boldsymbol{Q})$ with zero total angular momentum, where $\hat{H}$ is the Watson Hamiltonian (Eq. 3.22 in Chapter 3), and $\boldsymbol{Q} = [Q_1 \cdots Q_m]$ denotes the m modes coupled in the calculation. The potential $V(\boldsymbol{Q})$ in the Hamiltonian is the full potential of FAD with the remaining modes fixed at zero.

Since here the spectrum in C–H and O–H stretching region is of interest, all the out-of-plane modes were not considered in the anharmonic calculation, and they were fixed at zero. Fifteen modes of the minimum were coupled in the calculation. These 15 modes are mode 4, 7, 8, and 13–24 (see the table above), and they belong to A_g and B_u symmetry of C_{2h} point group.

For this specific calculation of FAD, the potential is expressed in 4MR. (The termi-

nologies such as nMR, m-mode basis, MAXBAS, and MAXSUM have been described in Chapter 3) In the VSCF step, 23 harmonic basis functions were used for mode 4; 17 basis functions for mode 7 and 8; 15 basis functions for mode 13–20; and 13 basis functions for mode 21–24. In the VCI calculation, I used 4-mode basis, that is, 4 modes can be excited simultaneously. In the 1-mode basis, the MAXBAS is 14 for mode 4; 8 for mode 7 and 8; 6 for mode 13–20; and 4 for mode 21–24. In the 2-mode basis, the MAXBASs are 13, 7, 5, and 3 for mode 4, mode 7–8, mode 13–20, and mode 21–24, respectively. In 3-mode basis, the MAXBASs are 12, 6, 4, 2, and in the 4-mode basis, they are 11, 5, 3, 2. The MAXSUM is always 14 for 1-, 2-, 3-, and 4-mode basis. With all these restrictions, the size of the Hamilton matrix in two symmetry blocks are 94247 and 88805, respectively. The matrix size was reduced to 23270 and 23034 based on a perturbation test to eliminate the rows and columns of the matrices, which has been described in detail in Ref. 45 and 46

Table 8.6 presents the fundamental frequencies of the 15 modes from VSCF+VCI calculation and comparison with experiments and VPT2 calculation. For most of the modes, the anharmonic fundamental frequencies from VSCF+VCI and VPT2, and the experimental measurement agree well with each other. The VSCF+VCI results indicate that these modes don't have strong coupling with other modes, and in this situation, VPT2 is also capable to provide good frequencies. On the other hand, however, the C=O in-phase stretch, the two C–H (in-phase and out-of-phase) stretches and two O–H stretches couple strongly with other modes. For the in-phase C=O stretch, it couples with the combination mode of dimer stretch and C–O–H bend and the combination mode of dimer stretch and O=C–O bend overtone, and three VCI states are identified that contain large contribution from this mode. The O–H stretches are more complicated: for the asymmetric (out-of-phase) O–H stretch, three VCI states contain large contribution

Table 8.6:   Anharmonic fundamental frequencies (cm^{-1}) of FAD from VSCF+VCI calculations, and comparison with VPT2 calculation and experiments.

Mode	Symmetry	VSCF+VCI	VPT2 [b]	Experiments
4	A_g	208	199	194[c]
7	A_g	692	686	680[c]
8	B_u	703	720	698[d]
13	A_g	1248	1236	1214[e]
14	B_u	1234	1234	1230[d]
15	B_u	1365	1373	1364[d]
16	A_g	1374	1372	1375[e]
17	B_u	1407	1428	1454[d]
18	A_g	1455	1479	1415[e]
19	A_g	1638, 1647, 1682[a]	1644	1670[e]
20	B_u	1730	1738	1746[d]
21	A_g	2953, 2959, 2962[a]	2882	2949[e]
22	B_u	2943, 2959[a]	2872	2939[d], 2944[f], 2957[g]
23	A_g	2583, 2597[a]	2698	complex
24	B_u	2825, 2842, 2972[a]	2836	3000[f], 3084[c], 3110[g]

[a] Strong mixing
[b] B3LYP/VTZ, see Ref. 274
[c] Raman spectroscopy, see Ref. 248
[d] FTIR spectroscopy, see Ref. 246
[e] Raman spectroscopy, see Ref. 243
[f] IR spectroscopy, see Ref. 244
[g] Infrared spectroscopy, see Ref. 279

of this stretch; on the other hand, since the barrier of the proton transfer is only about 2900 cm^{-1}, the symmetric (in-phase) O–H experience large anharmonicity so that the fundamental frequency is about 2600 cm^{-1}.

8.4   Summary and Conclusions

A semi-global, full-dimensional potential energy surface for the formic acid dimer is presented. This PES utilizes high-level CCSD(T)-F12a electronic structure theory with haTZ basis set. The analytical potential is a linear least-squares fit to 13475 *ab initio* geometries and energies, using permutationally invariant polynomial basis, with weighted rms fitting error of 11 cm^{-1}. I demonstrate the accuracy and capability of this potential by applying it to calculate the tunneling splitting and anharmonic fundamentals of FAD. The best estimate of the tunneling splitting is about 0.0366 cm^{-1}, which is about twice as large as the experimental measurement. Nevertheless, the agreement between the theory and experiments is excellent. The tunneling splittings of a few excited states are also presented. I have performed VSCF+VCI using the global minimum as reference to calculate the anharmonic fundamental frequencies. For most of the modes, the calculation agrees with early VPT2 calculations as well as FTIR and Raman measurements. On the other hand, for C–H and O–H stretches, the calculations indicate that the mode-mixing is very strong, and further investigation of this region in the spectrum is necessary. For the symmetric O–H stretch (A_g), using minimum as the reference geometry may not be a correct choice, and a larger region of the PES, including two minima and the saddle point, has to be taken into account in the calculation.

Chapter 9

Vibrations of Methane Confined in Clathrate Cages

9.1 Overview

Vibrational spectroscopy is a valuable tool to investigate the properties of the methane clathrate hydrates, such as the structures, cage occupancies and hydrate composition. Raman spectroscopy has been applied to study the vibrational energies of the enclathrated methane molecule.[96,97,100,102,103,106,110] The symmetric stretch of the methane is Raman active, and its frequency red-shifts compared to the corresponding gas-phase one. Furthermore, the frequencies of methane in large cages ($5^{12}6^2$ and $5^{12}6^4$) are lower than the small cavity (5^{12}). Therefore, Raman spectroscopy has been used to identify the hydrate structures and the cage occupancies. A simple "tight cage and loose cage" model,[280] which was originally proposed to explain the frequency shifts of diatomic solutes due to interactions with liquid solvents, can be used to qualitatively explain the frequency shifts of the enclathrated methane. The IR spectrum of the methane stretching mode ex-

141

hibit substructure that resembles the gas-phase ro-vibrational lines, indicating that the trapped methane in the cage is a quasi rotor displaying gaseous behavior.[104] Later the IR spectrum of CH_4/CF_4 clathrate mixtures has been recorded to decipher the assignment of the stretching modes in different cages.[105] Since CF_4 always occupies the large cage, in the CH_4/CF_4 clathrate mixture, the absorption of methane in the large cage becomes weaker, and thus it can be distinguished from the absorption of the methane in the small cage. The authors discovered that the asymmetric stretching frequencies in the large $5^{12}6^2$ cage, similar to the symmetric stretch, are also lower than those in small 5^{12} cage. In addition, the spectrum for the overtones and combination modes of the trapped methane was also recorded and the transitions were assigned. The rotation-translation eigenstates of enclathrated guest methane were probed by inelastic neutron scattering.[139–145] The transitions between the three lowest rotational states are between 8 and 27 cm^{-1},[140] and translational excitations appear at higher energies;[143,145] however, the assignment of the peaks is complicated due to the lattice vibrations.

Theoretically, the intramolecular vibrations of enclathrated methane have been calculated using *ab initio* molecular dynamics simulations and Fourier transformation of the autocorrelation functions.[98,99,101,107,108] These simulations applied simple model potentials such as Kuwagai-Kawamura-Yokokawa[281] and consistent valence force field (CVFF)[282], or using density functional theory such as SIESTA[283] and Perdew-Burke-Ernzerhof (PBE).[284] These studies are able to reproduce the experimental trend of the frequency shift of the symmetric stretch but not quantitative agreement. In addition to molecular dynamics, the vibrations of confined methane has been investigated using direct harmonic normal mode analysis, applying model potential[285], or using computationally efficient method such as Hartree-Fock[86] and density functional theory.[86,88,111] As expected, the harmonic approximation can only achieve qualitative agreement with the experimental trend. It is

also worth noting that the "independent molecule model" in Ref. 285 is very similar to "local monomer model" (which has been described in Chapter 3) at the harmonic level. The translation-rotation energy levels of enclathrated methane molecule have been investigated via fully coupled six-dimensional quantum calculations, using a simple pairwise additive potential for methane-water interaction.[150] The calculated results for rotational and translational transitions agree with the experiments reasonably well. The angular anisotropy of the methane-cage interaction is exaggerated, and the translational fundamentals are underestimated, due to the deficiencies of the potential applied in the study.

However, the early investigations of the guest vibrations does not apply accurate potential energy surface (PES) for the methane hydrate. The potential was either evaluated by efficient low-level *ab initio* theories (for instance, density functional theory, Hartree-Fock or second-order Møllet-Plesset) or by assuming the methane-water interaction is pairwise additive. Furthermore, in calculations of the guest intramolecular vibrations, the methods applied are normal mode analysis or molecular dynamics, which are not able to account for anharmonicity or quantum effects. Therefore, more reliable results would be expected if accurate PES and rigorous method for vibrations were applied. In Chapter 5 I have presented full-dimensional PESs for clathrate hydrates using the many-body expansion form. In terms of vibrational calculations, vibrational self-consistent field (VSCF) and virtual state configuration interaction (VCI)[37] combined with "local monomer model"[48] is used here.

I employed the new many-body PES of $CH_4(H_2O)_n$ and perform local monomer quantum anharmonic calculations for the intramolecular vibrations of the guest methane in different clathrate cages. Specifically, the frequency of methane symmetric stretch has been calculated and compared to experimental Raman spectroscopy data, and the frequencies of asymmetric stretches, a few overtones and combination bands are reported.

Bending fundamentals are also given even though they have not been measured exper-
imentally. The vibrational ground state properties have been characterized by rigorous
quantum diffusion Monte Carlo (DMC) calculations. The binding energy of methane with
two cages is also presented.

9.2 Potential energy surface

The many-body potential of $CH_4(H_2O)_n$ is described in Chapter 5:

$$
\begin{aligned}
V_{CH_4(H_2O)_n} =& V_{CH_4}^{(1)} + \sum_i V_{H_2O(i)}^{(1)} + \sum_i V_{CH_4-H_2O(i)}^{(2)} + \sum_{i<j} V_{H_2O(i)-H_2O(j)}^{(2)} + \\
& \sum_{i<j} V_{CH_4-H_2O(i)-H_2O(j)}^{(3)} + \sum_{i<j<k} V_{H_2O(i)-H_2O(j)-H_2O(k)}^{(3)},
\end{aligned}
\tag{9.1}
$$

where $V^{(1)}$, $V^{(2)}$ and $V^{(3)}$ are monomer one-body, intrinsic two-body and three-body
energy, respectively. In the $CH_4(H_2O)_n$ potential, this expansion is truncated at three-
body level. As is suggested in the study of Deible et al.[190], the sum of the contributions
from higher-order terms is less than 10% of the binding energy of $CH_4(H_2O)_{20}$, and thus
these terms are dropped in our many-body potential.

The methane monomer potential is due to Yurchenko et al.[170] This potential is of
near-spectroscopic accuracy for methane vibrations. The fit "F-4211/5" (see Chapter 5)
is used for methane-water intrinsic two-body; however, additional 6463 points have been
added to the database to fix unphysical regions in the PES. The latest root-mean-square
(rms) fitting error is 4.1 cm^{-1}. The methane-water-water three-body potential is the one
labeled "PP-422111*/4" in Chapter 5, with a new database that contains 540 more points
to fix the unphysical region and to improve the harmonic frequencies of the clusters. The
rms fitting error now is 9.6 cm^{-1}.

These two particular fits are selected because they achieve good accuracy and computational efficiency. The remaining components are all included in the WHBB water potential,[28] which consists of spectroscopically accurate monomer potential,[169] CCSD(T)/aVTZ water two-body[178,179] and MP2/aVTZ three-body potentials.[27]
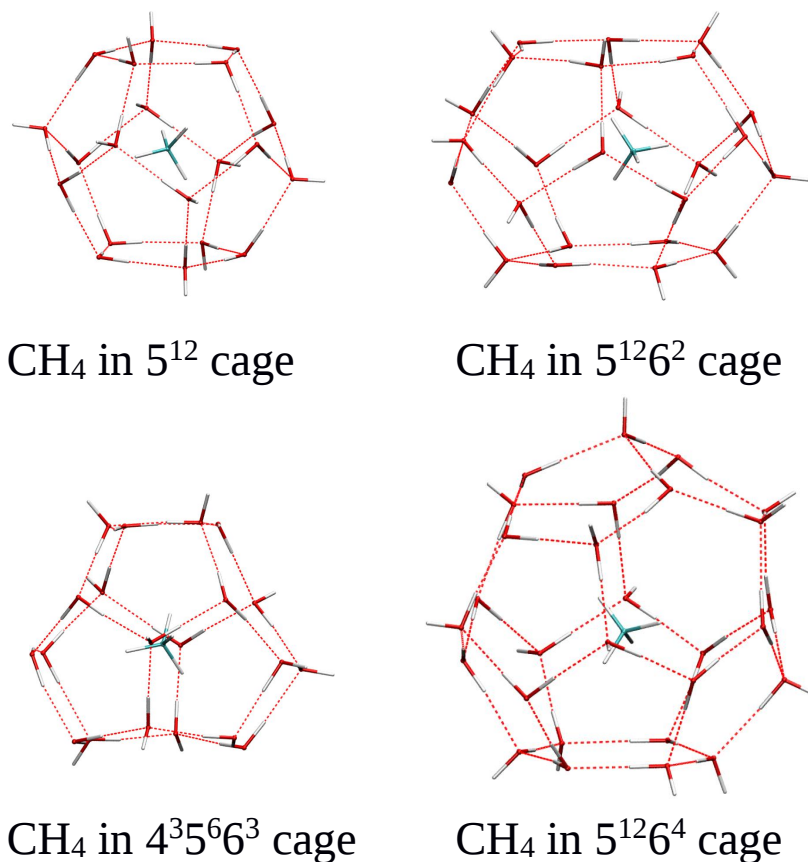
Figure 9.1:   The geometries of methane in four different cages.

The initial geometries of the isolated 5^{12} and $5^{12}6^2$ cages were extracted from the sI crystal structure reported in Ref. 67, while the isolated $5^{12}6^4$ and $4^35^66^3$ cages were

extracted from the Structure II and H in Ref. 85. The 5^{12}, $5^{12}6^2$, $5^{12}6^4$ and $4^35^66^3$ cages consist of 20, 24, 28 and 20 water molecules, respectively. The methane molecule was added to the cages and the geometries of these clusters were fully optimized using the analytical potential. The optimized geometries are shown in Figure 9.1.

9.3 Local monomer model

In this work, the intramolecular vibrations of methane are of interest, so the local monomer model is expected to work well, as the interaction between methane and the cage is weak. In this model, one monomer is treated at a time, but interacting with all the other monomers that are held fixed. This model has been explained in details in Chapter 3
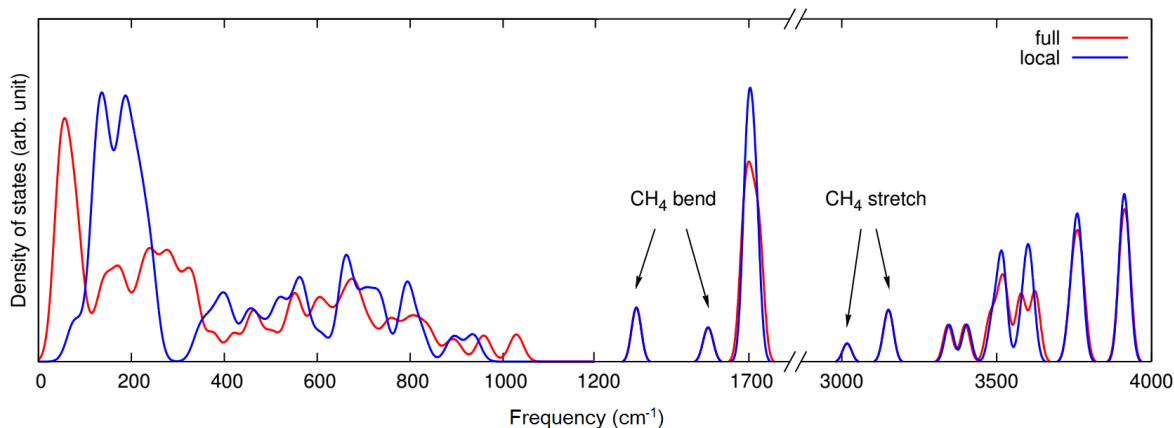
Figure 9.2: Vibrational density of states calculated at harmonic level using local monomer and full-dimensional normal mode analysis. The intramolecular vibrations of methane are labeled.

The accuracy of the local monomer model was investigated at the harmonic level by

comparing the result of local monomer normal mode analysis for $CH_4@(H_2O)_{20}$ to the full-dimensional one. In the local monomer approach, the computation of the monomer Hessian and the diagonalization was repeated for all the monomers (one methane plus twenty water molecules). In the full-dimensional normal mode analysis, the Hessian is 195×195, and 189 normal modes are obtained. Each mode can be represented using a stick with uniform height at the corresponding frequency, and each stick was replaced with a Gaussian function that has a standard deviation of 15 cm^{-1}. In this way I obtained smooth curves for the harmonic vibrational density of states. Figure 9.2 shows these for $CH_4@(H_2O)_{20}$, calculated with local monomer and full normal mode analysis. As expected, the local monomer model is not able to describe the low-frequency collective motions very well, as is shown by the fair to poor agreement between 0 and 1100 cm^{-1}. However, for the intra-monomer vibrations, the agreement between local monomer and full normal mode analysis is excellent, especially for the methane vibrations. Since in this work I mainly focused on the intramolecular vibrations of methane, the good agreement between local monomer and full normal mode analysis in this region is very encouraging. A detailed comparison for these modes is given in Table 9.1 for four cages. The isolated gas-phase results are also given. The agreement between the local and full normal mode analysis is excellent, with the deviations for each mode no larger than 1 cm^{-1}. In addition, it is obvious that the degeneracy in the gas phase splits in the cages, due to the anisotropy of the methane-cage interaction. Note that due to the smoothing procedure, this splitting is not resolved in Figure 9.2. Finally, the harmonic frequencies of the symmetric stretch (ω_1) in four cages is lower than that of gas phase, and those in larger cages ($5^{12}6^2$ and $5^{12}6^4$) are more red-shifted, which agrees with the experimental trend.

Table 9.1: Harmonic frequencies (cm^{-1}) of CH_4 confined in the four indicated cages, calculated by local monomer and full (in parenthesis) normal mode analysis, as well as the values of gas-phase methane calculated using the *ab initio* monomer PES of reference 170.

Mode [a]	5^{12}	$5^{12}6^2$	$4^35^66^3$	$5^{12}6^4$	gas
ω_4	1332 (1332)	1335 (1336)	1327 (1328)	1335 (1335)	1347
	1336 (1337)	1340 (1340)	1341 (1342)	1338 (1338)	1347
	1342 (1343)	1345 (1345)	1346 (1347)	1351 (1352)	1347
ω_2	1562 (1562)	1567 (1567)	1566 (1566)	1568 (1568)	1574
	1575 (1574)	1570 (1569)	1570 (1569)	1572 (1572)	1574
ω_1	3017 (3017)	3009 (3009)	3016 (3016)	3007 (3007)	3037
ω_3	3142 (3142)	3127 (3127)	3143 (3143)	3121 (3121)	3156
	3152 (3152)	3139 (3139)	3145 (3145)	3133 (3133)	3156
	3156 (3156)	3144 (3144)	3147 (3147)	3151 (3151)	3156

[a] The modes are labeled using standard gas-phase spectroscopic notation.

9.4   VSCF+VCI calculations

To go beyond the harmonic approximation, the nuclear Schrödinger equation of the embedded methane monomer, m:

$$\left[\hat{T}_m + \hat{V}_m(\vec{Q}_m)\right]\psi_m(\vec{Q}_m) = E\psi_m(\vec{Q}_m). \tag{9.2}$$

is solved. In the equation, $\vec{Q}_m$ is the set of nine intramolecular local normal modes of methane, obtained from local normal mode analysis. $\hat{T}_m$ is the kinetic energy operator (with vibrational angular momentum terms included), and $\hat{V}_m(\vec{Q}_m)$ is the full potential of methane, perturbed by the water cage, and it depends dynamically on the nine local normal modes of methane, with all the water molecules frozen.

To solve this Schrödinger equation, the VSCF+VCI approach was applied, using the code MULTIMODE. In brief, in the VSCF calculation, the total vibrational wave function

is given by a single direct product of one-mode functions, and these one-mode functions are optimized via the self-consistent field procedure. The solutions give the VSCF ground state and virtual states. In the VCI calculation, the VSCF ground state and excited, virtual states are used as basis functions to calculate the Hamiltonian matrix. The states obtained by diagonalizing the Hamiltonian matrix are eigenstates of the system, and they are labeled by the dominant VSCF virtual state.

The VSCF+VCI calculation was first applied to isolated methane to test the convergence of our calculation with respect to the excitation space chosen in the VCI. We employed an efficient 4MR for the potential. The maximum excitations are 11, 10, 9, 8 for the five bending modes and 9, 8, 7, 6 for the four stretching modes in 1-, 2-, 3- and 4-mode basis, respectively, and the maximum sum of quanta is 11. The four fundamentals calculated are 1311, 1534, 2917 and 3021 cm^{-1}. These are in very good agreement with the corresponding converged variational values of 1311, 1533, 2916 and 3019 cm^{-1},[170] which in turn are in good agreement with experiment, 1306, 1534, 2917 and 3019 cm^{-1}. The same numerical parameters were used in local monomer calculations of methane in four cages. The CI matrix size is 55848. The size of the matrix can be reduced, based on a perturbation test to eliminate the rows and columns of the matrix. The details of this strategy have been described in Ref. 45 and 46 as well as Chapter 3. The reduced matrix size is roughly 14000. I employed the iterative block-Davidson method[286] to obtain eigenvalues and eigenvectors, since I was only interested in several hundred eigenstates.

9.4.1   Fundamental frequencies

Table 9.2 lists the calculated anharmonic frequencies of the symmetric stretch of methane in four cages, as well as experimental results from Raman spectroscopy[96,106] and the

recent calculation using Car-Parrinello molecular dynamics (CP-MD).[108] As seen, the frequencies from different experiments agree well, except for the $4^35^66^3$ cage. In the early experiment by Sum et al.[96], the frequency of symmetric stretch in this cage is close to that in two larger cages; on the contrary, a recent experiment[106] suggests that the frequency in the $4^35^66^3$ cage is only slightly lower than that in the 5^{12} cage. In our calculation, the anharmonic frequency of the symmetric stretch of methane in $4^35^66^3$ is only 1 cm^{-1} lower than that of 5^{12} cage, and the trend is in agreement with the more recent experiment. The overall agreement with experiment is very good; however, there appears to be systematic underestimation of the frequencies by about 10 cm^{-1}. The difference between the theory and experiments may due to the accuracy of the PES (such as the level of *ab initio* calculations, the lack of methane-water four-body or even higher order interactions), the limitation of the local monomer model (no coupling between methane and lattice vibrations and no coupling with frustrated translations and rotations of methane), and the model systems we applied in the calculation (isolated cages without inclusion of more water molecules and the order of the protons in hydrogen bond network). Nevertheless, the level of accuracy of the current calculations is well beyond previous calculations, such as the CP-MD.

The calculated fundamentals of asymmetric stretches of methane in sI cages (5^{12} and $5^{12}6^2$), as well as the recent CP-MD results, are shown in Table 9.3. However, the assignment of transitions in the experimental Fourier transform infrared spectrum (FTIR) is challenging due to relatively low resolution,[104,105] as the methane absorption overlaps with low wavelength wing of the ice feature, as well as the splitting of the asymmetric stretches caused by anisotropic crystal field. The asymmetric stretch of methane in $5^{12}6^2$ cage is at about 3000 cm^{-1}, while that of methane in 5^{12} cage is at about 3016 cm^{-1}. Our calculations give three frequencies for asymmetric stretches, and those in 5^{12} cage

Table 9.2: Anharmonic frequencies (cm^{-1}) of methane symmetric stretch in four cages calculated by MULTIMODE, and comparison with Raman spectra and CP-MD simulation.

Cage	MULTIMODE	Raman		CP-MD
5^{12}	2902	2914 [a,b]	2915 [a,c]	2876 [d], 2879 [e]
$5^{12}6^2$	2893	2901 [b]	2905 [c]	2865 [d]
$4^35^66^3$	2901	2910 [b]	2905 [c]	2875 [e]
$5^{12}6^4$	2888	2902 [b]	2904 [c]	

[a] 5^{12} cage of structure I;
[b] Ref. 106;
[c] Ref. 96;
[d] 5^{12} cage of structure I from Ref. 108;
[e] 5^{12} cage of structure H from Ref. 108.

is higher, which agrees with the experiment. The difference between our calculation and experiment is again about 10 cm^{-1}.

Table 9.3: Anharmonic frequencies (cm^{-1}) of methane asymmetric stretches in four cages calculated by MULTIMODE, and comparison with FTIR and CP-MD simulation.

Cage	MULTIMODE	FTIR	CP-MD
5^{12}	3010, 3021, 3027	$\sim$3016 [a]	2979 [b]
$5^{12}6^2$	2994, 3007, 3014	$\sim$3000 [a]	2963 [b]

[a] Ref. 104 and 105;
[b] Ref. 108

In recognition of the fact that methane exhibits large-amplitude angular motion in the cages (see below), I performed addition VSCF+VCI calculations for five randomly selected orientations of methane in the 5^{12} and $5^{12}6^2$ cages. The geometries of the cages were kept the same as the minima, and the orientation of the methane was randomly

sampled. All the parameters in the VSCF+VCI calculations are kept the same. Table 9.4 summarizes the frequencies of the symmetric stretches at different orientations and the corresponding energies of that particular orientation. The small variation of the frequency (about 20 cm^{-1}) at different orientations indicates that the angular anisotropy of the methane-cage interaction is small but not negligible. A correlation exist between the frequency of the stretching mode and the energy, and the general trend is that higher frequency corresponds to the orientation with higher energy.

To get an estimate of the average frequency when the orientation is considered, we calculated the "thermal-averaged" frequencies for methane in these two cages, with each frequency weighted by the Boltzmann factor $\exp(-\beta\Delta V)$. Two temperatures are chosen, corresponding to the temperatures in two experimental measurements: 100 K according to the experiment by Ohno et al.[106]; 270 K from the experiment by Sum et al.[96]. At 100 K, the average frequencies in the 5^{12} and $5^{12}6^2$ cages are 2902 and 2894 cm^{-1}, respectively. They are only 0 – 1 cm^{-1} higher than the frequencies of the minimum orientation. However, at 270 K, the average frequencies in two cages become 2909 and 2896 cm^{-1}, which shift towards the experimental values, and are 7 and 3 cm^{-1} higher than those of the minimum. The temperature dependence may be responsible for the slight difference in the two measurements. In fact, the experiment at lower temperature (100 K) reported slightly lower frequencies than those from the measurement at 270 K; our calculation also predicts this trend. Of course we are aware that this thermal average approach is not a rigorous analysis. On the one hand, only five random orientations are not sufficient to sample all the possible orientations; on the other hand, averaging with a Boltzmann weight is not rigorous (though should be a good approximation at these two temperatures) here. However, qualitatively, this averaging approach illustrates the trend of the up-shift of the frequency when the rotational delocalization of the confined

methane is taken into account.

Table 9.4: Frequencies (cm^{-1}) of methane symmetric stretches in 5^{12} and $5^{12}6^2$ cages at six orientations (including the minimum), and the corresponding energies (cm^{-1}) of each orientation.

orientation	5^{12} cage		$5^{12}6^2$ cage	
	freq.	energy	freq.	energy
min	2902	0	2893	0
1	2917	392	2894	66
2	2919	288	2898	212
3	2919	350	2899	148
4	2919	396	2910	585
5	2924	511	2914	685

In addition to the symmetric and asymmetric stretches of the confined methane, our calculations also provide fundamental frequencies of the bending modes, which haven't been measured experimentally. These frequencies are reported in Table 9.5. As expected, these results show splittings relative to isolated methane, where mode 2 is doubly degenerate and mode 4 is triply degenerate (see, Table 9.1.) These results are of further interest, as there are experimental measurements of overtones and combination bands involving these modes. These are discussed next.

9.4.2 Overtones and combination bands

Some overtones and combination bands of methane in sI clathrate hydrate have been measured in Raman[102,103,110] and FTIR[105]. In the Raman spectrum, the band at about 2570 cm^{-1} is assigned to the overtone of the bend ($2\nu_4$), and the band at about 3050 cm^{-1} to the overtone of asymmetric bending ($2\nu_2$). In FTIR, the absorption up to 6000

Table 9.5: Fundamental frequencies (cm^{-1}) of CH$_4$ bending modes in four cages, calculated by MULTIMODE.

Mode [a]	5^{12}	$5^{12}6^2$	$4^35^66^3$	$5^{12}6^4$
ν_4	1332	1335	1327	1335
	1336	1340	1341	1338
	1342	1345	1346	1351
ν_2	1562	1567	1566	1568
	1575	1570	1570	1572

[a] The modes are labeled using standard gas-phase spectroscopic notation.

cm^{-1} has been assigned, and particularly, the $\nu_1 + \nu_4$ and $\nu_3 + \nu_4$ combination mode of methane in small and large cages has been distinguished by tuning the CH$_4$/CF$_4$ ratio in the mixed clathrate. In these two combination modes, the frequencies in the small cage are also 10 to 20 cm^{-1} higher than in the large cage, as is the case for the CH$_4$ stretches.

Table 9.6: Energies (cm^{-1}) of some overtones and combination modes calculated by MULTIMODE, and comparison with experiments. The "s" and "l" in the parenthesis indicate the small or large cage.

Transition	Theory	Experiment
$2\nu_4$	2575–2617 (s), 2579–2625 (l)	~2570 [a]
$2\nu_2$	3052–3074 (s), 3056–3061 (l)	~3050 [a]
$\nu_1 + \nu_4$	4195, 4198, 4205 (l)	4188, 4193, 4197 (l) [b]
	4201, 4207, 4212 (s)	4201, 4207, 4211 (s) [b]
$\nu_3 + \nu_4$	4301–4333 (s), 4286–4326 (l)	4312–4332 (s), 4284–4303 (l) [b]
$\nu_2 + \nu_3$	4529–4562 (s), 4516–4542 (l)	4507–4540 [b]

[a] Raman, Ref. 102 and 110
[b] FTIR, Ref. 105.

Table 9.6 shows the comparison between the results from our calculations and experi-

mental measurements. Due to the splitting caused by the anisotropy of the environment, our calculation can predict the energies of states that were not resolved by the FTIR experiments. For certain transitions such as $2\nu_4$, due to this splitting, as many as nine frequencies can be associated to it within a relatively small energy range; therefore we only present the range in this paper instead of listing all the frequencies explicitly. For the two overtones, the experimental values are very close to, but slightly outside our calculated lower bounds. For the combination modes, our calculation agrees with the FTIR results very well.

9.5   Diffusion Monte Carlo calculations

The diffusion Monte Carlo method was applied to study the zero-point properties of the confined methane molecule. Due to the computational cost, treating the methane and the water cage in full dimensionality is not feasible. However, since the interaction between the confined guest molecule and the water cage is relatively weak, we fixed the water cage, and treat explicitly the confined methane molecule in full dimensionality (15-dimensional). Thus, the calculations characterize the vibration-translation-rotation motion of the enclathrated methane molecule.

In the DMC simulations, the simple unbiased algorithm described in Ref. 58 and Chapter 3 of this work was applied. These calculations were done for the four cages. For each cage, five simulations were performed, and in each 20000 walkers were propagated for 30000 steps with step size, $\Delta\tau$, of 5.0 au. The walkers were first equilibrated for 10000 steps, and then the reference energy was collected. It is worth noting that the simulation is still very expensive, as about 10^9 potential evaluations are needed per simulation, and each potential evaluation requires 20 to 28 methane-water two-body and 190 to 378

methane-water-water three-body potential evaluations. The most time-consuming step is to evaluate the three-body potential, and our "PP-422111*/4" potential is efficient enough to allow such simulations. In fact, a single simulation of the $CH_4@(H_2O)_{20}$ (the smallest system) still takes about four days of CPU time on a sixteen-processor computer, and the $CH_4@(H_2O)_{28}$ takes about nine days.

The nuclear wave functions of methane, represented as isosurfaces, are shown in Figure 9.3. The isovalue is 40% of the maximum wave function amplitude in all the figures. The ball-and-stick models in the figures represent the minimum geometries of these four isolated clusters, while the "clouds" represent the nuclear wave functions. Since the coordinates of water cages were always fixed during a simulation, the nuclear wave function can be obtained by simply superimposing the walkers from the simulation. Compared to the VCI calculation, which was restricted to the nine intra-molecular vibrations, the DMC nuclear wave functions provide additional information on the translations and hindered rotations of methane in the cage. It can be clearly seen that the wave functions of methane in the large cages are more extended than those in the small cage. For example, the wavefunction of methane in the $5^{12}6^2$ cage is extended along the long axis of the cage. (This can be clearly seen by comparing the wavefunctions of the carbon atom.) This agrees with the fact that the one-dimensional potential cut along this axis is looser than the small cage. In addition, note that we start to see the delocalization of the hydrogen wave function at 40% of the maximum amplitude. Though we did not quantify the hindered-rotor barrier heights, the random sampling of orientations suggests that the barrier height is on the order of hundreds of wavenumbers (see Table 9.4).

The vibration-translation-rotation ZPEs of the confined methane in the two cages are reported in Table 9.7. Thus, the measurable dissociation energy (D_0) of methane in the cages can be estimated. First, the electronic dissociation energy (D_e) was calculated as
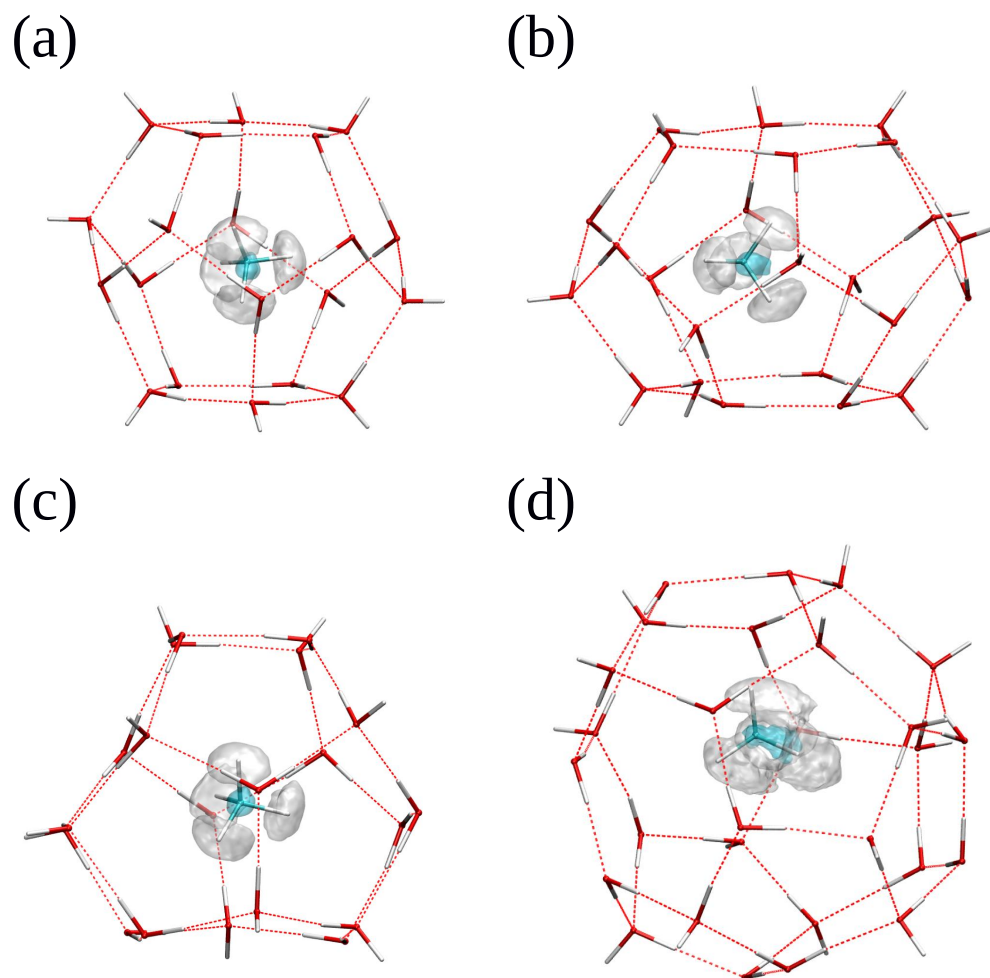
Figure 9.3: Ground state nuclear wave function of methane in 5^{12}, $5^{12}6^2$, $4^35^66^3$ and $5^{12}6^4$ clathrate cages.

the energy difference between $CH_4@(H_2O)_n$ cluster and the isolated cage plus methane. Then the D_0 was estimated using

$$D_0 \approx D_e - ZPE_{V\text{-}T\text{-}R} + ZPE_{CH_4}, \tag{9.3}$$

where $ZPE_{V\text{-}T\text{-}R}$ is the ZPE of the vibration-translation-rotation motion, and ZPE_{CH_4} is the vibrational ZPE of gas-phase methane. The latter was calculated in two approaches. One approach was DMC simulations on an isolated methane molecule, and the ZPE is 9701 ± 2 cm^{-1}; the other was quantum VSCF+VCI calculation using MULTIMODE, and the ZPE calculated is 9702 cm^{-1}. Both methods are rigorous for methane, and the results agree with each other. Therefore, our estimates of D_0 for methane in 5^{12} and $5^{12}6^2$ are 5.55 and 5.42 kcal/mol, respectively.

In addition to the total vibration-translation-rotation ZPEs and the dissociation energy, the vibrational ZPEs of the confined methane were calculated using local monomer VSCF+VCI, and the results are shown in Table 9.7. Therefore, we were able to estimate the ZPE of the translation-rotation motions, by calculating the difference between the ZPEs of the vibration-translation-rotation motions and the vibrational ZPEs. These values are also listed in the table. Matanović et al.[150] have performed rigorous six-dimensional quantum calculations for translation-rotation eigenstates of methane in these two cages, though with approximate pairwise additive potential for the CH_4-cage interaction. They reported the ZPEs of the translation-rotation motions in two cages as 165.2 and 107.0 cm^{-1}, respectively. Our results are about 120 cm^{-1} higher, but the difference in the ZPEs for two cages is about the same. The difference between these previous and the present calculations results from the different potentials used and the different geometry of the cages. The results of translation-rotation motions in $4^35^66^3$ and

$5^{12}6^4$ cages are also given in the table.

Table 9.7:   The vibration-translation-rotation ZPE (denoted V-T-R ZPE), vibration-only ZPE (denoted Vib ZPE), the difference (denoted T-R ZPE) (cm^{-1}) for methane in four cages, and the electronic and physical dissociation energy (kcal/mol) of $CH_4@(H_2O)_{20}$ and $CH_4@(H_2O)_{24}$. The vibrational ZPE of gas-phase methane is also shown.

Cage	V-T-R ZPE	Vib ZPE	T-R ZPE	D_e	D_0
5^{12}	9961±3	9671	290±3	6.29	5.55
$5^{12}6^2$	9877±2	9648	229±2	5.92	5.42
$4^35^66^3$	9924±3	9664	260±3		
$5^{12}6^4$	9850±3	9645	205±3		
gas	-	9702	-	-	-

9.6   Summary and conclusions

The PES for methane clathrate I developed has been applied to calculate the intramolecular vibrations of enclathrated methane. These are nine-dimensional, local monomer quantum calculations that couple all the intramolecular vibrational modes of methane. The calculations employed the VSCF+VCI approach and were performed using the code MULTIMODE. For the symmetric stretch of confined methane, my calculations reproduce the same experimental trend that the frequency in the small cage is higher than that in the large cage. The absolute frequencies of the symmetric stretch in different cages were only underestimated by about 10 cm^{-1}. For the symmetric stretches, overtones and combination modes, the VSCF+VCI calculations also agree with experiments well. This suggests that the accuracy of the PES is good, and "local monomer" approximation is adequate to capture the dynamics of intramolecular vibrations of confined methane.

Diffusion Monte Carlo calculations were performed on methane in rigid cages to characterize the zero-point properties of the vibration-translation-rotation of methane confined in these cages. The nuclear wave functions obtained in the DMC simulations suggest that the methane molecule confined in the cages could tunnel through the hindered-rotor barriers, which agrees with early findings. With the ZPEs calculated from DMC and MULTIMODE, I estimated the D_0 for methane in 5^{12} and $5^{12}6^2$ to be 5.55 and 5.42 kcal/mol, respectively, and the ZPEs of translation-rotation motions in the two cages to be 290 and 229 cm^{-1}.

Having verified the accuracy of our potential for $CH_4(H_2O)_n$ system, future work will involve the application of this PES to investigate more properties of the methane hydrates. For instance, the translation-rotation motion of confined methane in the water cage and the lattice vibrations. The temperature dependence of properties could also be studied, when thermodynamics approaches are incorporated in the simulations using the PES.

Part IV

Dynamics in Gas-phase Molecules

Chapter 10

Thermal Decomposition of Methanol

10.1 Overview

The rovibrational spectroscopy of methanol has been the subject of numerous experimental[287–294] and theoretical[42,295–303] works, with a focus on the facile internal torsional motion. Signatures of that motion in the vibrational spectrum of the fundamentals and overtones of the CH and OH-stretch modes have reported in recent experiments. It is a challenging system for theoretical approaches, owing both to the dimensionality of the configuration space (12 degrees of freedom) and also the need to accurately describe the low-barrier torsional motion. High-level theoretical work on the vibration/torsion energies of methanol has made use of *ab initio*-based force fields and potential energy surfaces (PESs).[42,299–303] The most recent of these[42] is a fit to electronic energies obtained using CCSD(T) theory with aug-cc-pVTZ (aVTZ) basis. This PES has been employed in MULTIMODE-reaction path calculations[42,303] of low-lying vibration/torsion energies, which are in good agreement with experiment.

However, these force field and PESs do not describe dissociation or near dissociation

162

of any fragments. The thermal decomposition of methanol and the recombination of the fragments are important precesses in combustion chemistry and therefore has been studied over a range of temperatures and pressures for several decades in both experiments and theoretical calculations.[304–315] Recent work can be found in Ref. [316–331]. Methanol is also widely found in the interstellar medium and its mechanism of formation is still a subject of discussion.[332,333]

The thermal decomposition of methanol involves several reaction channels, including $CH_3 + OH$, $^1CH_2 + H_2O$, $H_2 + H_2CO$, $H_2 + cis/trans-HCOH$, $H + CH_2OH$, $H + CH_3O$, etc. Based on most of the experimental and theoretical work, the main product channel is the $CH_3 + OH$. High-level theoretical modeling of the thermal decomposition and recombination of methanol has been reported by a number of groups, including variational RRKM study of the rate constants using G2M[334] *ab initio* theory,[316] (variational) RRKM theory with CCSD(T) energetics,[317,318] MRCI characterization of the stationary points on the PES and *ab initio* molecular dynamics simulations,[319] and transition state theory combined with QCISD(T) energetics.[322] However, these theoretical works are all based on the characterization of the stationary points on the PES. Therefore, the goal here is to construct a full-dimensional, analytical PES that describes the bound region as well as the dissociation channels. It should be noted that a model, empirical potential has been reported for $CH_3 + OH$ recombination and used in quasiclassical trajectory calculations.[327] Yet the properties of the bound region of the PES were not reported and evidently were not included in that work. Thus, the description of CH_3OH is certainly below the level needed for spectroscopic analysis. Very recently, a full-dimensional PES was reported,[331] which is a permutationally invariant fit to about 340000 electronic energies calculated by the MRCI+Q/aVTZ level of theory. [1]

---

[1]The work presented in this chapter was done nearly at the same time of this reference.

In this chapter, I present the full-dimensional PES of methanol I have constructed, and the molecular dynamics simulations to model the thermal decomposition of CH_3OH using this PES. Some of the reaction channels, such as $CH_3 + OH$ and $H + CH_2OH/CH_3O$, are challenging for electronic structure theory, due to the multi-reference character. These will be discussed in the following sections.

10.2   Potential Energy Surface

The construction of this PES generally follows the procedures described in Chapter 2. A schematic of the PES is shown in Figure 10.1, with all the stationary configurations labeled. The PES can describe six dissociation channels.

10.2.1   Sampling of configuration space

The structures of the stationary points (minimum, T-TS, TS1–4) were optimized using CCSD(T)-F12b/aVDZ level of theory. The complete database consists of geometries in the following four subsets. The first set of geometries came from *ab initio* molecular dynamics simulations using DFT/B3LYP, which were initiated from the transition states. These geometries mostly describe the regions that connect the minima and saddle points. The second subset consists of the 19315 geometries from the previous PES[42]. This subset focuses on the bound region of methanol and the barrier of the CH_3 torsion. The third subset contains fragment data in dissociation channels. For each channel, the configurations of each fragment were sampled using direct dynamics, and the two fragments were combined with different separations (the distance between two center-of-mass) and different orientations. The last subset was obtained by running diffusion Monte Carlo and molecular dynamics simulations to locate the un-physical regions of the PES. The
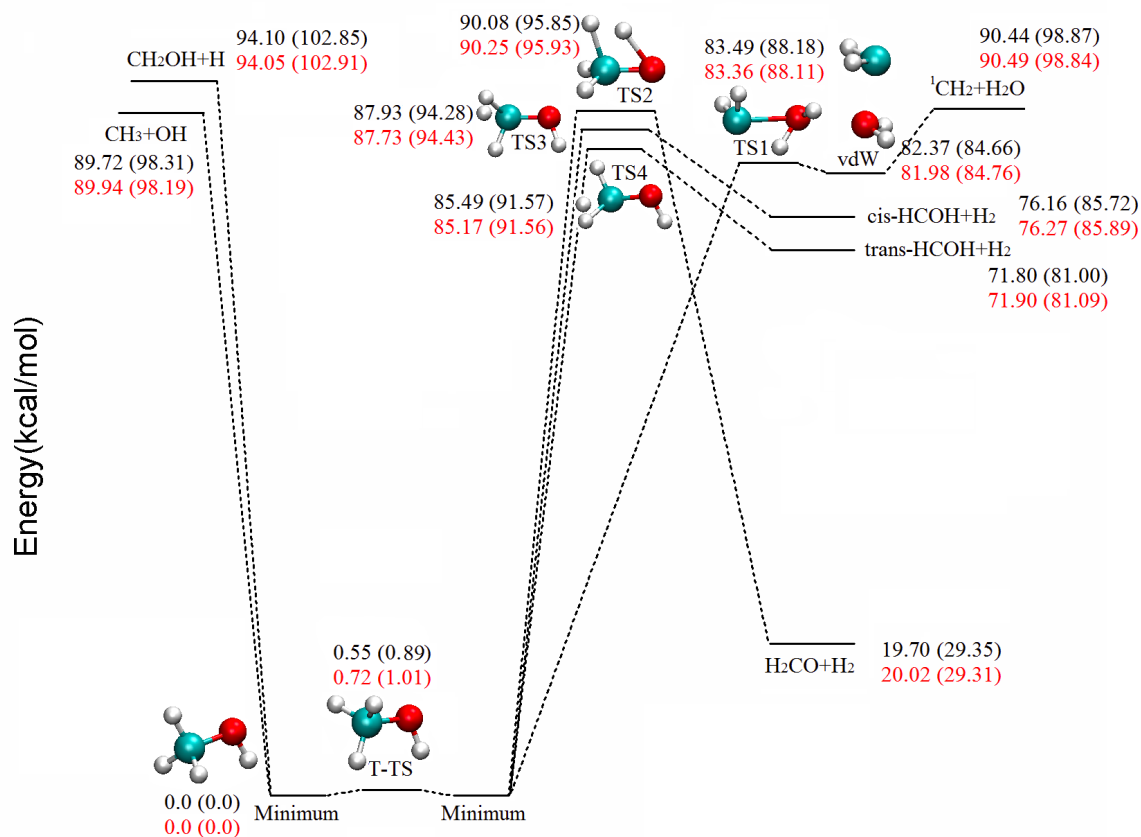
Figure 10.1: Schematic of the methanol potential energy surface. The energies from CCSD(T)-F12b/aVDZ (red) and the fitted PES (black) with or without (in parenthesis) harmonic zero-point correction are also shown.

total number of configurations in the database is 181765.

10.2.2   Ab initio calculations and potential fitting

As mentioned, some of the channels are challenging for electronic structure calculations due to the multireference character. For example, Figure 10.2 shows two cuts for increasing R_{CO} using CCSD(T)-F12b and MRCI theory. It is clear that in this case CCSD(T)-F12b starts to fail when the C-O distance reaches 5 Bohr, and the T_1 diagnostic becomes large.
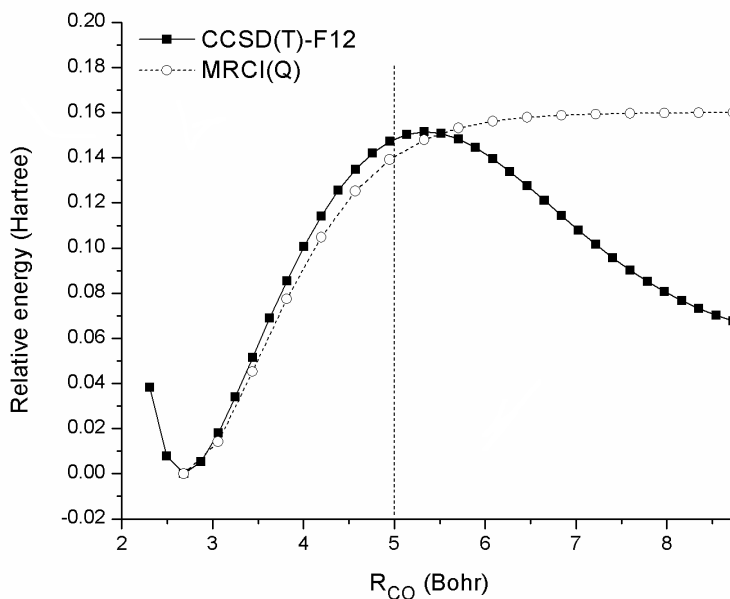
Figure 10.2: Comparison of CCSD(T)-F12b and MRCI cuts for $CH_3OH \rightarrow CH_3 + OH$

However, given the large computational expense of high-level multi-reference methods and the fact that the PES is dominated by closed-shell electronic configurations, I

undertook a hybrid approach for the PES. For geometries for which a single-reference method is valid, I employed the CCSD(T)-F12b/aVDZ method.[32,33] For geometries in the multi-reference region (where the T_1 diagnostic of CCSD(T)-F12b is larger than 0.02), I employed CASPT2/aVDZ. The single-state CASPT2 calculations used CASSCF with 10 active electrons and 10 active orbitals (CAS(10,10)) as the reference, and the energy of the lowest state was calculated. Here CASPT2 was employed for the multi-reference region instead of MRCI because generally the results from the two methods are quite close for methanol, but the cost of a CASPT2 calculation is much less than an MRCI one (3 minutes per point using CASPT2 vs. 1 hour per point using MRCI). CCSD(T)-F12b calculations were also done for the non-interacting, separated fragments, which individually can be treated by this method (however, unrestricted coupled-cluster, UCCSD(T), should be used for some fragments). Therefore, this PES does not describe the long-range interaction between the fragments correctly, but this error is small compared to the energy scale of this PES, as most of the transition states and the dissociation channels are 70–100 kcal/mol above the CH_3OH minimum. All the coupled-cluster calculations were performed using the software MOLPRO 2008,[335] and the CASPT2 calculations were carried out using MOLCAS Version 7.8.[336–338]

However, there are several issues using this hybrid CCSD(T)-F12b/CASPT2 approach to generate data for the fit. Firstly, the absolute energy from the two methods are different; therefore, a shift to the CASPT2 ones must be applied so that they are compatible with the CCSD(T) ones. This is done by shifting the CASPT2 energies by the difference between CCSD(T)-F12b and CASPT2 energies at the dissociation limit (with the fragments at their equilibrium). Secondly, in the regions of the PES where the CCSD(T)-F12b theory is applicable, those energies, which dominate the dataset, are more accurate than corresponding CASPT2 ones.

The PES is a least-squares fit to all the *ab initio* energies in the database. The fit is permutationally invariant with respect to the exchange of H atoms. The maximum fitting order is six, leading to 3338 linear coefficients. In this fit, a weight was assigned to each data point, depending on the energy of each point. The weight is given by $0.25/(0.25+\Delta E)$, where ΔE is the energy relative to the global minimum in Hartree. The weight of CASPT2 energies was further lowered by a factor of 0.6 because the energies obtained by shifting CASPT2 ones are not as accurate as the CCSD(T)-F12b ones.

10.2.3   Properties of the potential energy surface

The overall root-mean-square (rms) fitting error of the PES is 606 cm^{-1}. The relation between the rms fitting error and energy (relative to the minimum) and the number of points that are below that energy is shown in Figure 10.3. The number of configurations grow rapidly between 30000 and 50000 cm^{-1}, and there are about 120000 configurations in this energy range. That's because most of the dissociation channels and the transition states have energies in this range. The rms fitting error increases almost linearly as a function of the energy cut-off.

The structures and the energies of the stationary points corrected with harmonic zero-point energy (ZPE) are also presented in Figure 10.1. In addition, I present the electronic energies in parenthesis. The values in red are CCSD(T)-F12b/aVDZ energies computed with MOLPRO, and the values in black are energies from the PES. One can see good agreement between the PES and *ab initio* energies for the stationary points and the dissociation channels.

Normal mode analyses were carried out at all stationary structures. The harmonic
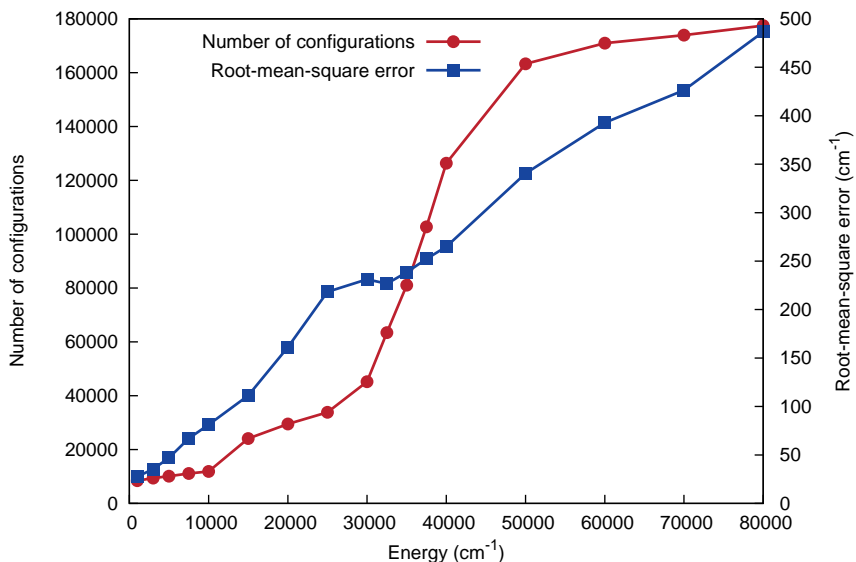
Figure 10.3:   Number of points and rms error of the methanol PES below each energy.

frequencies and ZPE obtained in *ab initio* calculations (CCSD(T)-F12b/aVDZ) and from the PES are presented in Table 10.1–10.3. In general, these harmonic frequencies are in good agreement with CCSD(T)-F12b results.

To further test the fidelity of the PES from the bound region to dissociation, I show 1-D cuts of the PES in different dissociation channels. Figure 10.4 shows six cuts in the $CH_3 + OH$ channel at different CH_3 and OH orientations, as a function of the C-O distance. The CCSD(T)-F12b, CASPT2, and MRCI energies along these cuts are also shown in the figure. Several points can be made from these plots. Firstly, in the multi-reference region (in general, R_{CO} between 4 and 9 Bohr), the PES faithfully represents the CASPT2 energies, for a large range of fragment orientation angles. In the strongly attractive region, the PES agrees well with direct calculated CCSD(T)-F12b energies; however, the CASPT2 and MRCI energies do not agree well with the coupled-cluster ones. This is not surprising due to the limited accuracy of these method, at least in the

Table 10.1: Comparison of harmonic frequencies (in cm^{-1}) of the minimum and T-TS of methanol calculated by CCSD(T)-F12b/aVDZ level of theory and the PES.

Mode	Minimum		T-TS	
	PES	*ab initio*	PES	*ab initio*
1	282	289	278i	285i
2	1055	1064	1044	1069
3	1084	1090	1057	1100
4	1182	1178	1196	1192
5	1409	1381	1425	1366
6	1483	1481	1473	1488
7	1504	1505	1519	1499
8	1531	1515	1530	1527
9	3022	3013	3030	3030
10	3057	3072	3090	3101
11	3138	3133	3105	3106
12	3908	3865	3948	3902

Table 10.2: Comparison of harmonic frequencies (in cm^{-1}) of TS1 and vdW calculated by CCSD(T)-F12b/aVDZ level of theory and the PES.

Mode	TS1		vdW	
	PES	*ab initio*	PES	*ab initio*
1	937i	870i	10	44
2	262	371	334	353
3	384	446	713	646
4	869	738	743	668
5	1037	991	1116	1101
6	1150	1097	1207	1153
7	1403	1406	1408	1402
8	1598	1543	1811	1670
9	2726	2701	2961	3943
10	2995	3031	3028	3010
11	3096	3121	3867	3783
12	3854	3820	3891	3868

Table 10.3:   Comparison of harmonic frequencies (in cm^{-1}) of the TS2, TS3, and TS4 calculated by CCSD(T)-F12b/aVDZ level of theory and the PES.

Mode	TS2 PES	TS2 ab initio	TS3 PES	TS3 ab initio	TS4 PES	TS4 ab initio
1	2094i	2122i	848i	954i	944i	1000i
2	667	857	493	557	444	562
3	941	933	653	658	641	667
4	1125	1153	751	903	857	953
5	1148	1202	1178	1002	1136	1026
6	1291	1263	1302	1220	1167	1192
7	1361	1455	1352	1246	1330	1258
8	1530	1501	1439	1401	1472	1437
9	2039	1923	1560	1441	1701	1467
10	2262	2351	2832	2813	2917	2758
11	3124	2963	2981	2913	3021	2990
12	3135	3013	3735	3747	3733	3807

single-reference region. (One measure of the CASPT2 inaccuracy is that the CASPT2 electronic dissociation energy for $CH_3OH \rightarrow CH_3 + OH$ is roughly 8 kcal/mol lower than the CCSD(T)-F12b one of 98.2 kcal/mol.) Figure 10.5 shows two cuts in the CH_2OH + H channel, as well as CCSD(T)-F12b and shifted CASPT2 energies. This channel also involves the multi-reference region, and hybrid data were also used for this channel. Similar to $CH_3 + OH$, the energies in the multi-reference region agree very well with the CASPT2 calculations, and the strongly attractive region of the PES agrees with coupled-cluster energies. Figure 10.6 shows the potential along a rectilinear reaction coordinate, namely the imaginary-frequency normal coordinate of the saddle points (TS1–4), denoted Q_{im}. The potential shown is the one minimized with respect to the remaining $3N-7$ (11) normal modes of the saddle point for each value of Q_{im}. These regions can be described correctly by single reference electronic structure theory, so only CCSD(T)-F12b energies

are shown in the figures. Again, the agreement between the PES and the *ab initio* theory is good.

Finally consider the measurable dissociation energy D_0 for each channel. The ZPE of the minimum and all the fragments were calculated rigorously using diffusion Monte Carlo (DMC) simulation. The algorithm described in Chapter 3 were applied. For each system, five simulations were performed, and each simulation was propagated for 20000 steps, with step size of 5.0 au. In each simulation, the system was equilibrated for the first 2000 steps and the energies in the remaining steps were collected to compute the ZPE. The uncertain in the ZPE was estimated by the standard deviation of the five simulations of a particular system, and the uncertainty in the dissociation energy was estimated based on the uncertainties in the ZPEs. The ZPEs, the D_0 values calculated by DMC, and the experimental dissociation energies are listed in Table 10.4. One can see good agreement between theoretical calculation and the experiments.

Table 10.4: ZPEs (cm^{-1} of the methanol dissociation channels and the theoretical and experimental dissociation energies (kcal/mol).

	ZPE (cm^{-1})	D_0 (kcal/mol)	Experiment [a]
$CH_3 + OH$	42641 ± 9	90.04 ± 0.04	90.25
$^1CH_2 + H_2O$	42829 ± 14	90.83 ± 0.06	90.83
trans-HCOH + H_2	36303 ± 5	71.92 ± 0.03	72.48
cis-HCOH + H_2	37830 ± 4	76.29 ± 0.03	77.12
$H_2CO + H_2$	18127 ± 4	19.96 ± 0.03	20.33
$CH_2OH + H$	43949 ± 5	93.79 ± 0.03	94.55
Minimum	11148 ± 5	-	-

[a] From Ref. 339
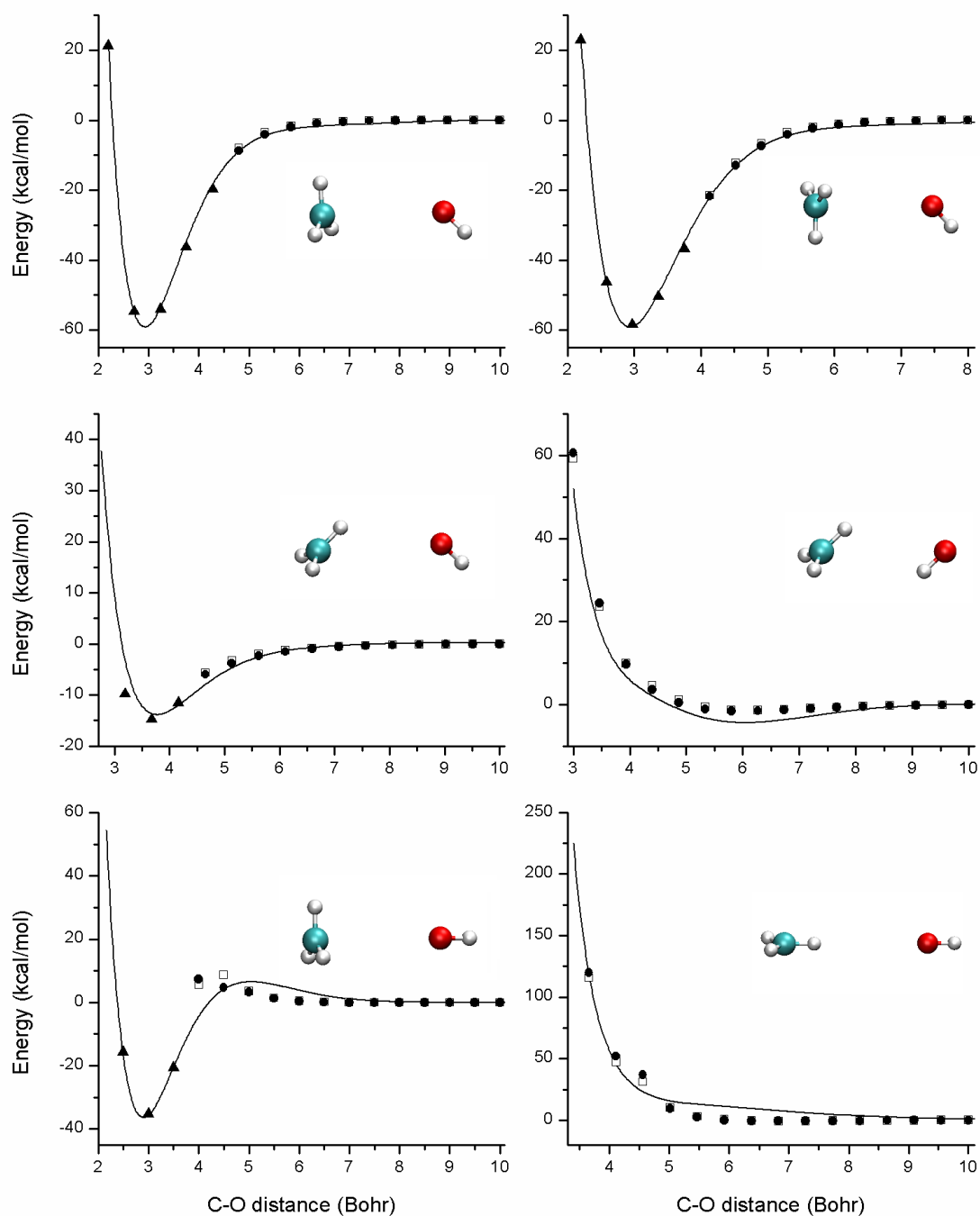
Figure 10.4:   Unrelaxed one-dimensional cuts from the PES (line) for different CH_3 and OH orientations, compared to CCSD(T)-F12b (black triangles), CASPT2 (black circles) and MRCI (open squares) calculations.
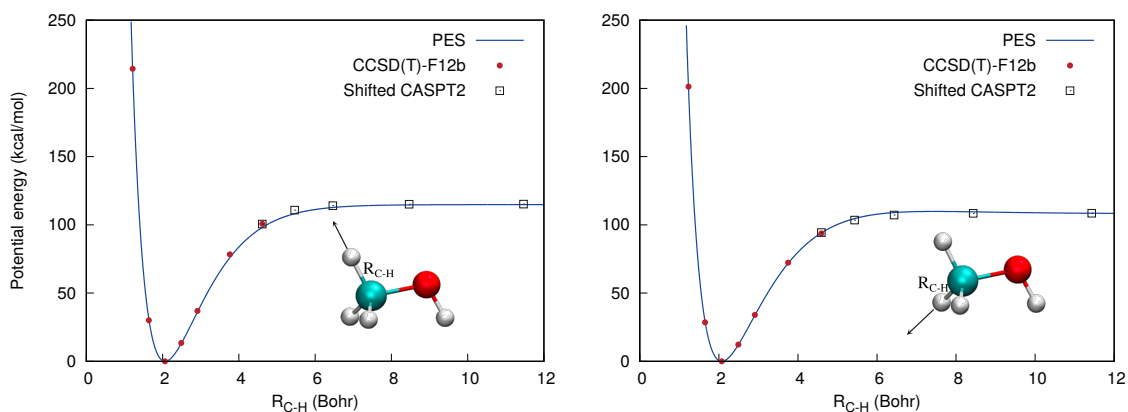
Figure 10.5:   Unrelaxed one-dimensional cuts from the PES (line) for $CH_2OH + H$ channel, compared to CCSD(T)-F12b (red dots) and shifted CASPT2 (open squares) calculations.
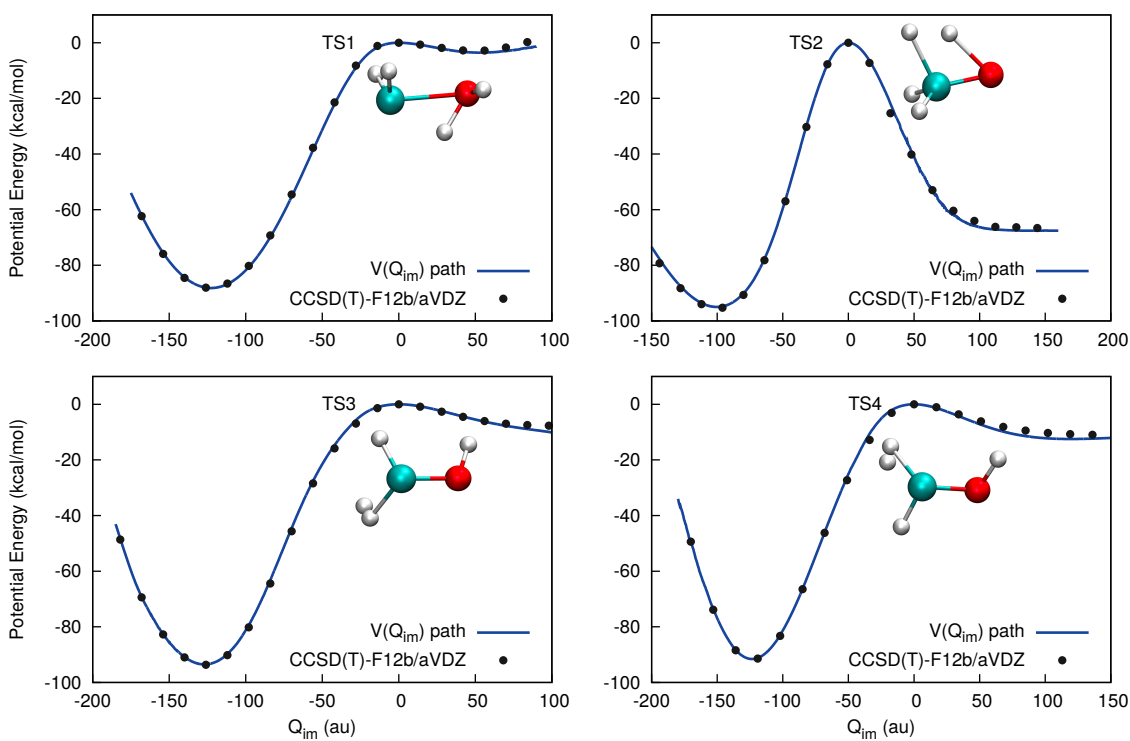
Figure 10.6:   The potential along the imaginary-frequency normal coordinate of the saddle points (TS1–4), compared to CCSD(T)-F12b energies.

10.3 Molecular Dynamics Simulations

10.3.1 Computational details

The molecular dynamics trajectories were initiated at the global minimum. Microcanonical sampling was employed to prepare the initial conditions of the trajectories, with zero total angular momentum. In addition, I calculated the energy in each normal mode of the minimum, and the initial condition was re-assigned until the energy in each mode was larger than its harmonic ZPE. I carried out MD simulations for nine different initial internal energies (the energy of the minimum is zero): 43000, 44000, 45000, 46000, 47000, 48000, 49000, 50000, 51000 cm^{-1}; these energies are 91.07, 93.93, 96.79, 99.65, 120.51, 105.37, 108.23, 111.09, and 113.95 kcal/mol relative to the ZPE of the minimum. The lowest internal energy, 91.07 kcal/mol, is just slightly higher than the CH_3 + OH and $^1CH_2$ + H_2O channels and TS1–TS4. For each initial internal energy, 40000 trajectories were carried out. The velocity Verlet algorithm was applied to propagate the trajectory, with step size of 0.121 fs. The maximum number of steps for these trajectories is 5000000, corresponding to 604.8 ps. When a trajectory reaches the maximum number of steps, or when the largest internuclear distance exceeds 15.0 Bohr, the trajectory stops.

In this work, I mainly focus on the branching ratio of each dissociation channel. Therefore, the number of trajectories that ended up in each channel was counted, and the fraction of each channel was calculated. Note that when the initial energy is low, the vibrational energy of the final products could be smaller than the ZPE. These trajectories are "un-physical" and should not be considered in the analysis. I employed the soft ZPE-constraint to remove these un-physical trajectories. To do this, for each fragment, the translational energy was first removed. The rotational energy can be calculated using Eq. 4.11 in Chapter 4, and then the vibrational energy can be obtained using Eq. 4.12. If

the sum of the vibrational energy of two fragments are smaller than the Harmonic ZPE of them in a trajectory, that trajectory was discarded.

10.3.2   Results and discussions

The branching ratio of each channel obtained from the MD trajectories at different initial internal energy are summarized in Figure 10.7. At the lowest internal energy (91.07 kcal/mol), in principle, all the dissociation channels except $CH_2OH + H$ are open. In simulations, I observed trajectories end up in the $CH_3 + OH$, cis/trans-HCOH + H_2, and $H_2CO + H_2$; however, I did not find the $^1CH_2 + H_2O$ product. This might due to the fact that the initial energy is only about 0.6 kcal/mol higher than the minimal energy to that channel, and the number of trajectories that dissociate is not adequate to give good statistics. At this energy, only about 3000 trajectories dissociated and had enough vibrational energy in fragments. The dominant channel at this energy is the cis/trans-HCOH + H_2, because the relatively low barrier to the products.

As the initial internal energy increases, I can observe the $^1CH_2 + H_2O$ products in the simulation: at 96.79 kcal/mol, the $CH_2OH + H$ opens up, and this energy threshold is in fairly good agreement with the D_0 of this channel (94.5 kcal/mol). One can see that at high energies, the $CH_3 + OH$ and $CH_2OH + H$ products start to dominate, because only a single bond cleavage is involved in these two channels, while the molecule has to go through transition states for other products. For the $H_2CO + H_2$, the ratio is very small (about 1%) in the whole range of initial internal energy.

Based on the MD simulations, I confirm that the $CH_3 + OH$ is the major product in the thermal decomposition of methanol. However, the atomic H product could be significant at higher energy. In the simulation, I observe the $^1CH_2 + H_2O$, but the ratio
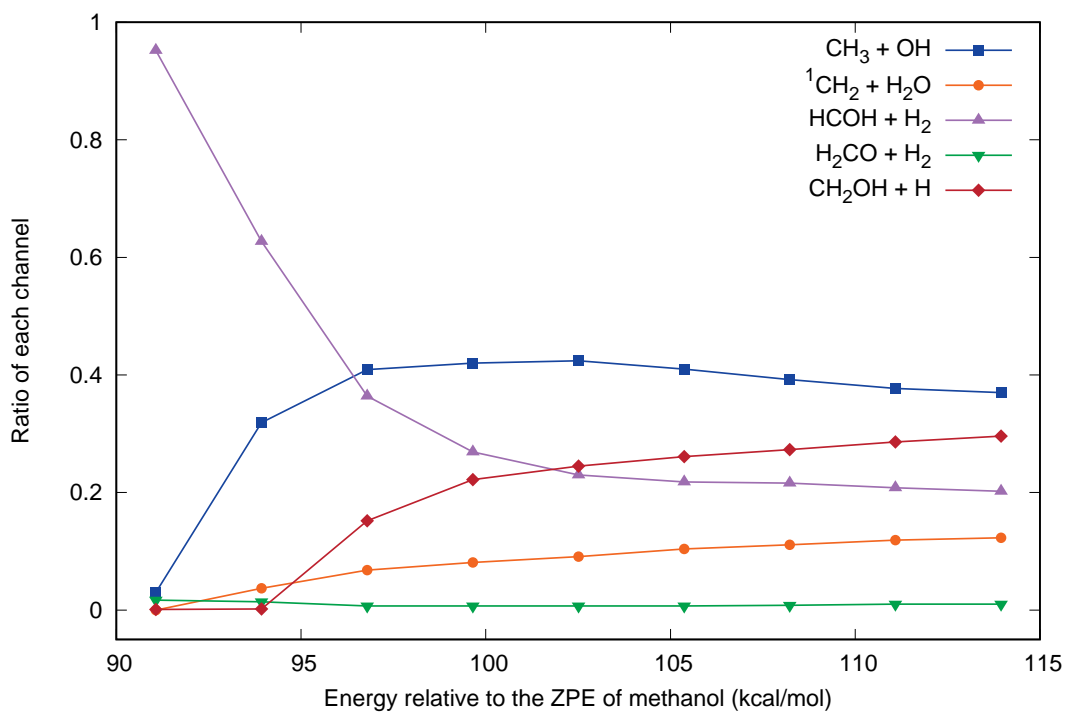
Figure 10.7:   Branching ratio of methanol dissociation obtained from molecular dynamics simulations.

is not as large as what the previous experiments show. Furthermore, I find that at low internal energy, the cis/trans-HCOH + H_2 could be dominant, and even at high internal energy, the ratio of these two channels are still non-negligible.

10.4   Summary, Conclusions, and Remarks

In this work, a full-dimensional potential energy surface of methanol is constructed. It describes the CH_3 + OH, $^1CH_2$ + H_2O, CH_2OH + H, H_2 + H_2CO, and H_2 + cis/trans-HCOH dissociation channels. This PES is a permutationally invariant fit to 181765 *ab initio* energies, calculated with CCSD(T)-F12/aVDZ and CASPT2/aVDZ theories. One-dimensional cuts show that this PES agrees with CCSD(T)-F12b energies in the single-reference region, and with CASPT2 ones in multi-reference region. The fidelity of the PES is further confirmed by the good agreement in dissociation energies with experiments.

Microcanonical molecular dynamics simulations have been performed, in order to investigate the thermal decomposition of methanol. The simulations confirmed that the CH_3 + OH is the dominant product, while the cis/trans-HCOH + H_2 channel is also significant. However, these are microcanonical calculations, i.e., the molecule has a fixed total energy, and pressures were not considered in the simulations; the results should not be directly compared to experiments, as the experiments are conducted at certain temperatures and pressures. Simulations using canonical ensemble will be carried out in the future to model the thermal decomposition of methanol.

Chapter 11

Dissociation of Vinyl Chloride

11.1 Overview

Vinylidene, H_2CC, is a key reaction intermediate and an important initially-formed product in many photochemical reactions.[340–342] Perhaps the most frequently cited example, which provides spectroscopic proof that vinylidene is formed, is the vibrationally resolved $C_2H_2^-$ negative ion photoelectron spectrum.[343,344] The linewidths in this spectrum are widely cited as showing that the isomerization lifetime of vinylidene in its zero-point vibrational level is $\sim$400 fs. Coulomb Explosion Imaging (CEI) experiments[345] of neutral vinylidene 3.5 s after anion photodetachment showed that roughly 50% of the observed structures are vinylidene-like and 50% acetylene-like. This proves that the vinylidene structure "lives" for at least 3.5 μs. How can this observation be reconciled with a 400 fs isomerization lifetime?

The resolution of this paradox will emerge as we recall that eigenstates are stationary. The issue is whether one can produce C_2H_2 eigenstates that are predominantly vinylidene in character. Such eigenstates were shown to exist in the first full-dimensional quantum

calculations by Zou and Bowman,[346] and seen consistently in potential energy surfaces (PESs) of ever-increasing accuracy since then.[347–349] However, one key to success in experimental production of these eigenstates is that the vinylidene be rotationally cold, as rotation has been shown to promote intramolecular vibrational relaxation (IVR), which profoundly increases the density of acetylene vibrational states into which vinylidene can isomerize.[350,351]
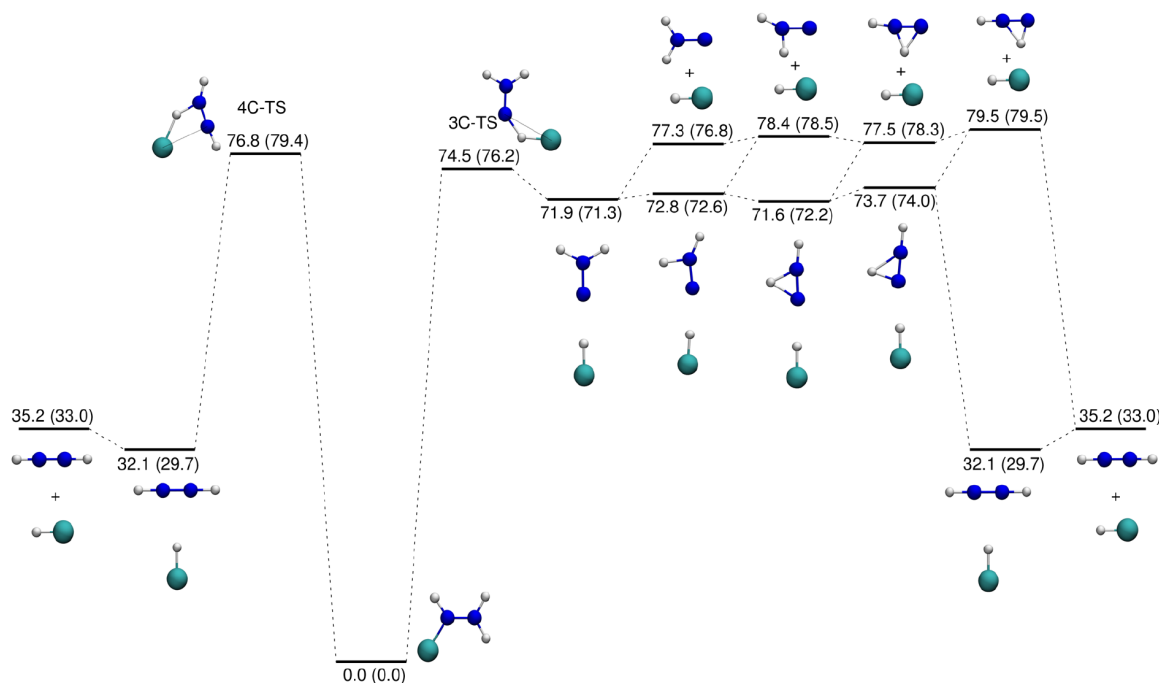
Figure 11.1: Energies (kcal/mol) of stationary points on the vinyl chloride potential energy surface relevant to HCl elimination from DFT-M06-2X/aug-cc-pVDZ calculations and from CCSD(T)-F12/aug-cc-pVDZ given in parentheses.

Photodissociation of vinyl chloride has been studied extensively at 193 nm using a broad range of techniques, which include resonant ionization detection of HCl,[352–354] time-resolved FTIR,[355] and photofragment translational spectroscopy with vacuum ultraviolet

photoionization product detection.[356] Theoretical work has included a detailed mapping of the stationary points on the ground state PES by Riehl and Morokuma[357] and direct dynamics studies by Nunes et al.[358,359] For HCl elimination, which is the lowest energy decay path and the focus here, there are two reaction channels as depicted in Figure 11.1: via a 3-center (3C) transition state (3C-TS) to HCl + vinylidene, with a zero-point corrected reverse barrier of 2.5 kcal/mol, or by a 4-center (4C) 4C-TS that is 52 kcal/mol above the HCl + acetylene asymptote.

The well-studied 193 nm dissociation includes both 3C and 4C channels, in a ratio estimated from the rotational distributions in HCl to be 4:1. The rotational distribution for the 3C channel was seen in the earlier dynamics study[358] to reach a maximum around $J = 5$ and extend to $J = 40$. The 4C channel, on the other hand, extends broadly from $J = 18$ to 40 with undetectable population in low rotational levels. This underscores the problem that precludes 193 nm dissociation as a route to synthesis of cold vinylidene: the excess energy yields vinylidene with such high internal excitation that the product vinylidene character will be diluted into many excited acetylene levels and lost.

Thus experimentalists turned to infrared photodissociation as a possible route to cold vinylidene. In this joint experiment/theory work, Suits and co-workers[360] carried out infrared multiphoton dissociation (IRMPD) experiment by dissociating vinyl chloride in a molecular beam using a TEA-CO_2 laser, then probing the HCl product state specifically using $2 + 1$ resonant ionization. They obtained the rotational distribution for the HCl product in $v = 0$, and recorded images on a number of rotational levels in $v = 0$ and $v = 1$. I carried out molecular dynamics simulations to provide theoretical support for this experiment.

11.2   Computational Details

I have performed direct dynamics trajectory studies to determine the translational energy release and product state distributions following excitation at energies just above the 3C-TS, both for comparison to experiment, and to probe the nascent C_2H_2 rotational excitation.

The direct dynamics simulations were carried out using Gaussian 09 package[361] with the M06-2X density functional[362] and aug-cc-pVDZ basis set. This functional was found to give satisfactory energetics compared to higher level CCSD(T)-F12/aug-cc-pVDZ calculations. The trajectories were initiated at the 3C saddle point and standard microcanonical normal mode sampling was employed.[60] An additional 7.0 kcal/mol energy was added to the imaginary-frequency mode. This energy was chosen as a compromise between the experimental energy (which is somewhat above the threshold for dissociation) and consideration of the computational cost of running direct-dynamics. Any spurious angular momentum was removed, so the initial angular momentum was zero ($J = 0$) for all the trajectories. The step size is 5 a.u. (0.121 fs), and the maximum number of steps for a trajectory is 4000 (483.8 fs). Each trajectory required roughly 24 hours on a single node of our compute cluster. In total, 452 trajectories dissociated, and the total translational energy and angular momenta of the fragments were calculated and analyzed here, using the procedures mentioned in Chapter 4 and Ref.[61]

11.3   Results and Discussion

Figure 11.2(A) shows the HCl $v = 0$ resonance-enhanced multiphoton ionization (REMPI) spectrum Suits and co-workers obtained following IRMPD of vinyl chloride. No signal

was detected in rotational levels 20 or 25, despite the fact that these levels are expected to be well-populated via the 4C pathway. The HCl rotational level populations obtained from the trajectory calculations are shown in Figure 11.2(B). A Boltzmann fit (inset) gives a rotational temperature of 270 K for the experimental spectrum and 510 K for the trajectory results. This difference may be due in part to the additional 7 kcal/mol above the 3C-TS provided in the trajectory calculations.
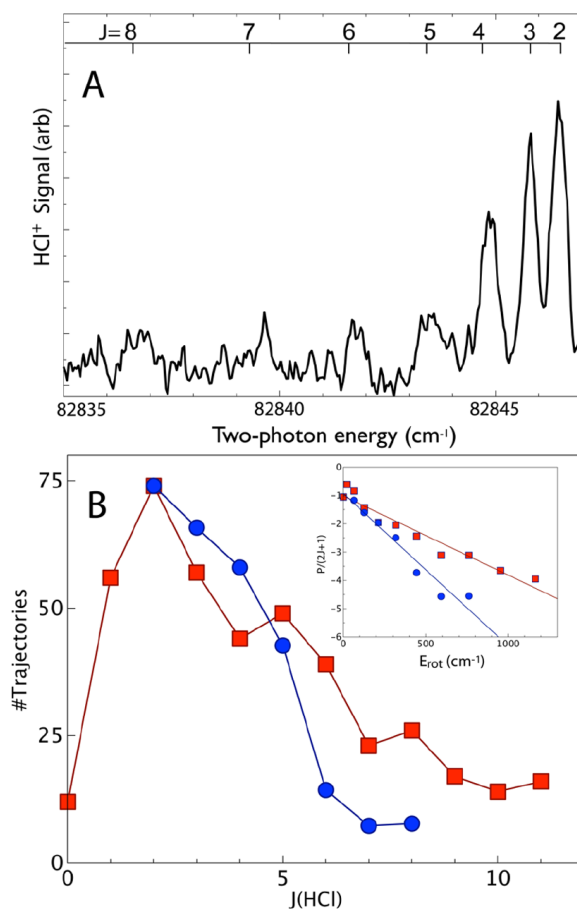
Figure 11.2: HCl ($v = 0$) rotation distribution following IRMPD of vinyl chloride. (A) Experimental REMPI spectrum; (B) trajectory results (red squares) and experimental populations (blue circles) with Boltzmann plot inset.

DC slice images of a range of rotational levels of HCl in $v = 0$ and $v = 1$ are given in Figure 11.3, as well as the total translational energy distributions derived from the images. All of the images are isotropic and show low translational energy release, peaking at 3–5 kcal/mol with an average total translational energy of 4–5 kcal/mol. Results for HCl $v = 1$ are similar, although the signal is significantly weaker and the average translational energy release lower at 3 kcal/mol. The low translational energy release seen here is in stark contrast to the results at 193 nm, which peak at 15 kcal/mol and extend beyond 60 kcal/mol. The translational energy distribution obtained from the trajectory data is also given in Figure 11.3, showing an average translational energy release of 2.5 kcal/mol, in good agreement with the experimental results. The low translational energy release, resembling the reverse barrier for the 3C-TS, combined with low rotational excitation in HCl, indicate clearly that the product we detect originates in the 3C elimination of HCl from vinyl chloride, making vinylidene as a 1:1 co-product. The good agreement with the theory for dissociation starting from the 3C-TS confirms this. The absence of the 4C product in the experiments is readily understood from the 3 kcal/mol higher energy of the 4C-TS, as well as entropic factors that favor the 3C channel.

Now consider the predicted internal excitation in the vinylidene co-product. For this only the trajectory calculations could be used, as information about vinylidene is not yet directly available from experiment. The results, obtained from a classical calculation of the C_2H_2 rotational excitation in each trajectory, are given in Figure 11.4. Sixty-five percent of all trajectories result in $J = 20$ or below for C_2H_2, and 25% in $J = 10$ or lower. This low rotational excitation in the C_2H_2 product is extremely significant. Perry and Herman showed that high rotation results in complete IVR on the acetylene side of the isomerization barrier.[350,351] As a result, vinylidene (and local-bender acetylene) character is diluted into many eigenstates, thereby reducing both the single rotation-vibration
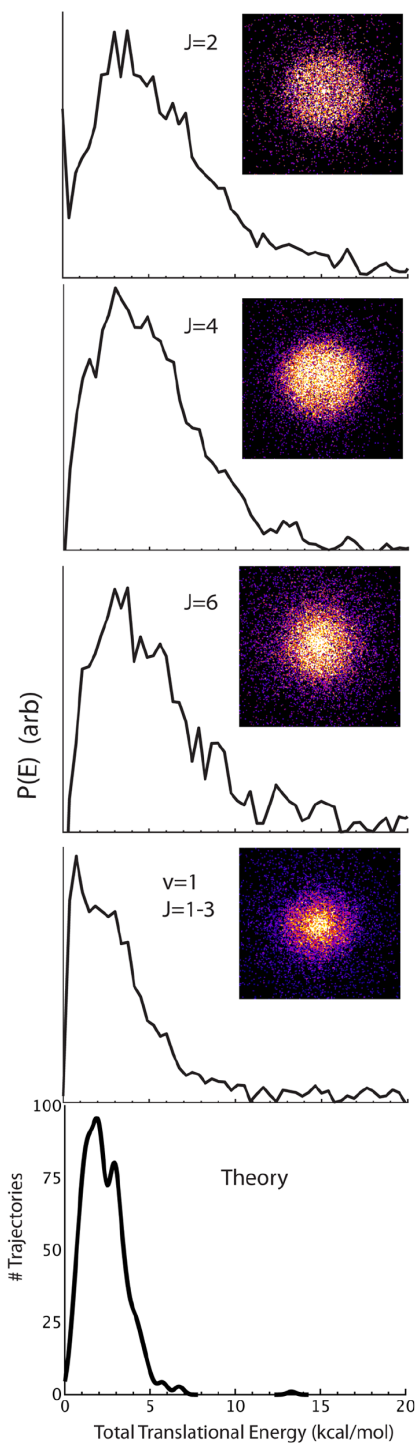
Figure 11.3:   HCl DC sliced images and total translational energy distributions for indicated rotational level, and corresponding trajectory result.

level populations and the transition moments, rendering all $J = 0 \rightarrow 1$ transitions unde-

tectably weak. In the absence of C_2H_2 rotational excitation, eigenstates of predominantly

vinylidene character are seen to persist.
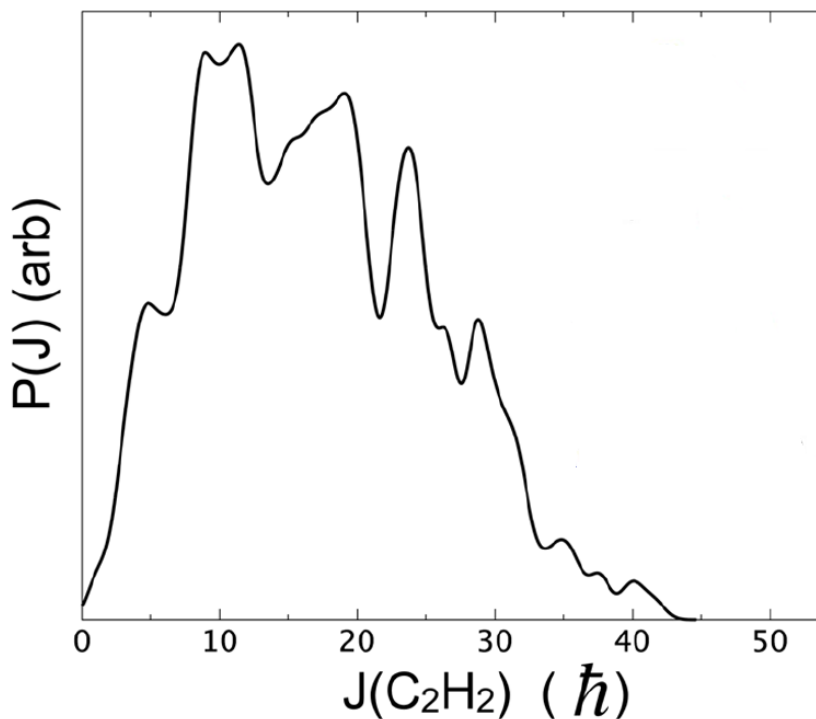
Figure 11.4: C_2H_2 total rotational distribution obtained from trajectories. Inset shows a typical trajectory that persists as vinylidene, with snapshots every 90 fs.

Shown in Figure 11.5 is a typical trajectory that persists as vinylidene, to highlight

that the 3C elimination indeed initially forms the vinylidene structure. However, one

must refrain from thinking too classically about this. In these experiments, a chemical

"pluck" of the system creates, at $t = 0$, a pure vinylidene quantum mechanical superpo-

sition state. The time evolution of this initially formed state will depend on the number,

nature, and energy spacings of the eigenstates that express this $t = 0$ state. Different
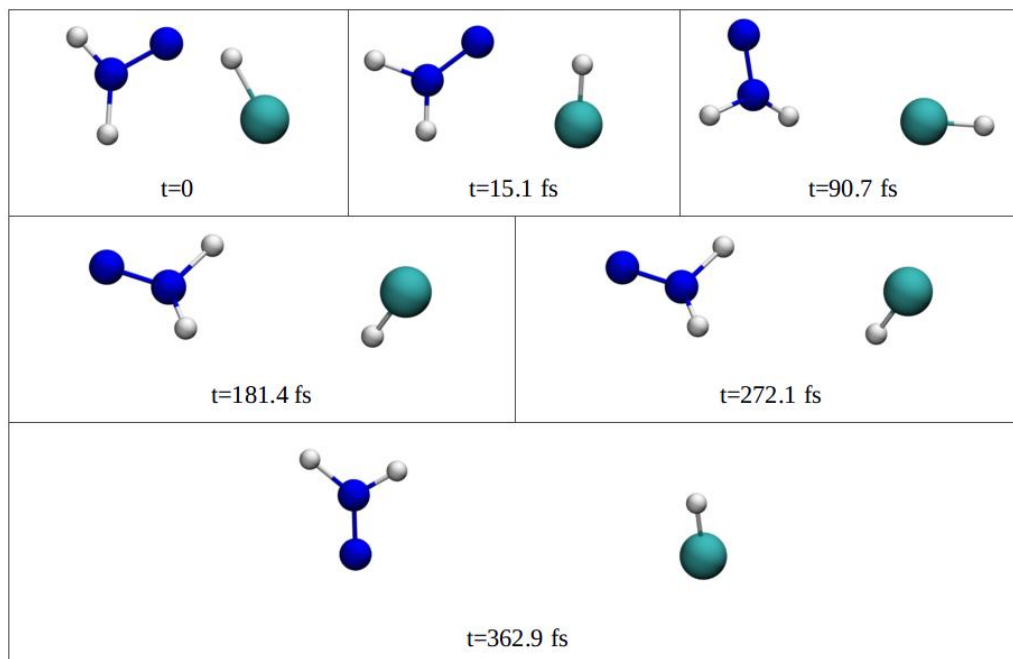
Figure 11.5:   A typical trajectory of vinyl chloride dissociation that persists as vinylidene

vinylidene vibrational levels will have different time behaviors. In general, there will be a fast initial decay of the phased-up vinylidene character. But if there are only two or three dominant eigenstates, the vinylidene character will be manifest as nearly perfectly recurring quantum beats, as seen in the CEI experiments.

11.4   Summary and Conclusions

The combination of the experiments and trajectory calculations shows clearly that IRMPD of vinyl chloride creates vinylidene states (via the 3C transition state) at $t = 0$. That is, IRMPD of vinyl chloride gives rise to 3C elimination of HCl with the co-product C_2H_2 born as vinylidene with low rotational excitation. This $t = 0$ vinylidene state will have a particularly simple quantum mechanical eigenstate description, ideal conditions

for future direct spectroscopic detection.

Chapter 12

Adiabatic Switching Method for Initial Conditions

12.1 Overview

Computational simulations have become significant tools to investigate chemical reactions, thanks to the drastic enhancement in the performance of computers. Ideally, in the case of chemical reactions, where the motions of nucleus and electrons are involved, quantum mechanical scattering theory for the nuclear motion should to be applied. However, exact quantum calculations are very computationally demanding that they have rarely been applied in more than six degrees of freedom, and for the relevant example of reactions of atoms with methane far from full (12) dimensionality.

When nuclear quantum effects are not significant, molecular dynamics (MD) simulations, which treat the nuclei as classical particles, represent an alternative way to simulate the reaction process. One limitation of the basic MD simulation is that it fails to describe the zero-point motion of the molecule, even classically. The zero-point energy (ZPE) of a

polyatomic molecule is usually a large amount of energy (tens of kcal/mol), so the lack of it could lead to poor estimate of reaction barriers or thresholds. Furthermore, the original MD method is not able to treat mode-specific reactions, when a certain vibrational mode of the molecule is excited. Quasiclassical trajectory (QCT) calculations offer an improvement to the basic MD method by incorporating the semiclassical quantization of molecular vibrations as the initial condition. Thus, the QCT method is able to describe the zero-point motion and mode-specific conditions, and has been extensively applied to dynamics simulations of gas-phase chemical reactions. These methods have been reviewed in detail by Hase[60,61] and the methods have been adopted in the code, VENUS, that performs QCT calculations.[363]

One widely-used approach to prepare the initial conditions in QCT calculations is normal-mode sampling method.[60] To be specific, consider the $X + CH_4$ reaction, where X is an atom. A normal-mode analysis is done for the molecule, e.g., CH_4, using the given molecular potential that contained in the full potential energy surface (PES) describing the reaction. This results in a separable sampling procedure, because the vibrational motion is treated as uncoupled harmonic oscillators. For the zero-point state, the harmonic ZPE of each mode is assigned to the molecule. For excited vibrational states, the same procedure is used. The problem with this procedure is obvious, because the PES of any real molecule does not consists of simple uncoupled harmonic oscillators but is inherently anharmonic. Typically, the harmonic ZPE is on the order of one to several hundred wavenumbers higher than the correct ZPE. In addition, the initial state prepared in this way is not a stationary state of the real molecular Hamiltonian, meaning that vibrational energy flows back and forth among the vibrational modes. However, when averaged over an ensemble of trajectories, the harmonic action has been shown to be maintained for thousands of time steps, as for example in the recent QCT study of mode-specificity in

the Cl + CHD$_3$ reaction.[364] Thus, normal-mode sampling generally does provide good and robust results. This is illustrated in the 2014 review of recent QCT calculations of the X + CH$_4$ (and isotopologs) reaction for both the vibrational ground and excited state reactions, where X is H, F, Cl, Br and O(^{3}P),[365] and also more recent application to mode-specific effects in O(^{3}P) + CH$_4$.[366]

Experiments and QCT calculations of mode-specificity in reactions of CH$_4$ (and isotopologs) have been the focus of numerous studies in the gas phase, e.g., references 364–370. In the QCT studies, normal mode sampling have been performed, using accurate analytical potential energy surfaces.[364–366,370] The mode-specific dissociation of methane on a metal surface is also a prototype system when investigating the mode selectivity in gas-surface reactions, and it is also the rate-limiting step in steam reforming.[371–374]

This apparent success of normal-mode sampling notwithstanding, it has been known for years that rigorous phase-space sampling of initial states in QCT calculations should be based on semiclassical quantization of ro-vibrational states of polyatomic molecules. The field of semiclassical quantization of molecular motion, in particular vibrational motion, is large, with many contributions and advances made in the 1980s.[375–388] Nevertheless, the methodology is complex, as the forces, even at zero-point energies, are non-linear and the search for periodic orbits is challenging. Perhaps the most recent and successful application of a state-of-the-art semiclassical theory to vibrational state quantization was done in 2011 in a demonstration to H$_2$CO.[389] This work, which was computationally intensive, was aimed at determining eigenvalues only.

Perhaps the first use of semiclassical quantization of vibrational energies (using classical perturbation theory) for a collision system was in the context of energy transfer in triatomic molecules.[390] That review is an excellent source for the details involved in performing semiclassical quantization at that time. The sophisticated fast Fourier transform

method[378,379] was employed recently to quantize final states of the NH_2 product in the H + NH_3 reaction.[391] Comparison with the standard harmonic analysis showed only small differences, again confirming the robustness of that approach.

Among the numerous semiclassical methods available, adiabatic switching (AS)[381–388] is considered here. The basic idea of adiabatic switching is as follows: the Hamiltonian of the polyatomic molecule can be written as the sum of a zeroth-order separable, and non-separable parts, $H = H_0 + \Delta H$. The separable part H_0 is easily quantized semi-classially. Then the Hamiltonian becomes time-dependent, being switched from H_0 to H sufficiently slowly, and according to the adiabatic theorem, the quantized state of H_0 will slowly evolve to the corresponding quantized state associated with the true Hamiltonian H. The application of AS in semiclassical quantization has been investigated and reviewed.[381–388] The method, as will become clear below, is straightforward to apply and so it offers the prospect of being readily implemented in QCT calculations involving poly-atomic reactants (and products). Recently, AS has been applied successfully to obtain the Wigner distribution for anharmonic coupled oscillators, starting with a zero-order separable distribution.[392]

To the best of my knowledge, AS has been applied twice in QCT calculations. The first time was in 1995 to a full-dimensional model of the H + CD_4 reaction,[393] and then in 2006 to a study of the Cl + CH_4 reaction, using an *ab initio*-based potential.[394] In both cases, the ZPE of CH_4 was quantized using AS. The former study focused on the reaction cross section and ro-vibrational state distributions of the HD product at one collision energy. Standard normal-mode sampling was also done and results from the two approaches were compared, with the conclusion "However, in application to the H + $CD_4 \rightarrow$ HD + CD_3 reaction, we find no discernible difference between the two sampling methods." Thus, the authors did not recommend AS for use in QCT calculations. In addition, the AS zero-

point energy had a standard deviation of roughly 170 cm^{-1}, much larger than had been reported in previous realistic applications to H_2O, HCO and H_2CO.[388] In the more recent study, the standard deviation of the ZPE was reported as 35 cm^{-1} using a switching time of 0.67 ps. In both studies, the absence of accurate quantum calculations of the ZPE meant that an assessment of the accuracy of the AS ZPE was not possible. However, Castillo et al.[394] did note that the AS result of 27.5 kcal/mol was in good agreement with the "experimental" value of 27.1 kcal/mol, i.e., a difference of 129 cm^{-1}.

In this work, I revisit AS for methane for the ZPE and two fundamentals, using an accurate *ab initio*-based PES for which exact quantum energies are available. I come to a different conclusion with respect to the accuracy of AS quantization than one made in 1995 and suggest that AS may be an effective, simple and general way to perform semiclassical quantization in the context of QCT calculations. CH_4 is challenging for semiclassical quantization, since it has nine vibrational degrees of freedom, two sets of which are triply degenerate, one set doubly degenerate and thus only one singly degenerate mode. Thus, to the best of my knowledge, the present calculations represent an application of semiclassical quantization to the largest polyatomic molecule beyond the ZPE.

12.2   Theory and Computational Details

12.2.1   Adiabatic switching

Adiabatic switching is founded in the adiabatic theorem of classical mechanics,[395] which states that certain constants of the motion may evolve invariantly in time. For semi-classical quantization, these are the good action variables.[381–385] The time-dependent

Hamiltonian in AS is given by

$$H(t) = H_0 + s(t)(H - H_0), \tag{12.1}$$

where H_0 is the zeroth-order Hamiltonian, $s(t)$ is a switching function that varies monotonically from 0 to 1 over a finite time interval T and remains 1 for $t > T$.

Here the zeroth-order Hamiltonian is the harmonic one,

$$H_0 = \sum_{i=1}^{3N-6} \left(\frac{P_i^2}{2} + \frac{\omega_i^2 Q_i^2}{2} \right) = K + V_0, \tag{12.2}$$

where Q_i the are the mass-scaled normal modes and ω_i are the corresponding harmonic frequencies. The switching function $s(t)$ is chosen as[385,388]

$$s(t) = \frac{t}{T} - \frac{1}{2\pi} \sin \frac{2\pi t}{T}, \tag{12.3}$$

where T is the switching time. Therefore $H - H_0 = V - V_0$, where V and V_0 are full and harmonic potentials, respectively, and thus $H(t) = H_0 + s(t)(V - V_0)$.

The semiclassical quantization conditions of H_0 are the usual ones,

$$\oint P_i dQ_i = 2\pi(n_i + 1/2)\hbar, \tag{12.4}$$

where n_i are integers and these variables are classical actions. Since the H_0 is a separable harmonic-oscillator Hamiltonian, the semiclassical quantization can be achieved trivially, as shown next.

12.2.2 Quantization of H_0

A standard normal-mode analysis is performed at the global minimum structure of the molecule, in the present case methane. A set of harmonic frequencies ω_i and the corresponding normal mode eigenvectors L_i ($i = 1, 2, \cdots, 3N - 6$) are obtained.

For each mode, the normal coordinate Q_i and the corresponding momentum P_i are in terms of action/angle variables by

$$Q_i = [(2n_i + 1)\hbar/\omega_i]^{1/2} \cos(\omega_i t + \phi_i), \tag{12.5}$$

$$P_i = -[(2n_i + 1)\hbar\omega_i]^{1/2} \sin(\omega_i t + \phi_i), \tag{12.6}$$

where n_i is the integral quantum number of mode i, and ϕ_i is the phase of the i-th oscillator, which varies uniformly from 0 to 2π.

For sampling purposes, e.g., in QCT calculations, at $t = 0$, the phase for each mode is randomly sampled from a uniform distribution on $(0, 2\pi)$. Once the random phase ϕ_i are determined, Q_i and P_i are obtained and then transformed rigorously to the Cartesian coordinates q_i and momenta p_i via

$$\boldsymbol{q} = \boldsymbol{q_0} + \boldsymbol{M}^{-1/2}\boldsymbol{L}\boldsymbol{Q}, \tag{12.7}$$

$$\boldsymbol{p} = \boldsymbol{M}^{1/2}\boldsymbol{L}\boldsymbol{P}, \tag{12.8}$$

where $\boldsymbol{q_0}$ is a vector of the Cartesian coordinates of the minimum; $\boldsymbol{L}$ is a matrix consists of the normal mode eigenvectors; $\boldsymbol{M}$ is a diagonal matrix whose elements are the masses of atoms.

These are then the initial conditions for the AS trajectory. AS can be done with a single trajectory, or as is more typical, for an ensemble of trajectories.

12.2.3 Propagation

For general utility, the AS is implemented in Cartesian coordinates and momenta. In this way, the method can be applied to any molecule, cluster, etc. Thus, the equations of motion

$$\dot{q}_i = \frac{\partial H(t)}{\partial p_i}, \ \dot{p}_i = -\frac{\partial H(t)}{\partial q_i} \tag{12.9}$$

are integrated numerically, and $H(t) = H_0 + s(t)(V - V_0)$, as stated above. In order to evaluate the harmonic potential, V_0, at each time step, the coordinate system is transformed to the Eckart frame, to eliminate the rotation of the molecule due to either numerical inaccuracy or rotation-vibration coupling. The transformation to the Eckart frame is done by a rotation of the coordinate system to a new one that satisfies the Eckart conditions. This is done by rotating the coordinates $\mathbf{r}_i$ to satisfy these conditions. The rotation matrix, $\mathbf{C}$ is computed using the method of Dymarsky and Kudin[396]. The details of the procedure used are given elsewhere,[365,370] where the context was the final state analysis of products. In brief, $\mathbf{C}$ is determined from the equation

$$\sum_{i=1}^{N} m_i \mathbf{r}_i^{eq} \times (\mathbf{C}\mathbf{r}_i - \mathbf{r}_i^{eq}) = 0, \tag{12.10}$$

where $\mathbf{r}_i^{eq}$ is the reference configuration where the normal mode analysis was performed. Once the Cartesian coordinates in the Eckart frame are obtained, the reference set of normal coordinates is obtained as usual, and V_0 can be easily evaluated as

$$V_0 = \sum_{i=1}^{3N-6} \frac{\omega_i^2 Q_i^2}{2}, \tag{12.11}$$

and subtracted from the full potential. Note that the transformation to the Eckart frame is only performed to evaluate the harmonic potential, otherwise the classical propagation proceeds as usual in the original set of Cartesian coordinates and momenta. This transformation is easily implemented into any trajectory code.

12.2.4   Computational details

I performed AS calculations for methane, with different switching times T for the zero-point state and two fundamentals. The velocity Verlet algorithm was applied to numerically integrate the equations of motion, and the gradient at each step was calculated by numerical finite difference. The step size used in all the trajectory calculations was 0.06 fs. For each quantized state, three different switching times have been used, namely, $T = 0.24$, 0.48, and 1.21 ps. After the full potential was completely turned on, the molecule was further propagated for 5000 steps using the full potential energy surface. For each switching time, 1000 trajectories were run to obtain statistically well-converged averages and standard deviations of the final quantized energies.

An *ab initio*-based potential energy surface, of near spectroscopic accuracy and for which accurate quantum vibrational energies are available,[170] is used in the present calculations.

12.3   Results and Discussion

12.3.1   CH$_4$ zero-point energy

The ZPE as a function of time for a single trajectory and three total switching times is shown in Figure 12.1. As seen, the initial harmonic ZPE (9847 cm^{-1}) changes as the

potential is switched to the full potential and the vibrational energy of CH_4 converges to a value that is close to the exact quantum ZPE of 9702 cm^{-1}. The decrease in energy is generally monotonic with small oscillations.
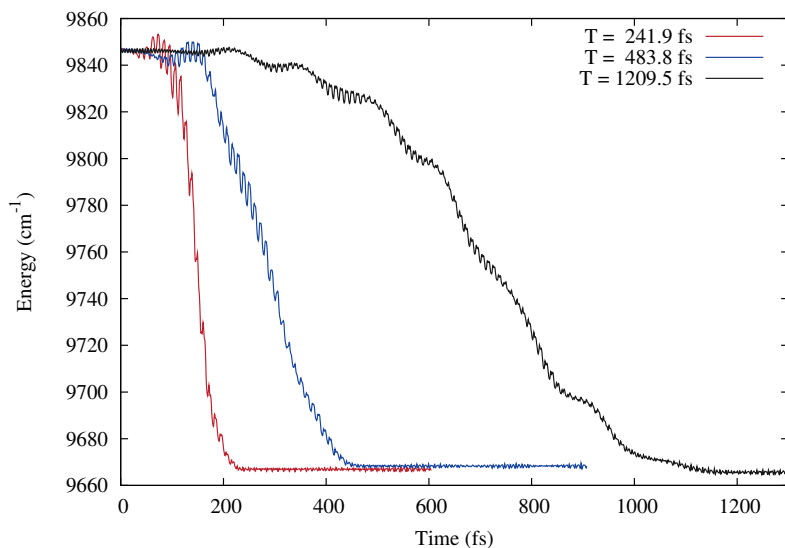
Figure 12.1:   Zero-point vibrational energy of CH_4 using adiabatic switching for three switching times.

In principle, the quantized energy in the molecule should be independent of the trajectory initial conditions after the potential is completely switched to the full one, assuming that the adiabatic switching process is slow enough. However, due to the finite switching time, the final energy has a distribution, centered at the semiclassical anharmonic ZPE. I propagated 1000 trajectories for each switching time, and the final energy of each trajectory was recorded. For each energy, I applied a Gaussian function centered at that energy with width of 7.5 cm^{-1}, and the superposition of the 1000 Gaussian functions represents the distribution of the 1000 energies for a particular switching time. The results are shown in Figure 12.2. The three distributions are all centered at about 9670 cm^{-1},
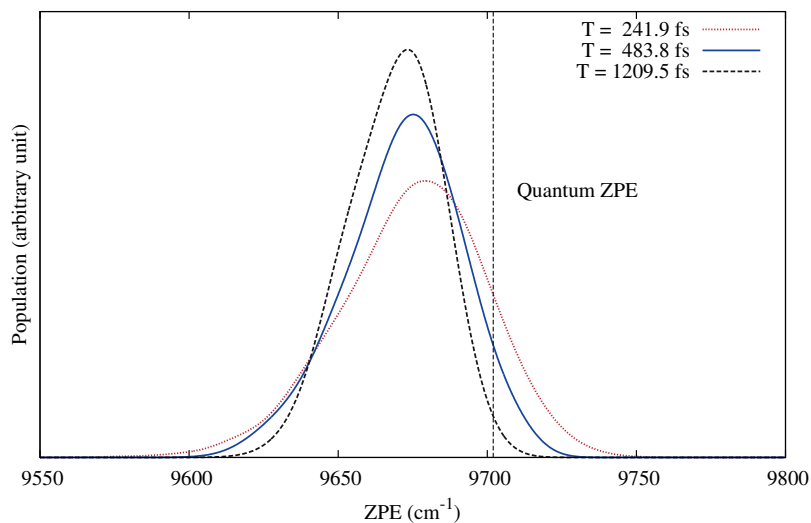
Figure 12.2:   The distribution of the semiclassical anharmonic ZPE of CH_4 from 1000 trajectories, for three switching times.

which is only about 30 cm^{-1} lower than the exact quantum ZPE. Therefore, I believe that the correct semiclassical vibrational ground state of methane is obtained using the adiabatic switching method. The standard deviations for the three switching times are 23.9, 18.8 and 14.3 cm^{-1}, verifying the expectation that a longer switching time leads to more precise results.

In these calculations, I also monitored the normal coordinates of the methane molecule (specifically, the six zero-frequency rotational and translational modes) along the trajectory. At each step, the Cartesian coordinates of the molecule were transformed to the normal coordinates directly without aligning to the Eckart frame. Of course, initially the normal coordinates for those six modes were zero, but during the propagation, the normal coordinates of the three rotational modes can be very large (50 to 100 a.u.), owing to vibration rotation coupling, without transformation to the Eckart frame. The translational modes remain zero as there is no coupling to those modes. After transforming

to the Eckart frame when evaluating the potential energy, the coordinates of the three rotational modes are nearly zero, as they should be. Therefore, the transformation to the Eckart frame, when calculating the potential, is an important procedure in the AS trajectory calculations.

Note, the present standard deviations are significantly smaller than the one reported in 1995 by Huang et al. [393] for CD_4 of 171 cm^{-1}, despite a much longer switching time of 7.8 ps used by that group. I can only speculate about this large difference in the standard deviations; however, that group cited several possible sources for the discouragingly large standard deviation. One was their implementation of AS, which appears to be similar to the one used here, with the possible exception of not transforming to the Eckart frame to determine the harmonic potential. This important aspect of the current implementation is not mentioned by Huang *et al.* In any case, the results here for the ZPE are consistent with previous results using AS, e.g., for H_2CO, where differences with exact quantum calculations are roughly 10 cm^{-1} and standard deviations are roughly half that. [388]

12.3.2   Excited states

To further test the AS method, I prepared the initial conditions for the excited state of the symmetric stretching and asymmetric stretching normal modes, to verify if the molecule could evolve to the corresponding excited state on the full potential semiclassically. The average energies relative to the semiclassical ZPE averaged for 1000 trajectories and three switching times are given in Table 12.1. As is seen from the table, after the switching process, the vibrational energy agrees well with the corresponding quantum energy. This indicates that after the adiabatic switching, the methane molecule is in the correct semiclassically quantized state that corresponds to the desired quantum state.

Table 12.1: The energy relative to the semiclassical ZPE in cm^{-1} and the standard deviation (in parentheses) over 1,000 trajectories for the specified excited states and switching time in picoseconds. The fundamentals from quantum calculations are also listed in the last column.

Mode excited	$T = 0.242$	$T = 0.484$	$T = 1.209$	Quantum [a]
sym. str.	2915 (46.5)	2907 (41.9)	2901 (27.1)	2917
asym. str. 1	3014 (48.5)	3015 (40.1)	3017 (29.7)	3019
asym. str. 2	3008 (63.6)	3016 (40.6)	3018 (28.6)	3019
asym. str. 3	3010 (56.5)	3016 (42.2)	3018 (29.2)	3019

[a] Quantum results from Ref. 170

The agreement with exact quantum results is very good, although the standard deviations are larger than those for the ZPE. Note that the aysmmetric stretch is triply degenerate and the three AS energies are nearly identical, being within one wavenumber of each other. While these degenerate states are uncoupled at $t = 0$, it is likely that they mix as the full potential is switched on. No attempt to analyze the extent of mixing was made. It is also worth noting that resonances, e.g., Fermi resonances, present challenges for semiclassical quantization, including AS. Analysis of these, along with strategies to deal with them, are beyond the scope of this paper; however, the interested readers are referred to reference 26 for a discussion of this.

So, having established that AS does provide good accuracy compared to exact quantum calculations, next I describe how AS can be implemented to provide semiclassical initial conditions in quasiclassical trajectory calculations.

12.3.3 Implementation in quasiclassical trajectory calculations

To begin, recall that in standard normal-mode sampling, the initial Cartesian coordinates and momenta are obtained from uniform (and typically random) sampling of the normal

mode coordinates and momenta, c.f., Eq. 12.6. The resultant propagation using the full Hamiltonian is not stationary and further, each set of initial conditions, in general, results in a different total energy. This is mostly due to the anharmonicity of the potential; however, the vibrational angular momentum terms also contribute. The variation in the total energy can be several hundred to a thousand or so wavenumbers. Scaling of the initial kinetic energy is typically done to restore the total energy to the desired value.[60,365]

An alternative normal-mode sampling results from selecting initial conditions in Cartesian coordinates and momenta from trajectories in these coordinates and momenta using the harmonic potential, with initial conditions determined from each normal-mode coordinate and momentum. Although these trajectories do not obviously manifest the underlying periodic motion they can be used to collect Cartesian coordinates and momenta uniformly in time and then randomly sampled as initial conditions in a simulation of a collision with an atom, molecule, surface, etc.

For general, anharmonic molecular potentials, locating the semiclassical invariant tori of a polyatomic molecule is a major challenge. Even with successful quantization using AS, locating the adiabatically evolved tori is problematic.[397] Thus, sampling initial conditions using the generalization of Eq. 12.6, i.e., with the new action/angle variables is not feasible. However, sampling can be done using Cartesian coordinates and momenta of an adiabatically switched trajectory, provided it is done uniformly in time. This is the analog of the alternative way to perform normal-mode sampling in the case of a harmonic potential, just described. Thus, initial conditions are obtained by simply sampling the Cartesian coordinates and momenta of an AS trajectory provided the trajectory has been propagated long enough to fully sample the phase space. Sampling from several AS trajectories can result in a some dispersion of the total energy, owing to the small dispersion in the AS energies (relative to the harmonic case).

In summary, the procedure for a quasiclassical trajectory calculation using AS for initial quantization, is as follows. Use AS for the non-interacting molecular reactants to establish the quantized trajectory in Cartesian coordinates and momenta of the reactants, using the procedure described here for quantization of CH_4. Select initial conditions for the internal motions of each reactant from one or more AS trajectories, uniformly in time, and then add the kinetic energy of relative motion in the usual way and sample the initial relative momentum, impact parameter, etc. The additional computational cost, relative to standard normal-mode sampling, is just in generating the AS trajectory(ies).

Finally, AS can also be used to analyze the final state(s) of the products. This was done in[393]. Currently harmonic analysis is typically done to determine final actions and to assign final states,[365] and this does appear to be a robust procedure. Indeed, the final vibrational-state distribution of the NH_2 product in the $H + NH_3$ reaction obtained using harmonic analysis differed from the one using fast-Fourier-transform semiclassical analysis by only a few percent.[391] However, given both its simplicity and generality, AS could replace harmonic analysis as the routine way to quantize the reactants and analyze the final states of the products.

12.4   Summary and Conclusions

I have calculated the vibrational energies of CH_4 for the ground state and two fundamentals using AS with an existing *ab initio*-based potential energy surface. AS was done using a standard separable harmonic normal mode zeroth-order Hamiltonian to the full one in Cartesian coordinates. Details of the procedure were given, with special note taken of the transformation from Cartesian coordinates of the AS trajectory to the reference normal mode coordinates. Comparison with available accurate quantum energies showed

good agreement, i.e., differences between 2 and 30 cm^{-1}.

This approach can be used to prepare molecules with the correct semiclassical phase space for initial conditions in quasiclassical trajectory calculations. This, in principle, eliminates the inaccuracies that exist in using non-stationary, harmonic phase space for initial conditions. As noted already, these are evidently not large, provided a sufficient number of trajectories are used to average the results. However, future calculations comparing the outcomes of the two approaches would be useful.

References

[1] Schatz, G. C. *Rev. Mod. Phys.* **1989**, *61*, 669.

[2] Ischtwan, J.; Collins, M. A. *J. Chem. Phys.* **1994**, *100*, 8080.

[3] Thompson, K. C.; Jordan, M. J. T.; Collins, M. A. *J. Chem. Phys.* **1998**, *108*, 8302.

[4] Hollebeek, T.; Ho, T.-S.; Rabitz, H. *Annu. Rev. Phys. Chem.* **1999**, *50*, 537.

[5] Bettens, R. P. A.; Collins, M. A. *J. Chem. Phys.* **1999**, *111*, 816.

[6] Majumder, M.; Ndengue, S. A.; Dawes, R. *Mol. Phys.* **2016**, *114*, 1.

[7] Marquardt, R.; Quack, M. In *Handbook of High-resolution Spectroscopy*; Quack, M., Merkt, F., Eds.; John Wiley & Sons, Ltd., 2011; p 511.

[8] Blank, T. B.; Brown, S. D.; Calhoun, A. W.; Doren, D. J. *J. Chem. Phys.* **1995**, *103*, 4129.

[9] Brown, D. F. R.; Gibbs, M. N.; Clary, D. C. *J. Chem. Phys.* **1996**, *10*, 7597.

[10] Raff, L. M.; Malshe, M.; Hagan, M.; Doughan, D. I.; Rockley, M. G.; Komanduri, R. *J. Chem. Phys.* **2005**, *122*, 084104.

[11] Manzhos, S.; Wang, X.; Dawes, R.; Carrington, T. *J. Phys. Chem. A* **2006**, *110*, 5295.

[12] Handley, C. M.; Popelier, P. L. A. *J. Phys. Chem. A* **2010**, *114*, 3371.

[13] Behler, J. *Phys. Chem. Chem. Phys.* **2011**, *13*, 17930.

[14] Chen, J.; Xu, X.; Xu, X.; Zhang, D. H. *J. Chem. Phys.* **2013**, *138*, 154301.

[15] Gastegger, M.; Marquetand, P. *J. Chem. Theory Comput.* **2015**, *11*, 2187.

[16] Manzhos, S.; Dawes, R.; Carrington, T. *Int. J. Quantum Chem.* **2015**, *115*, 1012.

[17] Braams, B. J.; Bowman, J. M. *Int. Rev. Phys. Chem.* **2009**, *28*, 577.

[18] Xie, Z.; Bowman, J. M. *J. Chem. Theory Comput.* **2010**, *6*, 26.

[19] Bowman, J. M.; Braams, B. J.; Carter, S.; C., C.; Czakó, G.; Fu, B.; Huang, X.; Kamarchik, E.; Sharma, A. R.; C., S. B.; Wang, Y.; Xie, Z. *J. Phys. Chem. Lett.* **2010**, *1*, 1866.

[20] Bowman, J. M.; Czakó, G.; Fu, B. *Phys. Chem. Chem. Phys.* **2011**, *13*, 8094.

[21] Shao, K.; Chen, J.; Zhao, Z.; Zhang, D. H. *J. Chem. Phys.* **2016**, *145*, 071101.

[22] Jiang, B.; Li, J.; Guo, H. *Int. Rev. Phys. Chem.* **2016**, *35*, 479.

[23] Derksen, H.; Kemper, G. *Computational Invariant Theory*; Springer-Verlag, Berlin, 2002.

[24] Bosma, W.; Cannon, J.; Playoust, C. *J. Symb. Comp.* **1997**, *24*, 235.

[25] Paukku, Y.; Yang, K. R.; Varga, Z.; Truhlar, D. G. *J. Chem. Phys.* **2013**, *139*, 044309.

[26] Conte, R.; Houston, P. L.; Bowman, J. M. *J. Chem. Phys.* **2014**, *140*, 151101.

[27] Wang, Y.; Shepler, B. C.; Braams, B. J.; Bowman, J. M. *J. Chem. Phys.* **2009**, *131*, 054511.

[28] Wang, Y.; Huang, X.; Shepler, B. C.; Braams, B. J.; Bowman, J. M. *J. Chem. Phys.* **2011**, *134*, 094509.

[29] Mancini, J. S.; Bowman, J. M. *J. Phys. Chem. A* **2014**, *118*, 7367.

[30] Mancini, J. S.; Bowman, J. M. *J. Phys. Chem. Lett.* **2014**, *5*, 2247.

[31] Samanta, A. K.; Wang, Y.; Mancini, J. S.; Bowman, J. M.; Reisler, H. *Chem. Rev.* **2016**, *116*, 4913.

[32] Adler, T. B.; Knizia, G.; Werner, H.-J. *J. Chem. Phys.* **2007**, *127*, 221106.

[33] Knizia, G.; Adler, T. B.; Werner, H.-J. *J. Chem. Phys.* **2009**, *130*, 054104.

[34] Dunning, T. H. *J. Chem. Phys.* **1989**, *90*, 1007.

[35] Nielson, H. H. *Rev. Mod. Phys.* **1951**, *23*, 90.

[36] Barone, V. *J. Chem. Phys.* **2005**, *122*, 014108.

[37] Christoffel, K. M.; Bowman, J. M. *Chem. Phys. Lett.* **1982**, *85*, 220.

[38] Carter, S.; Bowman, J. M.; Hancy, N. C. *Theor. Chem. Acc.* **1998**, *100*, 191.

[39] Bowman, J. M.; Carter, S.; Huang, X. *Int. Rev. Phys. Chem.* **2003**, *22*, 533.

[40] Watson, J. K. G. *Mol. Phys.* **1968**, *15*, 479.

[41] Miller, H., William; Handy, N. C.; Adams, J. E. *J. Chem. Phys.* **1980**, *72*, 99.

[42] Bowman, J. M.; Huang, X.; Handy, N. C.; Carter, S. *J. Phys. Chem. A* **2007**, *111*, 7317.

[43] Carter, S.; Handy, N. C. *J. Chem. Phys.* **2000**, *113*, 987.

[44] Tew, D. P.; Handy, N. C.; Carter, S.; Irle, S.; Bowman, J. M. *Mol. Phys.* **2003**, *101*, 3513.

[45] Handy, N. C.; Carter, S. *Mol. Phys.* **2004**, *102*, 2201.

[46] Wang, X.; Carter, S.; Bowman, J. M. *J. Phys. Chem. A* **2015**, 11632.

[47] Burcl, R.; Carter, S.; Handy, N. C. *Chem. Phys. Lett.* **2003**, *380*, 237.

[48] Wang, Y.; Bowman, J. M. *J. Chem. Phys.* **2011**, *134*, 154510.

[49] Wang, Y.; Bowman, J. M. *J. Chem. Phys.* **2012**, *136*, 144113.

[50] Liu, H.; Wang, Y.; Bowman, J. M. *J. Phys. Chem. Lett.* **2012**, *3*, 3671.

[51] Liu, H.; Wang, Y.; Bowman, J. M. *J. Chem. Phys.* **2015**, *142*, 194502.

[52] Mancini, J. S.; Bowman, J. M. *J. Chem. Phys.* **2013**, *139*, 164115.

[53] Bowman, J. M.; Wang, Y.; Liu, H.; Mancini, J. S. *J. Phys. Chem. Lett.* **2015**, *6*, 366.

[54] Liu, H.; Wang, Y.; Bowman, J. M. *J. Am. Chem. Soc.* **2014**, *136*, 5888.

[55] Anderson, J. B. *J. Chem. Phys.* **1975**, *63*, 1499.

[56] Anderson, J. B. *J. Chem. Phys.* **1976**, *65*, 4121.

[57] Suhm, M. A.; Watts, R. O. *Phys. Rep.* **1991**, *204*, 293–329.

[58] Kosztin, I.; Faber, B.; Schulten, K. *Am. J. Phys.* **1996**, *64*, 633.

[59] McCoy, A. B. *Int. Rev. Phys. Chem.* **2006**, *25*, 77.

[60] Hase, W. L. In *Encyclopeida of Computational Chemistry*; Allinger, N. L., Ed.; Wiley: New York, 1998; p 402.

[61] Hase, W. L. In *Encyclopeida of Computational Chemistry*; Allinger, N. L., Ed.; Wiley: New York, 1998; p 399.

[62] Sloan, E. D.; Koh, C. A. *Clathrate Hydrates of Natural Gases*, 3rd ed.; CRC Press, Taylor & Francis Group, 2008.

[63] Koh, C. A. *Chem. Soc. Rev.* **2002**, *31*, 157.

[64] Su, F.; Bray, C. L.; Carter, B. O.; Overend, G.; Cropper, C.; Iggo, J. A.; Khimyak, Y. Z.; Fogg, A. M.; Cooper, A. I. *Adv. Mater.* **2009**, *21*, 2382.

[65] Di Profio, P.; Arca, S.; Rossi, F.; Filipponi, M. *Int. J. Hydrogen Energy* **2009**, *34*, 9173.

[66] Ripmeester, J. A.; Tse, J. S.; Ratcliffe, C. I.; Powell, B. M. *Nature* **1987**, *325*, 135.

[67] Sparks, K. A. Configurational properties of water clathrates through molecular simulation. Ph.D. thesis, Massachusetts Institute of Technology, USA, 1991; http://hdl.handle.net/1721.1/13759.

[68] Khan, A. *J. Chem. Phys.* **1999**, *110*, 11884.

[69] Mao, W. L.; Mao, H.-K.; Goncharov, A. F.; Struzhkin, V. V.; Guo, Q.; Hu, J.; Shu, J.; Hemley, R. J.; Somayazulu, M.; Zhao, Y. *Science* **2002**, *297*, 2247.

[70] Patchkovskii, S.; Tse, J. S. *Proc. Natl. Acad. Sci. USA* **2003**, *100*, 14645.

[71] Mao, W. L.; Mao, H.-K. *Proc. Natl. Acad. Sci. USA* **2004**, *101*, 708.

[72] Florusse, L. J.; Peters, C. J.; Schoonman, J.; Hester, K. C.; Koh, C. A.; Dec, S. F.; Marsh, K. N.; Sloan, E. D. *Science* **2004**, *306*, 469.

[73] Lokshin, K. A.; Zhao, Y.; He, D.; Mao, W. L.; Mao, H.-K.; Hemley, R. J.; Lobanov, M. V.; Greenblatt, M. *Phys. Rev. Lett.* **2004**, *93*, 125503.

[74] Lee, H.; Lee, J.; Kim, D. Y.; Park, J.; Seo, Y.-T.; Zeng, H.; Moudrakovski, I. L.; Ratcliffe, C. I.; Ripmeester, J. A. *Nature* **2005**, *434*, 743.

[75] Alavi, S.; Ripmeester, J. A.; Klug, D. D. *J. Chem. Phys.* **2005**, *123*, 024507.

[76] Strobel, T. A.; Taylor, C. J.; Hester, K. C.; Dec, S. F.; Koh, C. A.; Miller, K. T.; Sloan, E. D. *J. Phys. Chem. B* **2006**, *110*, 17121.

[77] Papadimitriou, N. I.; Tsimpanogiannis, I. N.; Papaioannou, A. T.; Stubos, A. K. *J. Phys. Chem. B* **2008**, *112*, 10294.

[78] Martín, Á.; Peters, C. J. *J. Phys. Chem. B* **2009**, *113*, 7558.

[79] Sugahara, T.; Haag, J. C.; Prasad, P. S. R.; Warntjes, A. A.; Sloan, E. D.; Sum, A. K.; Koh, C. A. *J. Am. Chem. Soc.* **2009**, *131*, 14616.

[80] Román-Pérez, G.; Moaied, M.; Soler, J. M.; Yndurain, F. *Phys. Rev. Lett.* **2010**, *105*, 145901.

[81] Chattaraj, P. K.; Bandaru, S.; Mondal, S. *J. Phys. Chem. A* **2011**, *115*, 187.

[82] Willow, S. Y.; Xantheas, S. S. *Chem. Phys. Lett.* **2012**, *525-526*, 13.

[83] Ramya, K. R.; Venkatnathan, A. *J. Phys. Chem. A* **2012**, *116*, 7742.

[84] Lu, H.; Wang, J.; Liu, C.; Ratcliffe, C. I.; Becker, U.; Kumar, R.; Ripmeester, J. *J. Am. Chem. Soc.* **2012**, *134*, 9160.

[85] Takeuchi, F.; Hiratsuka, M.; Ohmura, R.; Alavi, S.; Sum, A. K.; Yasuoka, K. *J. Chem. Phys.* **2013**, *138*, 124504.

[86] Martos-Villa, R.; Francisco-Márquez, M.; Mata, M. P.; Sainz-Díaz, C. I. *J. Mol. Graph. Model.* **2013**, *44*, 253.

[87] Cox, S. J.; Towler, M. D.; Alfe, D.; Michaelides, A. *J. Chem. Phys.* **2014**, *140*, 174703.

[88] Cao, X.; Su, Y.; Liu, Y.; Zhao, J.; Liu, C. *J. Phys. Chem. A* **2014**, *118*, 215.

[89] Koh, D.-Y.; Kang, H.; Jeon, J.; Ahn, Y.-H.; Park, Y.; Kim, H.; Lee, H. *J. Phys. Chem. C* **2014**, *118*, 3324.

[90] Grim, R. G. A spectroscopic study of the structure and occupancies of clathrate hydrates incorporating hydrogen. Ph.D. thesis, Colorado School of Mines, Colorado, USA, 2014; (Publication No. AAT 3638879).

[91] Narayanan, T. M.; Imasato, K.; Takeya, S.; Alavi, S.; Ohmura, R. *J. Phys. Chem. C* **2015**, *119*, 25738.

[92] Andersson, O.; Nakazawa, Y. *J. Phys. Chem. B* **2015**, *119*, 3846.

[93] Nguyen, A. H.; Koc, M. A.; Shepherd, T. D.; Molinero, V. *J. Phys. Chem. C* **2015**, *119*, 4104.

[94] Tang, L.; Shi, R.; Su, Y.; Zhao, J. *J. Phys. Chem. A* **2015**, *119*, 10971.

[95] Burnham, C. J.; English, N. J. *J. Chem. Phys.* **2016**, *144*, 164503.

[96] Sum, A. K.; Burruss, R. C.; Sloan, E. D. *J. Phys. Chem. B* **1997**, *101*, 7371.

[97] Tulk, C. A.; Ripmeester, J. A.; Klug, D. D. *Ann. N. Y. Acad. Sci.* **2000**, *912*, 859.

[98] Itoh, H.; Kawamura, K. *Ann. N. Y. Acad. Sci.* **2000**, *912*, 693.

[99] Tse, J. S. *J. Supramol. Chem.* **2002**, *2*, 429.

[100] Subramanian, S.; Sloan, E. D. *J. Phys. Chem. B* **2002**, *106*, 4348.

[101] Greathouse, J. A.; Cygan, R. T.; Simmons, B. A. *J. Phys. Chem. B* **2006**, *110*, 6428.

[102] Chazallon, B.; Focsa, C.; Charlou, J.-L.; Bourry, C.; Donval, J.-P. *Chem. Geol.* **2007**, *244*, 175.

[103] Hester, K. C.; Dunk, R. M.; White, S. N.; Brewer, P. G.; Peltzer, E. T.; Sloan, E. D. *Geochim. Cosmochim. Acta* **2007**, *71*, 2947.

[104] Dartois, E.; Deboffle, D. *Astron. Astrophys.* **2008**, *490*, L19.

[105] Dartois, E.; Deboffle, D.; Bouzit, M. *Astron. Astrophys.* **2010**, *514*, A49.

[106] Ohno, H.; Kida, M.; Sakurai, T.; Iizuka, Y.; Hondoh, T.; Narita, H.; Nagao, J. *ChemPhysChem* **2010**, *11*, 3070.

[107] Hiratsuka, M.; Ohmura, R.; Sum, A. K.; Yasuoka, K. *J. Chem. Phys.* **2012**, *136*, 044508.

[108] Hiratsuka, M.; Ohmura, R.; Sum, A. K.; Yasuoka, K. *J. Chem. Phys.* **2012**, *137*, 144306.

[109] Ramya, K. R.; Venkatnathan, A. *J. Chem. Phys.* **2013**, *138*, 124305.

[110] Qin, J.; Kuhs, W. F. *AlChE J.* **2013**, *59*, 2155.

[111] Liu, Y.; Ojamäe, L. *J. Phys. Chem. C* **2015**, *119*, 17084.

[112] Anderson, R.; Chapoy, A.; Tohidi, B. *Langmuir* **2007**, *23*, 3440.

[113] Walsh, M. R.; Koh, C. A.; Sloan, E. D.; Sum, A. K.; Wu, D. T. *Science* **2009**, *326*, 1095.

[114] Jacobson, L. C.; Hujo, W.; Molinero, V. *J. Am. Chem. Soc.* **2010**, *132*, 11806.

[115] Srivastava, H. K.; Sastry, G. N. *J. Phys. Chem. A* **2011**, *115*, 7633.

[116] Jacobson, L. C.; Matsumoto, M.; Molinero, V. *J. Chem. Phys.* **2011**, *135*, 074501.

[117] Knott, B. C.; Molinero, V.; Doherty, M. F.; Peters, B. *J. Am. Chem. Soc.* **2012**, *134*, 19544.

[118] Pirzadeh, P.; Kusalik, P. G. *J. Am. Chem. Soc.* **2013**, *135*, 7278.

[119] Lauricella, M.; Meloni, S.; English, N. J.; Peters, B.; Ciccotti, G. *J. Phys. Chem. C* **2014**, *118*, 22847.

[120] Barnes, B. C.; Knott, B. C.; Beckham, G. T.; Wu, D. T.; Sum, A. K. *J. Phys. Chem. B* **2014**, *118*, 13236.

[121] Yagasaki, T.; Matsumoto, M.; Andoh, Y.; Okazaki, S.; Tanaka, H. *J. Phys. Chem. B* **2014**, *118*, 11797.

[122] Wang, X.; Sang, D. K.; Chen, J.; Mi, J. *Phys. Chem. Chem. Phys.* **2014**, *16*, 26929.

[123] Xu, J.; Gu, T.; Sun, Z.; Li, X.; Wang, X. *Mol. Phys.* **2016**, *114*, 34.

[124] Borchardt, L.; Nickel, W.; Casco, M.; Senkovska, I.; Bon, V.; Wallacher, D.; Grimm, N.; Krause, S.; Silvestre-Albero, J. *Phys. Chem. Chem. Phys.* **2016**, *18*, 20607.

[125] Holzammer, C.; Finckenstein, A.; Will, S.; Braeuer, A. S. *J. Phys. Chem. B* **2016**, *120*, 2452.

[126] Xu, P.; Lang, X.; Fan, S.; Wang, Y.; Chen, J. *J. Phys. Chem. C* **2016**, *120*, 5392.

[127] Okuchi, T.; Moudrakovski, I. L.; Ripmeester, J. A. *Appl. Phys. Lett.* **2007**, *91*, 171903.

[128] Alavi, S.; Ripmeester, J. A. *Angew. Chem. Int. Ed.* **2007**, *46*, 6102.

[129] Frankcombe, T. J.; Kroes, G.-J. *J. Phys. Chem. C* **2007**, *111*, 13044.

[130] Peters, B.; Zimmermann, N. E. R.; Beckham, G. T.; Tester, J. W.; Trout, B. L. *J. Am. Chem. Soc.* **2008**, *130*, 17342.

[131] Yoshioka, H.; Ota, M.; Sato, Y.; Watanabe, M.; Inomata, H.; Smith, R. L.; Peters, C. J. *AIChE J.* **2011**, *57*, 265.

[132] Gorman, P. D.; English, N. J.; MacElroy, J. M. D. *J. Chem. Phys.* **2012**, *136*, 044506.

[133] Pefoute, E.; Kemner, E.; Soetens, J. C.; Russina, M.; Desmedt, A. *J. Phys. Chem. C* **2012**, *116*, 16823.

[134] Cao, H.; English, N. J.; MacElroy, J. M. D. *J. Chem. Phys.* **2013**, *138*, 094507.

[135] Trinh, T. T.; Waage, M. H.; van Erp, T. S.; Kjelstrup, S. *Phys. Chem. Chem. Phys.* **2015**, *17*, 13808.

[136] Burnham, C. J.; English, N. J. *J. Phys. Chem. C* **2016**, *120*, 16561.

[137] Hjertenæs, E.; Trinh, T. T.; Koch, H. *Phys. Chem. Chem. Phys.* **2016**, *18*, 17831.

[138] Liang, S.; Liang, D.; Wu, N.; Yi, L.; Hu, G. *J. Phys. Chem. C* **2016**, *120*, 16298.

[139] Tse, J. S.; Ratcliffe, C. I.; Powell, B. M.; Sears, V. F.; Handa, Y. P. *J. Phys. Chem. A* **1997**, *101*, 4491.

[140] Gutt, C.; Asmussen, B.; Press, W.; Merkl, C.; Casalta, H.; Greinert, J.; Bohrmann, G.; Tse, J. S.; Hüller, A. *Europhys. Lett.* **1999**, *48*, 269.

[141] Gutt, C.; Press, W.; Hüller, A.; Tse, J. S.; Casalta, H. *J. Chem. Phys.* **2001**, *114*, 4160.

[142] Gutt, C.; Press, W.; Hüller, A.; Tse, J. S. *Appl. Phys. A* **2002**, *74*, S1299.

[143] Baumert, J.; Gutt, C.; Shpakov, V. P.; Tse, J. S.; Krisch, M.; Müller, M.; Requardt, H.; Klug, D. D.; Janssen, S.; Press, W. *Phys. Rev. B* **2003**, *68*, 174301.

[144] Kamiyama, T.; Seki, N.; Iwasa, H.; Uchida, T.; Ebinuma, T.; Narita, H.; Igawa, N.; Ishii, Y.; Bennington, S. M.; Kiyanagi, Y. *Physica B* **2006**, *385*, 202.

[145] Prager, M.; Press, W. *J. Chem. Phys.* **2006**, *125*, 214703.

[146] Tait, K. T.; Trouw, F.; Zhao, Y.; Brown, C. M.; Downs, R. T. *J. Chem. Phys.* **2007**, *127*, 134505.

[147] Ulivi, L.; Celli, M.; Giannasi, A.; Ramirez-Cuesta, A. J.; Bull, D. J.; Zoppi, M. *Phys. Rev. B* **2007**, *76*, 161401(R).

[148] Xu, M.; Sebastianelli, F.; Bačić, Z. *J. Chem. Phys.* **2008**, *128*, 244715.

[149] Sebastianelli, F.; Xu, M.; Bačić, Z. *J. Chem. Phys.* **2008**, *129*, 244706.

[150] Matanović, I.; Xu, M.; Moskowitz, J. W.; Eckert, J.; Bačić, Z. *J. Chem. Phys.* **2009**, *131*, 224308.

[151] Witt, A.; Sebastianelli, F.; Tuckerman, M. E.; Bačić, Z. *J. Phys. Chem. C* **2010**, *114*, 20775.

[152] Valdés, Á.; Kroes, G.-J. *Phys. Chem. Chem. Phys.* **2011**, *13*, 2935.

[153] Valdés, Á.; Kroes, G.-J. *J. Phys. Chem. C* **2012**, *116*, 21664.

[154] Felker, P. M. *J. Chem. Phys.* **2013**, *138*, 174306.

[155] Colognesi, D.; Celli, M.; Ulivi, L.; Xu, M.; Bačić, Z. *J. Phys. Chem. A* **2013**, *117*, 7314.

[156] Valdés, A.; Arismendi-Arrieta, D. J.; Prosmiti, R. *J. Phys. Chem. C* **2015**, *119*, 3945.

[157] Powers, A.; Marsalek, O.; Xu, M.; Ulivi, L.; Colognesi, D.; Tuckerman, M. E.; Bačić, Z. *J. Phys. Chem. Lett.* **2016**, *7*, 308.

[158] Ungemach, S. R.; Schaefer III, H. F. *J. Am. Chem. Soc.* **1974**, *96*, 7898.

[159] Bolis, G.; Clementi, E.; Wertz, D. H.; Scheraga, H. A.; Tosi, C. *J. Am. Chem. Soc.* **1983**, *105*, 355.

[160] Woon, D. E.; Zeng, P.; Beck, D. R. *J. Chem. Phys.* **1990**, *93*, 7808.

[161] Novoa, J. J.; Tarron, B.; Whangbo, M.-H.; Williams, J. M. *J. Chem. Phys.* **1991**, *95*, 5179.

[162] Szczęśńiak, M. M.; Chałasiński, G.; Cybulski, S. M.; Cieplak, P. *J. Chem. Phys.* **1993**, *98*, 3078–3089.

[163] Rovira, M. C.; Novoa, J. J.; Whangbo, M.-H.; Williams, J. M. *Chem. Phys.* **1995**, *200*, 319.

[164] Cao, Z.; Tester, J. W.; Trout, B. L. *J. Chem. Phys.* **2001**, *115*, 2550.

[165] Akin-Ojo, O.; Szalewicz, K. *J. Chem. Phys.* **2005**, *123*, 134311.

[166] Copeland, K. L.; Tschumper, G. S. *J. Chem. Theory Comput.* **2012**, *8*, 1646.

[167] Werner, H.-J. et al. MOLPRO, version 2010.1, a package of ab initio programs. 2010; see http://www.molpro.net.

[168] Warmbier, R.; Schneider, R.; Sharma, A. R.; Braams, B. J.; Bowman, J. M.; Hauschildt, P. H. *Astron. Astrophys.* **2009**, *495*, 655.

[169] Partridge, H.; Schwenke, D. W. *J. Chem. Phys.* **1997**, *106*, 4618.

[170] Yurchenko, S. N.; Tennyson, J.; Barber, R. J.; Thiel, W. *J. Mol. Spectrosc.* **2013**, *291*, 69.

[171] Lodi, L.; Tennyson, J.; Polyansky, O. L. *J. Chem. Phys.* **2011**, *135*, 034113.

[172] Dore, L.; Cohen, R. C.; Schmuttenmaer, C. A.; Busarow, K. L.; Elrod, M. J.; Loeser, J. G.; Saykally, R. J. *J. Chem. Phys.* **1994**, *100*, 863.

[173] Suenram, R. D.; Fraser, G. T.; Lovas, F. J.; Kawashima, Y. *J. Chem. Phys.* **1994**, *101*, 7230.

[174] Carter, S.; Shnider, H. M.; Bowman, J. M. *J. Chem. Phys.* **1999**, *110*, 8417.

[175] Jasper, A. W.; Miller, J. A. *J. Phys. Chem. A* **2009**, *113*, 5612.

[176] Troe, J.; Ushakov, V. G. *J. Chem. Phys.* **2012**, *136*, 214309.

[177] Conte, R.; Houston, P. L.; Bowman, J. M. *J. Phys. Chem. A* **2013**, *117*, 14028.

[178] Huang, X.; Braams, B. J.; Bowman, J. M.; Kelly, R. E. A.; Tennyson, J.; Groenenboom, G. C.; Van Der Avoird, A. *J. Chem. Phys.* **2008**, *128*, 034312.

[179] Shank, A.; Wang, Y.; Kaledin, A.; Braams, B. J.; Bowman, J. M. *J. Chem. Phys.* **2009**, *130*, 144314.

[180] Zhang, Q.; Ma, Y.; Fish, F.; Szczęśńiak, M. M.; Buch, V. *J. Chem. Phys.* **1992**, *96*, 6039.

[181] Weida, M. J.; Nesbitt, D. J. *J. Chem. Phys.* **1999**, *110*, 156.

[182] Wang, X.-G.; Carrington, T. *J. Chem. Phys.* **2011**, *134*, 044313.

[183] Zeng, T.; Li, H.; Le Roy, R. J.; Roy, P.-N. *J. Chem. Phys.* **2011**, *135*, 094394.

[184] van der Avoird, A.; Nesbitt, D. J. *J. Chem. Phys.* **2011**, *134*, 044314.

[185] Ziemkiewicz, M. P.; Pluetzer, C.; Nesbitt, D. J.; Scribano, Y.; Faure, A.; van der Avoird, A. *J. Chem. Phys.* **2012**, *137*, 084301.

[186] Hodges, M. P.; Wheatley, R. J.; Schenter, G. K.; Harvey, A. H. *J. Chem. Phys.* **2004**, *120*, 710.

[187] Faure, A.; Valiron, P.; Wernli, M.; Wiesenfeld, L.; Rist, C.; Noga, J.; Tennyson, J. *J. Chem. Phys.* **2005**, *122*, 221102.

[188] Valiron, P.; Wernli, M.; Faure, A.; Wiesenfeld, L.; Rist, C.; Kedžuch, S.; Noga, J. *J. Chem. Phys.* **2008**, *129*, 134306.

[189] Schwenke, D. W. *J. Chem. Phys.* **1988**, *89*, 2076.

[190] Deible, M. J.; Tuguldur, O.; Jordan, K. D. *J. Phys. Chem. B* **2014**, *118*, 8257.

[191] Garberoglio, G.; Jankowski, P.; Szalewicz, K.; Harvey, A. H. *J. Chem. Phys.* **2012**, *137*, 154308.

[192] Patkowski, K.; Cencek, W.; Jankowski, P.; Szalewicz, K.; Mehl, J. B.; Garberoglio, G.; Harvey, A. H. *J. Chem. Phys.* **2008**, *129*, 094304.

[193] Hinde, R. J. *J. Chem. Phys.* **2008**, *128*, 154308.

[194] Babin, V.; Leforestier, C.; Paesani, F. *J. Chem. Theory Comput.* **2013**, *9*, 5395.

[195] Babin, V.; Medders, G. R.; Paesani, F. *J. Chem. Theory Comput.* **2014**, *10*, 1599.

[196] Medders, G. R.; Babin, V.; Paesani, F. *J. Chem. Theory Comput.* **2014**, *10*, 2906.

[197] Fanourgakis, G. S.; Xantheas, S. S. *J. Chem. Phys.* **2008**, *128*, 074506.

[198] Conte, R.; Qu, C.; Bowman, J. M. *J. Chem. Theory Comput.* **2015**, *11*, 1631.

[199] Xantheas, S. S. *Can. J. Chem. Eng.* **2012**, *90*, 843.

[200] Duley, W. W. *Astrophys. J.* **1996**, *471*, L57.

[201] Petrie, S.; Bohme, D. K. *Mass Spectrom. Rev.* **2007**, *26*, 258.

[202] Snow, T. P.; Bierbaum, V. M. *Annu. Rev. Anal. Chem.* **2008**, *1*, 229.

[203] Drossart, P.; Maillard, J.-P.; Caldwell, J.; Kim, S. J.; Watson, J. K. G.; Majewski, W. A.; Tennyson, J.; Miller, S.; Atreya, S. K.; Clarke, J. T.; Waite, J. H.; Wagener, R. *Nature* **1989**, *340*, 539.

[204] Geballe, T. R.; Oka, T. *Nature* **1996**, *384*, 334.

[205] Nagashima, U.; Morokuma, K.; Tanaka, H. *J. Phys. Chem.* **1992**, *96*, 4294.

[206] Štich, I.; Marx, D.; Parrinello, M.; Terakura, K. *J. Chem. Phys.* **1997**, *107*, 9482.

[207] Barbatti, M.; Jalbert, G.; Nascimento, M. A. C. *J. Chem. Phys.* **2001**, *114*, 7066.

[208] Chermette, H.; Ymmud, I. V. *Phys. Rev. B* **2001**, *63*, 165427.

[209] Prosmiti, R.; Villarreal, P.; Delgado-Barrio, G. *J. Phys. Chem. A* **2003**, *107*, 4768.

[210] Yamaguchi, Y.; Gaw, J. F.; Remington, R. B.; Schaefer, I., H. F. *J. Chem. Phys.* **1987**, *86*, 5072.

[211] Xie, Z.; Braams, B. J.; Bowman, J. M. *J. Chem. Phys.* **2005**, *122*, 224307.

[212] Aguado, A.; Barragán, P.; Prosmiti, R.; Delgado-Barrio, G.; Villarreal, P.; Roncero, O. *J. Chem. Phys.* **2010**, *133*, 024306.

[213] Barragán, P.; Prosmiti, R.; Roncero, O.; Aguado, A.; Villarreal, P.; Delgado-Barrio, G. *J. Chem. Phys.* **2010**, *133*, 054303.

[214] Barragán, P.; Prosmiti, R. *Int. J. Quantum Chem.* **2012**, *113*, 651.

[215] Barragán, P.; Prosmiti, R.; Wang, Y.; Bowman, J. M. *J. Chem. Phys.* **2012**, *136*, 224302.

[216] Ohta, Y.; Ohta, K.; Kinugawa, K. *J. Chem. Phys.* **2004**, *121*, 10991.

[217] Acioli, P. H.; Xie, Z.; Braams, B. J.; Bowman, J. M. *J. Chem. Phys.* **2008**, *128*, 104318.

[218] Pérez de Tudela, R.; Barragán, P.; Prosmiti, R.; Villarreal, P.; Delgado-Barrio, G. *J. Phys. Chem. A* **2011**, *115*, 2483.

[219] McGuire, B. A.; Wang, Y.; Bowman, J. M.; Widicus Weaver, S. L. *J. Phys. Chem. Lett.* **2011**, *2*, 1405.

[220] Lin, Z.; McCoy, A. B. *J. Phys. Chem. Lett.* **2012**, *3*, 3690.

[221] Lin, Z.; McCoy, A. B. *J. Phys. Chem. A* **2013**, *117*, 11725.

[222] Cheng, T. C.; Bandyopadyay, B.; Wang, Y.; Carter, S.; Braams, B. J.; Bowman, J. M.; Duncan, M. A. *J. Phys. Chem. Lett.* **2010**, *1*, 758.

[223] Cheng, T. C.; Jiang, L.; Asmis, K. R.; Wang, Y.; Bowman, J. M.; Ricks, A. M.; Duncan, M. A. *J. Phys. Chem. Lett.* **2012**, *3*, 3160.

[224] Sanz-Sanz, C.; Roncero, O.; Valdés, A.; Prosmiti, R.; Delgado-Barrio, G.; Villarreal, P.; Barragán, P.; Aguado, A. *Phys. Rev. A* **2011**, *84*, 060502.

[225] Aguado, A.; Sanz-Sanz, C.; Villarreal, P.; Roncero, O. *Phys. Rev. A* **2012**, *85*, 032514.

[226] Valdés, A.; Prosmiti, R.; Delgado-Barrio, G. *J. Chem. Phys.* **2012**, *136*, 104302.

[227] Valdés, A.; Barragán, P.; Sanz-Sanz, C.; Prosmiti, R.; Villarreal, P.; Delgado-Barrio, G. *Theor. Chem. Acc.* **2012**, *131*, 1210.

[228] Valdés, A.; Prosmiti, R. *J. Phys. Chem. A* **2013**, *117*, 9518.

[229] Song, H.; Lee, S.-Y.; Yang, M.; Lu, Y. *J. Chem. Phys.* **2013**, *138*, 124309.

[230] Okumura, M.; Yeh, L. I.; Lee, Y. T. *J. Chem. Phys.* **1985**, *83*, 3705.

[231] Okumura, M.; Yeh, L. I.; Lee, Y. T. *J. Chem. Phys.* **1988**, *88*, 79.

[232] Young, J. W.; Cheng, T. C.; Bandyopadhyay, B.; Duncan, M. A. *J. Phys. Chem. A* **2013**, *117*, 6984.

[233] Barbatti, M.; Nascimento, M. A. C. *J. Chem. Phys.* **2003**, *119*, 5444.

[234] Peterson, K. A.; Adler, T. B.; Werner, H.-J. *J. Chem. Phys.* **2008**, *128*, 084102.

[235] Madeja, F.; Havenith, M. *J. Chem. Phys.* **2002**, *117*, 7162.

[236] Ortlieb, M.; Havenith, M. *J. Phys. Chem. A* **2007**, *111*, 7355.

[237] Gutberlet, A.; Schwaab, G. W.; Havenith, M. *Chem. Phys.* **2008**, *343*, 158.

[238] Birer, Ö.; Havenith, M. *Annu. Rev. Phys. Chem.* **2009**, *60*, 263.

[239] Havenith, M.; Birer, O. In *Handbook of high-resolution spectroscopy*; Quack, M., Merkt, F., Eds.; Wiley, 2011; Vol. 2; p 1119.

[240] Goroya, K. G.; Zhu, Y.; Sun, P.; Duan, C. *J. Chem. Phys.* **2014**, *140*, 164311.

[241] Bertie, J. E.; Michaelian, K. H. *J. Chem. Phys.* **1982**, *76*, 886.

[242] Bertie, J. E.; Michaelian, K. H.; Eysel, H. H.; Hager, D. *J. Chem. Phys.* **1986**, *85*, 4779.

[243] Wachs, T.; Borchardt, D.; Bauer, S. H. *Spectrochim. Acta A* **1987**, *43*, 965.

[244] Maréchal, Y. *J. Chem. Phys.* **1987**, *87*, 6344.

[245] Ito, F.; Nakanaga, T. *Chem. Phys.* **2002**, *277*, 163.

[246] Georges, R.; Freytes, M.; Hurtmans, D.; Kleiner, I.; Vander Auwera, J.; Herman, M. *Chem. Phys.* **2004**, *305*, 187.

[247] Ito, F. *Chem. Phys. Lett.* **2007**, *447*, 202.

[248] Zielke, P.; Suhm, M. A. *Phys. Chem. Chem. Phys.* **2007**, *9*, 4528.

[249] Ito, F. *J. Chem. Phys.* **2008**, *128*, 114310.

[250] Olbert-Majkut, A.; Ahokas, J.; Lundell, J.; Pettersson, M. *Chem. Phys. Lett.* **2009**, *468*, 176.

[251] Chang, Y.-T.; Yamaguchi, Y.; Miller, W. H.; Schaefer, H. F. *J. Am. Chem. Soc.* **1987**, *109*, 7245.

[252] Shida, N.; Barbara, P. F.; Almlöf, J. E. *J. Chem. Phys.* **1991**, *94*, 3633.

[253] Vener, M. V.; Kühn, O.; Bowman, J. M. *Chem. Phys. Lett.* **2001**, *349*, 562.

[254] Tautermann, C. S.; Voegele, A. F.; Liedl, K. R. *J. Chem. Phys.* **2004**, *120*, 631.

[255] Smedarchina, Z.; Fernández-Ramos, A.; Siebrand, W. *Chem. Phys. Lett.* **2004**, *395*, 339.

[256] Mil'nikov, G. V.; Kühn, O.; Nakamura, H. *J. Chem. Phys.* **2005**, *123*, 074308.

[257] Mil'nikov, G.; Nakamura, H. *Phys. Chem. Chem. Phys.* **2008**, *10*, 1374.

[258] Barnes, G. L.; Sibert, E. L. *J. Chem. Phys.* **2008**, *129*, 164317.

[259] Barnes, G. L.; Squires, S. M.; Sibert, E. L. *J. Phys. Chem. B* **2008**, *112*, 595.

[260] Matanović, I.; Došlić, N.; Johnson, B. R. *J. Chem. Phys.* **2008**, *128*, 084103.

[261] Luckhaus, D. *Phys. Chem. Chem. Phys.* **2010**, *12*, 8357.

[262] Jain, A.; Sibert, E. L. *J. Chem. Phys.* **2015**, *142*, 084115.

[263] Kim, Y. *J. Am. Chem. Soc.* **1996**, *118*, 1522.

[264] Lim, J.-H.; Lee, E. K.; Kim, Y. *J. Phys. Chem. A* **1997**, *101*, 2233.

[265] Miura, S.; Tuckerman, M. E.; Klein, M. L. *J. Chem. Phys.* **1998**, *109*, 5290.

[266] Kohanoff, J.; Koval, S.; Estrin, D. A.; Laria, D.; Abashkin, Y. *J. Chem. Phys.* **2000**, *112*, 9498.

[267] Markwick, P. R. L.; Doltsinis, N. L.; Marx, D. *J. Chem. Phys.* **2005**, *122*, 054112.

[268] Ushiyama, H.; Takatsuka, K. *J. Chem. Phys.* **2001**, *115*, 5903.

[269] Fillaux, F. *Chem. Phys. Lett.* **2005**, *408*, 302.

[270] Ivanov, S. D.; Grant, I. M.; Marx, D. *J. Chem. Phys.* **2015**, *143*, 124304.

[271] Florio, G. M.; Zwier, T. S.; Myshakin, E. M.; Jordan, K. D.; Sibert, E. L. *J. Chem. Phys.* **2003**, *118*, 1735.

[272] Matanović, I.; Došlić, N. *Chem. Phys.* **2007**, *338*, 121.

[273] Barnes, G. L.; Sibert, E. L. *J. Mol. Spectrosc.* **2008**, *249*, 78.

[274] Pitsevich, G. A.; Malevich, A. E.; Kozlovskaya, E. N.; Doroshenko, I. Y.; Sablinskas, V.; Pogorelov, V.; Dovgal, D.; Balevicius, V. *Vib. Spectrosc.* **2015**, *79*, 67.

[275] Miliordos, E.; Xantheas, S. S. *J. Chem. Phys.* **2015**, *142*, 094311.

[276] Kamarchik, E.; Wang, Y.; Bowman, J. *J. Phys. Chem. A* **2009**, *113*, 7556.

[277] Wang, Y.; Bowman, J. M. *J. Chem. Phys.* **2008**, *129*, 121103.

[278] Wang, Y.; Bowman, J. M. *J. Chem. Phys.* **2013**, *139*, 154303.

[279] Millikan, R. C.; Pitzer, K. S. *J. Am. Chem. Soc.* **1958**, *80*, 3515.

[280] Pimentel, G. C.; Charles, S. W. *Pure Appl. Chem.* **1963**, *7*, 111.

[281] Kumagai, N.; Kawamura, K.; Yokokawa, T. *Mol. Sim.* **1994**, *12*, 177.

[282] Dauber-Osguthorpe, P.; Roberts, V. A.; Osguthorpe, D. J.; Wolff, J.; Genest, M.; Hagler, A. T. *Proteins.* **1988**, *4*, 31.

[283] Soler, J. M.; Artacho, E.; Gale, J. D.; García, A.; Junquera, J.; Ordejón, P.; Sánchez-Portal, D. *J. Phys. Condens. Matter* **2002**, *14*, 2745.

[284] Perdew, J. P.; Burke, K.; Ernzerhof, M. *Phys. Rev. Lett.* **1996**, *77*, 3865.

[285] Yoshioki, S. *J. Mol. Graph. Model.* **2007**, *25*, 856.

[286] Davidson, E. R. *J. Comput. Phys.* **1975**, *17*, 87.

[287] Serrallach, A.; Meyer, R.; Günthard, H. *J. Mol. Spectrosc.* **1974**, *52*, 94.

[288] Xu, L.-H.; Wang, X.; Cronin, T. J.; Perry, D. S.; Fraser, G. T.; Pine, A. S. *J. Mol. Spectrosc.* **1997**, *185*, 158.

[289] Boyarkin, O. V.; Lubich, L.; Settle, R. D. F.; Perry, D. S.; Rizzo, T. R. *J. Chem. Phys.* **1997**, *107*, 8409.

[290] Boyarkin, O. V.; Rizzo, T. R.; Perry, D. S. *J. Chem. Phys.* **1999**, *110*, 11346.

[291] Rueda, D.; Boyarkin, O. V.; Rizzo, T. R.; Chirokolava, A.; Perry, D. S. *J. Chem. Phys.* **2005**, *122*, 044314.

[292] Twagirayezu, S.; Perry, D. S.; Neill, J. L.; Muckle, M. T. *J. Mol. Spectrosc.* **2010**, *262*, 65.

[293] Twagirayezu, S.; Clasp, T. N.; Perry, D. S.; Neill, J. L.; Muckle, M. T.; Pate, B. H. *J. Phys. Chem. A* **2010**, *114*, 6818.

[294] Twagirayezu, S.; Wang, X.; Perry, D. S.; Neill, J. L.; Muckle, M. T.; Pate, B. H.; Xu, L.-H. *J. Phys. Chem. A* **2011**, *115*, 9748.

[295] Xu, L. H.; Hougen, J. T. *J. Mol. Spectrosc.* **1995**, *169*, 396.

[296] Xu, L.-H.; Hougen, J. T. *J. Mol. Spectrosc.* **1995**, *173*, 540.

[297] Wang, X.; Perry, D. S. *J. Chem. Phys.* **1998**, *109*, 10795.

[298] Xu, L.-H. *J. Chem. Phys.* **2000**, *113*, 3980.

[299] Miani, A.; Hanninen, V.; Horn, M.; Halonen, L. *Mol. Phys.* **2000**, *98*, 1737.

[300] Fehrensen, B.; Luckhaus, D.; Quack, M.; Willeke, M.; Rizzo, T. R. *J. Chem. Phys.* **2003**, *119*, 5534.

[301] Hänninen, V.; Halonen, L. *Mol. Phys.* **2003**, *101*, 2907.

[302] III, E. L. S.; Castillo-Chará, J. *J. Chem. Phys.* **2005**, *122*, 194306.

[303] Carter, S.; Handy, N. C.; Bowman, J. M. *Mol. Phys.* **2009**, *107*, 727.

[304] Aronowitz, D.; Naegell, D. W.; Glassman, I. *J. Phys. Chem.* **1977**, *81*, 2555.

[305] Harding, L. B.; Schlegel, H. B.; Krishnan, R.; Pople, J. A. *J. Phys. Chem.* **1980**, *84*, 3394.

[306] Hidaka, Y.; Oki, T.; Kawano, H.; Higashihara, T. *J. Phys. Chem.* **1989**, *93*, 7134.

[307] Jordan, M. J. T.; Smith, S. C.; Gilbert, R. G. *J. Phys. Chem.* **1991**, *95*, 8685.

[308] Anastasi, C.; Beverton, S.; Ellermann, T.; Pagsberg, P. *J. Chem. Soc. Faraday Trans.* **1991**, *87*, 2325.

[309] Bauschlicher, C. W.; Langhoff, S. R.; Walch, S. P. *J. Chem. Phys.* **1992**, *96*, 450.

[310] Oser, H.; Stothard, N. D.; Humpfer, R.; Grotheer, H. H. *J. Phys. Chem.* **1992**, *96*, 5359.

[311] Walch, S. P. *J. Chem. Phys.* **1993**, *98*, 3163.

[312] Fagerstrom, K.; Lund, A.; Mahmoud, G.; Jodkowski, J. T.; Ratajczak, E. *Chem. Phys. Lett.* **1993**, *204*, 226.

[313] Fagerstrom, K.; Lund, A.; Mahmoud, G.; Jodkowski, J. T.; Ratajczak, E. *Chem. Phys. Lett.* **1994**, *224*, 43.

[314] Pereira, R. D. A.; Baulch, D. L.; Pilling, M. J.; Robertson, S. H.; Zeng, G. *J. Phys. Chem. A* **1997**, *101*, 9681.

[315] Wilson, C.; Balint-Kurti, G. G. *J. Phys. Chem. A* **1998**, *102*, 1625.

[316] Xia, W. S.; Zhu, R. S.; Lin, M. C.; Mebel, A. M. *Faraday Discuss.* **2001**, 191.

[317] Chang, A. H. H.; Lin, S. H. *Chem. Phys. Lett.* **2002**, *363*, 175.

[318] Chang, A. H. H.; Lin, S. H. *Chem. Phys. Lett.* **2004**, *384*, 229.

[319] Yu, H.-G.; Muckerman, J. T. *J. Phys. Chem. A* **2004**, *108*, 8615.

[320] Krasnoperov, L. N.; Michael, J. V. *J. Phys. Chem. A* **2004**, *108*, 8317.

[321] Fockenberg, C.; Weston, R. E. J.; Muckerman, J. T. *J. Phys. Chem. B* **2005**, *109*, 8415.

[322] Jasper, A. W.; Klippenstein, S. J.; Harding, L. B.; Ruscic, B. *J. Phys. Chem. A* **2007**, *111*, 3932.

[323] Srinivasan, N. K.; Su, M.-C.; Michael, J. V. *J. Phys. Chem. A* **2007**, *111*, 3951.

[324] Xu, K.; Xu, Z. F.; Lin, M. C. *Mol. Phys.* **2007**, *105*, 2763.

[325] Vasudevan, V.; Cook, R. D.; Hanson, R. K.; Bowman, C. T.; Golden, D. M. *Int. J. Chem. Kinet.* **2008**, *40*, 488.

[326] Lu, K.-W.; Matsui, H.; Huang, C.-L.; Raghunath, P.; Wang, N.-S.; Lin, M. C. *J. Phys. Chem. A* **2010**, *114*, 5493.

[327] Ree, J.; Kim, Y. H.; Shin, H. K. *Int. J. Chem. Kinet.* **2011**, *43*, 455.

[328] de M. Rodrigo, R. C.; Bauerfeldt, G. F. *Int. J. Quantum Chem.* **2012**, *112*, 3132.

[329] Sangwan, M.; Chesnokov, E. N.; Krasnoperov, L. N. *J. Phys. Chem. A* **2012**, *116*, 8661.

[330] Fu, J.; Liu, J.; Xu, Z.; Ren, C.; Deng, B. *Energy* **2013**, *55*, 778.

[331] Shao, K.; Fu, B.; Zhang, D. H. *Phys. Chem. Chem. Phys.* **2015**, *17*, 24098–24107.

[332] Martín, S.; Martín-Pintado, J.; Mauersberger, R. *Astron. Astrophys.* **2006**, *450*, L13.

[333] Whittet, D. C. B.; Cook, A. M.; Herbst, E.; Chiar, J. E.; Shenoy, S. S. *Astrophys. J.* **2011**, *742*, 28.

[334] Mebel, A. M.; Morokuma, K.; Lin, M. C. *J. Chem. Phys.* **1995**, *103*, 7414.

[335] Werner, H.-J. et al. MOLPRO, version 2008.1, a package of ab initio programs. 2008; see http://www.molpro.net.

[336] Karlström, G.; Lindh, R.; Malmqvist, P. A.; Roos, B. O.; Ryde, U.; Veryazov, V.; Widmark, P. O.; Cossi, M.; Schimmelpfennig, B.; Neogrády, P.; Seijo, L. *Comput. Mater. Sci.* **2003**, *28*, 222.

[337] Veryazov, V.; Widmark, P. O.; Serrano-Andres, L.; Lindh, R.; Roos, B. O. *Int. J. Quantum Chem.* **2004**, *100*, 626.

[338] Aquilante, F.; De Vico, L.; Ferré, N.; Ghigo, G.; Malmqvist, P.-A.; Neogrády, P.; Pedersen, T. B.; Pitoňák, M.; Reiher, M.; Roos, B. O.; Serrano-Andrés, L.; Urban, M.; Veryazov, V.; Lindh, R. *J. Comput. Chem.* **2010**, *31*, 224.

[339] Ruscic, B.; Boggs, J. E.; Burcat, A.; Császár, A. G.; Demaison, J.; Janoschek, R.; Martin, J. M. L.; Morton, M. L.; Rossi, M. J.; Stanton, J. F.; Szalay, P. G.; Westmoreland, P. R.; Zabel, F.; Bérces, T. *J. Phys. Chem. Ref. Data* **2005**, *34*, 573.

[340] Jacobson, M. P.; Field, R. W. *J. Phys. Chem. A* **2000**, *104*, 3073.

[341] Chen, C.; Braams, B.; Lee, D. Y.; Bowman, J. M.; Houston, P. L.; Stranges, D. *J. Phys. Chem. Lett* **2010**, *1*, 1875.

[342] Homayoon, Z.; Vazquez, S. A.; Rodriguez-Fernandez, R.; Martinez-Nunez, E. *J. Phys. Chem. A* **2011**, *115*, 979.

[343] Burnett, S. M.; Stevens, A. E.; Feigerle, C. S.; Lineberger, W. C. *Chem. Phys. Lett.* **1983**, *100*, 124.

[344] Ervin, K. M.; Ho, J.; Lineberger, W. C. *J. Chem. Phys.* **1989**, *91*, 5974.

[345] Levin, J.; Feldman, H.; Baer, A.; Ben-Hamu, D.; Heber, O.; Zajfman, D.; Vager, Z. *Phys. Rev. Lett.* **1998**, *81*, 3347.

[346] Zou, S. L.; Bowman, J. M. *J. Chem. Phys.* **2002**, *117*, 5507.

[347] Xu, D. G.; Guo, H.; Zou, S. L.; Bowman, J. M. *Chem. Phys. Lett.* **2003**, *377*, 582.

[348] Han, H. X.; Li, A. Y.; Guo, H. *J. Chem. Phys.* **2014**, *141*, 244312.

[349] Ren, Y.; Bian, W. *J. Phys. Chem. Lett.* **2015**, *6*, 1824.

[350] Perry, D. S.; Martens, J.; Amyay, B.; Herman, M. *Mol. Phys.* **2012**, *110*, 2687.

[351] Perry, D. S.; Miller, A.; Amyay, B.; Fayt, A.; Herman, M. *Mol. Phys.* **2010**, *108*, 1115.

[352] Huang, Y. B.; He, G. X.; Yang, Y. G.; Hashimoto, S.; Gordon, R. J. *Chem. Phys. Lett.* **1994**, *229*, 621.

[353] Huang, Y. B.; Yang, Y. A.; He, G. X.; Gordon, R. J. *J. Chem. Phys.* **1993**, *99*, 2752.

[354] Reilly, P. T. A.; Xie, Y. J.; Gordon, R. J. *Chem. Phys. Lett.* **1991**, *178*, 511.

[355] Lin, S. R.; Lin, S. C.; Lee, Y. C.; Chou, Y. C.; Chen, I. C.; Lee, Y. P. I. *J. Chem. Phys.* **2001**, *114*, 160.

[356] Blank, D. A.; Sun, W. Z.; Suits, A. G.; Lee, Y. T.; North, S. W.; Hall, G. E. *J. Chem. Phys.* **1998**, *108*, 5414.

[357] Riehl, J. F.; Morokuma, K. *J. Chem. Phys.* **1994**, *100*, 8976.

[358] Nunez, M. E.; Vazquez, S. A.; Aoiz, F. J.; Banares, L.; Castillo, J. F. *Chem. Phys. Lett.* **2004**, *386*, 225.

[359] Nunez, E. M.; Fernandez-Ramos, A.; Vazquez, S. A.; Aoiz, F. J.; Banares, L. *J. Phys. Chem. A* **2003**, *107*, 7611.

[360] Fernando, R.; Qu, C.; Bowman, J. M.; Field, R. W.; Suits, A. G. *J. Phys. Chem. Lett.* **2015**, *6*, 2457.

[361] Frisch, M. J. et al. Gaussian 09, revision C.01. 2010.

[362] Zhao, Y.; Truhlar, D. G. *Theor. Chem. Acc.* **2008**, *120*, 215.

[363] Hu, X.; Hase, W. L.; Pirraglia, T. *J. Comp. Chem.* **1991**, *12*, 1014.

[364] Czakó, G.; Bowman, J. M. *Science* **2011**, *334*, 343.

[365] Czakó, G.; Bowman, J. M. *J. Phys. Chem. A* **2014**, *118*, 2839.

[366] Espinosa-Garcia, J.; Rangel, C.; Garcia-Bernaldez, J. C. *Phys. Chem. Chem. Phys.* **2015**, *17*, 6009.

[367] Yan, S.; Wu, Y. T.; Zhang, B.; Yue, X.-F.; Liu, K. *Science* **2007**, *316*, 1723.

[368] Zhang, W.; Kawamata, H.; Liu, K. *Science* **2009**, *325*, 303.

[369] Troya, D.; Weiss, P. J. E. *J. Chem. Phys.* **2006**, *124*, 074313.

[370] Czakó, G. *J. Phys. Chem. A* **2012**, *116*, 7467.

[371] Beck, R. D.; Maroni, P.; Papageorgopoulos, D. C.; Dang, T. T.; Schmid, M. P.; Rizzo, T. R. *Science* **2003**, *302*, 98.

[372] Juurlink, L. B. F.; Smith, R. R.; Killelea, D. R.; Utz, A. L. *Phys. Rev. Lett.* **2005**, *94*, 208303.

[373] Sacchi, M.; Wales, D. J.; Jenkins, S. J. *J. Phys. Chem. C* **2011**, *115*, 21832.

[374] Hundt, P. M.; Ueta, H.; van Reijzen, M. E.; Jiang, B.; Guo, H.; Beck, R. D. *J. Phys. Chem. A* **2015**, *119*, 12442.

[375] Noid, D. W.; Koszykowski, M. L.; Marcus, R. A. *J. Chem. Phys.* **1980**, *73*, 391.

[376] De Leon, N.; Heller, E. J. *J. Chem. Phys.* **1984**, *81*, 5957.

[377] Miller, W. H. *J. Chem. Phys.* **1984**, *81*, 3573.

[378] Eaker, C. W.; Schatz, G. C.; De Leon, N.; Heller, E. J. *J. Chem. Phys.* **1984**, *81*, 5913.

[379] Martens, C. C.; Ezra, G. S. *J. Chem. Phys.* **1985**, *83*, 2990.

[380] Ezra, G. S.; Martens, C. C.; Fried, L. E. *J. Phys. Chem.* **1987**, *91*, 3721.

[381] Solov'ev, E. A. *Sov. Phys. JETP* **1978**, *48*, 635.

[382] Johnson, B. R. *J. Chem. Phys.* **1985**, *83*, 1204.

[383] Skodje, R. T.; Borondo, F.; Reinhardt, W. P. *J. Chem. Phys.* **1985**, *82*, 4611.

[384] Skodje, R. T.; Borondo, F. *J. Chem. Phys.* **1986**, *84*, 1533.

[385] Johnson, B. R. *J. Chem. Phys.* **1987**, *86*, 1445.

[386] Zakrzewski, J.; Saini, S.; Taylor, H. S. *Phys. Rev. A* **1988**, *38*, 3877.

[387] Saini, S.; Zakrzewski, J.; Taylor, H. S. *Phys. Rev. A* **1988**, *38*, 3900.

[388] Sun, Q.; Bowman, J. M.; Gazdy, B. *J. Chem. Phys.* **1988**, *89*, 3124.

[389] Wong, S. Y. Y.; Benoit, D. M.; Lewerenz, M.; Brown, A.; Roy, P. N. *J. Chem. Phys* **2011**, *134*, 094110.

[390] Schatz, G. In *Molecular Collision Dynamics*; Bowman, J., Ed.; Springer-Verlag, Berlin, 1983; pp 25–60.

[391] Corchado, J. C.; Espinosa-Garcia, J. *Phys. Chem. Chem. Phys.* **2009**, *11*, 10157.

[392] Bose, A.; Makri, N. *J. Chem. Phys.* **2015**, *143*, 114114.

[393] Huang, J.; Valentini, J. J.; Muckerman, J. T. *J. Chem. Phys.* **1995**, *102*, 5695.

[394] Castillo, J. F.; Aoiz, F. J.; Bañares, L. *J. Chem. Phys.* **2006**, *125*, 124316.

[395] Landau, L.; Lifshitz, E. M. *Mechanics*, 3rd ed.; Pergamon: Oxford, 1976.

[396] Dymarsky, A. Y.; Kudin, K. N. *J. Chem. Phys.* **2005**, *122*, 124103.

[397] W. P. Reinhardt, I. D. *Proc. R. Soc. Lond.* **1987**, *413*, 157.